Supplement of Atmos. Meas. Tech., 15, 3527–3553, 2022
https://doi.org/10.5194/amt-15-3527-2022-supplement
© Author(s) 2022. CC BY 4.0 License.

Atmospheric Measurement Techniques
Open Access

Supplement of

Ozone Monitoring Instrument (OMI) collection 4: establishing a 17-year-long series of detrended level-1b data

Quintus Kleipool et al.

Correspondence to: Antje Ludewig (antje.ludewig@knmi.nl)

The copyright of individual parts of the supplement might differ from the article licence.

Royal Netherlands
Meteorological Institute
Ministry of Infrastructure
and Water Management

Algorithm Theoretical Basis Document for the collection 4 L01b data processing of the Ozone Monitoring Instrument

document number : AURA-OMI-KNMI-L01B-0002-SD
version : 24170
date : 2021-07-16

Copyright statement

This work is licensed under
the Creative Commons Attribution-NonCommercial-NoDerivs 3.0 Unported License.
To view a copy of this license, visit `http://creativecommons.org/licenses/by-nc-nd/3.0/`
or send a letter to Creative Commons, 444 Castro Street, Suite 900, Mountain View, California, 94041, USA.

Disclaimer

The Royal Netherlands Meteorological Institute KNMI does not represent or endorse the accuracy or reliability of any of the information or content (collectively the “Information”) contained in this document. The reader hereby acknowledges that any reliance upon any Information shall be at the reader’s sole risk. The Royal Netherlands Meteorological Institute KNMI reserves the right, in its sole discretion and without any obligation, to make improvements to the Information or correct any error or omissions in any portion of the Information.

THE INFORMATION IS PROVIDED BY THE ROYAL NETHERLANDS METEOROLOGICAL INSTITUTE KNMI ON AN “AS IS” BASIS, AND THE ROYAL NETHERLANDS METEOROLOGICAL INSTITUTE KNMI EXPRESSLY DISCLAIMS ANY AND ALL WARRANTIES, EXPRESS OR IMPLIED, INCLUDING WITHOUT LIMITATION WARRANTIES OF MERCHANTABILITY AND FITNESS FOR A PARTICULAR PURPOSE, WITH RESPECT TO THE INFORMATION. IN NO EVENT SHALL THE ROYAL NETHERLANDS METEOROLOGICAL INSTITUTE KNMI BE LIABLE FOR ANY DIRECT, INDIRECT, INCIDENTAL, PUNITIVE, OR CONSEQUENTIAL DAMAGES OF ANY KIND WHATSOEVER WITH RESPECT TO THE INFORMATION.

Contributing authors
Antje Ludewig (editor)
Daley Adrichem
David Haffner (NASA)
Raoul Harel
Mirna van Hoek
Glen Jaross (NASA)
Quintus Kleipool
Jonatan Leloux
Erwin Loots
Emiel van der Plas
Nico Rozemeijer

Contents

List of Tables 8
List of Figures 9
1 Introduction 10
1.1 Mission status 10
1.2 Purpose and objective 10
1.3 Document overview 10
2 Reference documents 11
3 Terms, definitions and abbreviated terms 13
3.1 Terms and definitions 13
3.2 Acronyms and Abbreviations 13

I Mission overview 15
4 Introduction 15
5 Mission timeline 15
5.1 Pre-flight calibration 15
5.2 Launch and early operations 16
5.3 In-flight anomalies 17
5.3.1 Folding mirror mechanism anomaly 17
5.3.2 Row anomaly 17
5.3.3 Survival mode anomaly 18
5.3.4 WLS anomaly 18
5.4 Changes to the thermal configuration 18
5.5 Constellation exit and decommissioning 19
6 Calibration evolution in-flight 20
6.1 Collection 1 20
6.2 Collection 2 20
6.3 Collection 3 20
6.3.1 Irradiance radiometric calibration 20
6.3.2 Radiance radiometric calibration 20
6.3.3 Row anomaly detection and flagging 21
6.4 Collection 4 21
6.4.1 Dataformat and products 21
6.4.2 Changes to correction algorithms 21
6.4.3 Wavelength annotation 23
6.4.4 Time annotation 23
6.4.5 Geolocation line-of-sight assignment 23
6.4.6 Quality Flags 23

II Instrument description 25
7 Overview 25
8 Mechanical and thermal description 26
9 Optical design description 28
9.1 Telescope and instrument slit 29
9.2 UV spectrometer (bands 1 and 2) 30
9.3 VIS channel 30
10 Instrument electronics and detectors 31
10.1 Detector modules 31
10.2 Electronics unit (ELU) 34
10.3 Interface adapter module (IAM) 34

11 Calibration sources ... **34**
11.1 Mechanisms ... 34
11.1.1 Folding mirror mechanism (FMM) ... 35
11.1.2 Sun aperture mechanism (SAM) and solar mesh ... 35
11.1.3 Diffuser mechanism (DIFM) ... 35
11.2 Solar irradiance ... 35
11.3 White light source ... 36
11.4 Light emitting diodes ... 37

III Instrument operations **38**
12 Orbit definition ... **38**
13 Operational baseline ... **39**
14 Main observation modes ... **40**
14.1 Earth radiance measurements ... 40
14.2 Solar irradiance measurements ... 41
14.3 Background measurements ... 41
15 Instrument configuration ... **41**
15.1 Orbit-type activities ... 41
15.2 Stored command sequences ... 42
15.3 Stored instruction sequences ... 42
15.4 Electronic unit states ... 43

IV Correction algorithms for L01b processing **44**
16 Overview of algorithms and general remarks ... **44**
16.1 Uncorrected effects ... 46
16.2 Conventions ... 46
16.2.1 Units ... 46
16.2.2 Mathematical conventions ... 46
16.2.3 Correction algorithms ... 47
16.3 Noise and error propagation ... 47
17 Co-addition correction ... **48**
18 ADC conversion ... **48**
19 Offset correction ... **48**
19.1 Dynamic offset computation ... 49
20 Gain overshoot correction ... **49**
21 Gain correction ... **50**
21.1 Used parameters and symbols ... 50
21.2 Algorithm description ... 51
22 Voltage-to-charge correction ... **51**
23 Non-linearity correction ... **51**
23.1 Algorithm description ... 52
23.2 Used parameters and symbols ... 52
24 Binning factor correction ... **52**
25 Background correction ... **52**
25.1 Used parameters and symbols ... 53
25.2 Algorithm description ... 53
26 Smear ... **53**
27 Exposure time division ... **54**
27.1 Used parameters and symbols ... 54
27.2 Algorithm description ... 54
27.3 Error propagation ... 54

28 Pixel response non-uniformity 55
28.1 Used parameters and symbols 55
28.2 Algorithm description 55
28.3 Error propagation 55
29 Straylight correction 55
29.1 Used parameters and symbols 56
29.2 Algorithm description 56
30 Slit irregularity correction 57
30.1 Used parameters and symbols 57
30.2 Algorithm description 57
30.3 Error propagation 58
31 On irradiance, radiance and BSDF 58
32 Irradiance responsivity 58
32.1 Used parameters and symbols 58
32.2 Algorithm description 58
32.3 Error propagation 59
33 Radiance responsivity 59
33.1 Used parameters and symbols 59
33.2 Algorithm description 59
33.3 Error propagation 59
33.4 Earth-Sun distance normalization 60
33.4.1 Used parameters and symbols 60
33.4.2 Algorithm description 60
33.4.3 Error propagation 60
34 Irradiance responsivity as a function of diffuser incident angle 60
34.1 Used parameters and symbols 60
34.2 Algorithm description 61
35 Temporal CKDs and degradation 61
35.1 Diffuser degradation 61
35.2 Radiance degradation 61
35.3 Used parameters and symbols 62
35.4 Algorithm description 62
35.5 Error propagation 62
36 Irradiance averaging 62
36.1 Used parameters and symbols 62
36.2 Algorithm description and error propagation 63
36.3 Error propagation 63

V Annotation 64

37 Wavelength characterization 64
37.1 Nominal wavelength annotation 64
37.2 Wavelength correction due to the Doppler effect 65
37.3 Wavelength correction due to instrument temperature variations 65
37.4 Wavelength correction due to inhomogeneous slit illumination 65
38 Time bases and conversions 66
39 Geometrical definitions 69
39.1 Reference frame definitions 69
39.1.1 WGS84 Earth reference ellipsoid 69
39.1.2 Inertial reference frame 69
39.1.3 Mean-of-date reference frame 70
39.1.4 True-of-date reference frame 70
39.1.5 Earth-fixed reference frame 70
39.1.6 Topocentric reference frame 71
39.1.7 Local orbital reference frame 72

39.1.8 Local relative orbital reference frame 72
39.1.9 Spacecraft reference frame and LOS angles 73
39.1.10 Optical alignment reference frame 74
39.1.11 Fundamental reference frame 74
39.2 Reference frame transformations 75
39.2.1 Spacecraft reference frame to inertial reference frame 75
39.2.2 Aberration of Light 76
39.2.3 Inertial reference frame to Earth-fixed reference frame 76
39.2.4 Geocentric to geodetic coordinates 79
39.2.5 Earth-fixed reference frame to topocentric reference frame 79
39.2.6 Inertial reference frame to local orbital reference frame 80
39.2.7 Spacecraft reference frame to Optical Alignment reference frame 81
39.2.8 Earth-fixed reference frame to Fundamental reference frame 81
39.3 Intersection between a line and an ellipsoid 81

40 Geometrical algorithms 83
40.1 Ground pixel position 83
40.1.1 Ground pixel corner points 84
40.2 Satellite position 85
40.2.1 Satellite position and velocity interpolation 85
40.2.2 Satellite attitude interpolation 86
40.2.3 Sub-satellite point and altitude 86
40.2.4 Orbit phase 86
40.3 Solar angles 86
40.3.1 Position of the Sun in the true-of-date reference frame 87
40.3.2 Solar line of sight in the optical alignment reference frame 88
40.3.3 Velocity of spacecraft towards Sun 88
40.3.4 Spacecraft and Sun lines of sight from ground pixel 88
40.3.5 Atmospheric Refraction of Light 89

41 Quality assessment 91
41.1 Spacecraft in South Atlantic Anomaly 91
41.1.1 Point-in-polygon problem 91
41.2 Spacecraft manoeuvring 93
41.3 Irradiance solar elevation out-of-range 93
41.4 Spacecraft in Earth’s shadow 94
41.5 Ground pixel in Solar eclipse 95
41.5.1 Eclipse geometry 95
41.5.2 Eclipse period 98
41.5.3 Solar eclipse flagging 98
41.6 Ground pixel in Sun glint 99
41.7 Ground pixel night 99
41.8 Ground pixel descending 100
41.9 Ground pixel on boundary 100
41.10 Row anomaly flagging 100
41.11 Transient pixel flagging 100
41.11.1 Detection algorithm 101
41.11.2 Transient signals in radiance and irradiance measurements 101
41.12 Detector pixel quality flagging 102
41.13 Random telegraph signal pixels 102
41.14 Saturation flagging 102
41.15 Other notable flags 103
41.15.1 Offset flagging 103
41.15.2 Thermal instability 103

VI Appendix 104

A Philosophy on noise and errors 104
A.1 Signal, noise and error 104
A.1.1 Error 104
A.1.2 Noise 105
A.1.3 Summary 105
A.2 Signal propagation and flagging 105
A.3 Measurement noise propagation 106
A.4 Noise propagation in forward and reverse directions; rules and characteristics 106
B Binning 109
B.1 Binning tables 109
B.2 Effects of binning on signal and variance 111
B.2.1 Effect of binning on the signal 111
B.2.2 Effects of binning on error propagation 112
C Smear 114
C.1 Used parameters and symbols 114
C.1.1 Algorithm description: general 114
C.2 Algorithm description: binning, skipping and flagging 116
C.3 Algorithm description: co-addition 119
C.4 Algorithm description: computing the inverse of the matrix 120
C.5 Practical aspects 121
C.6 On two approaches 121
C.7 Error propagation 122
C.8 Concluding remarks 125
D Nonlinearity 126
D.1 Used parameters and symbols 126
D.2 Algorithm description 126
D.3 Error propagation 126
E Stored instruction sequences for calibration measurements 129
E.1 Solar calibration SIS 129
E.2 LED calibration SIS 129
E.3 WLS calibration SIS 130
E.4 Dark calibration SIS 131
E.5 Dark orbit SIS 131

List of Tables

1 Orbit parameters 16
2 FMM anomaly and test orbits. 17
3 Spectral range, resolution and sampling distances 25
4 OMI temperatures 27
5 Imaging properties 29
6 Groundpixel sizes 32
7 Reference orbit of the Aura mission 38
8 Binning factors and across-track ground pixel sizes for Earth radiance measurements 40
9 Characteristics of the main observation modes 41
10 L01b time bases 66
11 L01b time types 67
12 L01b time epochs 67
13 Leap seconds 68
14 Parameters to describe a solar eclipse 96
15 OMI binning scheme 109
16 OMI binning scheme for global Earth radiance measurements. 110
17 OMI binning scheme for spatial zoom-in Earth radiance measurements. 110
18 Appendix: Solar calibration SIS. 129
19 Appendix: Exit codes solar SIS 129
20 Appendix: LED calibration SIS. 130

21 Appendix: Exit codes LED SIS 130
22 Appendix: WLS calibration SIS. 130
23 Appendix: Exit codes WLS SIS 130
24 Appendix: Dark calibration SIS. 131
25 Appendix: Exit codes dark SIS 131
26 Appendix: Dark orbit calibration SIS. 131
27 Appendix: Exit codes dark orbit SIS 132

List of Figures

1 OMI measurement principle 16
2 OMI ground pixel size 16
3 Row anomaly over time 18
4 Functional overview of OMI 25
5 Thermal and mechanical design 26
6 Optical bench temperature 27
7 UV detector temperature 27
8 Instrument overview 28
9 Polarization scrambler 30
10 Optics of the VIS channel 31
11 Conceptual design of OMI 32
12 Layout of the detectors 33
13 DEM and ELU 34
14 QVD degradation 35
15 WLS supply voltage 36
16 WLS output during the mission 36
17 Aura orbit overview 38
18 OMI operations orbit definition 38
19 OMI original 466 orbits operations baseline 39
20 The new, simpler OMI operations baseline 40
21 L01b processing flow 45
22 Long term difference between UT1 and UTC. 68
23 Geocentric versus geodetic coordinates. 70
24 Definition of the inertial reference frame. 71
25 Definitions of the Earth-fixed and the topocentric reference frame. 72
26 Local orbital reference frame versus local relative orbital reference frame definition. 73
27 LOS angles definition within the Spacecraft reference frame. 74
28 Solar eclipse fundamental reference frame definition. 75
29 Precession and nutation of the Earth 77
30 Plot of the polar coordinate 77
31 Ground pixel extent definition. 85
32 Definition of the orbit phase. 87
33 Definition of the LOS angles from ground pixel to spacecraft and Sun. 89
34 The Van Allen radiation belts. 91
35 South Atlantic Anomaly at NASA's AURA OMI altitude. 92
36 Contour plots of the South Atlantic Anomaly (SAA) at OMI altitude. 92
37 Shadow of solar eclipse on 23 October 2014. 95
38 Definition of solar eclipse umbra, antumbra and penumbra. 96
39 Definition of solar eclipse geometry parameters. 97
40 Sun glint example of OMI. 99

1 Introduction

The Ozone Monitoring Instrument (OMI) was launched on the National Aeronautics and Space Administration's (NASA) Earth Observing System (EOS) Aura satellite on July 15, 2004, with an expected mission lifetime of 5 years. The primary objective of the Dutch-Finnish build OMI is to obtain global measurements at high spatial and spectral resolution of a number of trace gases in both the troposphere and stratosphere. Using these measurements, science questions on the recovery of the ozone layer, the depletion of ozone at the poles, tropospheric air pollution, and climate change were and are still being addressed.

1.1 Mission status

After more than 16 years in orbit the instrument is still functioning satisfactorily, and in principle can do so for many years. The NASA headquarter Senior Review for both 2017 and 2020 judged the OMI excellent and formally decided to extend the mission up to 2023 in order to continue the data sets acquired by OMI and the Microwave Limb Sounder (MLS). The 2023 Senior Review will onwards decide whether the mission can even be extended further up to 2026.

The Aura satellite currently has only fuel to perform a last Inclination Adjustment Maneuver (IAM) in Fall 2021. From that point onwards, no orbit control maneuvers will be performed, and the satellite Local Time Ascending Node (LTAN) crossing will drift towards later in the afternoon. The required fuel to exit the constellation and meet the 25-year re-entry requirement can be maintained until end 2024, at which point Aura will exit the A-train, and the LTAN has drifted up to 14h00. After this event, the power budget from the Solar panels will become the limiting factor, and it is estimated that the mission must terminate end 2025.

1.2 Purpose and objective

In order to ensure that the mission can be continued up to the year 2025, actions have been taken to ensure the proper functioning of the OMI instrument operations, the data processing and the calibration monitoring system.

For the data processing it was decided to develop a new Level 0 to Level 1b data processor. The rationale is to upgrade to new, modern data formats and meta-data standards, and to address the instrument gentle aging over the past 16 years. Moreover, improved data correction algorithms are available based on insights from the OMI successor instrument, TROPOMI, on ESA's Sentinel 5 precursor satellite. The new data processor will be robust for the aforementioned changes in the satellite's orbital parameters, and will have in-flight dynamic calibration functionality to maintain the OMI calibration status to the end of the mission in 2025.

The currently active Ground Data Processing System (GDPS) in the OSIPS generates version 3 L1b data, as part of the overall collection 3 data set, in near-real time (NRT) mode as well as forward mode. Once the new L01b data processor has been successfully integrated, processing will commence in the OSIPS in both NRT and forward mode, in parallel to the existing collection 3 stream. In addition, all mission data will be re-processed thus yielding the OMI collection 4 data set, which is expected to be the final data Collection for OMI.

This Algorithm Theoretical Basis Document (ATBD) serves to describes the instruments functioning, and all correction and conversion algorithms that are needed to process the raw Level 0 instrument readings into calibrated physical units, annotated with timestamps and geolocation information, which constitutes the L1b data set for collection 4.

1.3 Document overview

After this introduction, the document is divided in 5 major parts. In Part I, an elaborate overview is given of the mission so-far, including the day-zero calibration, the instrument (thermal) evolution and the major anomalies. This is followed in Part II with the instrument description and the instrument operations in Part III. The correction algorithms that are used to the convert measurements registered as raw L0 data into calibrated Earth radiances and Sun irradiances is given in Part IV. In Part V the annotations algorithms are described that are needed for geolocation assignment and time stamping of the observations. The appendices in Part VI give additional information that are not included in the main text.

2 Reference documents

[1] M. R. Dobber, R. J. Dirksen, P. F. Levelt *et al.*; Ozone monitoring instrument calibration. *IEEE T GEOSCI REMOTE*; **44** (2006) (5), 1209; 10.1109/TGRS.2006.869987.

[2] G. H. J. van den Oord, N. C. Rozemeijer, V. Schenkelaars *et al.*; OMI level 0 to 1b processing and operational aspects. *IEEE Transactions on Geoscience and Remote Sensing*; **44** (2006) (5), 1380; 10.1109/TGRS.2006.872935.

[3] M. Dobber, Q. Kleipool, R. Dirksen *et al.*; Validation of Ozone Monitoring Instrument level 1b data products. *Journal of Geophysical Research: Atmospheres*; **113** (2008) (D15); 10.1029/2007JD008665.

[4] M. Dobber, R. Voors, R. Dirksen *et al.*; The High-Resolution Solar Reference Spectrum between 250 and 550 nm and its Application to Measurements with the Ozone Monitoring Instrument. *Solar Physics*; **249** (2008), 281–291; 10.1007/s11207-008-9187-7.

[5] G. Jaross and J. Warner; Use of Antarctica for validating reflected solar radiation measured by satellite sensors. *Journal of Geophysical Research: Atmospheres*; **113** (2008) (D16); https://doi.org/10.1029/2007JD008835. URL `https://agupubs.onlinelibrary.wiley.com/doi/abs/10.1029/2007JD008835`.

[6] Input output data specification for the collection 4 L01b data processing of the Ozone Monitoring Instrument.
source: KNMI; **ref:** AURA-OMI-KNMI-L01B-0005-SD.

[7] Metadata specification for the collection 4 L01b data processing of the Ozone Monitoring Instrument.
source: KNMI; **ref:** AURA-OMI-KNMI-L01B-0007-SD.

[8] Algorithm theoretical basis document for the TROPOMI L01b data processor.
source: KNMI; **ref:** S5P-KNMI-L01B-0009-SD.

[9] Input/output data specification for the TROPOMI L01b data processor.
source: KNMI; **ref:** S5P-KNMI-L01B-0012-SD.

[10] Metadata specification for the TROPOMI L1b products.
source: KNMI; **ref:** S5P-KNMI-L01B-0014-SD.

[11] OMI Algorithm theoretical basis document for L01b processing.
source: Dutch Space; **ref:** RP-OMIE-0000-DS-146.

[12] GMES Sentinel-5 Precursor system requirement document.
source: ESA; **ref:** S5p-RS-ESA-SY-0002; **issue:** 4 rev. 1 – Redlined Version - RLa; **date:** 2011-04-29 –Redlined version: 2012-07-04.

[13] Department of Defense World Geodetic System 1984.
source: NIMA; **ref:** NIMA TR8350.2; **issue:** Third Ed.; **date:** 2000-01-03.

[14] IERS Technical Note No. 36 - IERS Conventions (2010).
source: IERS; **ref:** IERS Technical Note No. 36.

[15] Supplement to Department of Defense World Geodetic System 1984 Technical Report: Part I - Methods, Techniques, and Data Used in WGS84 Development.
source: DMA; **ref:** DMA TR 8350.2-A; **issue:** Second Printing; **date:** 1987-12-01.

[16] Toshio Fukushima; Transformation from Cartesian to geodetic coordinates accelerated by Halley's method. *Journal of Geodesy*; **79** (2006), 689; 10.1007/s00190-006-0023-2.

[17] Sean E. Urban and P. Kenneth Seidelmann (editors) *Explanatory Supplement to the Astronomical Almanac* (University Science Books, 2013); 3rd edition.

[18] T. C. van Flandern and K. F. Pulkkinen; Low-precision Formulae for Planetary Positions. *Astrophysical Journal Supplement Series*; **41** (1979), 391.

[19] J. Meeus; *Astronomical Algorithms* (Willman-Bell, Inc., 1998); 2nd edition; ISBN 0-943396-61-1.

[20] Method for the Calculation of Spacecraft Umbra and Penumbra Shadow Terminator Points. **source:** Lyndon B. Johnson Space Center, NASA; **ref:** Technical Paper 3547; **issue:** 1 rev. 2.

[21] URL `http://eclipse.gsfc.nasa.gov/SEcat5/SE2001-2100.html`.

3 Terms, definitions and abbreviated terms

Terms, definitions and abbreviations that are specific to this document can be found below.

3.1 Terms and definitions

Aura	The satellite carrying OMI and other instruments, Latin for "air" or "breeze".
DLED	Detector LED mounted close to the detectors.
HIRDLS	High Resolution Dynamics Limb Sounder, instrument on Aura.
MLS	Microwave Limb Sounder, instrument on Aura.
TES	Tropospheric Emission Spectrometer, instrument on Aura.
QVD	Quasi (or quartz) volume diffuser, in the OMI Sun port. The QVD is used to measure daily irradiance for L2 processing.
UV	Ultraviolet spectral range
VIS	Visible spectral range
WLS	White light source, quartz tungsten halogen lamp in the OMI calibration unit.

3.2 Acronyms and Abbreviations

The following acronyms and abbreviations are specific to this document.

AAI	Aerosol absorbing index
ADC	Analogue to digital converter
AOD	Aerosol optical depth
APID	Application process identifier
ATBD	Algorithm theoretical basis document
BAP	Baseline activity profile
BOL	Beginning of life
BRDF	Bi-directional reflection distribution function
CCD	Charged coupled device
CDS	Correlated double sampling
CKD	Calibration key data
CTE	Charge transfer efficiency
CTI	Charge transfer inefficiency
DIFM or DifM	Diffuser mechanism
DC	Dark current
DEM	Detector module
DEM	Digital elevation model
DMU	Drag makeup maneuver
DOY	Day of year
EDOS	EOS data operations system
ELU	Electronics unit
EFRF	Earth-fixed reference frame
ESA	European Space Agency
EOL	End of life
EOS	Earth Observing System
ERE	Earth reference ellipsoid
FMM	Folding mirror mechanism
FOT	Flight operations team (at NASA GSFC)
FOV	Field of view
FWHM	Full width half maximum

GDPS	Ground data processing system
GSFC	Goddard Space Flight Center
IAM	Interface adapter module
IAM	Inclination adjust maneuver
ICID or IcID	Instrument configuration identifier
IODS	Input output data specification
IOT	Instrument operations team
IRF	(Earth-centered) inertial reference frame
ISRF	Instrument spectral response function
KNMI	Koninklijk Nederlands Meteorologisch Instituut, Royal Netherlands Meteorological Institute
LED	Light emitting diode
LOS	Line of sight
LTAN	Local time ascending node
MCL	Master command load
MCP	Master clock period
MMS	Mission management system
NASA	National Aeronautics and Space Administration
NRT	Near-real time
OA	Optical assembly
OARF	Optical alignment reference frame
OBM	Optical bench module
OBT	On-board time
OMI	Ozone Monitoring Instrument
OPB	Optical bench
OPF	Operational parameter file
OSAB	OMI science advisory board
OSIPS	OMI science investigator-led processing systems
OVT	OPF version table
PDS	Production data set
PRNU	Pixel response non-uniformity
QE	Quantum efficiency
RBD	Rate buffered data
ROD	Read-out discipline
RTS	Random telegraph signal
SAA	South Atlantic Anomaly
SAM	Solar aperture mechanism
S/C	Spacecraft
SCS	Stored command sequence
SIFOV	Sun in field-of-view
SIPS	Science investigator-led processing systems
SIS	Stored instruction sequence
SRF	Spacecraft reference frame
TDOPF	Time dependent operational parameter file
TRF	Topocentric reference frame
VFD	Very fast delivery
WGS84	World geodetic system 1984

Part I

Mission overview

4 Introduction

The Ozone Monitoring Instrument (OMI) is a space-borne nadir viewing hyperspectral imager with two separate spectrometers that measure the solar radiation scattered back by the Earth's atmosphere and surface over the entire wavelength range from 270 to 500 nm with a spectral resolution of about 0.5 nm. OMI is on NASA's Earth Observing System (EOS) Aura satellite. Other instruments on Aura are the Microwave Limb Sounder (MLS), Tropospheric Emission Spectrometer (TES) and the High Resolution Dynamics Limb Sounder (HIRDLS).

The objective of OMI is measuring a number of trace gases in both the troposphere and stratosphere in a high spectral and spatial resolution. The heritage of OMI are the European ESA instruments GOME and SCIAMACHY, which introduced the concept of measuring the complete spectrum in the ultraviolet/visible/near-infrared wavelength range with a high spectral resolution. This enables the retrieval of several trace gases from the same spectral measurement. The American predecessor of OMI is NASA's TOMS instrument. TOMS used only 8 wavelength bands, from which the ozone column was obtained. TOMS had the advantage that it had a fairly small ground-pixel size (50 km × 50 km) combined with a daily global coverage. OMI combines the advantages of GOME and SCIAMACHY with the advantages of TOMS, measuring the complete spectrum in the ultraviolet/visible wavelength range with a very high spatial resolution and daily global coverage. This is possible by using two-dimensional detectors. OMI was built by Dutch Space (now Airbus Defence and Space Netherlands) and TNO Science & Industry (formerly TNO-TPD) in The Netherlands, in co-operation with Finnish subcontractors VTT and Patria Finavitec. The instrument was financed by the Netherlands Agency for Aerospace Programmes (NIVR, now Netherlands Space Office NSO) and the Finnish Meteorological Institute (FMI).

The OMI instrument operates in a push-broom configuration with a wide swath as shown in Figure 1. The 115° viewing angle of the telescope together with a polar circular orbit of about 705 km altitude corresponds to a 2600 km wide swath on the surface. This allows OMI to achieve daily coverage of the complete Earth. Light from the entire swath is recorded simultaneously and dispersed by gratings onto one direction of the two-dimensional detectors. The spectral information for each position is projected onto the other direction of the detectors. The obtained spectra are used to retrieve the primary data products: ozone total column, ozone vertical profile, UV-B flux, nitrogen dioxide total column, aerosol optical thickness, effective cloud cover, and cloud top pressure. In addition the following secondary data products are retrieved: total column SO_2, BrO, CH_2O, and ClO_2. In normal global operation mode the spatial sampling size at nadir is $13 \times 24\,\mathrm{km}^2$ (along × across track) for bands 2 and 3 (UV-2 and VIS) as shown in Figure 2, and $13 \times 48\,\mathrm{km}^2$ for band 1 (UV-1).

The Sun is measured on a daily basis via a dedicated solar port. The data is used to account for the variability of the solar output in the Earth's reflectance and for calibration purposes.

5 Mission timeline

Originally the OMI mission was planned for a lifetime of 5 years, by now the mission has lasted already more than three times longer. In the following an overview of the mission history is given. This covers the most important anomalies and changes to the instrument up to now.

5.1 Pre-flight calibration

The integration of the OMI proto-flight model was completed in 2001 and followed by a testing and performance verification campaign. Afterwards an extensive on-ground calibration measurement campaign took place from April to November 2002. The on-ground calibration was performed partly in ambient and partly under flight representative conditions in thermal vacuum. The on-ground calibration campaign is described in detail in [1]. Once the calibration campaign was completed, the instrument was shipped from the Netherlands to the United States for integration on the EOS Aura platform. From November 2002 until March 2004 tests on spacecraft level were performed.

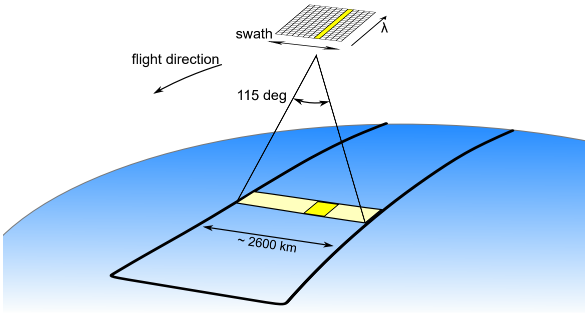

Figure 1: OMI measurement principle. The wide field of view in across track direction is imaged along one dimension of the detector while the spectral information is imaged onto the other direction. The spatial sampling distance in flight direction (along track) is determined by the co-addition time.

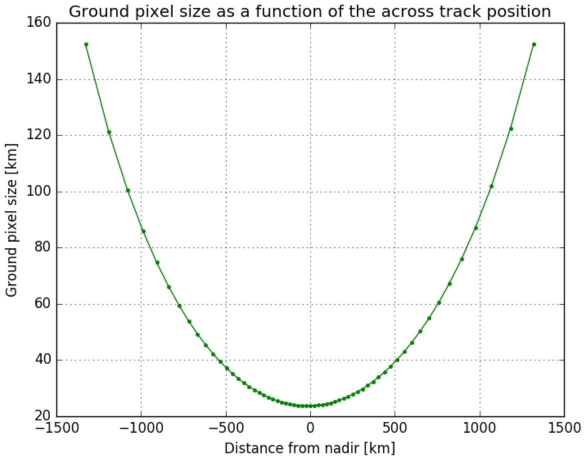

Figure 2: Spatial sampling size along the swath (across track) for the normal global operation mode for bands 2 and 3. It is smallest at nadir. Band 1 follows approximately the same shape but has double the sampling size across track, i.e. half the point density along the curve.

5.2 Launch and early operations

The Aura satellite was successfully launched on 15 July 2004. It was launched from the Vandenberg Western Test Range in the United States of America on-board a Delta II 7920-10L two stage expendable rocket. Aura is flying in formation with other Earth observing satellites in the so-called A-Train. The main orbit parameters of AURA are shown in Table 1.

Orbit type:	Polar (98.2° inclination), sun-synchronous
Average altitude:	705 km (438 miles)
Orbit period:	98 minutes and 53 seconds
Mean local time ascending node:	13:45 (1.45 PM)
Repeat cycle:	16 days (233 orbits)

Table 1: Orbit parameters of Aura.

The launch and early operations phase (LEOP) for check-out and verification of spacecraft and instruments and commissioning lasted in total about three months, split in two parts. During the first part until the 26 of September 2004 various special purpose measurements were performed and it was confirmed that the performance of OMI had not been changed by the launch from what had been observed during on-ground measurements. During the first four weeks in orbit (until orbit 470), the optical bench and detector temperatures were increased to 303 K to facilitate the outgassing of the instrument. The outgassing was performed to reduce the risk of ice-formation on the surfaces of the detectors or the optical components. After this inital outgassing the temperatures were lowered to the nominal operational values. On two more occasions during LEOP the temperatures were raised to 303 K for a week, starting orbit in orbits 535 and 921. In orbit 1034 on 24 September 2004 the instrument was again at the nominal operational temperatures, ready to start nominal operations measurements.

Additional commissioning measurements were performed in the time period 19 November 2004 (orbit 1846) until and including 5 December 2004 (orbit 2093). During this period unbinned zoom radiance measurements for science (orbits 1846–01932) and dark measurements were performed (orbits 1933–2093). In addition the CCD heater gain setting was set to a non-nominal value In orbits 2035–02064.

5.3 In-flight anomalies

Many types of events can have impact on the acquisition or quality of science data. In the following the most important malfunctions or anomalies of the instrument which affect(ed) OMI data quality or acquisition are described. This does not include events concerning spacecraft maneuvers, either for orbit maintenance or special measurements for other Aura instruments. Events of increased solar activity are also not listed here. Some anomalies on spacecraft level only have an indirect or very small impact on OMI, these are also not included here.

5.3.1 Folding mirror mechanism anomaly

The behavior of the folding mirror mechanism (FMM) changed in the last week of February 2006, and in orbit 8632 on the 28th of February 2006 the FMM did not return to its commanded nominal position. After in-depth investigations and various tests the hypothesis was formed that the FMM bounced back from its end-stop. By changing the moving sequence of the stepper motor, this bouncing can be reduced. All calibration measurements where the FMM is used, had been updated by 11 June 2006. The anomaly has not occurred since. Table 2 lists the orbits when the anomaly occurred and tests were performed.

Orbits	Event	Description, test activity
08632–08675	major	FMM anomaly, OMI in Idle mode (not generating science data)
09268	major	FMM test #6, FMM positions during test: 79,5,4,3,2,75,76,77,78,79
09283	major	FMM test #7, FMM positions during test: 79,5,4,3,2,75,76,77,78,79
09355	major	FMM test #8, FMM positions during test: 79,5,4,3,2,75,76,77,78,79
09441	major	FMM test #9, FMM positions during test: 79,5,3,2,1,75,76,77,78,79
09442	major	FMM test #10, FMM positions during test: 79,5,3,2,1,75,76,77,78,79
09485	major	FMM test #11, FMM positions during test: 79,5,4,3,2,1,0,75,76,77,78,79
09676	major	FMM test #12, FMM positions during test: 79,5,4,3,2,1,0,75,76,77,78,79; WLS used, IC=255, Meas.Class=2 (WLS)
09777	major	FMM test #13, FMM positions during test: 79,3,2,1,0,-1(0),-2(2),-3(1),-4(0), 1,2,3,75, 76,77,78,79; WLS used, IC=255, Meas.Class=2 (WLS)
09847	minor	FMM test: run dark SIS. Short periods without measurement data at ICID transitions.
09848	minor	FMM test: run dark SIS. Short periods without measurement data at ICID transitions.
09876	minor	FMM test: run dark SIS. Short periods without measurement data at ICID transitions.
09877	minor	FMM test: run dark SIS. Short periods without measurement data at ICID transitions.
09964	minor	FMM test: run dark SIS. Short periods without measurement data at ICID transitions.
09965	minor	FMM test: run dark SIS. Short periods without measurement data at ICID transitions.
09978	minor	FMM test: FMM functional test. Short periods without measurement data at ICID transitions.

Table 2: FMM anomaly and test orbits.

5.3.2 Row anomaly

The "row anomaly" affects the quality of the OMI radiance data for all wavelengths at certain viewing angles. Viewing angles correspond to rows on the detector, hence the name row anomaly. For viewing angles affected by the row anomaly the signal is lower (or higher) than expected and the spectral response has changed. The anomaly affects rows in all bands. The impact of the anomaly changes during an orbit, towards higher latitudes in the northern atmosphere the signal increases, while it is decreased in other parts of the orbit. The affected rows also change over time. Rows affected by the row anomaly are flagged in the L01b processor.

Indications for a row anomaly in rows 53 and 54(binned, zero-based) were detected soon after launch. Only after the effect worsened on 25 June 2007 it could be quantified as a signal reduction for bands 2 and 3. From 11 May 2008 on also rows 37–41 and from January 2009 on rows 27–44 of bands 2 and 3 have also been affected by the row anomaly. Band 1 (UV1) is also affected in rows 15-22. Also a signal increase is observed in the northern latitudes. Investigations into the nature of the anomaly were performed on various occasions between June and November 2008 (between orbits 20721 and 23141). These tests consisted mainly of radiance measurements with adapted settings extending over the north pole until the start of the spacecraft eclipse.

Since July 5th, 2011, rows 42–45 have been affected by the row anomaly over the complete orbit. These rows were already affected, but only over a partial orbit.

Since then the row anomaly has shown only small changes every now and then. Consequently the row anomaly flags must then be updated in the Level 1B and Level 2 data. This is done by post-processing the level 1B data, followed by a re-processing of the Level 2 data.

The row anomaly has various effects: part of the earthshine is blocked decreasing the signal in the affected rows. The inhomogeneous illumination of the slit changes the slit response function and with that the wavelength assignment of the affected pixels. Out-of-field straylight from Sun and Earth reaches some rows and increases the signal, this can also depend on the latitude.

Detectors and electronics have been ruled out as a cause for the anomaly. The most likely explanations is that a reflective object is blocking part of the field of view of the Earth port. Irradiance measurements are not affected. The object could be located within the OMI instrument, in that case the object's size was estimated to be about 1 mm. However, an object inside the instrument does not explain the signal increase close to the north pole. It was therefore concluded that the object is outside the instrument with a estimated size of a couple of centimeters with a distance from OMI of about 50 cm. The blocking object could be a loose piece of multi-layer insulation (MLI). It is reflective and might explain the increase of signal by reflecting light from the Sun or the Earth close to the north pole. Additional evidence for this is the observation in irradiance data that UV1 rows 14–22 have larger degradation rates than at other rows.

Since version 1.1.2 of the GDPS (activated in forward stream on 8 October 2008), a geolocation field called XTrackQualityFlags in the Level-1b radiance products flags ground pixels affected by the row anomaly (see also Section 41.10). The updating of the row anomaly flag was changed with later GDPS versions to better allow for changes in the affected rows. L2 users are advised to not use pixels flagged for the row anomaly. As shown in Figure 3 for unbinned detectors rows, the row anomaly affects a big part of each detector. This means that OMI provides full global coverage within 2 days, and not - as initially foreseen - on a daily basis.

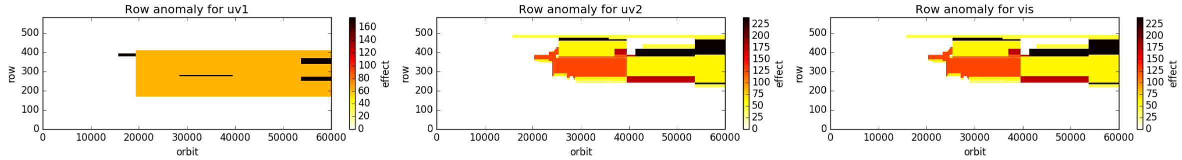

Figure 3: The unbinned rows flagged for row anomaly for bands 1–3 (left to right). The numbered color bar shows the sum of the different effects contributing to the flag: 16 is added for an observed wavelength shift, 32 for a blockage or earth light, 64 for observed straylight from the Sun, and 128 is added for observed out-of-field straylight from Earth.

5.3.3 Survival mode anomaly

During survival mode anomalies OMI switches off entirely and is also not thermally stabilized. The reason for this anomaly could not be established as all housekeeping and logging data is lost during the switch-off. So far this anomaly occurred twice: on 29 May 2016 (orbits 63151-63371) and on 12 March 2017 (orbits 67327-67391). After OMI is switched on again, it takes around 45 orbits to recover the thermal stability.

5.3.4 WLS anomaly

The white light source (WLS) stopped working on 19 September 2019 (in orbit 80737). Shortly after that all calibration measurements employing the WLS were removed from the nominal operations baseline. More details on the WLS output and supply voltage can be found in Section 11.3.

5.4 Changes to the thermal configuration

Degradation of the thermal radiator reduces its ability to remove heat from the instrument. For constant thermal settings, this leads to a slow heating of the optical bench and detectors. The detectors are thermally stabilized by a P-type control loop with a heater with pulse width modulation (PWM), see also Section 8 for a detailed description of the thermal design of the instrument. From around orbit 70000 on, it was observed that the duty cycle of the PWM of the UV detector heater occasionally dropped to zero, so in fact not stabilizing the temperature at all times anymore. After two tests where instrument thermal settings were adapted temporarily, new thermal settings were made active on 26 November (DOY 330) 2019 (orbit 81729). The tests were performed on 10–11 October 2019 and on 11–12 November 2019 during radiance zoom measurements. The best solution to regain control over the detector temperature stability was to reduce the heater power for the OPB level heaters from 10 W to 8 W. This reduced the thermal load to detectors and radiator and lowered the OBP temperature by about 1 K and the detector temperatures by about 40 mK. The duty cycle for the UV detector heater PWM increased from an average of around 3 % to about 13 %, this should leave enough headroom until the end of the mission. For plots and an overview of instrument temperatures during the mission so far see Section 8.

5.5 Constellation exit and decommissioning

Initially the mission was planned for a nominal lifetime of 5 years. After more than 16 years the OMI and MLS instruments on Aura are still operational and NASA will continue the mission. However, the remaining fuel on-board has to be sufficient to fulfill the requirements on end-of-life decommissioning. According to current predictions, the remaining fuel can support one more inclination adjust maneuver in fall 2021. From then on the local time ascending node (LTAN) will drift away from around 13:45 to later in the afternoon. At the moment it is estimated that EOS Aura will perform maneuvers to exit the A-train constellation and lower the perigee at the end of 2024. By then the LTAN should have reached 14:00. In summer 2025 the power generated by solar panels in the new orbit is estimated to be insufficient to operate instruments and spacecraft. This is expected to be the start of the final mission phase, the disposal phase. At the moment the plan is to continue with scientific measurements as long as OMI can stay switched on. The nominal operations baseline (see Section 13) has been adapted to support this approach.

6 Calibration evolution in-flight

In each orbit OMI produces about 0.5 GByte Level 0 data. This Level 0 data is converted by the ground data processing software (GDPS) to about 1–1.5 GByte L01b data. The correction and calibration algorithms employed in the GDPS need calibration data as input. These calibration parameters are stored in operational parameter files (OPF). During the mission the OPF files and the processor have been updated several times. The first calibration data was derived from on-ground calibration measurements, later the data was updated to account for in-flight changes and new insights. With the collection 4 update some of the processing and operational aspects will change with respect to the original design as described in [2].
In the following the main changes which were performed in-flight to processor and calibration parameters are discussed.

6.1 Collection 1

Pre-flight calibration parameters were retrieved from on-ground calibration measurements which were partly performed in thermal vacuum and partly in ambient. The absolute radiometric calibration for the radiance was performed only at nadir with a calibrated FEL lamp in thermal vacuum, due to the wide field of view of the radiance port. The off-nadir angles were derived from the BSDF measurements performed with a xenon lamp both in vacuum and ambient. For the absolute irradiance calibration the signal-to-noise achieved with the FEL lamp was much lower, the keydata was therefor derived from BSDF and absolute radiance calibration. The on-ground calibration is described in [1]. Collection 1 was active until 25 March 2005.

6.2 Collection 2

Re-analysis of on-ground measurements lead to a replacements of radiometric key data. The resulting calibration characteristics are described in great detail in [1]. Furthermore the straylight limits were adapted, the gain of the DEMs (detector electronics modules) and the dark current were updated, and the non-linearity threshold was increased. Collection 2 was active in forward processing from 26 March 2005. The updates to the key data are covered by OPF versions 8–20.

6.3 Collection 3

Collection 3 covers a major update of processor and calibration key data. Insights from in-flight measurements and comparison with models served as input for this update. The papers [3] and [4] describe these updates in great detail.

6.3.1 Irradiance radiometric calibration

For the absolute radiometric calibration of the irradiance at the nadir row a high-resolution composite solar irradiance spectrum (SIS) was derived from various sources (see [4]). The correction to the absolute irradiance at nadir is between -2 % and +3 % and shows some spectral structure below 360 nm. After the update the OMI irradiance data differs around -1 % to +0.5 % from the reference spectrum. Around 400 nm, the difference amounts to -5 %. The correction curve and a comparison to different solar irradiance spectra is shown in [4]. The absolute irradiance calibration in other rows than the nadir row was adapted using the new reference at the nadir row. This reduced the row dependence in the irradiance calibration from about 2 % in the collection 2 data to about 0.4 % for UV1 and 0.2 % for UV2 and VIS.

The solar angle dependency correction (goniometry or dIRRAD) of the irradiance measurements in collection 2 suffered from limited sampling in both azimuth and elevation direction and low signal-to-noise. The update for collection 3 is based on fits to 2.5 years of in-flight data. For the quartz volume diffuser, which is used for the nominal irradiance product, the accuracy was improved to about 0.5 % for UV1 and about 0.3 % for UV2 and VIS. Outside the azimuth angle range of 18.3°– 31.2° the accuracy reaches about 1 %.

6.3.2 Radiance radiometric calibration

The absolute radiometric calibration of the radiance measurements was adapted based on comparison to theoretical predictions of the Sun-normalized radiance of snow, ice and land surfaces. To minimize the sensitivity to non-Lambertian reflective properties of the surface types, scenes with appropriate viewing and illumination conditions were chosen. The viewing angle (row direction) dependence is derived relative to the response at nadir. By comparing the Sun-normalized radiance, calibration errors common to radiance and irradiance cancel out and are not included in the calibration update. For the evaluation of the measured OMI radiance over Antarctica a surface reflectivity model accounting for non-Lambertian effects was used in combination with a radiative transfer model to compute the reflectance values at the top of the atmosphere, see [5]. For the land scenes Rayleigh scattering dominates the reflectance in the UV and scenes with low Aerosol contamination were used for the comparison.

The resulting adaptations of the radiometry are shown in [3] and the accuracy is estimated to be within 2 % for both radiance above ice and above land. The adaptions show no spectral dependance but a viewing angle dependence of up to 4 %. The corrections to the radiance calibration for UV2 and VIS are roughly parabola shaped with spatial features. The correction increases for higher viewing angles. After the update the variations in row direction are within 1 %. The corrections for UV1 are based on UV2 and have no spatial features but the same principle shape. Comparisons with radiance predictions using ozone climatology which were performed later, suggest the UV1 swath dependence adjustment is nearly correct, but it should also include some spatial structure as in UV2 and VIS. Compared to collection 2, the nadir row of radiance and the BSDF calibration changed by a factor 1.025 in addition to the swath dependent updates.

In addition to the radiometric corrections described above, the correction algorithm and OPF parameters of the spectral straylight correction were improved. In March 2007 collection 3 reprocessing was performed with OPF version 41. From about November 2007 on collection 3 was active in the forward stream.

6.3.3 Row anomaly detection and flagging

After activation in the forward stream, the main updates to processor and key data were in response to the discovery of the row anomaly (see Section 5.3.2). A row anomaly flag was introduced on 8 October 2008 with GDPS version 1.1.2. The fixed flag values were replaced in subsequent updates by a look-up table in the OPF to account for the changes in the row anomaly.

6.4 Collection 4

For collection 4, the software for the L01b data processor was redesigned, inspired by the recent development for TROPOMI. This collection 4 processor now uses modern data-formats and meta-data standards that are in line with current instruments. From a calibration perspective, in-flight monitoring data of the entire mission has been analyzed to derive time-dependent calibration key data which addresses and corrects the instrument aging over the mission. In the following the most relevant changes to the processor and the calibration key data are described. More details on the changes in output format can be found in the IODS [6], the metadata is described in [7]. The forward processing of collection 4 L1b data is planned to start in April 2021.

6.4.1 Dataformat and products

The collection 4 L1b products will be in NetCDF-4 format instead of HDF-EOS2 (which was based on HDF4). The products follow a completely different format structure, which is largely based on S5p/TROPOMI as described in [8], [9], [10].

Radiance and irradiance data are now stored in ascending order of wavelength. This means that for band 1 the spectral dimension is reversed compared to collection 3. The units of the radiance data have changed from photons.s^{-1}.nm^{-1}.cm^{-2}.sr^{-1} to mol.s^{-1}.nm^{-1}.m^{-2}.sr^{-1}, to be in line with the S5p/TROPOMI convention. Accordingly, the irradiance data units have changed from photons.s^{-1}.nm^{-1}.cm^{-2} to mol.s^{-1}.nm^{-1}.m^{-2}. To convert back to the collection 3 unit, multiply with $\frac{6.02214076\times10^{23}}{10000}$. The data is no longer split into a separate mantissa and exponent and instead of storing a noise value directly, the noise is provided as a signal-to-noise-ratio on a dB scale. The collection 4 products no longer support re-binning. This means zoom data will no longer be re-sampled to the global resolution.

6.4.2 Changes to correction algorithms

For the correction algorithms and their respective calibration key data (CKD), the biggest change is that the instrument aging over the mission is taken into account with collection 4. Other small changes to key data and correction algorithms in the processor have been performed, these can have a small impact and are described in the following.

Absolute radiometric calibration Updates to the radiometric calibration of both radiance and irradiance have been investigated for the collection 4 update. Because no significant improvement could be realized, it was decided to keep the absolute radiometric calibration in the same as in collection 3, while the degradation in radiance and irradiance is corrected. In the L01b processor both the radiance and irradiance data are now corrected for the Earth-Sun-distance, i.e. normalized to 1 au, see Section 33.4. The absolute radiometric calibration key data has been improved at the very edges of the detected wavelength range. There the values were much higher than can be expected. The values have now been clipped to fall within a reasonable range. The two most extreme across track positions also show extreme values, however clipping of these values has shown no improvement and they therefore remain as in collection 3. Outside the science region the radiometry has also been adapted to allow for more stable fitting of interpolation algorithms. There the previously very large values have been replaced by the values in adjacent rows or columns inside the science region.

Radiance degradation correction Over the course of the mission, the radiance signal of OMI showed signs of degradation. In collection 4 the degradation is corrected by a row dependent factor that increases as a linear function of orbit number. The correction is bases on analysis of Earth shine radiances of Antarctic ice at 340 nm. The correction is independent of the wavelength and the same for all three bands of OMI. For each (binned) detector row a compensation factor for the degradation is given as a function of the orbit number. For orbits beyond the calibration key data range, the values are extrapolated linearly.

Irradiance degradation correction The quasi volume diffuser (QVD) which is used for the nominal daily irradiance measurements (see also Section 11.2) has been degrading over time. With collection 4 the degradation of the QVD is corrected in the L01b processor. The diffuser degradation correction has been determined at the solar reference angle (azimuth angle = 23.75° and elevation angle = 0.0°) relative to the irradiance signal at the start of the mission assuming a constant solar irradiance over the mission. The calibration key data varies with time (orbit number), spatial dimension and wavelength. The key data is extrapolated to orbits far beyond the expected remaining duration of the mission. The degradation correction is independent of the degradation correction applied to the radiance data. For the aluminum diffusers no degradation correction was derived as they are not used for the nominal L1b irradiance product.

Instrument BSDF The instrument BSDF decreases over time in line with the introduction of the degradation corrections for the radiance and the irradiance via the quasi volume diffuser. The decrease is smooth in the spectral direction and strongest for the short wavelengths.

Relative irradiance (dIRRAD) correction The collection 3 calibration key data for the relative irradiance (dIRRAD or goniometry) correction was based on only one year of in-flight data and the solar angle dependence was fitted using high order polynomials. This key data consisted of the fit coefficients for each across track position and 11 azimuth bins and 10 elevation bins. With the collection 4 update the key data consists of the actual correction factors (dIRRAD) as a function of azimuth angle (equidistant grid with 280 grid points), elevation angle (equidistant grid with 200 grid points), across track position and wavelength band. The analysis has been performed for the QVD diffuser using daily degradation corrected irradiance data of the period 2005—2016. For the aluminum 1 and aluminum 2 diffusers the old (polynomial) key data has been used to convert the dIRRAD correction to the new format. No new analysis was performed as only the QVD data is used for the L1b irradiance product.

Gain ratio The calibration key data in collection 4 now has a temporal axis because the gain ratios are known to drift in time. For all orbits that contain the dedicated gain ratio calibration measurements, the four gain ratios are computed and combined in a look-up table. The L01b processor interpolates linearly between the orbits in the table to obtain the gain ratio in the orbit under consideration. For orbits beyond the orbit range of the calibration key data, the last calibration value in the series is used.

Non-linearity The algorithm for the non-linearity correction has been updated to use Chebyshev polynomials as input. This approach is equal to the one used in the TROPOMI L01b processor.

Conversion factors: DN2V and V2C The L01b processor implements the inverse of this signal chain, i.e. converting the output signal of the ADC in DN to Volts, to electrons and in the end to photon flux. Due to a historic mistake, in the old OMI L01b processor as well as throughout the entire on-ground calibration campaign, an erroneous value of 4096 DN $/5.0$ V $= 819.2$ DN/V was used as the ADC conversion factor. As this erroneous factor was used consistently, this error was compensated by the calibrated voltage-to-charge conversion factor.

For the new OMI L01b processor, the ADC conversion factor has been corrected to the actual conversion factor that was established during ELU unit testing. To ensure that the overall calibration remains unchanged, all CKDs used between the DN-to-voltage conversion and the voltage-to-charge conversion have been adjusted as well to match these changes.

6.4.3 Wavelength annotation

Collection 4 L1b products no longer provide a calibrated wavelength that is derived by fitting a reference solar spectrum to the data. The algorithms for temperature dependence and inhomogeneous illumination have been updated and new key data has been derived based on in-flight data. The polynomial fit to the wavelength has been improved and the number of wavelength polynomial coefficients in the CKD has been reduced from 5 to 4. For backwards compatibility, still 5 coefficients are stored, but the last coefficient is set to 0. As an alternative for the polynomials, the L1b radiance products directly provide the nominal wavelength for each ground pixel and spectral channel without the need for calculation. The values in the field are not corrected for temperature effects and inhomogeneous illumination. A first order approximation of these effects provided separately given for each scanline and ground pixel. For irradiance the wavelength for each pixel and spectral channel includes corrections for both temperature effects and Doppler shift.

6.4.4 Time annotation

The measurements are now annotated with timestamps using time in UTC seconds since the epoch 2010-01-01 00:00:00 UTC. Note that since the epoch is 2010 and EOS-Aura was launched in 2004, the value can be negative. For backwards compatibility, the TAI-93 timestamps that were used in the collection 3 products are provided as a convenience in the `time_TAI93` field. For more details see Appendix A in [6].

6.4.5 Geolocation line-of-sight assignment

The geolocation azimuth and elevation line-of-sight (LOS) angles have been derived anew, but are based on the original calibration data. The angles have been averaged for each row over the columns included in the detector science region for each band. Previously this row-averaging was done by the processor in the LOS binning algorithm. For the collection 4 processor this step has been done once beforehand in the CKD creation process, as it is always the same operation and leads to the same results. The binning of multiple rows is still handled in the LOS binning algorithm depending on the binning scheme.

6.4.6 Quality Flags

The quality flags have substantially changed from collection 3 to collection 4. Field names have changed, some flags have become obsolete and new flags have been defined. For the changes to the flags please refer to Appendix A in [6]. Apart from the flag definitions also the levels where flags are raised have changed. This is most notably for the DPQF and RTS flagging, resulting in fewer flagged pixels and consequently more available data for L2 processing.

South Atlantic anomaly flagging The area flagged as SAA was a rectangular bounding box in previous processor versions. With collection 4 the SAA is described as a polygon. The enclosed area has been determined from transient flagging maps for the entire mission. As the center-point of the SAA polygon is slowly moving towards the west, the calibration key data is a set of polygons for different years. The movement of the center-point has been extrapolated until 2030. For the SAA flagging the polygons are interpolated to match the current position of the SAA.

Solar eclipse flagging The solar eclipse flagging algorithm has been updated to flag each individual ground pixel which is in an eclipse shadow as described in Section 41.5. Up to collection 4 entire measurements were flagged in case of a solar eclipse. The solar eclipse data in the CKD has been amended with data up to the year 2100.

Row anomaly flagging Based on re-analysis of in-flight data of the entire mission up to the end of 2020, the row anomaly calibration key data has been updated for UV2 and VIS. For UV1 the flags remain as used in collection 3. Each across track position has been analyzed individually without combining the affected rows into regions as has been attempted previously. The analysis has been based both on an observed decrease (blockage) of the signal and an increase of the signal due to increased straylight caused by the anomaly. The rows affected by the row anomaly change over time. Rows which have apparently recovered from the anomaly are only removed from the anomaly flag map if the change is persistent for longer than 90 days. Pixels where the flag shows a seasonal recovery are also kept flagged for all seasons. This conservative approach has been chosen to facilitate long-term trend analysis for L2.

The resulting flags give a first indication which ground pixels are impaired by the row anomaly. Depending on the sensitivity of a specific L2 retrieval algorithm to this instrument feature, retrievals might profit from altering the amount of flagged pixels.

Transient pixel flagging A new transient detection algorithm (see Section 41.11) has been implemented in the processor and the flagging thresholds for the different processing classes and ICIDs have been optimized using in-flight data.

Detector pixel quality flagging Data of the entire mission has been re-analyzed for pixels showing an anomaly in their response. High dark current is not used as a criterion anymore, as all pixels show an increase of dark current over the mission. The dark current is corrected in the processor. As a result the number of flagged pixels has reduced substantially. The remaining number of flagged pixels has stayed fairly constant over the mission and a static flagging map has been derived for the entire mission.

Random telegraph signal flagging The meaning and purpose of the random telegraph signal (RTS) map has been changed. RTS is only a problem if it occurs at a higher frequency than the background radiance measurements are collected. For collection 4 the RTS flag for a pixel is raised if the dark signal shows a variation higher than a threshold during the last 15 orbits, see also Section 41.13.

Saturation flagging Based on analysis of in-flight data, the register full well values for saturation flagging have been lowered from 2500000 e^- (UV, UVIS) to 2350000 e^- for the UV and 2300000 e^- for the VIS detector.

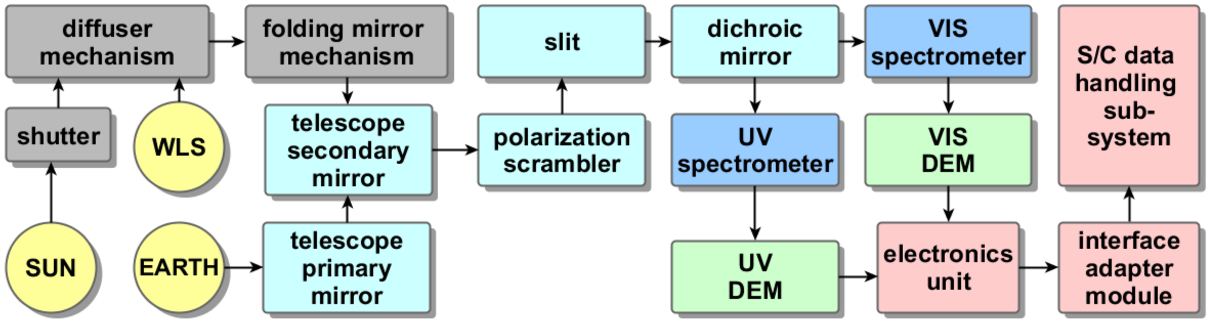

Figure 4: The overall architecture of OMI. Light from the Earth passes through both telescope mirrors via the polarization scrambler to the slit. Light from the Sun or the white light source (WLS) bypasses the primary telescope mirror via the diffuser mechanism and the folding mirror. The dichroic mirror transmits VIS light and reflects UV light. In the spectrometers the light is dispersed and imaged on the detector modules (DEMs). The signals detected by the spectrometers are digitized in the electronics module (ELU). Via the interface adapter module the data is transferred to the spacecraft data handling system from where it is transmitted to a ground station.

Part II

Instrument description

After a general overview of the instrument design, the relevant sub-systems will be described in more detail in the following sections. A detailed instrument description has previously been published in [1].

7 Overview

Figure 4 shows the functional overview of the the overall architecture of the OMI instrument. The light reflected from the Earth's atmosphere and surface is imaged by two telescope mirrors onto the entrance slit. Before the slit the incoming light is depolarized by a scrambler. After the slit the light is split by a dichroic mirror into two wavelength ranges 264–383 nm (bands 1 and 2, UV) and 349–504 nm (band 3, VIS) and guided to the two spectrometers. The wavelength range, spectral resolution and sampling are listed per band in Table 3.

Band	**Total range**	**Average spectral resolution (FWHM)**	**Average spectral sampling distance**
Band 1 (UV-1)	264–311 nm	0.63 nm	0.33 nm / pixel
Band 2 (UV-2)	307–383 nm	0.42 nm	0.14 nm / pixel
Band 3 (VIS)	349–504 nm	0.63 nm	0.21 nm / pixel

Table 3: Spectral range, resolution and sampling distances of the OMI instrument. Note that there is a small spectral overlap between bands 1 and 2. Bands 1 and 2 are imaged separately onto detector 1 to allow for different spatial sampling and higher signal to noise in band 1. The numbers are as reported in [1].

In the spectrometers the light is dispersed and imaged onto CCD detectors. The CCD signals are digitized and co-added in the electronics unit (ELU). Further data formatting is performed in the interface adapter module (IAM) before the data is transmitted to the S/C data handling sub-system. In addition to the Earth's radiance, light from the Sun can be measured by opening a shutter and moving the folding mirror mechanism in between the two telescope mirrors. The solar light is reflected by either one of three diffusers. A white light source (WLS) can also be coupled into the telescope via the folding mirror.
In the following, the different parts of the instrument are described in more detail.

8 Mechanical and thermal description

The OMI instrument weighs 65 kg, consumes about 66 W of power and has a size of 50 cm × 40 cm × 35 cm. Pre-launch tests showed that the CCD detectors needed extra protection from cosmic radiation. To this end, 10 kg of aluminum shielding was placed around the CCD detectors, reaching an average thickness of 29 mm. The instrument consists of the optical assembly (OA) and the electronic assembly (EA), as shown in the left panel of Figure 5. The optical assembly consists of the optical bench (OPB), detector modules (DEMs) the radiator and other thermal hardware.

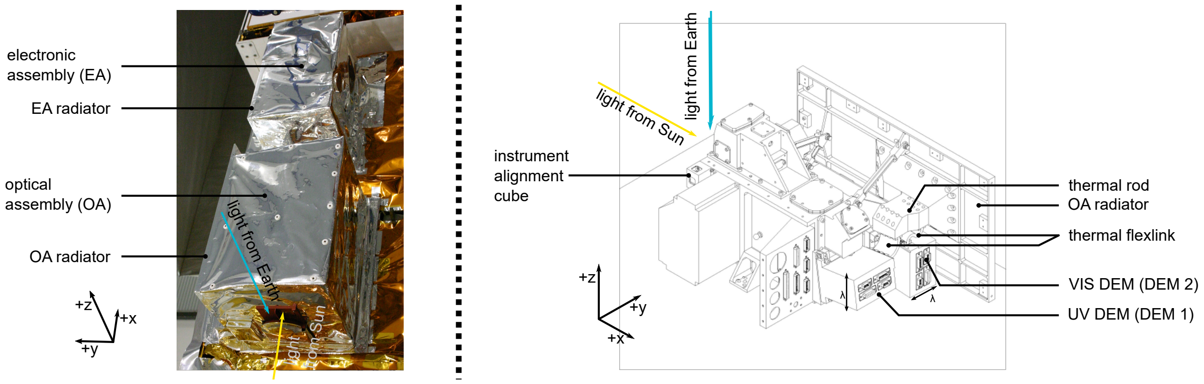

Figure 5: Thermal and mechanical design of OMI. The left panel shows the integrated instrument with the MLI shielding. The radiators for optical assembly (OA) and electronic assembly (EA) are located on the left hand side. The right panel shows the optical assembly as a technical drawing. The spectral dimension is imaged on the CCD detectors inside the DEMs as indicated by the arrows. Only the DEMs are connected directly to the radiator by thermal flexlinks. The thermal connection of the OPB is via the DEMs. In both panels the spacecraft reference frame (see also Sec. 39.1.9) is indicated.

The electronic assembly (EA) is separated from the optical assembly as shown in the left panel of Figure 5. It consists of the electronics unit (ELU) and its thermal radiator. All optical elements are mounted within a monolithic aluminum structure, the optical bench (OPB). The two detector modules (DEMs) are attached to the optical bench as shown in the right panel of Figure 5. Most mirrors and their mounts are made from aluminum, making the instrument less sensitive to thermal variations. The optical bench and the DEMs are thermally stabilized by heaters and a thermal radiator. The passive radiator of the optical assembly has the dimensions of about 40 × 30 cm. The CCD detectors each have an active thermal control (ATC) system, while the optical bench temperature is set by level heaters. The ATCs consist of a thermistor inside the CCD package, a P-type controller and a foil heater element mounted at the rear of the CCD support plate. The heater is operated by pulse width modulation (PWM). The controller is implemented in the ELU. As it is a P-type controller it cannot compensate for a temperature offset with respect to the setpoint.

The four OPB level heaters have different powers (1,2,4 and 8 W) to allow different heater powers in steps of 1 W. The heater power is not controlled in a closed loop but set by a command from ground.

The optical bench is mounted on the spacecraft using thermally insulating kinematic mounts. The two DEMs are each connected via a flexlink to the thermal rod which is attached to the thermal radiator. There is no separate connection of the OPB to the radiator. The thermal links and radiators are shown schematically in Figure 13 and in the technical drawing in the right hand side of Figure 5. The thermal link of the UV detector is a bit longer than the one for the VIS detector.

Without heating, the optical bench is designed to cool to about 255 K in flight. Due to aging of the radiant cooler since launch, this value has changed by now. The in-flight aging of the radiant cooler also leads to a slow heating of detectors and OPB during the mission, this can be seen in Figures 6 and 7. The operational temperature of the OPB at the beginning of life was 264 K rising to about 265.5 K before changes to the level heater settings. Due to the radiator degradation, less heat is removed from the instrument. As the detectors are stabilized by heating them, the headroom of the detector ATCs decreases when the detectors get warmer. For the UV detector there were are already periods during an orbit when the duty cycle of the PWM dropped to 0 % and no active stabilization was performed, this can be seen in the broader temperature excursions in Figure 7. In November 2019 settings have been adapted to regain thermal stabilization over the entire orbit, see also Section 5.4. This was done by reducing the overall thermal load to the radiator. The level heater power of the OPB was reduced from 10 W to 8 W while keeping the detector temperature setpoint at 265.15 K.

This lowered the OPB temperature by about 1 K and the detector temperatures by about 40 mK. The duty cycle for the UV detector PWM increased from an average of around 3 % to about 13 %, this should leave enough headroom until the end of the mission. For the VIS detector PWM the duty cycle increased from about 5 % to about 18 %. Table 4 lists typical temperatures of OPB and detectors during different times in the mission.

Parameter	**BOL**	**Orbit 80000**	**End Nov. 2019**
Operational CCD temperature UV	265.13 K	265.19	265.15
Operational CCD temperature VIS	265.21 K	265.27	265.23
In-orbit CCD temperature excursion UV	±5 mK	±20 mK	±10 mK
In-orbit CCD temperature excursion UVIS	±5 mK	±10 mK	±10 mK
Operational optical bench temperature	264.0 K	265.5	264.5
In-orbit optical bench temperature excursion	±200 mK	±200 mK	±200 mK

Table 4: Observed temperature and stability for detectors and optical bench. The setting change in orbit 81729 on 26 November 2019 lowered the temperatures closer to the beginning of life (BOL) values.

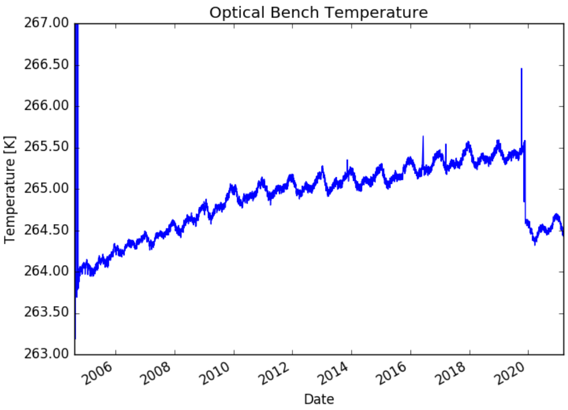

Figure 6: The optical bench temperature over the mission so far. End of November 2019 (in orbit 81729) the level heater power was reduced from 10 W to 8 W. Before that the temperature increased continuously.

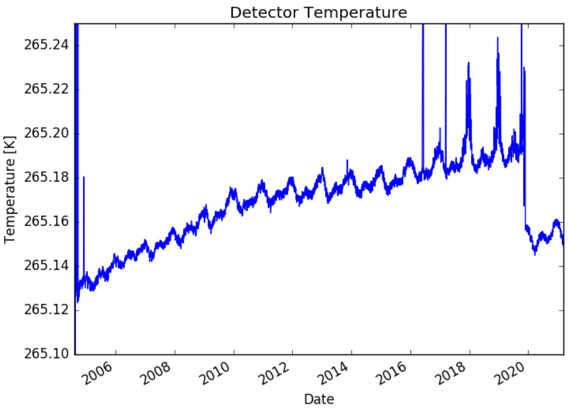

Figure 7: The UV detector temperature over the mission so far. From around 2017 on (about orbit 70000) the excursions to higher temperatures get larger before the OPB level heater power was reduced.

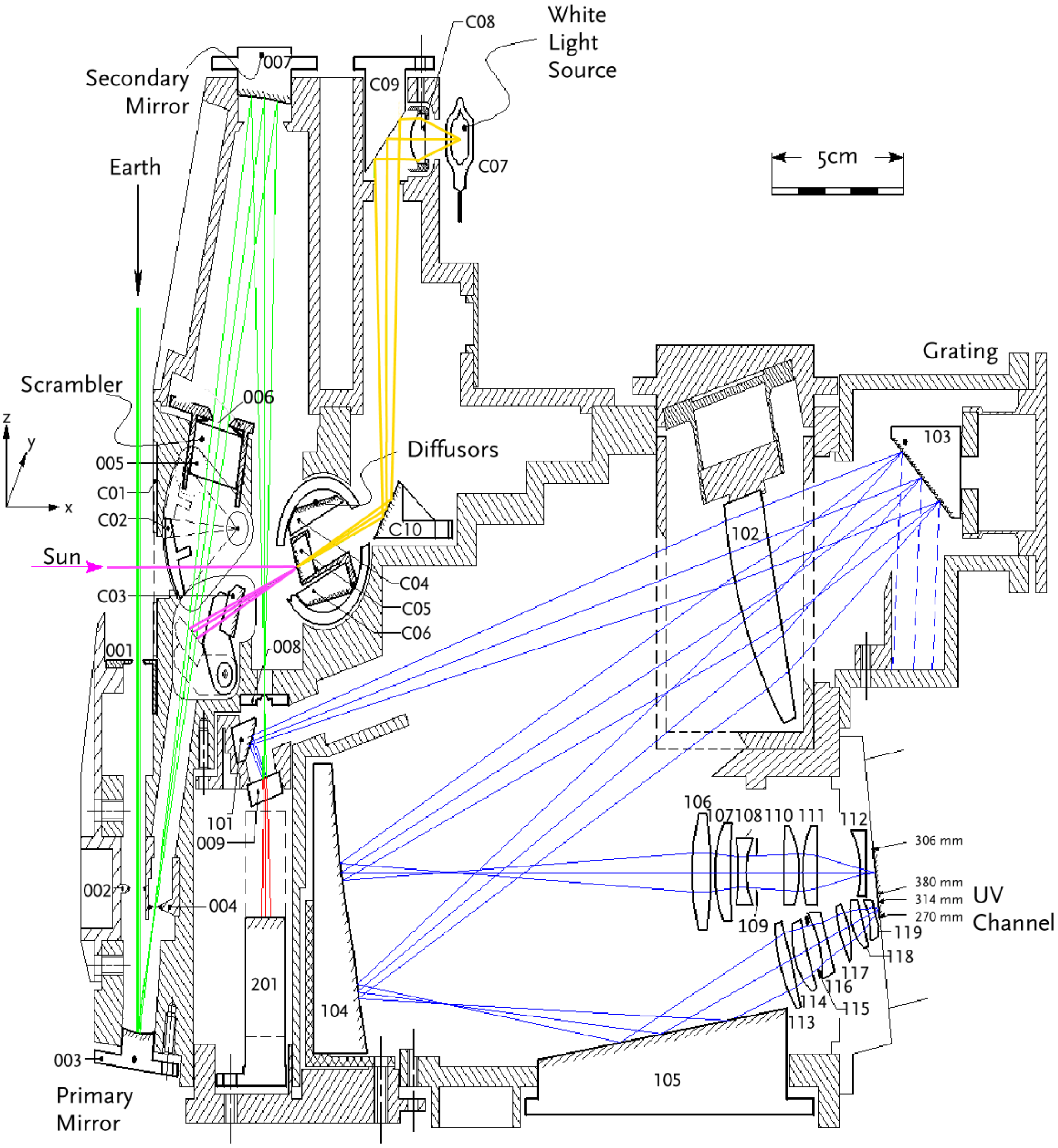

Figure 8: Optical design of the telescope, calibration unit and UV spectrometer (bands 1 and 2). The numbered items are described in the text. The green lines show the optical path of the light from Earth via the telescope to the dichroic (elements 001–009), where the light is split into the UV channel (blue lines) and the VIS channel (red lines). The VIS channel is out of plane and shown in Figure 10. Light from the Sun is shown in magenta. It reflects of a diffuser (C05), the closed folding mirror C03 and from there on follows the same path as the light from Earth (green). Light from the white light source (yellow line) passes through a transmission diffuser, is reflected by the folding mirror and then follows the same path as the light from Earth.

9 Optical design description

The detailed design of the OMI instrument is shown in Figures 8 and 10. The two spectrometers have orthogonal optical planes. Figure 8 shows the telescope, calibration unit and UV spectrometer (bands 1 and 2) while Figure 10 shows the UVIS spectrometer (band 3). The numbered items in the figures are described in the following.

9.1 Telescope and instrument slit

The main elements of the telescope are the primary 003 and the secondary mirror 007, with aperture stop 006 and the the polarization scrambler 005. The light reflected from the Earth's atmosphere and surface enters the instrument via the nadir port (element 001 in Figure 8). The entrance aperture of the nadir port 001 is a curved slit. The light is imaged by a wide field telecentric telescope, which consists of two aluminum spherical mirrors (003 and 007), onto the entrance slit 008. A small aperture 002 with an area of about 1 cm^2 in front of the primary telescope mirror reduces the risk of in-orbit contamination and lowers the spatial straylight. The reduction of straylight is also the purpose othe oversized slit 004 in the focal plane of the primary telescope mirror. The system pupil stop 006 is placed in the focal plane of the secondary mirror 007. This makes the telescope telecentric for the instantaneous field of view (IFOV) in swath (across track) direction (115°) and the various viewing angles are imaged onto different locations along the length of the slit 008. The image in the spatial direction on the detectors displays a spatial smile: the edges of the swath (±57°) face about 6° more backward along track then at 0° swath angle (nadir). The along track instantaneous field of view (IFOV) is about 1°.
The system pupil stop 006 is 7.6 mm wide in swath direction and 5.6 mm in the orthogonal direction. More imaging properties of OMI are listed in Table 5. In between the primary and secondary telescope mirror is the telescope aperture stop 006 with a polarization scrambler 005. The scrambler is used to depolarize incident light, as other optical elements within the instruments have polarization dependent responses. This holds especially for the dichroic mirror 009 and for the gratings 103 (UV) and 207 (VIS). The scrambler is a dual Babinet pseudo-depolarizer made of two wedge pairs rotated with respect to each other. The wedges are made of birefringent quartz material with a wedge angle of about 6° and their optic axis oriented perpendicular to the direction of the transmitted light. This geometry introduces a continuous phase difference between ordinary and extraordinary beam, effectively distributing different polarization states across the beam. A second wedge with its optic axis perpendicular to the first one compensates beam displacement and refraction while preserving the polarization state of the light coming from the first wedge. To also cover the polarization state corresponding to the ordinary ray in the first wedge a second wedge pair is placed with its optic axes rotated by 45° with respect to the first pair's axes. Due to remaining birefringence, light with perpendicular polarization is imaged on slightly different places on the detectors, causing the so-called diamond effect. Furthermore spectral features can be introduced. Detailed results of the testing of the polarization scrambler are presented in [1]. The end faces of wedge 2 and 4 (shown in red in Figure 9) and the front face of wedge 3 are anti-reflection coated with MgF$_($2) optimized at 290 nm. The first surface of the scrambler is left intentionally uncoated to compensate for the polarization dependent reflectance of the first telescope mirror 003.

Parameter	UV1	UV2	VIS
Aperture size	2.6 mm^2	2.6 mm^2	2.6 mm^2
Focal length at nadir	21.73 mm	21.73 mm	21.73 mm
F-number	$f/1.5$	$f/3.2$	$f/5.0$
IFOV across track	115°	115°	115°
IFOV along track	1°	1°	1°
Swath width on-ground	2600 km	2600 km	2600 km
Groundpixel along track	13 km	13 km	13 km
Groundpixel across track at nadir	48 km	24 km	24 km

Table 5: The imaging properties of OMI. The groundpixel size is given for nominal radiance settings.

The secondary telescope mirror 007 has an optical coating to suppress straylight from 500 nm up towards longer wavelengths and to reduce the light intensity in the visible channel. The coating reduces the mirror's reflectivity from 20 % at 500 nm to about 8 % at 750 nm.

The incoming light is imaged by the two telescope mirrors on the instrument entrance slit 008. The entrance slit 008 determines a number of instrument properties. The slit is 44 mm long and 300 µm wide. The field of view of 115° in the across track (swath) direction is a result of the long dimension of the slit. The spectral resolution and field-of view in flight direction is determined by the slit width. The instantaneous field of view of the telescope in along track direction is 0.8° which is increased by the polarization scrambler to about 1°. For a OMI CCD pixel viewing this corresponds on-ground to a IFOV of about 10 km along track. OMI measurements are co-added during 2 s, with a ground speed of the Aura spacecraft of about 7 km/s, this results in ground pixel size of 13 km in the flight (along track) direction. Note that a measurement contains some information of

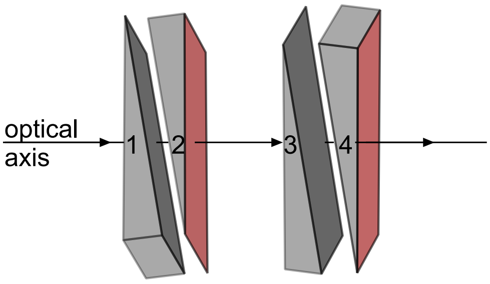

Figure 9: Exploded schematic of the polarization scrambler. The scrambler consists of two wedge pairs. The light propagates in the direction indicated by the arrows. The end faces of wedge 2 and 4 (shown in red) and the front face of wedge 3 are anti-reflection coated.

the outside the 13 km in the flight direction, due to the IFOV of 10 km. In the swath (across track) direction, pixels are binned (see Section 10.1). For nominal radiance measurements this results in a ground pixel size of about 24 km for UV2 and VIS and 48 km for UV1. The sizes differ due to the spatial imaging of the UV1 light as explained in Section 9.2. The pixel-size in the swath-direction increases from nadir towards the swath edge. This effect is shown in Figure 2.

The width of the slit can vary over the slit length, slit-irregularities in the order of 10 µm wide have been observed under the microscope. These irregularities cause variations of the throughput over the swath angles. They are wavelength independent and are visible as stripes on the detectors over all columns, this is shown in [1].

Behind the entrance slit a dichroic mirror 009 reflects the light in the UV spectral range (264–383 nm) to the folding mirror 101 and transmits the UVIS spectral range (349–504 nm) to a flat mirror 201. The flat mirror reflects the light at 90° out of the plane of Figure 8. The characteristics of the dichroic mirror define a spectral overlap between UV and UVIS of about 30 nm. The backside of the dichroic mirror has an antireflection coating for the visible wavelength range.

9.2 UV spectrometer (bands 1 and 2)

From the dichroic mirror 009 the UV light is reflected by folding mirror 101 and collimated by the plano-convex fused silica field lens 102. The dispersion of the wavelengths is done by holographic reflection grating with a blazing angle of 28°. The grating has 2880 lines per mm and is used in first order. The diffracted first order spectrum of the grating is imaged by the lens 102 close to the field mirror 104. This mirror consists of two spherical concave mirrors that split the UV channel into the UV1 channel (264–311 nm) and the UV2 channel (307–383 nm). The layout of the UV channel is determined to a large extent by the straylight requirements, especially for the UV1 spectral region. Within the UV spectral range the variation in radiance from the Earth between the shortest wavelength (< 290 nm) and the longer wavelength (> 320 nm) varies by more than three orders of magnitude. Without proper measures the straylight at wavelengths below 290 nm would exceed the signal itself. This straylight originates from wavelengths between 310 to 380 nm. To avoid this unwanted situation, the UV channel is split into to sub-channels UV1 and UV2. As the intermediate image of the spectrum is located just before and not on mirror 104, a small spectral overlap is created between UV1 and UV2. Mirror 104 also has position dependent (= wavelength) coating with variable reflection. For the lower part of the mirror, which images the shorter wavelengths, the coating suppresses longer wavelengths. This reduces spectral straylight to up to an order of magnitude. The system aperture stop 006 is re-imaged by mirror 104 at the apertures 115 (UV1) and 109(UV2). By splitting the UV spectral range in two parts, the straylight that is caused by internal reflections in the UV2 imaging objective (elements 106–112) has no effect on the UV1 spectrum at the detector surface.

The UV1 objective (elements 113-119) scales the spatial part of the image down by a factor of 2 on the CCD detector as compared to the UV2 image. This is done in order to improve the signal-to-noise performance of the UV1 channel by a factor of $\sqrt{2}$, at the cost of doubling the groundpixel size in the swath direction. Both UV1 and UV2 are imaged onto the same CCD detector. The light in the UV1 range is reflected via a bare aluminium mirror 105 onto the UV1 objective. This reverses the spectrum of UV1 with respect to UV2, as shown in Figure 8.

9.3 VIS channel

In Figure 10 the optical layout of the visible channel is shown. Note that the orientation of the plane of drawing of this figure is perpendicular to that of the UV channel depicted in Figure 8. The visible part of the spectrum

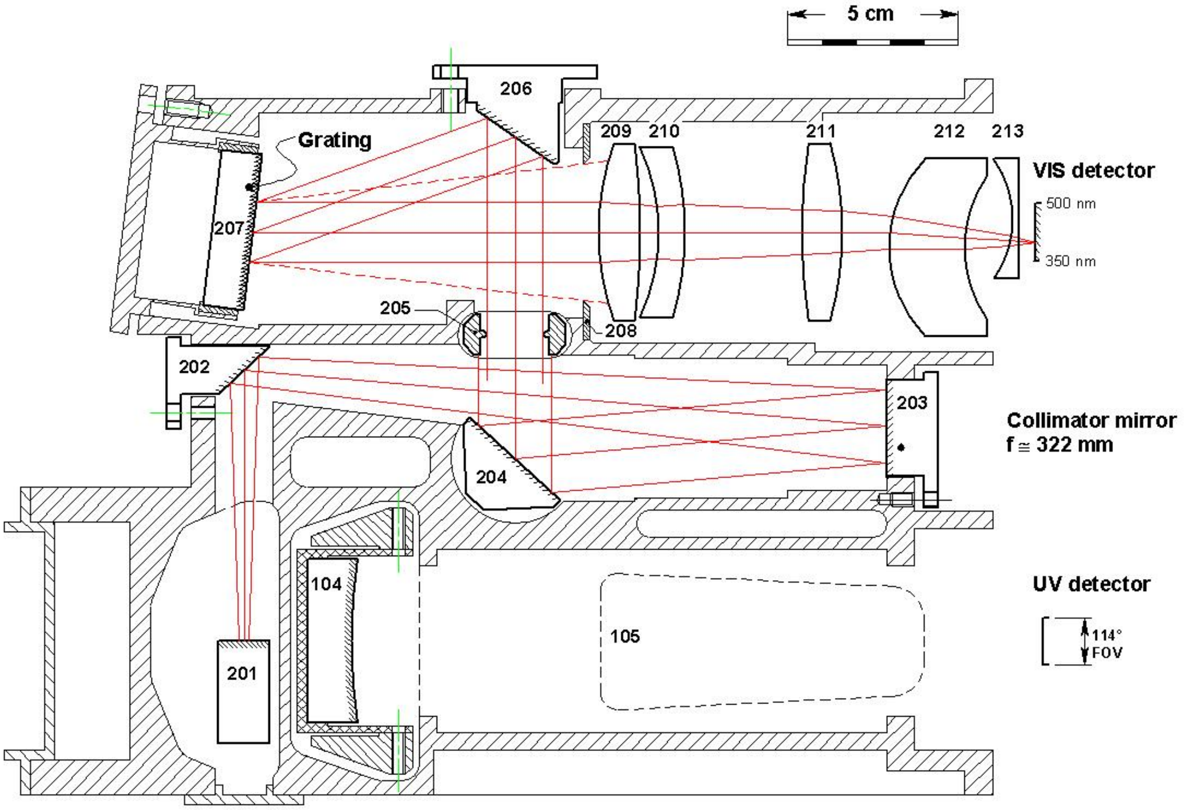

Figure 10: Optical design of the VIS spectrometer (band 3). The VIS spectrometer has its optical plane orthogonal to the UV spectrometer (see Figure 8). The numbered elements are described in the text.

(349–504 nm) is reflected at 90° by a flat mirror 201 towards the VIS spectrometer.

The VIS light is directed via folding mirror 202, collimating mirror 203, and folding mirrors 204 and 206 towards the grating 207. All mirrors are made from aluminum and coated with MgF_2. The grating is a reflective holographic grating with blazing angle of 17° and 1350 lines per mm. The VIS objective (elements 209–213) images the diffracted beams on the second VIS CCD detector. The aperture 205 is the effective aperture stop for the VIS channel.

10 Instrument electronics and detectors

The instrument electronics is divided in two parts: the two detector modules (DEMs) each containing a charge coupled device (CCD) detector and the electronics unit (ELU). The ELU is part of the electronic read-out chain for the detector signals but also used to control the detectors, the thermal control, and the internal light sources and the mechanisms. Figure 11 shows an overview of the control electronics, in Figure 13 the different steps of the signal read-out chain are shown. The interface adapter module (IAM) forms the link with the spacecraft communication and data handling system.

10.1 Detector modules

The detector modules consist each of a charge coupled device (CCD) and basic read-out electronics. The CCDs are thinned, back-illuminated CCDs with a HfO_2 anti-flection coating to increase the quantum efficiency in the UV. The quantum efficiency in the UV is about 55 % at 270 nm, the UVIS detector reaches about 65 % at 500 nm.

The detectors are used in frame-transfer mode and have three regions: an image region, a storage region and a read-out region as shown in the right panel of Figure 12. After each exposure the entire frame is transferred rapidly (within 4.32 ms) from the illuminated image section to the shielded storage section. From the storage section the image is moved row by row to the read-out register (ROR) at the edge of the detector

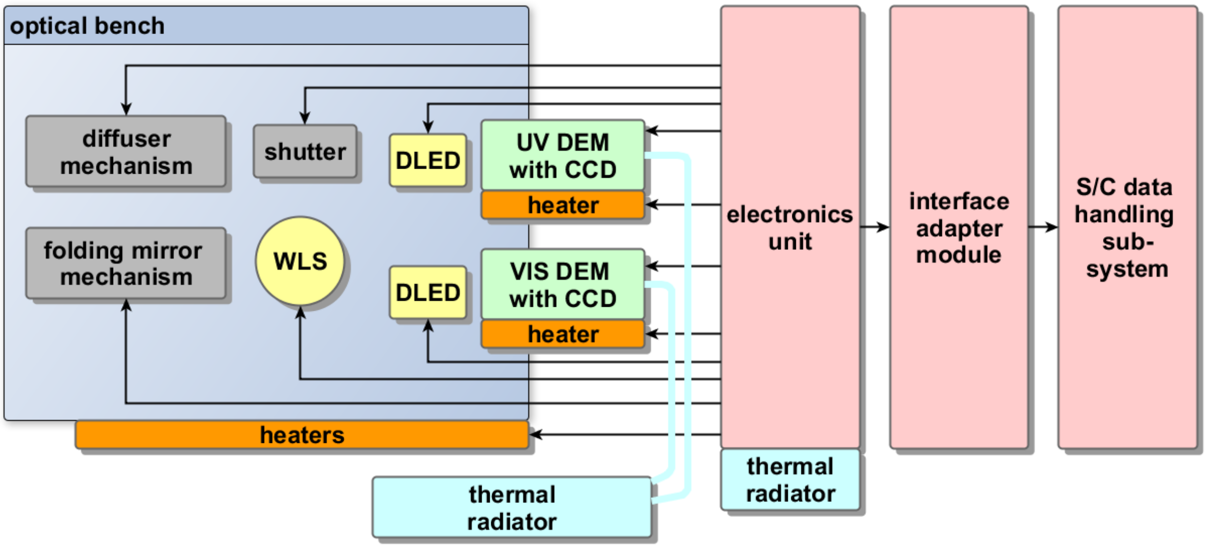

Figure 11: Conceptual design of OMI showing the control of the various subsystems. The optical bench and the electronics unit are thermally connected to their own radiators.

and read out while the exposure of the next frame takes place in the image section. This allows a continuous coverage of the Earth without data gaps.

The CCDs have 576 rows (spatial dimension, swath) and 780 columns (spectral dimension) in both the image and the storage section. The size of each pixel is $22.5 \times 22.5\,\mu\text{m}^2$. The pixel full well is $6{\times}10^5$ electrons, but in practice the pixel filling is kept below $3{\times}10^5$ electrons to prevent the ellipsoid effect and pixel blooming occurs. The ellipsoid effect is an increase in pixel noise and described in detail in [1]. There is no light-insensitive area between the pixels.

The read-out register (ROR) is located at the lower end of the storage section. The ROR pixels are larger than the image and storage pixels to allow for binning. A register pixel can hold about $2.5{\times}10^6$ electrons. When row binning is performed, the charge of multiple rows is collected in the ROR before read-out, this allows for shorter read-out times, higher signal-to-noise ratio and lower data rate but it also lowers the resolution in the spatial direction of the measurement. Examples of different binning settings and their respective groundpixel sizes at nadir are shown in Table 6.

The read-out register also allows for skipping rows during the read-out. For this, the drain-dump on the ROR is activated while the charge of the rows to be skipped is being shifted into the ROR and immediately cleared through the drain dump. After that, read-out continues by deactivating the drain-dump. The ELU uses a fixed binning and skipping scheme with configurable parameters, as described in appendix B.

Purpose	Binning factor	UV1	UV2 & VIS
Nominal global radiance	8	48 km	24 km
Zoom-in radiance	4	24 km	12 km
Unbinned calibration	1	6 km	3 km

Table 6: Groundpixel size across track at nadir for different binning settings.

The nominal exposure time of the CCD varies between 0.4 s (for tropical latitudes) and 1.0 s (for arctic latitudes). In order to improve the signal-to-noise and to reduce the downlink data rate, five sequentially taken exposures within the master clock period (MCP) of 2 s are co-added on-board in the electronics unit. This results in the 13 km spatial resolution in the flight direction.

The pixel transfer time is 7.5 µs both for a vertical shift (rows) and a horizontal shift (columns). This results in the frame transfer time of 4.32 ms and the read-out time of a complete (binned) row of 6.11 ms. The signal is clocked in one directions towards the read-out node as indicated by the arrow in the right panel of Figure 12. In the read-out node the charge in a read-out register pixel is converted into a voltage by a capacitor. The analogue signals are amplified on chip and then sampled and digitized in the ELU. The gain of the on-chip amplifier can be set by the ELU.

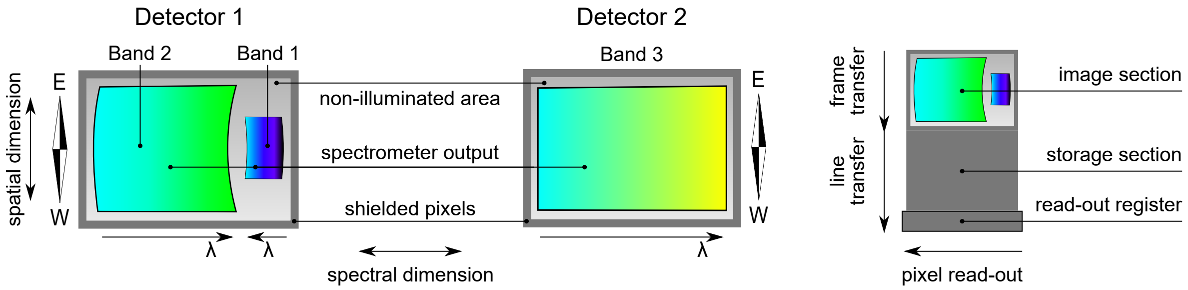

Figure 12: Illustration of the layout of the CCD detectors as viewed along the propagation direction of the incoming light. Bands 1 (UV1) and 2 (UV2) are both imaged onto detector 1, the low wavelengths are imaged towards the detector edges for both bands. Both the UV (1) and the VIS (2) detectors have pixels which are shielded by a mask and pixels which are not illuminated directly. After an exposure, the entire image frame is transferred to the masked storage area. Then the image is read out line by line during the following exposure. The East-West orientation is shown for the day-side of an orbit.

During the frame transfer of each image a draindump is performed on the register. After the frame transfer, at the start of the read-out, the cleared register is read-out. This signal can be used to determine the read-out noise and the electronic offset values. The ROR has 17 additional pixels at each side of the CCD edges. The pre-and post-scan pixels do not have a draindump. The pre-scan pixels, and depending on the settings the post-scan pixels as well, are read out with every row and their signal can also be used for calibration purposes.

As indicated in Figure 12 only part of the image region is illuminated by light from the Earth or Sun. This science region is about 240 × 160 pixels large for band 1, about 480 × 560 pixels large for band 2 and about 480 × 750 pixels large for band 3. The extreme rows and columns of the image area are masked and not sensitive to light.These masked rows can be used to determine the dark signal (columns) and exposure smear (rows). Between the illuminated area and the masked areas there are rows which are not illuminated directly but can serve to determine spatial straylight. These rows are binned to improve the signal-to-noise ratio.

Ideally, the spectral and spatial dimension would be imaged orthogonally onto the detectors. However, they are optical distortions both in spatial and spectral dimension. Lines of equal viewing direction are imaged with a curvature ("‘spatial smile"') and equal wavelengths are not imaged onto the same column ("‘spectral smile"'). The optical design has been optimized to minimize to the distortion in the spatial direction. The optical distortion in the spectral direction is more pronounced than the distortion in the spatial direction. The UV detector shows a stronger spectral smile than the UVIS detector as indicated in Figure 12.

Cosmic radiation, mainly high energetic protons, can damage individual CCD detector pixels. As a result, the dark current of the individual CCD pixels and the average dark current of the complete CCD detector increases over the mission. The low operating temperature and shielding around the detectors (see Section 8) help to slow down this process and a regularly updated background or dark correction can minimize the impact on the science data. The dark current increase can be either permanent or change back and forth between different dark current levels. The latter effect is called random telegraph signal (RTS). Depending on the duration between signal jumps, RTS can be corrected with the normal background correction. If the jumps occur too quickly after each other, pixels can also be flagged and discarded for scientific use.

Each CCD is directly connected and integral part of a detector electronics module (DEM). The signal read out from the CCD enters the video signal chain as shown in Figure 13. Within the DEM, signal limiting and DC decoupling is performed. The DEM also contains an amplifier stage (which consists of multiple amplifiers) that implements the gain switching of OMI: For four different regions in the science region of the CCD a different gain can be set to optimize the signal for the available ADC range. The gain switching takes place at identical columns for every row. When a gain switch occurs the read-out process is temporarily stalled to allow the amplifier to settle, see also [1] for observed overshoot effects. The CCD read-out register uses the same gain switching as the image area. In this way electronic offset values for all gain settings can be obtained. For the (binned) dark and stray areas no gain switching is applied. For these areas a different gain can be selected from the available gains, which applies to all columns in these areas.

The different gains are established by using 3 different amplifiers. In the first amplifier stage, the signal is switched between 2 different amplifiers which both have a fixed gain. In the second amplifier stage the signal is not switched between amplifiers, but instead the feedback loop of the amplifier is switched to obtain 2 different gains. As a result gain values of approximately factors of 1×, 4×, 10× and 40× can be set.

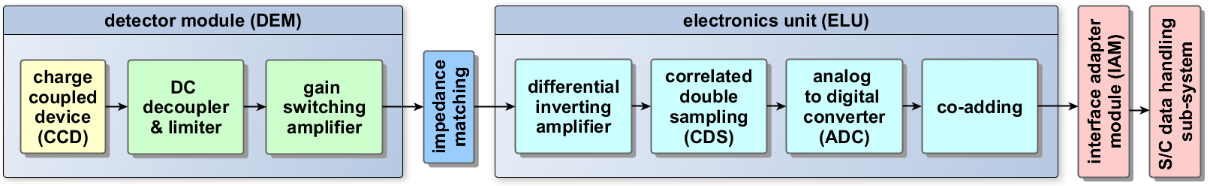

Figure 13: Schematic of a OMI detector module (DEM) with CCD detector and the electronics unit (ELU). The arrows indicate the path of the measured signal. The interface to the data handling of the S/C is via the interface adapter module (IAM).

10.2 Electronics unit (ELU)

From the DEM the video signal is transferred to the electronics unit (ELU). The input stage of the ELU is an inverting amplifier (gain -1×). The output impedance of the DEM (100 Ω) combined with the input impedance of the ELU (400 Ω), results in an effective gain of 0.8× for the interface. By correlated double sampling (CDS) in a clamping circuit the CCD reference level is subtracted from the CCD video level. The resulting signal contains offsets from CCD bias and an offset added by the ELU. The video signal is then digitized by the ELU using a 12 bits analog-digital converter (ADC). The conversion factors are 618.203 and 612.803 electrons per binary unit for the UV and VIS channels, respectively. After digitization the individual CCD frames can be co-added in the ELU. One column per detector can be stored without co-addition. These so called small pixels or small pixel columns can be used for example to determine inhomogeneous illumination. After co-addition the signals are passed to the interface adapter module (IAM).

All communication from and towards the CCD detectors goes via the ELU. The ELU triggers the CCD read-out and the gain switching in the DEM. The mechanisms, internal sources and thermal control of the instrument are also controlled via the ELU. In the ELU register instrument configuration value are defined, specifying exposure time, binning scheme, gain areas and other measurement specifics, see also Part III.

10.3 Interface adapter module (IAM)

The interface adapter module (IAM) provides the interface between the instrument and the spacecraft. It performs command buffering, data formatting, instrument control and provides the housekeeping data.

The IAM memory holds the stored instruction sequences (SIS). Some of the SISs are pre-defined sets of instructions such as powering-up the OMI instrument or setting it in safe mode; these are hard coded in the EEPROM of the IAM. Other SISs contain calibration sequences that can be adapted on-ground and uplinked to the memory of the IAM, see also Part III.

11 Calibration sources

For in-flight calibration and characterization several light sources can be used: solar irradiance via one of three diffusers, an internal white light source (WLS) and light emitting diodes (LEDs) placed close to the detectors. To couple the light from Sun or WLS into the instrument, moveable optical elements are employed: the folding mirror mechanism (FMM), the diffuser mechanism (DIFM) and the Sun aperture mechanism (SAM). The folding mirror C03 bypasses the primary telescope mirror 003 (numbered as in Figures 4 and 8), so when using solar measurements and the WLS to monitor degradation, the primary telescope mirror is not included.
In the following the different mechanisms and sources are described in more detail.

11.1 Mechanisms

The three mechanisms FMM, DIFM and SAM are similar, only the moveable optical elements differ. Each mechanism consists of a shaft that can be rotated by a stepper motor to different positions. The optical elements are connected to the shaft. The position of the mechanism is determined with opto-couplers and a slitted disc. The opto-couplers consist of infra-red LEDs and photo transistors mounted on opposing sides of the static part of the mechanism. The disc is attached to the moveable part and interrupts the signal at defined intervals allowing to determine the position.

The motor is a two-stepper motor with redundant windings. Only in the case of the FMM the redundant windings are connected to the drive circuits, allowing for redundancy if one set fails. The mechanism have

Barden 36H angular contact bearings and are lubricated by ion plated lead coating combined with lead bronze caging.

11.1.1 Folding mirror mechanism (FMM)

The folding mirror mechanism (FMM) operates an uncoated mirror C03 that can be moved in and out of the Earth radiance optical path between the primary and secondary telescope mirrors. The positions of the mechanism are defined by end-stops, see also Section 5.3.1. When the mirror blocks the Earth radiance optical path, it reflects either Sun light from one of the reflection diffusers or the white light source (WLS) light from the transmission diffuser towards the entrance slit of the spectrometer. The mirror C3 is concave and located about 5 cm from the aperture stop 006. The curvature of the mirror is intended to replace the function the primary telescope mirror 003 has for the radiance measurements. In this way the slit illumination via Sun and Earth port should be comparable. Any differences in illumination should be included in the absolute radiometric calibration and the spectral calibration.

11.1.2 Sun aperture mechanism (SAM) and solar mesh

The Sun aperture mechanism (SAM) C02 is a shutter which is opened only for solar irradiance measurements. The Sun is observed via a mesh C01 in front of the shutter. The mesh has many slits with dimensions 450 × 20 µm resulting in a transmission of about 10 %. The mesh is designed to avoid edge effects and diffraction in the OMI wavelengths. The positioning of the slits within the mesh is such that shadowing effects on the diffusers are minimized.

11.1.3 Diffuser mechanism (DIFM)

The diffuser mechanism has four diffusers: one quartz transmission diffuser C05 used with the WLS and on-ground sources (see Section 11.3), and for the solar calibration two aluminum surface reflection diffusers (ALU1 and ALU2) and one quartz volume reflection diffuser (QVD). Note that only the aluminum diffusers (C04 and C06) and the WLS diffuser are shown in Figure 8. The solar diffusers are 40 × 16 mm large and the reverse image of the slit has a curved shape and a size of about 28 × 8 mm on the diffusers.

11.2 Solar irradiance

As shown in Fig. 4 and Fig. 8 the optical paths for the Earth and solar measurements are not the same. For this reason the optical paths can degrade differently during the mission, which may produce an artificial trend in the Earth radiance to solar irradiance ratio (sun-normalized Earth reflectance).
To perform a solar calibration measurement the mechanisms described in Section 11.1 are moved in the right positions. The open Sun aperture mechanism allows sunlight into the instrument through the solar mesh. The

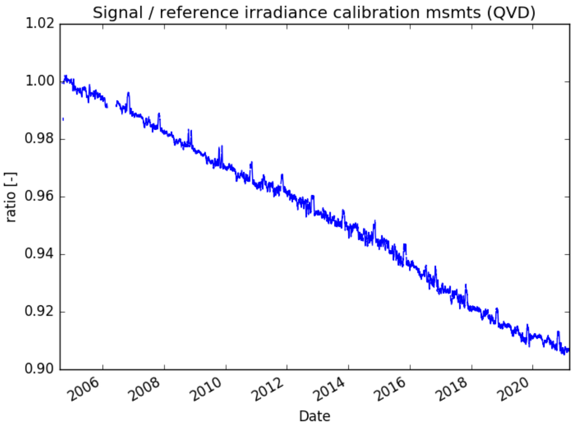

Figure 14: The irradiance signal for UV1 via the QVD relative to the start of the mission. In more than 16 years of mission the signal degraded by less than 10 %.

light is reflected by one of the three reflection diffusers within the diffuser mechanism (DIFM) onto the mirror C03 on the folding mirror mechanism (FMM) and from there via the scrambler 005 towards the secondary telescope mirror 007. The solar calibration measurements have a different optical path than the Earth radiation measurement, adding the mesh, the reflection diffuser and the FMM mirror C03, and bypassing the primary telescope mirror 003. In first approximation the folding mirror C03 and the primary telescope mirror 003, that are both made of uncoated aluminum, are expected to have a comparable degradation.

The quartz volume reflection diffuser is used on a daily basis to provide the irradiance spectrum for normalizing the Earth radiance spectra. The QVD shows less diffuser features than the aluminum diffusers and was therefore chosen for the nominal irradiance measurements. One surface reflection aluminum diffuser is used on a weekly basis (AL1, regular aluminum diffuser), while the other is used on a monthly basis (AL2, backup aluminum diffuser), see also Part III. The QVD shows little degradation when compared to other instruments. The irradiance signal dropped by less than 10 % in the UV1 spectral range over more than 16 years of mission as shown in Figure 14. For UV2 the degradation is less than 6 % and for VIS around 4 %.

11.3 White light source

The white light source (C07 in Figure 8) is a quartz tungsten halogen lamp with a UV-transparent bulb (5 W, 12 V). The light is imaged via the lens C08 and mirrors (C09 and C10) onto a transmission diffuser C05 inside the diffuser mechanism. The combination of cylindrical lens C08, flat mirror C09 and cylindrical mirror C10 images a point at the location of the WLS as a line on the transmission diffuser. With the folding mirror mechanism C03 in the closed position the light is reflected onto the secondary telescope mirror and from there on follows the same optical path as the radiance and illuminates the science region on the detectors (see Section 10.1). The WLS illuminates the detectors spatially and spectrally smooth, so it is useful to monitor the pixel response non-uniformity (PRNU), slit irregularity and the overall relative instrument throughput. The transmission diffuser's first surface is roughened while the second surface is polished. The diffuser also adds features to the illumination pattern on the detectors, which need to be taken into account when deriving instrument or detector properties. The diffuser features produce stripes on the detector which also have spectral dependency. This is unlike the slit irregularity, where only a variation in spatial direction occurs.

For on-ground calibration purposes it was also possible to remove the WLS and use an outside source to illuminate the entire slit simultaneously. The WLS ceased functioning on 19 September 2019 (in orbit 80737) after roughly 38 hours of operation in total and more than 15 years in orbit. Note that the in-flight voltage was higher than the specified 12 V. At the beginning of the mission the voltage was 12.8 V, it steadily increased to 14 V and decreased after about 13.5 years in orbit, see Figure 15. As shown in Figure 16 the output of the WLS decreased over the mission. Up to mid 2009 (around orbit 30 000) the WLS was switched on several times for a longer period to partially reverse the degradation. From about 2018 (around orbit 75000) the lowering in signal first partly reversed and then accelerated until it ceased functioning entirely.

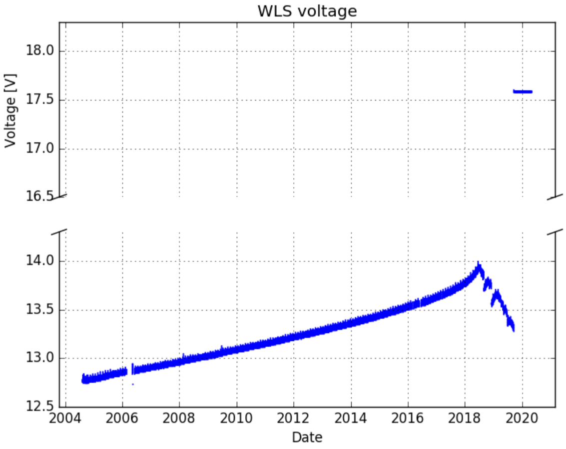

Figure 15: Supply voltage of the WLS. During the mission the voltage increased steadily to about 14 V before it started decreasing. The increase to around 17.6 V shows when the lamp ceased working.

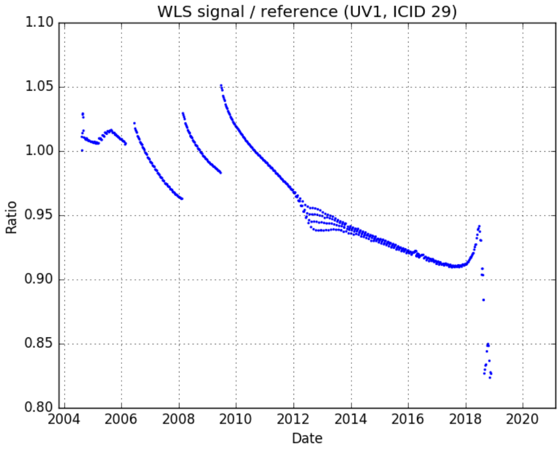

Figure 16: Output of the WLS for UV1 with respect to the start of the mission. The WLS stopped working on 19 September 2019. The jumps in the curve before mid 2009 reflect the trials to reverse the degradation by switching the lamp on for a longer time.

11.4 Light emitting diodes

All bands are equipped with pairs of green LEDs located close to the detectors. The position of the green LEDs in the VIS channel is at the aperture 208. The LEDs are imaged via the VIS objective onto the detector, so LED structures can be seen back in the illumination pattern. The LEDs illuminate a region spanning columns 33–778 and rows 32–552 of the VIS detector. For the UV channels two LEDs are placed between lenses 110 and 111 for band 2 and another 2 LEDs are located between lenses 116 and 117 for band 1. The LEDs are not directly imaged and therefore show a different illumination pattern than for the VIS detector. For the UV detector the LEDs illuminate columns 33–779 and rows 32–553. The LEDs are not shown in Figures 8 and 10 as they are located just above and below the plane of the drawings. The primary use of the LEDs is the identification of bad detector pixels, to obtain the relative electronic gain values, and to calibrate the non-linearity of the electronics in flight. As the LEDs emit in a narrow wavelength band around 500 nm, the detector response is not entirely representative for the response at other wavelengths. Properties such as the PRNU will differ when determined with LED illumination.

Part III

Instrument operations

12 Orbit definition

The orbit definition of the Aura mission plays an important role in the operational aspects. Both instrument operations and data processing use a (coordinated) orbital scenario. This orbital scenario is also linked to in-flight calibration of the instrument. Aura flies a sun-synchronous polar orbit. The orbital parameters for Aura are given in Table 7.

Operational parameter	Value
Repeat cycle	16 days
Semi-major axis	7080.7 km (4399.7 miles)
Cycle length	233 orbits
Eccentricity	0.0001111
Inclination	98.2°
Argument of perigee	89.5089°
Mean local time of ascending node crossing	13:45 hh:mm

Table 7: Reference orbit of the Aura mission.

Each Aura orbit has a day (lit) side and a night (dark) side, as illustrated in Figure 17. On the day side the spacecraft flies from south to north; on the night side it flies from north to south. Spacecraft midnight is defined as the time halfway the nadir day-night terminator and the nadir night-day terminator; spacecraft noon is the time halfway the nadir night-day terminator and the nadir day-night terminator. Data processing uses the spacecraft midnight as the start and end points of an orbit, however for instrument operations an orbit starts 2 minutes and 48 seconds (168 s) before the night/day terminator crossing, i.e. the start of the radiance measurements (see Figure 18). Due to seasonal variation, the position of the equator changes with respect to spacecraft midnight as indicated in Figure 17. As a result, spacecraft midnight is not at a fixed latitude.

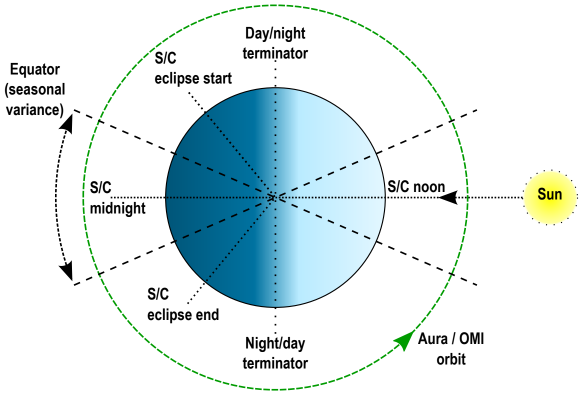

Figure 17: Aura orbit overview showing S/C midnight as halfway point between the day-night and night-day terminator. Aura flies from south to north on the illuminated side of the globe. The equator position changes over the season with respect to S/C midnight.

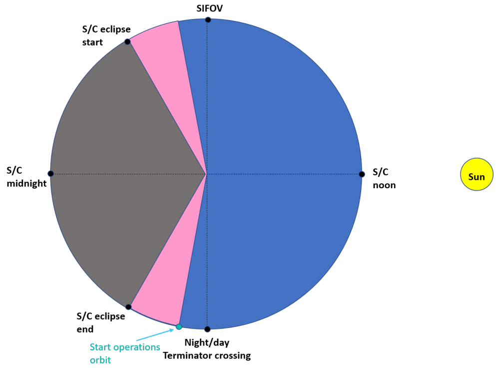

Figure 18: OMI operations orbit definition. The radiance measurements (blue) start shortly before the night-day terminator. In the dark eclipse side (gray) calibration measurements can be scheduled. The solar irradiance is measured when the Sun is in field-of-view of the solar port (SIFOV) at the north side of the orbit.

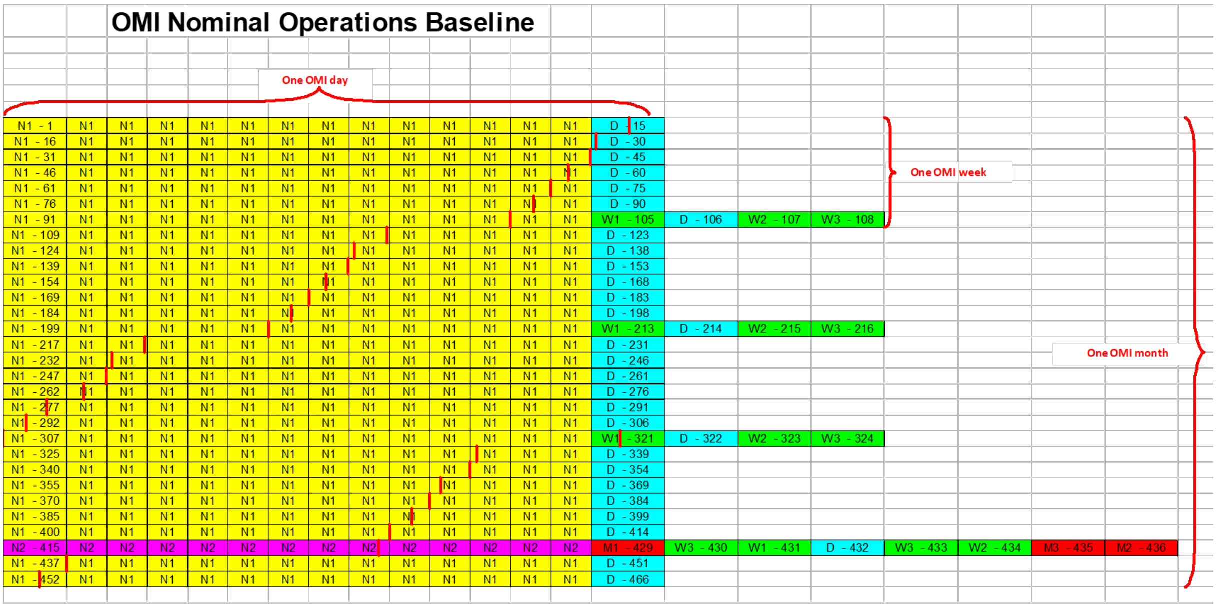

OMI Nominal Operations Baseline

N1 - 1	N1	N1	N1	N1	N1	N1	N1	N1	N1	N1	N1	N1	N1	D - 15							
N1 - 16	N1	N1	N1	N1	N1	N1	N1	N1	N1	N1	N1	N1	N1	D - 30							
N1 - 31	N1	N1	N1	N1	N1	N1	N1	N1	N1	N1	N1	N1	N1	D - 45							
N1 - 46	N1	N1	N1	N1	N1	N1	N1	N1	N1	N1	N1	N1	N1	D - 60							
N1 - 61	N1	N1	N1	N1	N1	N1	N1	N1	N1	N1	N1	N1	N1	D - 75							
N1 - 76	N1	N1	N1	N1	N1	N1	N1	N1	N1	N1	N1	N1	N1	D - 90							
N1 - 91	N1	N1	N1	N1	N1	N1	N1	N1	N1	N1	N1	N1	N1	W1 - 105	D - 106	W2 - 107	W3 - 108				
N1 - 109	N1	N1	N1	N1	N1	N1	N1	N1	N1	N1	N1	N1	N1	D - 123							
N1 - 124	N1	N1	N1	N1	N1	N1	N1	N1	N1	N1	N1	N1	N1	D - 138							
N1 - 139	N1	N1	N1	N1	N1	N1	N1	N1	N1	N1	N1	N1	N1	D - 153							
N1 - 154	N1	N1	N1	N1	N1	N1	N1	N1	N1	N1	N1	N1	N1	D - 168							
N1 - 169	N1	N1	N1	N1	N1	N1	N1	N1	N1	N1	N1	N1	N1	D - 183							
N1 - 184	N1	N1	N1	N1	N1	N1	N1	N1	N1	N1	N1	N1	N1	D - 198							
N1 - 199	N1	N1	N1	N1	N1	N1	N1	N1	N1	N1	N1	N1	N1	W1 - 213	D - 214	W2 - 215	W3 - 216				
N1 - 217	N1	N1	N1	N1	N1	N1	N1	N1	N1	N1	N1	N1	N1	D - 231							
N1 - 232	N1	N1	N1	N1	N1	N1	N1	N1	N1	N1	N1	N1	N1	D - 246							
N1 - 247	N1	N1	N1	N1	N1	N1	N1	N1	N1	N1	N1	N1	N1	D - 261							
N1 - 262	N1	N1	N1	N1	N1	N1	N1	N1	N1	N1	N1	N1	N1	D - 276							
N1 - 277	N1	N1	N1	N1	N1	N1	N1	N1	N1	N1	N1	N1	N1	D - 291							
N1 - 292	N1	N1	N1	N1	N1	N1	N1	N1	N1	N1	N1	N1	N1	D - 306							
N1 - 307	N1	N1	N1	N1	N1	N1	N1	N1	N1	N1	N1	N1	N1	W1 - 321	D - 322	W2 - 323	W3 - 324				
N1 - 325	N1	N1	N1	N1	N1	N1	N1	N1	N1	N1	N1	N1	N1	D - 339							
N1 - 340	N1	N1	N1	N1	N1	N1	N1	N1	N1	N1	N1	N1	N1	D - 354							
N1 - 355	N1	N1	N1	N1	N1	N1	N1	N1	N1	N1	N1	N1	N1	D - 369							
N1 - 370	N1	N1	N1	N1	N1	N1	N1	N1	N1	N1	N1	N1	N1	D - 384							
N1 - 385	N1	N1	N1	N1	N1	N1	N1	N1	N1	N1	N1	N1	N1	D - 399							
N1 - 400	N1	N1	N1	N1	N1	N1	N1	N1	N1	N1	N1	N1	N1	D - 414							
N2 - 415	N2	N2	N2	N2	N2	N2	N2	N2	N2	N2	N2	N2	N2	M1 - 429	W3 - 430	W1 - 431	D - 432	W3 - 433	W2 - 434	M3 - 435	M2 - 436
N1 - 437	N1	N1	N1	N1	N1	N1	N1	N1	N1	N1	N1	N1	N1	D - 451							
N1 - 452	N1	N1	N1	N1	N1	N1	N1	N1	N1	N1	N1	N1	N1	D - 466							

Figure 19: The original OMI operations baseline of 466 orbits which was used until autumn 2019. In yellow the Nominal orbit-types, in blue the Daily orbit-types, in green the Weekly orbit-types and in red the Monthly orbit types. The orbits containing the zoom measurements are indicated in purple.

13 Operational baseline

For OMI instrument operations, an orbital scheduling approach is used. An orbit is defined from radiance measurement start to radiance measurement start, as described in Section 12. Earth radiance measurements are performed on the day side of the orbit. At the north side of the orbit, near the day-night terminator, the Sun is visible in the instrument's solar port (SIFOV). Approximately once a day, a solar irradiance measurement is performed. The night side of the orbit is used for calibration and background measurements. The following constraints apply to the calibration measurements:

1. Background and calibration measurements can only be performed when the spacecraft is in eclipse.
2. No measurements can be taken around spacecraft midnight, in order to facilitate data processing.
3. All orbits must contain background measurements in the eclipse part of the orbit that match the radiance measurements on the day side for in-flight calibration by the L01b processor.
4. Calibration measurements must have a regular, fixed repetition interval.
5. Once a month measurements above Washington, de Bilt and Sodankyla should be performed in zoom mode.

To accommodate measurements in zoom mode above the same targets each month a scheme of 466 orbits is used. An OMI day is defined by 15 orbits. An OMI week is defined as 108 orbits (7 OMI days + 3 Weekly orbits). An OMI month is defined as 466 orbits (4 OMI weeks + 2 OMI days and 4 extra orbits). In Figure 19 this is illustrated. Blue indicates a Daily orbit-type, green a Weekly orbit-type, red a Monthly-orbit-type and purple indicates a zoom-mode orbit-type.

In 2009 the Aura re-phasing took place. As a consequence the zoom measurements were no longer performed over De Bilt, Washington and Sodankyla, but the original baseline scheme was maintained.

End of 2019 and during 2020 changes to the nominal baseline were made. The first change was to start using a 360 orbit baseline like it is done for TROPOMI. Also the zoom measurements were removed. All calibration measurements were reviewed and only useful calibration measurements were retained. When reviewing the measurements the future plans for the Aura mission were also taken into account (Aura will leave the A-train in 2024 and start drifting in MLT until decommissioning in 2025). The new, simpler baseline is shown in Figure 20.

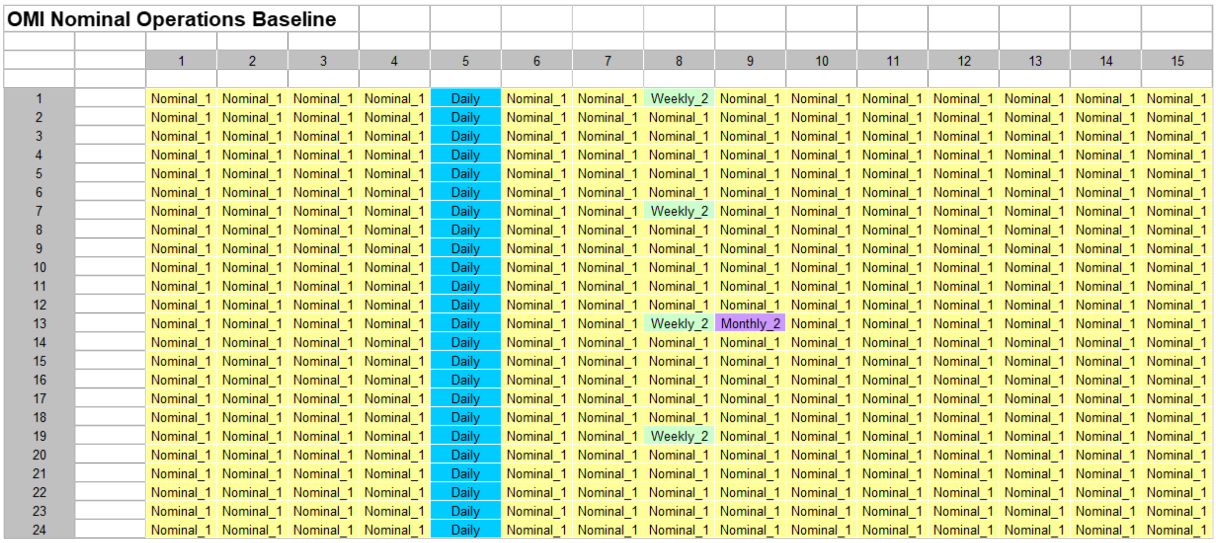

OMI Nominal Operations Baseline

		1	2	3	4	5	6	7	8	9	10	11	12	13	14	15
1		Nominal_1	Nominal_1	Nominal_1	Nominal_1	Daily	Nominal_1	Nominal_1	Weekly_2	Nominal_1	Nominal_1	Nominal_1	Nominal_1	Nominal_1	Nominal_1	Nominal_1
2		Nominal_1	Nominal_1	Nominal_1	Nominal_1	Daily	Nominal_1	Nominal_1	Nominal_1	Nominal_1	Nominal_1	Nominal_1	Nominal_1	Nominal_1	Nominal_1	Nominal_1
3		Nominal_1	Nominal_1	Nominal_1	Nominal_1	Daily	Nominal_1	Nominal_1	Nominal_1	Nominal_1	Nominal_1	Nominal_1	Nominal_1	Nominal_1	Nominal_1	Nominal_1
4		Nominal_1	Nominal_1	Nominal_1	Nominal_1	Daily	Nominal_1	Nominal_1	Nominal_1	Nominal_1	Nominal_1	Nominal_1	Nominal_1	Nominal_1	Nominal_1	Nominal_1
5		Nominal_1	Nominal_1	Nominal_1	Nominal_1	Daily	Nominal_1	Nominal_1	Nominal_1	Nominal_1	Nominal_1	Nominal_1	Nominal_1	Nominal_1	Nominal_1	Nominal_1
6		Nominal_1	Nominal_1	Nominal_1	Nominal_1	Daily	Nominal_1	Nominal_1	Nominal_1	Nominal_1	Nominal_1	Nominal_1	Nominal_1	Nominal_1	Nominal_1	Nominal_1
7		Nominal_1	Nominal_1	Nominal_1	Nominal_1	Daily	Nominal_1	Nominal_1	Weekly_2	Nominal_1	Nominal_1	Nominal_1	Nominal_1	Nominal_1	Nominal_1	Nominal_1
8		Nominal_1	Nominal_1	Nominal_1	Nominal_1	Daily	Nominal_1	Nominal_1	Nominal_1	Nominal_1	Nominal_1	Nominal_1	Nominal_1	Nominal_1	Nominal_1	Nominal_1
9		Nominal_1	Nominal_1	Nominal_1	Nominal_1	Daily	Nominal_1	Nominal_1	Nominal_1	Nominal_1	Nominal_1	Nominal_1	Nominal_1	Nominal_1	Nominal_1	Nominal_1
10		Nominal_1	Nominal_1	Nominal_1	Nominal_1	Daily	Nominal_1	Nominal_1	Nominal_1	Nominal_1	Nominal_1	Nominal_1	Nominal_1	Nominal_1	Nominal_1	Nominal_1
11		Nominal_1	Nominal_1	Nominal_1	Nominal_1	Daily	Nominal_1	Nominal_1	Nominal_1	Nominal_1	Nominal_1	Nominal_1	Nominal_1	Nominal_1	Nominal_1	Nominal_1
12		Nominal_1	Nominal_1	Nominal_1	Nominal_1	Daily	Nominal_1	Nominal_1	Nominal_1	Nominal_1	Nominal_1	Nominal_1	Nominal_1	Nominal_1	Nominal_1	Nominal_1
13		Nominal_1	Nominal_1	Nominal_1	Nominal_1	Daily	Nominal_1	Nominal_1	Weekly_2	Monthly_2	Nominal_1	Nominal_1	Nominal_1	Nominal_1	Nominal_1	Nominal_1
14		Nominal_1	Nominal_1	Nominal_1	Nominal_1	Daily	Nominal_1	Nominal_1	Nominal_1	Nominal_1	Nominal_1	Nominal_1	Nominal_1	Nominal_1	Nominal_1	Nominal_1
15		Nominal_1	Nominal_1	Nominal_1	Nominal_1	Daily	Nominal_1	Nominal_1	Nominal_1	Nominal_1	Nominal_1	Nominal_1	Nominal_1	Nominal_1	Nominal_1	Nominal_1
16		Nominal_1	Nominal_1	Nominal_1	Nominal_1	Daily	Nominal_1	Nominal_1	Nominal_1	Nominal_1	Nominal_1	Nominal_1	Nominal_1	Nominal_1	Nominal_1	Nominal_1
17		Nominal_1	Nominal_1	Nominal_1	Nominal_1	Daily	Nominal_1	Nominal_1	Nominal_1	Nominal_1	Nominal_1	Nominal_1	Nominal_1	Nominal_1	Nominal_1	Nominal_1
18		Nominal_1	Nominal_1	Nominal_1	Nominal_1	Daily	Nominal_1	Nominal_1	Nominal_1	Nominal_1	Nominal_1	Nominal_1	Nominal_1	Nominal_1	Nominal_1	Nominal_1
19		Nominal_1	Nominal_1	Nominal_1	Nominal_1	Daily	Nominal_1	Nominal_1	Weekly_2	Nominal_1	Nominal_1	Nominal_1	Nominal_1	Nominal_1	Nominal_1	Nominal_1
20		Nominal_1	Nominal_1	Nominal_1	Nominal_1	Daily	Nominal_1	Nominal_1	Nominal_1	Nominal_1	Nominal_1	Nominal_1	Nominal_1	Nominal_1	Nominal_1	Nominal_1
21		Nominal_1	Nominal_1	Nominal_1	Nominal_1	Daily	Nominal_1	Nominal_1	Nominal_1	Nominal_1	Nominal_1	Nominal_1	Nominal_1	Nominal_1	Nominal_1	Nominal_1
22		Nominal_1	Nominal_1	Nominal_1	Nominal_1	Daily	Nominal_1	Nominal_1	Nominal_1	Nominal_1	Nominal_1	Nominal_1	Nominal_1	Nominal_1	Nominal_1	Nominal_1
23		Nominal_1	Nominal_1	Nominal_1	Nominal_1	Daily	Nominal_1	Nominal_1	Nominal_1	Nominal_1	Nominal_1	Nominal_1	Nominal_1	Nominal_1	Nominal_1	Nominal_1
24		Nominal_1	Nominal_1	Nominal_1	Nominal_1	Daily	Nominal_1	Nominal_1	Nominal_1	Nominal_1	Nominal_1	Nominal_1	Nominal_1	Nominal_1	Nominal_1	Nominal_1

Figure 20: The new, simpler OMI operations baseline in use since May 2020. In yellow the Nominal orbit types, in blue the Daily orbit-types, in light green the Weekly orbit-types and in purple the Monthly orbit-types.

14 Main observation modes

The main modes of observation are radiance, irradiance and background measurements.

14.1 Earth radiance measurements

The Earth radiance measurements form the bulk of the measurements (shown blue in Figure 17). Apart from the optical properties of the instrument, there is some flexibility in the electronics that determines the Earth radiance ground pixel size. The co-addition period determines the ground pixel size in the along-track direction. Row binning determines the ground pixel size across-track. The parameter space is limited however, as choosing a smaller ground pixel size will increase the data rate and will decrease the signal-to-noise ratio for the individual ground pixels. The data rate is limited by both internal interfaces within the instrument as well as by the platform's on-board storage and down-link capabilities.

For the Earth radiance measurements the co-addition period is set to 2 s. This effectively results in a ground pixel size of approximately 13.5 km along-track. The ground pixel size varies across-track since the spatial dispersion (degrees per pixel) is constant, resulting in a ground pixel size that becomes larger towards the edges of the across-track field of view due to the Earth's curvature. In Table 8 the groundpixel size is given for different channels and binning factors.

Channel	Binning factor	Across-track ground pixel size
UV-1	4	24...66 km
UV-1	8	48...132 km
UV-2/VIS	4	12...33 km
UV-2/VIS	8	24...66 km

Table 8: Binning factors and across-track ground pixel sizes for Earth radiance measurements

Apart from the binning factor and the co-addition period, the remaining configuration parameters for the Earth radiance measurements, including exposure time and gains, are optimized for the best signal-to-noise ratio, without causing saturation of the detector or electronics. This optimization is based on scenes with the highest radiance levels, typically clouded scenes. Since the highest radiance level changes as a function of latitude, a total of three different settings for different latitude zones are created.

For radiance measurements there are three different observation modes: the global measurement mode, the spatial zoom-in measurement mode and the spectral zoom-in measurement mode. The global measurement mode is the default mode and samples the complete swath of 2600 km for the complete wavelength range for all bands. Note that the spectral zoom mode has only been used during commissioning phase. The characteristics of the observation modes are listed in Table 9.

Observation mode	**Spectral range**	**Swath width**	**Ground pixel size along × across track**	**Application**
Global mode band 1 (UV-1)	264–311 nm	2600 km	$13 \times 48\,\mathrm{km}^2$	global observation
Global mode bands 2–3 (UV-2 & VIS)	307–504 nm	2600 km	$13 \times 24\,\mathrm{km}^2$	of all products
Spatial zoom band 1 (UV-1)	264–311 nm	2600 km	$13 \times 24\,\mathrm{km}^2$	regional studies
Spatial zoom bands 2–3 (UV-2 & VIS)	307–504 nm	725 km	$13 \times 12\,\mathrm{km}^2$	of all products
Spectral zoom part of band 2 (UV-2)	307–364 nm	2600 km	$13 \times 12\,\mathrm{km}^2$	global observation
Spectral zoom part of band 3 (VIS)	349–432 nm	2600 km	$13 \times 12\,\mathrm{km}^2$	of some products

Table 9: Characteristics of the main observation modes.

14.2 Solar irradiance measurements

Every orbit the Sun is in the field-of-view the solar port, marked by SIFOV in Figure 18. Irradiance measurements are scheduled at least once day to determine the reflectance. The irradiance measurements used the same binning scheme as the radiance measurements to facilitate this. All other parameters have been optimized to improve the signal-to-noise ratio. By averaging the data in the L01b processor this can be further improved.

14.3 Background measurements

To be able to correct for the background signal each illuminated measurement has a corresponding background measurement. The instrument setting is - apart from the illumination - identical for the background measurement. However a different instrument configuration identifier (ICID) is used to distinguish the settings during L01b processing. The radiance background is measured in the eclipse side of the orbit, shown in gray in Figure 18, with an open FMM.

15 Instrument configuration

OMI operations are scheduled for at least one week in advance and are uplinked to the spacecraft. From the mission time line the orbit-type with its subroutines is called. The instrument commanding is performed partly via stored command sequences (SCSs) from the spacecraft and partly via stored instruction sequences (SISs) in the instrument adapter module (IAM).

15.1 Orbit-type activities

An orbit-type activity contains the commands for the different measurements that need to be performed during a particular orbit. In this way only one command needs to be scheduled per orbit instead of many commands. The timing in an orbit-type activity is with respect to the time the Sun is in field-of-view (SIFOV) of the solar port. The different activities are stored in the on-ground mission management system. Special versions have been defined of each orbit-type activity to avoid saturation due during ozone hole conditions. The special versions can be deployed during the ozone hole season, then the normal radiance measurements are replaced by measurements with shorter exposure times over Antarctica. In order to obtain a seasonal independent baseline it was decided at the end of 2019 to keep on using the most stringent special version of the orbit-type activities also outside the ozone hole season. In this version the switch to shorter exposure times is performed with the most margin.

The most used orbit-type activity is the Nominal_1 orbit. It contains only the global radiance and corresponding global radiance background measurements with an open FMM. Other nominal orbits are the Nominal_2, containing spatial zoom measurements, and Nominal_4, containing spectral zoom measurements. The Nominal_2 orbit-types where run during 1 day a month until the end of 2019. The Nominal_4 orbit-types were never run in E2 phase. When Aura leaves the A-train in 2023 the satellite will start drifting to overpass times in the late afternoon. As a consequence the duration of the eclipse will get shorter. Therefore, as of May 2020, the duration of the radiance background measurements in the Nominal_1 orbit-type activity has been increased and and placed closer to SC midnight to ensure that enough radiance background measurements remain in the dark to ensure good data quality.

There are 2 daily orbit-types. The Daily_1 contains, apart from global radiance measurements, a solar calibration measurement with the volume diffuser and binning factor 8, several long exposure measurements, and a LED measurement with binning factor 1. The Daily_ext_arc is as the Nominal_1 orbit-type, but the south arctic measurement (i.e. start of the orbit) starts 6 minutes and 3 seconds earlier for row anomaly investigation purposes.

There are three weekly orbit-type activities. The Weekly_1 contains, apart from global radiance measurements, also a solar calibration measurement using the volume diffuser and binning factor 1 and long exposure measurements with gain 1 and gain 4. As of May 2020 this orbit-type is no longer used.
The Weekly_2 contained, apart from global radiance measurements, also a solar calibration measurement using the regular diffuser and binning factor 8 , a WLS PRNU measurement and radiance background measurements with closed. As of May 2020, the WLS measurement in the Weekly_2 orbit-type activity is replaced by the LED stability measurement from the Weekly_3 orbit-type activity
The Weekly_3 contained, apart from global radiance measurements, also a radiance measurement with special instrument settings for row anomaly study, a LED stability measurement, a WLS stability measurement and radiance background measurements with closed FMM. As of May 2020 this orbit-type is no longer used.

There are 3 monthly orbit-type activities, only the adapted Monthly_2 is still used in the updated baseline. The Monthly_1 contains radiance, radiance background and solar calibration measurements in spatial zoom mode. Furthermore, it contains the LED linearity measurement. As of end of 2019 this orbit-type is no longer used. The Monthly_3 contains only dark measurements. As of end of 2019 this orbit-type is no longer used. The Monthly_2 contains, next to global radiance measurements, also a solar calibration using the backup diffuser, gain ratio LED measurements and gain ratio WLS measurements. As of May 2020, the WLS measurement in the Monthly_2 orbit-type activity is replaced by the LED linearity measurement from the Monthly_1 orbit-type activity.

15.2 Stored command sequences

The Aura S/C provides a stored command processing capability that allows the instrument and flight operation teams to control the operation of the spacecraft and instruments via on-board command sequences, referred to as stored command sequences (SCSs). The SCSs consists of S/C commands, instrument commands and control commands. There are 3 SCSs for fault management to stop all other SCSs, to switch OMI to idle mode or to switch OMI to survival mode. There are 12 SCSs for radiance measurements to perform global, spatial zoom and spectral zoom modes with tropical, mid-latitude, arctic and ozone-hole-season instrument settings. In 2008 a special SCS to perform global radiance measurement to investigate the row anomaly was created.

15.3 Stored instruction sequences

The interface adapter module (IAM) communicates with the S/C bus. The IAM has the capability to store and execute stored instruction sequences (SIS). A SIS is a software table that resides in the IAM, which contains a collection of instructions, telemetry checks, and other parameters that are performed upon execution of a SIS.The IAM flight software can autonomously send instructions to the OMI and perform telemetry checks at a much higher rate than the spacecraft processor. Using SISs reduces the amount of commands which need to be uplinked and allows for a quick succession of commands as is needed for example for the mechanism movements. In the IAM memory is available for maximum 10 SISs with a maximum length of 256 steps.

There are five SISs defined for nominal calibration and another five which were used in the LEO phase. In each SIS different calibration measurements are defined. A specific calibration sequence is selected by means of the instrument configuration parameter. This parameter has to be set before the SIS can be executed, but it can be changed by and during the execution of a SIS. Appendix E lists the possible values of the instrument configuration for each nominal calibration SIS. Within a SIS all the necessary commands for proper execution of the calibration measurement are given. These commands include amongst others: setting the mechanisms in the correct position, defining the CCD sequence parameters and setting the master clock period. At the end of a SIS OMI is brought back into the nominal configuration where the mechanisms are set to the nominal position (without holding torque), all calibration sources are switched off, the master clock period is set to 2 s, the CCD read-out is set to idle and an exit code is generated. The exit code can indicate problems with the mechanisms, the calibration sources or invalid instrument configuration settings (see Appendix E for details).

15.4 Electronic unit states

An electronic unit (ELU) state is an identifier in the instrument parameter database to indicate a set of instrument settings, like master clock period (MCP), exposure time, binning, gain definition, co-addition period and read-out discipline (ROD). An ELU state is defined for both the UV- and VIS channels. The MCP corresponds to the instrument's sampling grid in flight direction and is set to 2 s for nominal radiance measurements. The length of the co-addition period is the same as the length of the MCP, but they differ in phase.The MCP triggers the start of the exposures, whereas the co-addition period is timed to the read-out of the exposures. The CCD read-out can be configured in three different ways: the image read-out discipline (ROD) reads out an image while the next one is exposed, this ROD is used for most measurements, where the exposure time is longer than 400 ms. The idle ROD is the same as the image ROD but the data is not transmitted to reduce the data volume while keeping the CCDs thermally stable. The third ROD is for long exposures used for calibration measurements.

The ELU states can be set via a few commands in a SIS or a SCS. For L01b data processing it is important to distinguish between different kinds of measurements. An instrument configuration ID (ICID) uniquely identifies a particular measurement like radiance with arctic settings, radiance background with background settings, LED stability measurements, etc. But different kinds of measurement can use the same ELU states. The background measurements have the same instrument settings as the illuminated measurements. As a consequence the same ELU state can be used in several ICIDs. In the instrument database the ICIDs are linked to their respective ELU states and to the SIS and/or SCS they are used in.

Part IV

Correction algorithms for L01b processing

In this part the correction algorithms of the L01b processor are described. The starting point of the processor is the Level-0 data as received from the ground system. The main component of this input is the measurement data, or signal, S, expressed in digital numbers (DN).

Through a number of correction and calibration steps – referred to as 'algorithms' in this document – this digitized signal is transformed to give an estimate of the input stimulus that caused the measured signal, i.e., the Earth, the Sun, or one of the on-board light sources. Together with the signal, its variance σ^2 is also calculated and propagated through the L01b processor. The output is Level-1b data that includes geolocated and calibrated radiances, calibrated irradiances, and calibration measurement results. The latter are not described in this document.

After a description of the processing flow and some general remarks in Section 16, the remainder of this part describes the algorithms in detail, by giving for each algorithm the two main equations that describe the transformations of the signal and its variance per image pixel. Where needed, these are augmented by auxiliary equations and a table summarizing all the symbols used. The sections in this part are organized according to their order in the processing flow. Any annotation and flagging algorithms which do not transform the input signal are listed in Part V. The output is Level-1b data that includes geolocated and calibrated radiances, calibrated irradiances, and calibration measurement results.

16 Overview of algorithms and general remarks

In the L01b processor, the various calibration and correction algorithms are traversed in a well-defined order as shown in Figure 21. Correction algorithms are shown in yellow in Figure 21 and described in detail in the following sections in the order they are applied to the L0 data. The annotation and flagging algorithms are shown in green in the figure, they are described in Part V and are ordered not by usage in the processor but by subject. The processing order of the algorithms is determined by the reverse of the way the signal travels through the instrument from entrance aperture to digitized signal. That means, for example, that the conversion from voltage to digital numbers near the end of the electronic chain (the ADC converter) becomes, near the start of the processing order, a conversion from digital numbers to voltage. There are several exceptions to this main rule, for a number of reasons. Because the amount of information is decreased for example by binning, some steps do not have a proper inverse. Further, some processes are not concentrated to a specific location or element in the instrument (e.g. straylight) while for the correction algorithm a well-defined position in the processing flow has to be chosen.

Most of the processing steps shown in Figure 21, require input in the form of calibration key data (CKD), housekeeping data from instrument and spacecraft or design parameters. The input parameters are omitted in the figure.

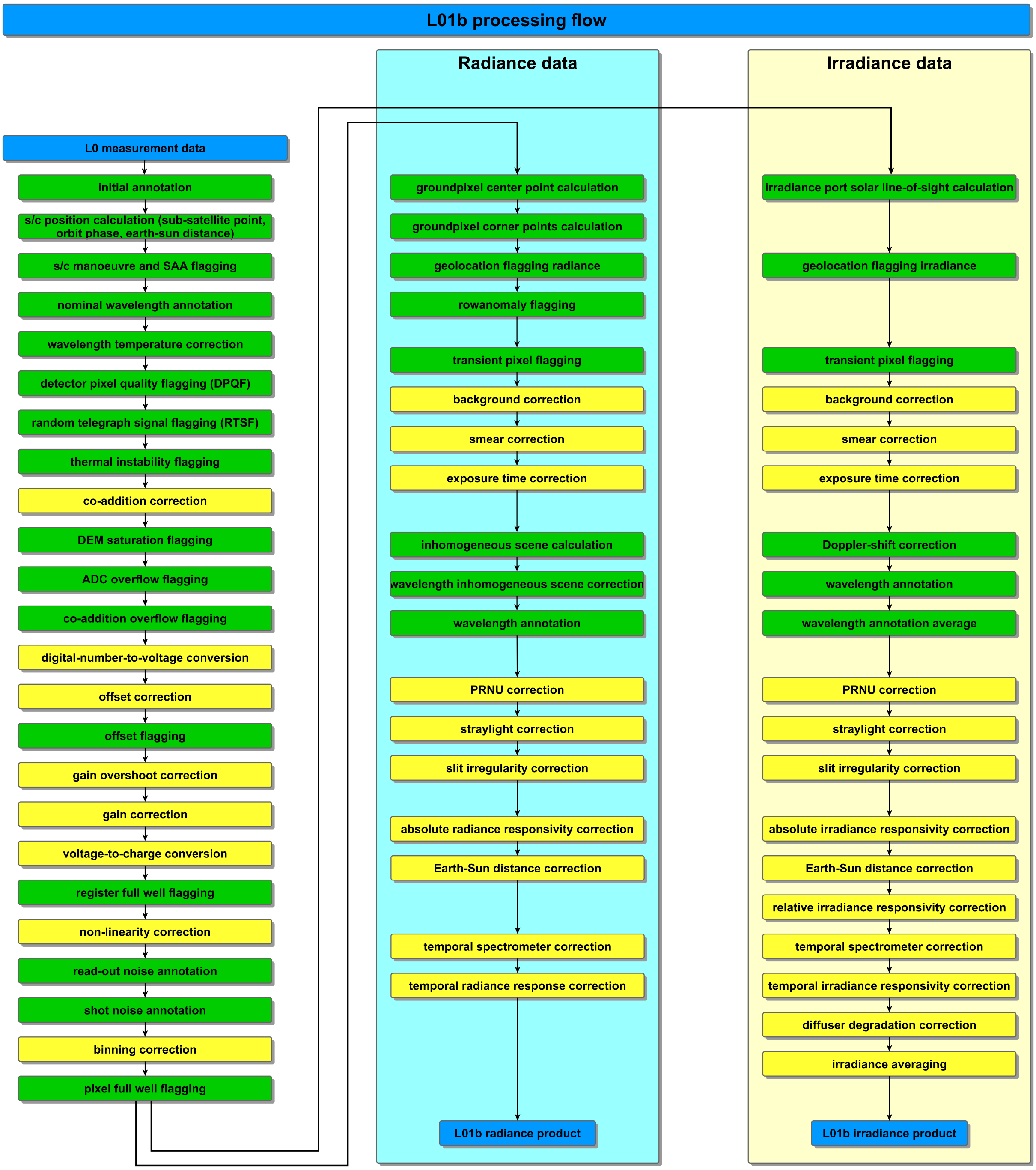

Figure 21: An overview of the processing flow in the L01b processor. Algorithms which apply corrections to the data are depicted in yellow, annotation and flagging steps are shown in green. Algorithms for monitoring and in-flight calibration are omitted in this schematic. The left column applies to all radiance and irradiance data. The middle and right columns show the steps for radiance and irradiance data respectively. The steps are shown in the order as they are applied in the L01b processor.

16.1 Uncorrected effects

Some instrument effects are deemed so small or are impossible to characterize with sufficient accuracy to allow for a correction in the L01b processor. Examples for non-corrected effects are remaining polarization and the ellipsoid or blooming effect. The latter is in practice difficult to distinguish from other saturation effects.

The charge transfer efficiency of the detectors is also not modeled in the L01b processor. From on-ground calibration measurements with deliberately imposed jumps from high to zero signal in row direction, no significant trace of charge inefficiency could be found. Even if the situation has changed during the mission, the difficulty and computational cost of this algorithm step is such that the merits will not outweigh the costs. Any diffusive effects that are present are handled with in other processing steps like PRNU and (especially) straylight. For a detailed description of remaining effects see [1].

16.2 Conventions

16.2.1 Units

This document generally employs the international system of units (SI). Notably, numbers of photons are expressed in mol, which complies with the NetCDF climate and forecast (CF) metadata convention. On the other hand, numbers of electrons are expressed in electrons (symbol e^-), which is not an SI unit and therefore does not comply with CF. This is however no problem as this unit is only used internal to the L01b processor. Dimensionless parameters are listed as having unit 1. This is to distinguish from enumerating parameters (such as spectral band), which are listed as having no applicable unit.

16.2.2 Mathematical conventions

Enumerators OMI has two detectors, which are numbered $d = 1, 2$. Since d is one of the enumerating parameters referred to in Section 16.2.1, arithmetic operations on d are meaningless. Therefore, it is also acceptable to ‘number’ $d =$ UV and VIS, respectively. The UV detector is divided in two (UV-1 and -2), giving a total of three spectral bands, numbered $b = 1,2,3$ from short to long wavelengths. b is another enumerating parameter.

Iterators Since the OMI detectors are two-dimensional, consisting of pixels on a rectangular grid, many concepts in the L01b processor (including the measured signal) are presented as matrices. Rows and columns of such a matrix are numbered using the iterating parameters r and c, respectively. Further, we often use the symbol $\mathbf{x}$ as a shorthand for r,c. Such matrices may be binned (where groups of pixels are aggregated, leading to a smaller-sized matrix) or unbinned (where such adding has not occurred and the matrix has the maximum size). In the former case, we speak of ‘image pixels’, $\mathbf{x}_{\text{img}}$, r_{img}, and c_{img}. In the latter, we speak of ‘detector pixels’, $\mathbf{x}_{\text{det}}$, r_{det}, and c_{det}.

Matrix indexation To reduce the amount of subscripts in mathematical equations and thus improve their readability, we sometimes use square brackets to denote elements of vectors or matrices, i.e., $M[i,j]$ for M_{ij}, especially if the indexes themselves have subscripts. Therefore, the signal S of a particular detector pixel is denoted as $S[r_{\text{det}}, c_{\text{det}}]$. Using the shorthand $\mathbf{x}$, a summation over an area A on the detector is now easily expressed as a single summation,

$$\sum_{\mathbf{x}_{\text{det}} \in A} S[\mathbf{x}_{\text{det}}] \ .$$

A specific application of this notation is in binning an unbinned parameter. For instance, the value of a parameter c for an image pixel $\mathbf{x}_{\text{img}}$ is expressed in the corresponding values for the detector pixel $\mathbf{x}_{\text{det}}$ as

$$c[\mathbf{x}_{\text{img}}] = \frac{\sum_{\mathbf{x}_{\text{det}} \in \mathbf{x}_{\text{img}}} c[r_{\text{det}}]}{N_{\mathbf{x}_{\text{det}} \in \mathbf{x}_{\text{img}}}} \ ,$$

where $\mathbf{x}_{\text{det}} \in \mathbf{x}_{\text{img}}$ denotes the set of detector pixels that corresponds with one image pixel.

Alternative arctangent function Some of the geometrical algorithms need a mathematical function that returns the angle between a vector (x,y) and the X-axis in 2-dimensional space. Since this is similar to the arctangent function, we denote this function $\arctan 2$ analogous to the corresponding function that is found in some computer languages. The relation between the two functions is given by:

$$\arctan 2(x,y) = 2\arctan \frac{y}{\sqrt{x^2+y^2}+x} \; .$$

Note that the $\arctan 2$ function gives values between $-\pi$ and $+\pi$ while the $\arctan$ function gives values between $-\pi/2$ and $+\pi/2$. However, the function is not defined for $y=0$, $x<0$ and may overflow around these regions, and gives an error for $\arctan 2(0,0)$. This has to be taken into account when implementing this equation.

16.2.3 Correction algorithms

The correction algorithms described in this Part IV usually consist of the four simple arithmetic operations of addition, subtraction, multiplication, and division. Of these, addition and subtraction are equally efficient for a computer program. However, division is computationally less efficient than multiplication. Therefore, the division of a matrix by a constant value is written as a multiplication of the matrix by the reciprocal of that constant value. That way, the division has to be carried out only once.

16.3 Noise and error propagation

During the process of converting the detector signal to an estimate of photons coming from the Sun or Earth, we have to deal with errors and noise. Errors involve imperfections of the algorithms and the calibration key data. They can involve single pixels or complete detector areas, and are estimated and propagated along the process. Noise involves the the nature of the measurement: both the physical process and the detector chain are prone to stochasticity, leading to a distribution around the value that we need to know. This distribution can be made narrower by taking repeated measurements, with a trade-off with respect to the precision of the measurement. The variance as result of the fluctuations in the amount of photons that hit the detector is called ‘shot noise’, and variance as a result of the physical set-up of the electronics in the read-out chain is called ‘read-out noise’. For more information see also Section A in the Appendix, which is copied from the TROPOMI ATBD [8].

17 Co-addition correction

A number of subsequent images along the flight path have been added in the ICU. During normal operation, the co-addition factor is expected to be related to the ratio of the ground pixel size and the chosen exposure time. However, the factor is directly set by the engineering data. The maximum allowed co-addition factor is 64. It is wise not to exceed 64 co-additions because if all individual exposures are saturated, their sum will overflow the ICU co-addition buffer.

The correction has to be performed for all detector pixels. Small pixels are obviously excluded. Note that the co-addition factor is the integer ratio of the master clock period and the exposure time.

$$S_\mathrm{o}[\mathbf{x}_\mathrm{img}] = S_\mathrm{i}[\mathbf{x}_\mathrm{img}]/N_\mathrm{coadd} \tag{1}$$

Parameter	**Description**	**Units**
$S_\mathrm{i}[\mathbf{x}_\mathrm{img}]$	signal in image pixel $\mathbf{x}_\mathrm{img}$ before correction	DN
$S_\mathrm{o}[\mathbf{x}_\mathrm{img}]$	signal in image pixel $\mathbf{x}_\mathrm{img}$ after correction	DN
N_coadd	number of co-additions	1

18 ADC conversion

In the analog-to-digital converter (ADC) the signal is converted from volts to digital numbers. The L01b processor implements the inverse of this signal chain, i.e. converting the output signal of the ADC in DN to Volts, to electrons and in the end to photon flux. Due to a historic mistake, in the old OMI L01b processor as well as throughout the entire on-ground calibration campaign, an erroneous value of 4096 DN $/5.0$ V $= 819.2$ DN/V was used as the ADC conversion factor. As this erroneous factor was used consistently, this error was compensated by the calibrated voltage-to-charge conversion factor.

For the collection 4 OMI L01b processor, the ADC conversion factor has been corrected to the conversion factor that was established during ELU unit testing. The voltage-to-charge conversion factor has been adjusted with the inverse of the change to the ADC conversion factor, so that the overall calibration has not changed. All calibration key data (CKD) used in the L01b processor between the DN-to-voltage conversion and the voltage-to-charge conversion has been adjusted as well to match these changes.

$$S_\mathrm{o}[\mathbf{x}_\mathrm{img}] = S_\mathrm{i}[\mathbf{x}_\mathrm{img}] \times f_\mathrm{adc} \tag{2}$$

Parameter	**Description**	**Units**
$S_\mathrm{i}[\mathbf{x}_\mathrm{img}]$	signal in image pixel $\mathbf{x}_\mathrm{img}$ before correction	DN
$S_\mathrm{o}[\mathbf{x}_\mathrm{img}]$	signal in image pixel $\mathbf{x}_\mathrm{img}$ after correction	V
f_adc	conversion factor from DN to Volts	V DN^{-1}

19 Offset correction

The electronic chains for the detector consist of a number of components that, combined, give rise to an (additive) electronic offset and a (multiplicative) electronic gain for which the L01b processor has to correct the observed signal.

As a first step, the offset will be corrected for. Since the offset can drift, a dynamically determined offset signal, acquired from the read-out register (ROR), will be used. If this dynamical offset signal is not available, a static alternative has to be used, which is available as calibration key data (CKD).

Note that the offset (and gain) can vary according to the chosen gain setting. The gain setting that is associated with each pixel in the measured image in a structured way, as follows. The instrument supports the use of different gain factors within one image. All dark and straylight areas share the same gain factor, which can be selected out of four possible gain factors. For the image (IMG) and ROR areas, it is possible to create up to four areas with a different gain factor, also selectable from (the same) four possible gain settings. These four areas are defined by so called gain switch columns. The position of these gain switch columns, and the

gain factor to use in between the gain switch columns are part of the instrument configuration.
For both detectors d we have:

$$S_\mathrm{o}[\mathbf{x}_\mathrm{img}] = S_\mathrm{i}[\mathbf{x}_\mathrm{img}] - O_{d,g} \tag{3}$$

The offset value O is either *dynamic* or *static*. When possible, the dynamic value is used. This value has been produced in the offset calculation algorithm that has been invoked before the current offset correction algorithm. In short, pixels in the image area are associated with the pixel with the same column number in the ROR: both pixels have the same gain code. From the pixels in the ROR, the dynamic offset value per gain setting is computed. Signals in pixels in other areas that happen to have non-matching gain codes have to be corrected with static offset values. Moreover, certain instrument settings cause the ROR signals to be not suitable for ROR offset value computations; in these cases the static offset also has to be used.

19.1 Dynamic offset computation

We assume that the ROR is divided in (at most) four regions, each with its own gain code g. The ROR signal consists of the offset and a specific shape; the latter has been independently calibrated. To acquire the offset signal in a ROR pixel:

$$S_{\mathrm{off},g}[c] = S_\mathrm{i}[0,c] - f_\mathrm{gain}(g) \cdot S_\mathrm{shape}[c] \tag{4}$$

Here the ROR has, per definition, row number zero. The relative gain $f_\mathrm{gain}(g)$ is described in Section 21. This gain factor is therefore needed in both the offset calculation algorithm and the gain correction algorithm. This is not a recursion problem since the gain factor is a CKD.

The dynamic offset calculation also produces an estimate for the read-out noise: while the dynamic offset (per gain setting) is derived from the *mean* of the offsets per pixel in the ROR, the read-out noise is the *variance* of these pixel offsets. More precisely, from the lists of offset pixels $S_{\mathrm{off},g}[c]$ the offset is defined as

$$O_g = \frac{\sum_{c\in\mathbb{X}_g} S_{\mathrm{off},g}[c]}{N_{c\in\mathbb{X}_g}} + c_0 + c_1 \cdot f_\mathrm{gain}(g). \tag{5}$$

Thus, besides taking the average over the appropriate pixels, two constants have to be added, one of them depending on the gain ratio factor $f_\mathrm{gain}(g)$. The initial estimate of the read-out noise is equal to the variance:

$$\varepsilon_g^2 = \mathrm{Var}_{\mathbb{X}_g} S_{\mathrm{off},g} \tag{6}$$

Note that at this stage in the algorithm chain, the read-out noise is still defined in Volts and has not been gain-corrected. Alternatively, the read-out noise can be acquired from a CKD parameter:

$$\varepsilon_g^2 = \frac{1}{N_\mathrm{coadd}} \cdot \varepsilon_{\mathrm{ckd},g}^2. \tag{7}$$

In fact, this is the baseline for the read-out noise annotation, with the difference that the CKD is expressed in electrons. The annotation procedure therefore is invoked only after the voltage-to-charge conversion.

Parameter	Description	Units
$S_\mathrm{i}[\mathbf{x}_\mathrm{img}]$	signal in image pixel $\mathbf{x}_\mathrm{img}$ before correction	V
$S_\mathrm{o}[\mathbf{x}_\mathrm{img}]$	signal in image pixel $\mathbf{x}_\mathrm{img}$ after correction	V
d	detector: UV or VIS	1
g	gain code associated with pixel	1
$O_\mathrm{d,g}$	offset value, per gain code	V
ε_g^2	read-out noise, per gain code	V^2
N_coadd	number of co-additions	1

20 Gain overshoot correction

For the IMG and ROR areas, it is possible to create up to four areas with a different gain factor, also selectable from (the same) four possible gain settings. These four areas are defined by so called gain switch columns. However, the signal in columns immediately to the right of (i.e. higher-numbered than) the gain switch columns

is affected and has to be corrected for. More precisely, there exists, for each detector, a transfer matrix $M_{\mathrm{prev,next}}[k]$, with k a column offset between 0 and $n_{\mathrm{overshoot}}$, the number of affected columns. Both prev and next can be one of the four gain codes, giving a total of 16 different corrections per detector.
So, for all gain switch columns gsc, for all pixels $\mathrm{gsc} \le c \le \mathrm{gsc} + n_{\mathrm{overshoot}}$:

$$S_{\mathrm{i}}[r_{\mathrm{img}}, c_{\mathrm{img}}] = S_{\mathrm{o}}[r_{\mathrm{img}}, c_{\mathrm{img}}] - M_{\mathrm{prev,next}}[c_{\mathrm{img}} - \mathrm{gsc}] \tag{8}$$

For all other pixels:

$$S_{\mathrm{i}}[r_{\mathrm{img}}, c_{\mathrm{img}}] = S_{\mathrm{o}}[r_{\mathrm{img}}, c_{\mathrm{img}}] \tag{9}$$

The noise is unaffected:

$$\varepsilon_{\mathrm{o}}^2[\mathbf{x}_{\mathrm{img}}] = \varepsilon_{\mathrm{i}}^2[\mathbf{x}_{\mathrm{img}}] \tag{10}$$

Parameter	**Description**	**Units**
$S_{\mathrm{i}}[\mathbf{x}_{\mathrm{img}}]$	signal in image pixel $\mathbf{x}_{\mathrm{img}}$ before correction	V
$S_{\mathrm{o}}[\mathbf{x}_{\mathrm{img}}]$	signal in image pixel $\mathbf{x}_{\mathrm{img}}$ after correction	V
$\varepsilon_{\mathrm{i}}^2[\mathbf{x}_{\mathrm{img}}]$	signal noise in image pixel $\mathbf{x}_{\mathrm{img}}$ before correction	V^2
$\varepsilon_{\mathrm{o}}^2[\mathbf{x}_{\mathrm{img}}]$	signal noise in image pixel $\mathbf{x}_{\mathrm{img}}$ after correction	V^2
prev	gain code associated with region left of the gain switch column	1
next	gain code associated with region right of the gain switch column	1
gsc	gain switch column	1
$n_{\mathrm{overshoot}}$	number of affected overshoot columns	1
$M_{\mathrm{prev,next}}[k]$	overshoot correction matrix	V

21 Gain correction

The electronic chains for the detector consist of a number of components that, combined, give rise to an (additive) electronic offset and a (multiplicative) electronic gain for which the L01b processor has to correct the observed signal. Concerning the gain part, four gain settings can be defined. One of the four is the so-called neutral gain, equivalent to a multiplication with one. The *relative* gain is defined by the ratio between the gain of the current gain setting and the gain of the neutral gain setting.

It has been found from analyzing the in-flight measurements that the gain ratio slightly drifts in time. This drift also needs correcting for.
The gain ratio can be computed on a monthly base using ICIDs 32-35. These measurements, after analysis, provide a snapshot in temporal sense of the four relative gain ratios.

21.1 Used parameters and symbols

Parameter	**Description**	**Units**
$S_{\mathrm{i}}[\mathbf{x}_{\mathrm{img}}]$	signal in image pixel $\mathbf{x}_{\mathrm{img}}$ before correction	V
$S_{\mathrm{o}}[\mathbf{x}_{\mathrm{img}}]$	signal in image pixel $\mathbf{x}_{\mathrm{img}}$ after correction	V
$\varepsilon_{\mathrm{i}}^2[\mathbf{x}_{\mathrm{img}}]$	signal noise in image pixel $\mathbf{x}_{\mathrm{img}}$ before correction	V^2
$\varepsilon_{\mathrm{o}}^2[\mathbf{x}_{\mathrm{img}}]$	signal noise in image pixel $\mathbf{x}_{\mathrm{img}}$ after correction	V^2
i_{orb}	current orbit number	1
f	gain ratio	1
g	gain setting code, defined for a region	1
$f_r(j_{\mathrm{orb}}, g, d)$	gain ratio factor from CKD LUT, per detector, for four gain settings, for orbits j	1

21.2 Algorithm description

The correction is not implemented as a closed loop model: instead, a table of correction factors is provided as CKD. The signal for a specific detector has to be corrected with the interpolated or extrapolated correction factor depending on the current orbit number and the provided orbit numbers in the table.

$$S_\mathrm{o}[\mathbf{x}_\mathrm{img}] = \frac{1}{f} \cdot S_\mathrm{i}[\mathbf{x}_\mathrm{img}] \ . \tag{11}$$

The noise is propagated:

$$\varepsilon_\mathrm{o}^2[\mathbf{x}_\mathrm{img}] = \frac{1}{f^2} \cdot \varepsilon_\mathrm{i}^2[\mathbf{x}_\mathrm{img}] \ . \tag{12}$$

Here the gain ratio factor f is acquired from linear interpolation of temporally neighboring gain ratio factors in the CKD table. The CKD table is defined for the four gain settings, although the values are always exactly one for gain code 1, i.e. the neutral gain setting. The gain code is constant in four column intervals, separated by the so-called gain switch columns. Hence we may write $g = g(c,d)$.

Here we note that the gain factor f is determined when the CKD is read, so not as part of the gain correction algorithm. If the gain factor is wanted for some orbit number i_orb and the CKD lists factors for two orbits $j_{\mathrm{orb},1}, j_{\mathrm{orb},2}$ where $j_{\mathrm{orb},1} < i_\mathrm{orb} < j_{\mathrm{orb},2}$, the factor f is given by

$$f = (1-\alpha) f_r(j_{\mathrm{orb},1}, g, d) + \alpha f_r(j_{\mathrm{orb},2}, g, d), \tag{13}$$

$$\text{and where} \quad \alpha = \frac{i_\mathrm{orb} - j_{\mathrm{orb},1}}{j_{\mathrm{orb},2} - j_{\mathrm{orb},1}}. \tag{14}$$

If the orbit number i_orb is larger than the highest orbit number in the CKD, the last value $f_r(j_{\mathrm{orb,last}}, g, d)$ is used.

22 Voltage-to-charge correction

In the CCD part of the electronic chain, the signal in forward direction is converted from charge to voltage. Therefore, in the reverse model, the inverse conversion takes place. The conversion, however, is not entirely linear as function of the signal. This non-linear behavior will be separately addressed, and corrected for, as described in Section 23 below.

$$S_\mathrm{o}[\mathbf{x}_\mathrm{img}] = f_\mathrm{v2c} \cdot S_\mathrm{i}[\mathbf{x}_\mathrm{img}] \tag{15}$$

$$\varepsilon_\mathrm{o}^2[\mathbf{x}_\mathrm{img}] = f_\mathrm{v2c}^2 \cdot \varepsilon_\mathrm{i}^2[\mathbf{x}_\mathrm{img}] \ . \tag{16}$$

Parameter	**Description**	**Units**
$S_\mathrm{i}[\mathbf{x}_\mathrm{img}]$	signal in image pixel $\mathbf{x}_\mathrm{img}$ before correction	V
$S_\mathrm{o}[\mathbf{x}_\mathrm{img}]$	signal in image pixel $\mathbf{x}_\mathrm{img}$ after correction	e−
$\varepsilon_\mathrm{i}^2[\mathbf{x}_\mathrm{img}]$	signal noise in image pixel $\mathbf{x}_\mathrm{img}$ before correction	V^2
$\varepsilon_\mathrm{o}^2[\mathbf{x}_\mathrm{img}]$	signal noise in image pixel $\mathbf{x}_\mathrm{img}$ after correction	e^{-2}
f_v2c	voltage to charge conversion factor	e^-/V

23 Non-linearity correction

The voltage-to-charge conversion performs two actions. The first, mentioned in Section 22, is a straightforward unit conversion, the second a more elaborate correction for the CCD non-linearity. The non-linearity stems from the charge-to-voltage conversion at each CCD output node. It is, by construction, the same for all pixels.

In principle, longer exposure to a signal leads to more charge being built up in the register of a pixel of the CCD. To lowest order, this shows a linear behavior. Deviations from this linear behavior are captured in the non-linearity calibration key data. A polynomial as a function of the signal $S_\mathrm{i}[\mathbf{x}_\mathrm{img}]$ has been determined from LED measurements with a range of exposure times. For more information on e.g. error propagation, see Appendix D and the TROPOMI ATBD [8].

23.1 Algorithm description

A polynomial function f_{ccd} is evaluated for the measured pixel signal; the outcome is subtracted from the signal.

$$S_{\mathrm{o}}[\mathbf{x}_{\mathrm{img}}] = S_{\mathrm{i}}[\mathbf{x}_{\mathrm{img}}] - f_{\mathrm{ccd}}(S_{\mathrm{i}}[\mathbf{x}_{\mathrm{img}}]) \; . \tag{17}$$

23.2 Used parameters and symbols

Parameter	Description	Units
$S_{\mathrm{i}}[\mathbf{x}_{\mathrm{img}}]$	signal in image pixel $\mathbf{x}_{\mathrm{img}}$ before correction	e−
$S_{\mathrm{o}}[\mathbf{x}_{\mathrm{img}}]$	signal in image pixel $\mathbf{x}_{\mathrm{img}}$ after correction	e−
$f_{\mathrm{ccd}}(S_{\mathrm{i}}[\mathbf{x}_{\mathrm{img}}])$	non-linearity correction function, per detector	e^{-} / e^{-}

24 Binning factor correction

OMI measurements are typically not performed at full resolution. Instead, multiple CCD detector rows will be shifted into the read-out register before the read-out register is read (and thereby emptied). This method of combining multiple detector rows into one image row is called ‘binning’, and the number of detector rows binned into one image row is called the ‘binning factor’. The binning factor need not be constant across the detector: one group of detector rows may be binned with another binning factor than other groups of detector rows. Also, groups of detector rows or columns may be indicated not to be read out at all (skipped). These skipped rows or columns have binning factor 0 by convention.

As rows on the detector correspond to the across-track spatial dimension on the ground, binning decreases the spatial resolution of the measurement. However, binning also has several advantages:

- it decreases the data volume;
- it enhances the signal-to-noise ratio.

Binning only occurs for rows, not for columns. The binning correction is

$$S_{\mathrm{o}}[\mathbf{x}_{\mathrm{img}}] = \frac{1}{C_g[r_{\mathrm{img}}]} S_{\mathrm{i}}[\mathbf{x}_{\mathrm{img}}],$$

where C_g is the binning factor for the C_g detector rows that constitute the image row $[r_{\mathrm{img}}]$. Formally, we write $C_g[r_{\mathrm{img}}] = \sum_{\mathbf{x}_{\mathrm{det}} \in \mathbf{x}_{\mathrm{img}}} 1$. C_g is never zero since a skipped row obviously does not exist as an image row. Specifics about the binning tables used and the error propagation can be found in Appendix B.

25 Background correction

For radiance measurements, a background image per ICID is constructed as an average from one day of orbits. It is expected that a background radiance measurement consists mainly of dark current. Dark current will, in general, slowly increase over time, although this increase per pixel is not deterministic; the dark current increase can also be negative for a while. Nevertheless, on average, the background images will show higher signals as the years progress.

The variation of the average background signal, per pixel, is a measure of the stability of the pixel in terms of RTS. More specific, if the measured standard deviation over this time interval considerably exceeds the theoretically computed noise, then the pixel probably suffers from RTS *on this timescale* and is flagged as such, see Section 41.13. Of course, it is still possible that the pixel suffers from long-term RTS (on a scale of weeks or even years), but since the same RTS signal is then also present in the radiance measurements, the background correction neatly removes this long-term RTS additional signal and the pixel can be considered stable during the associated orbits.

25.1 Used parameters and symbols

Parameter	Description	Units
$S_\mathrm{i}[\mathbf{x}_\mathrm{img}]$	signal in image pixel $\mathbf{x}_\mathrm{img}$ before correction	e−
$S_\mathrm{o}[\mathbf{x}_\mathrm{img}]$	signal in image pixel $\mathbf{x}_\mathrm{img}$ after correction	e−
S_back	Averaged background image at reference temperature	e$^-$
f_corr	Temperature correction factor	1
T	Detector temperature	K
T_ref	Detector reference temperature	K

25.2 Algorithm description

The background correction itself also takes temperature differences into account:

$$S_\mathrm{o}[\mathbf{x}_\mathrm{img}] = S_\mathrm{i}[\mathbf{x}_\mathrm{img}] - S_\mathrm{back}[\mathbf{x}_\mathrm{img}] \cdot f_\mathrm{corr} \tag{18}$$

where

$$f_\mathrm{corr} = \sum_{k=0}^{n} c_k (T - T_\mathrm{ref})^k \tag{19}$$

The correction can be considered valid since the background mainly consists of dark current and the coefficients c_k describe the dark current temperature dependence.

Note that during the collection of the background images, the signal has been corrected using the then-valid detector temperature, such that the reference temperature could be assumed then. Now, during the actual subtraction, the background has to be rescaled toward the current detector temperature.

26 Smear

The purpose of the smear correction algorithm is to negate the effect of frame transfer smear, or smear for short in this context. Per definition, smear is the added contribution of the signal due to continued exposure during read-out. More specifically, each row continues to receive photons during its transfer through the CCD image section. The smear is therefore always positive and the correction should consist of a subtraction.

The specifics of the computation and implementation of smear are given in Appendix C. Here we just give the nature of the correction,

$$S_\mathrm{o}[r_\mathrm{det}] = S_\mathrm{i}[r_\mathrm{det}] - \frac{\tau}{t_\mathrm{exp} + n\tau} n\overline{S_\mathrm{i}}, \tag{20}$$

where τ is the row transfer time, t_exp is the exposure time (excluding the frame transfer time), n the number of detector rows and the $\overline{S_\mathrm{i}}$ denotes the signal average over all rows in a column.

The fact that information about all signals in the column is needed to compute the smear signal in a specific pixel (i.e. the correction is not *local*) is a possible source of errors.

Thus, assuming all pixels can be properly read out, the smear as defined by explicitly inverting the forward-direction smear matrix (see the Appendix) is:

$$M(S_\mathrm{i}[\mathbf{x}_\mathrm{img}]) = M(S_\mathrm{i}[c_\mathrm{img}]) = \frac{\tau}{t_\mathrm{exp} + n\tau} \sum_{j=1}^{m} n_j S_\mathrm{i}[j, c_\mathrm{img}], \tag{21}$$

where m is the number of image rows and n_j the binning factor in row j. We do not use the concept of binning factor 0 for skipped rows here.

Because of unreliable flagged pixels and skipped rows, not all m image rows are available for reading. We can, however, divide the image rows in disjunct sets (or regions) for which we have a good guess of the values of the pixel signals therein:

$$M(S_\mathrm{i}[c_\mathrm{img}]) = \frac{\tau}{t_\mathrm{exp} + n\tau}\left[\sum_\mathrm{k}^\mathrm{regions}\left(\sum_{j=1}^{m_k} n_{j,k} S_\mathrm{i}[j_k, c_\mathrm{img}]\right)\right] \tag{22}$$

$$= \frac{\tau}{t_\mathrm{exp} + n\tau}\left[\sum_\mathrm{k}^\mathrm{regions}\left(n_k \overline{S_\mathrm{i}[k, c_\mathrm{img}]}\right)\right]. \tag{23}$$

Effectively, only the 'unproblematic', reliable pixels (say, q of them, with $1 \leq q \leq m_k$) in a region are summed, yielding the estimated region sum by multiplying with the extrapolation factor n_k/q. Thus, $\overline{S_\mathrm{i}[k, c_\mathrm{img}]}$ is the estimated average of the signal in region k, corrected for the binning factors. Moreover, the binned image rows m_k have in this averaging step been converted to detector rows n_k.

Now, a good choice is to have three regions: First the science region, which will be properly illuminated. Second, a darker region that contains only rows with a low signal (straylight, for example). Skipped rows that will have a signal of similar magnitude are also part of this region. Third, rows that are shielded and will, per definition, only contain the smear signal itself.
Therefore we have

$$M(S_\mathrm{i}[c_\mathrm{img}]) = \frac{\tau}{t_\mathrm{exp} + n\tau}\left[n_\mathrm{illum}\overline{S_\mathrm{i}[\mathrm{illum}, c_\mathrm{img}]} + n_\mathrm{dark}\overline{S_\mathrm{i}[\mathrm{dark}, c_\mathrm{img}]} + n_\mathrm{shield}M(c_\mathrm{img})\right] \tag{24}$$

$$\Longrightarrow M(S_\mathrm{i}[c_\mathrm{img}]) = \frac{\tau}{t_\mathrm{exp} + \tau(n - n_\mathrm{shield})}\left[n_\mathrm{illum}\overline{S_\mathrm{i}[\mathrm{illum}, c_\mathrm{img}]} + n_\mathrm{dark}\overline{S_\mathrm{i}[\mathrm{dark}, c_\mathrm{img}]}\right]. \tag{25}$$

In the last step, we moved the known term in the shielded region (without actually reading these signals) to the left-hand side of the equation.

It is of course also possible to directly retrieve (read) the smear from this shielded region, but the noise and chance of errors make that a less preferred strategy.

27 Exposure time division

The signal is divided by the exposure time. During part of this exposure time however, the frame is also transferred from the image section to the storage section, leading to image smear. As the smear correction algorithm (Section 26) corrects for this smear by subtracting a smear image, the correction in the present algorithm consists of a division by the difference between the exposure time and the frame transfer time. From here on, the signal is expressed in electrons per second. The exposure time is extracted from the engineering data.

27.1 Used parameters and symbols

Parameter	Description	Units
$S_\mathrm{i}[\mathbf{x}_\mathrm{img}]$	signal in image pixel $\mathbf{x}_\mathrm{img}$ before correction	e$^-$
$\sigma_\mathrm{i}^2[\mathbf{x}_\mathrm{img}]$	signal variance in image pixel $\mathbf{x}_\mathrm{img}$ before correction	e^{-2}
$S_\mathrm{o}[\mathbf{x}_\mathrm{img}]$	signal in image pixel $\mathbf{x}_\mathrm{img}$ after correction	e$^-$ s^{-1}
$\sigma_\mathrm{o}^2[\mathbf{x}_\mathrm{img}]$	signal variance in image pixel $\mathbf{x}_\mathrm{img}$ after correction	e^{-2} s^{-2}
t_exp	exposure time, excluding frame transfer time	s

27.2 Algorithm description

$$S_\mathrm{o}[\mathbf{x}_\mathrm{img}] = S_\mathrm{i}[\mathbf{x}_\mathrm{img}]/t_\mathrm{exp}\ . \tag{26}$$

As mentioned above, note that the exposure time does not include the frame transfer time.

27.3 Error propagation

The exposure time is expected to be known exactly:

$$\sigma_\mathrm{o}^2[\mathbf{x}_\mathrm{img}] = \sigma_\mathrm{i}^2[\mathbf{x}_\mathrm{img}]/t_\mathrm{exp}^2\ . \tag{27}$$

28 Pixel response non-uniformity

Pixel response non-uniformity (PRNU) means that different pixels in a detector do not have the same quantum efficiency. This is mainly caused by manufacturing aspects such as differing pixel sizes and detector surface treatment. The PRNU results in an image that has small variations from pixel to pixel. This high-frequency variation is in the order of five percent (UV) and two percent (VIS).

28.1 Used parameters and symbols

Parameter	**Description**	**Units**
$S_{\mathrm{i}}[\mathbf{x}_{\mathrm{img}}]$	signal in image pixel $\mathbf{x}_{\mathrm{img}}$ before correction	$\mathrm{e^{-}\,s^{-1}}$
$\sigma_{\mathrm{i}}^2[\mathbf{x}_{\mathrm{img}}]$	signal variance in image pixel $\mathbf{x}_{\mathrm{img}}$ before correction	$\mathrm{e^{-2}\,s^{-2}}$
$S_{\mathrm{o}}[\mathbf{x}_{\mathrm{img}}]$	signal in image pixel $\mathbf{x}_{\mathrm{img}}$ after correction	$\mathrm{e^{-}\,s^{-1}}$
$\sigma_{\mathrm{o}}^2[\mathbf{x}_{\mathrm{img}}]$	signal variance in image pixel $\mathbf{x}_{\mathrm{img}}$ after correction	$\mathrm{e^{-2}\,s^{-2}}$
$c_{\mathrm{prnu}}[\mathbf{x}_{\mathrm{det}}]$	PRNU factor	1
$s_{\mathrm{prnu}}^2[\mathbf{x}_{\mathrm{det}}]$	variance of PRNU factor	1

28.2 Algorithm description

$$S_{\mathrm{o}}[\mathbf{x}_{\mathrm{img}}] = S_{\mathrm{i}}[\mathbf{x}_{\mathrm{img}}] \frac{\sum_{\mathbf{x}_{\mathrm{det}} \in \mathbf{x}_{\mathrm{img}}} c_{\mathrm{prnu}}[\mathbf{x}_{\mathrm{det}}]}{N_{\mathbf{x}_{\mathrm{det}} \in \mathbf{x}_{\mathrm{img}}}} \; . \tag{28}$$

Here, c_{prnu} is the ratio between the smoothed and the original calibration measurement. A ratio smaller than 1 implies a local peak in the response. This local peak is therefore negated in the processing algorithm step.

28.3 Error propagation

The error is adjusted according to

$$\sigma_{\mathrm{o}}^2[\mathbf{x}_{\mathrm{img}}] = \left(\frac{\sum_{\mathbf{x}_{\mathrm{det}} \in \mathbf{x}_{\mathrm{img}}} c_{\mathrm{prnu}}[\mathbf{x}_{\mathrm{det}}]}{N_{\mathbf{x}_{\mathrm{det}} \in \mathbf{x}_{\mathrm{img}}}} \right)^2 \sigma_{\mathrm{i}}^2[\mathbf{x}_{\mathrm{img}}] + \overline{s_{\mathrm{prnu}}^2[\mathbf{x}_{\mathrm{det}}]}\, S_{\mathrm{i}}[\mathbf{x}_{\mathrm{img}}]^2 \; . \tag{29}$$

Note that the error in the PRNU correction is propagated directly using the product rule of the formal error propagation mechanism.

29 Straylight correction

Straylight is unwanted light in an optical system and it originates from both intended and unintended light sources. In the case of the former, the straylight follows optical paths that are not intended by the optical design and therefore reaches the detector at unintended positions. This gives rise to spurious signals at the detector.

The grating is considered the main component causing straylight and from a theoretical point of view, the grating is expected to cause most of its straylight in the plane of incidence than in other planes. This means that straylight is more likely to originate from the same viewing direction (i.e. the same row on the CCD) than from the same wavelength from another viewing direction (i.e. the same column). Apart from the effect from the grating, there is also an effect from the channel optics.

In general, two components of straylight are expected to exist: a smooth straylight surface from diffuse reflections and a strongly inhomogeneous surface in which specular reflections play a role (referred to as straylight ghosts). The design was optimised not to have such ghosts and, checking the on-ground straylight measurements, very little was found. That is, the integrated energy of ghosts was too low to be significant.

29.1 Used parameters and symbols

Parameter	Description	Units
$S_\mathrm{i}[\mathbf{x}_\mathrm{img}]$	signal in image pixel $\mathbf{x}_\mathrm{img}$ before correction	e$^-$
$\sigma_\mathrm{i}^2[\mathbf{x}_\mathrm{img}]$	signal variance in image pixel $\mathbf{x}_\mathrm{img}$ before correction	e^{-2}
$S_\mathrm{o}[\mathbf{x}_\mathrm{img}]$	signal in image pixel $\mathbf{x}_\mathrm{img}$ after correction	e$^-$ s^{-1}
$\sigma_\mathrm{o}^2[\mathbf{x}_\mathrm{img}]$	signal variance in image pixel $\mathbf{x}_\mathrm{img}$ after correction	e^{-2} s^{-2}
$\mathbf{R}$	straylight operator	1
$\mathbf{S}_\mathrm{stray}$	straylight signal	e$^-$ s^{-1}
α_k	polynomial coefficient to approximate part of $\mathbf{R}$	1
$\lambda[\mathbf{x}_\mathrm{img}]$	wavelength map, per pixel	nm
λ_0	wavelength offset for specific target region	nm

29.2 Algorithm description

From a mathematical point of view, therefore, we can regard straylight as a redistribution of signal. More specific, we cab construct a mathematical operation: a signal intended for pixel $\mathbf{x}_\mathrm{img} = [r_\mathrm{img}, c_\mathrm{img}]$ will partly be mapped to other pixels on the detector. So, given a vector $\mathbf{S}_\mathrm{intended}$ of length $n_\mathrm{pix} = n_\mathrm{rows} \times n_\mathrm{cols}$, there exists a linear operator (matrix) $\mathbf{R}$ of size $n_\mathrm{pix} \times n_\mathrm{pix}$ such that

$$\mathbf{S}_\mathrm{stray} = \mathbf{R} \cdot \mathbf{S}_\mathrm{intended}, \tag{30}$$

and the actual signal that the detector receives is then

$$\mathbf{S}_\mathrm{actual} = \mathbf{S}_\mathrm{intended} + \mathbf{S}_\mathrm{stray} \quad \text{forward model} \tag{31}$$

The straylight correction, known as the *reverse model*, consists of acquiring $\mathbf{S}_\mathrm{intended}$.

Equations 30 and 31 are the essence of any instrument straylight correction. If the straylight operator $\mathbf{R}$ has been correctly deduced from calibration measurements, then a perfect straylight correction can be achieved by applying the inverse operation of equation 31:

$$\mathbf{S}_\mathrm{intended} = (\mathbf{I} + \mathbf{R})^{-1} \cdot \mathbf{S}_\mathrm{actual} \quad \text{reverse model} \tag{32}$$

There exist several constraints that necessitate a simplification of this approach. $\mathbf{R}$ is too large to be constructed explicitly and any evaluation would be computationally too expensive. Further, the signal $\mathbf{S}$ should also include virtual pixels to take out-of-band straylight into account. Therefore, a simplified and much smaller approximation of $\mathbf{R}$ is constructed from on-ground calibration measurements: sets of bandpass filters that describe where intended signals from certain wavelength intervals actually end up on the detector. Thus, instead of a complete theoretical mapping from each *pixel* to every other pixel, the OMI straylight description is a list of mappings from source *blocks* to target blocks, where the blocks are directly related to the filters that have been used in the on-ground calibration.

In mathematical terms, we have lumped together sets of elements (pixels) of $\mathbf{S}$ and simultaneously reduced the straylight operator $\mathbf{R}$.

More explicitly, there exists a list of wavelength intervals (‘sources’) where the signals for all rows are collected. The wavelength interval is translated to a set of image pixels using the wavelength map. A proportional part of this signal is, as straylight, dumped on another detector area (‘target’). For each pixel in the target, an approximation of the straylight operator $\mathbf{R}$ is constructed by a polynomial:

$$S_\mathrm{stray,target}[\mathbf{x}_\mathrm{img}] = \left(\sum_{k=0}^{n} \alpha_k (\lambda(\mathbf{x}_\mathrm{img}) - \lambda_0)^k \right) S_\mathrm{source}[r_\mathrm{img}], \tag{33}$$

where $S_\mathrm{source}[r_\mathrm{img}]$ is the collected signal in the corresponding source region, per row.

Two refinements are possible for this general model. First, the straylight contribution can either be defined for each individual row, or being considered as a function of the collected source signal, but averaged over all rows.

Second, out-of-band straylight is modeled using an intermediate step: A proportional relation is supposed between an out-of-band source area and a nearby (’proxy’) area near the detector boundary. Thus, the straylight mapping between the non-measurable out-of-band source and the target area is replaced with a mapping between another source area just inside the detector and the target area. The coefficients α_k implicitly express the additional relation between the out-of-band source area and the in-band source area.

Finally, the collection of all straylight signals from all source-target combinations $\mathbf{S}_{\text{stray}}$ is subtracted from the signal:

$$S_{\text{o}}[\mathbf{x}_{\text{img}}] = S_{\text{i}}[\mathbf{x}_{\text{img}}] - S_{\text{stray}}[\mathbf{x}_{\text{img}}]. \tag{34}$$

Note that this subtraction corresponds to the first iteration of a Gauss-Jacobi iteration to obtain the inverse shown in equation 32. Given the small amount of straylight involved, this approach is sufficiently accurate. Note also that constraints of mass conservation do not apply: besides the difficult bookkeeping of straylight from inside the detector to the out-of-band regions, absolute radiometric calibration automatically takes any signal losses into account.

The straylight correction algorithm as described above uses potentially all signals in the science region of the current measurement. Outside the science region, signal that ends up in both straylight regions located at the extreme detector rows can provide additional information on the amount of straylight. A correction can be envisaged that constructs a straylight signal in the science region based on interpolation from the signals in these straylight regions. Such a correction is not implemented since it interferes with the straylight correction described above: it can cause overcorrection.

For further reading, a discussion of the historic OMI choices and approach to straylight can be found in [1], [3] and the original ATBD from industry [11], and references therein.

30 Slit irregularity correction

The manufacturing process of the slit is not perfect; that means that the slit width is not constant. Therefore a viewing angle dependence is expected to be present. This irregularity can be expressed in the slit irregularity function $f_{\text{slit}}[r_{\text{det}}]$, wherein a row dependency is expressed. Note that smile effects are already incorporated.

The retrieval of the slit irregularity from a WLS measurement includes a summing/averaging step in the spectral direction. By doing so, PRNU effects are removed, and a row-dependent response curve remains that includes both low-spatial-frequency variations and high-spatial-frequency variations. The latter variations are assigned to slit irregularity. Note that we hereby *define* the slit irregularity as the high-frequency row-to-row variation, where the average over all columns in each row is considered. That means that features that might exist in reality, like a spatial smile or a slight overall rotation of the slit with respect of the along-track direction, are not accurately described using this definition. However, this is not a major problem since these features are corrected by other algorithms like PRNU and radiance/irradiance. It is probably best to describe the slit irregularity correction as the correction of the *projection* of the slit irregularity on the row direction.

30.1 Used parameters and symbols

Parameter	Description	Units
$S_{\text{i}}[\mathbf{x}_{\text{img}}]$	signal in image pixel $\mathbf{x}_{\text{img}}$ before correction	$\text{e}^{-}\,\text{s}^{-1}$
$\sigma_{\text{i}}^2[\mathbf{x}_{\text{img}}]$	signal variance in image pixel $\mathbf{x}_{\text{img}}$ before correction	$\text{e}^{-2}\,\text{s}^{-2}$
$S_{\text{o}}[\mathbf{x}_{\text{img}}]$	signal in image pixel $\mathbf{x}_{\text{img}}$ after correction	$\text{e}^{-}\,\text{s}^{-1}$
$\sigma_{\text{o}}^2[\mathbf{x}_{\text{img}}]$	signal variance in image pixel $\mathbf{x}_{\text{img}}$ after correction	$\text{e}^{-2}\,\text{s}^{-2}$
$f_{\text{slit}}[r_{\text{det}}]$	slit irregularity factor	none

30.2 Algorithm description

Like the PRNU correction, the slit irregularity is expressed as a factor:

$$S_{\text{o}}[\mathbf{x}_{\text{img}}] = S_{\text{i}}[\mathbf{x}_{\text{img}}] \frac{\sum_{\mathbf{x}_{\text{det}} \in \mathbf{x}_{\text{img}}} f_{\text{slit}}[r_{\text{det}}]}{N_{\mathbf{x}_{\text{det}} \in \mathbf{x}_{\text{img}}}} \ . \tag{35}$$

30.3 Error propagation

The error caused by the slit irregularity correction is propagated directly using the product rule of the formal error propagation mechanism:

$$\sigma_{\rm o}^2[\mathbf{x}_{\rm img}] = \left(\frac{\sum_{\mathbf{x}_{\rm det}\in\mathbf{x}_{\rm img}} f_{\rm slit}[r_{\rm det}]}{N_{\mathbf{x}_{\rm det}\in\mathbf{x}_{\rm img}}}\right)^2 \sigma_{\rm i}^2[\mathbf{x}_{\rm img}] + \overline{s^2_{f_{\rm slit}}[r_{\rm det}]}\, S_{\rm i}[\mathbf{x}_{\rm img}]^2 \;. \tag{36}$$

Note that the variance of the slit irregularity function $f_{\rm slit}$ can depend on the row number.

31 On irradiance, radiance and BSDF

In the following sections the correction algorithms that transform light fluxes (measured in e^- s^{-1}) into radiance and irradiance (measured in mol s^{-1}m^{-2}nm^{-1} and mol s^{-1}m^{-2}nm^{-1}sr^{-1}, respectively) are described. The radiance and irradiance are connected via the OMI bidirectional scattering distribution function (BSDF).

For several reasons, including limitations following from measurement possibilities, the calibration measurements ultimately provide two CKDs for both radiance and irradiance, and a BSDF factor CKD. These are:

Irradiance: $f_{\rm absirr}[\mathbf{x}_{\rm det}]$ **and** $f_{\rm relirr}[\mathbf{x}_{\rm det},\phi,\varepsilon]$. The absolute conversion factor $f_{\rm absirr}$ describes the relation between the flux and irradiance for nominal Sun angles. Thereafter, a dimensionless correction factor $f_{\rm dIRRAD}$ describes the dependencies with non-nominal Sun angles. Hence the division between the two CKDs, each accompanied by their own error.

Radiance: $f_{\rm absrad}[\mathbf{x}_{\rm det}]$ **and** $f_{\rm relrad}[\mathbf{x}_{\rm det}]$. The absolute conversion factor $f_{\rm absrad}$ describes the relation between the flux and radiance.

BSDF: $f_{\rm bsdf}[\mathbf{x}_{\rm det}]$. Per definition, $f_{\rm bsdf} = \frac{f_{\rm absrad}}{f_{\rm absirr}}$. (Note that the instruments BSDF equals irradiance response divided by radiance response, but in the inverse model, with multiplicative factors f, we need the reciprocal expression!)

32 Irradiance responsivity

The irradiance responsivity correction implements the relation between the charge (measured in electrons) as generated in the detector and the absolute photon irradiance (measured in mol s^{-1}m^{-2}nm^{-1}) at the nominal Sun azimuth and elevation angles. For Sun positions other than the nominal one (zero azimuth and elevation), an additional correction is needed; this is described in Section 34.

32.1 Used parameters and symbols

Parameter	Description	Units
$S_{\rm i}[\mathbf{x}_{\rm img}]$	signal in image pixel $\mathbf{x}_{\rm img}$ before correction	e$^-$ s^{-1}
$\sigma_{\rm i}^2[\mathbf{x}_{\rm img}]$	signal variance in image pixel $\mathbf{x}_{\rm img}$ before correction	e^{-2} s^{-2}
$S_{\rm o}[\mathbf{x}_{\rm img}]$	signal in image pixel $\mathbf{x}_{\rm img}$ after correction	mol m^{-2}nm^{-1}s^{-1}
$\sigma_{\rm o}^2[\mathbf{x}_{\rm img}]$	signal variance in image pixel $\mathbf{x}_{\rm img}$ after correction	mol^{2}m^{-4}nm^{-2}s^{-2}
$f_{{\rm absirr},d}[\mathbf{x}_{\rm det}]$	conversion factor, depending on diffuser d	mol m^{-2}nm^{-1}(e$^-$)$^{-1}$
$s^2_{{\rm f,absirr},d}[\mathbf{x}_{\rm det}]$	variance of conversion factor	mol^{2}m^{-4}nm^{-2}(e$^-$)$^{-2}$

32.2 Algorithm description

$$S_{\rm o}[\mathbf{x}_{\rm img}] = \frac{\sum_{\mathbf{x}_{\rm det}\in\mathbf{x}_{\rm img}} f_{{\rm absirr},d}[\mathbf{x}_{\rm det}]}{N_{\mathbf{x}_{\rm det}\in\mathbf{x}_{\rm img}}} S_{\rm i}[\mathbf{x}_{\rm img}] \;. \tag{37}$$

The on-ground calibration provides the calibration key data $f_{{\rm absirr},d}[\mathbf{x}_{\rm det}]$.

32.3 Error propagation

The on-ground calibration provides the calibration key data $s^2_{\mathrm{f,absirr},d}[\mathbf{x}_{\mathrm{det}}]$. if we can assume that the variance is independent of rows and columns, then:

$$\sigma_{\mathrm{o}}^2[\mathbf{x}_{\mathrm{img}}] = \left(\frac{\sum_{\mathbf{x}_{\mathrm{det}}\in\mathbf{x}_{\mathrm{img}}} f_{\mathrm{absirr},d}[\mathbf{x}_{\mathrm{det}}]}{N_{\mathbf{x}_{\mathrm{det}}\in\mathbf{x}_{\mathrm{img}}}}\right)^2 \sigma_{\mathrm{i}}^2[\mathbf{x}_{\mathrm{img}}] + \frac{S_{\mathrm{i}}[\mathbf{x}_{\mathrm{img}}]^2}{N^2_{\mathbf{x}_{\mathrm{det}}\in\mathbf{x}_{\mathrm{img}}}} \sum_{\mathbf{x}_{\mathrm{det}}\in\mathbf{x}_{\mathrm{img}}} s^2_{\mathrm{f,absirr},d}[\mathbf{x}_{\mathrm{det}}] \; . \tag{38}$$

Here the N^2 in denominator follows from the averaging of the unbinned CKD. However, it is safer to assume at least some correlations. In that case, and up to cases of perfect correlation, we have an upper estimate:

$$\sigma_{\mathrm{o}}^2[\mathbf{x}_{\mathrm{img}}] = \left(\frac{\sum_{\mathbf{x}_{\mathrm{det}}\in\mathbf{x}_{\mathrm{img}}} f_{\mathrm{absirr},d}[\mathbf{x}_{\mathrm{det}}]}{N_{\mathbf{x}_{\mathrm{det}}\in\mathbf{x}_{\mathrm{img}}}}\right)^2 \sigma_{\mathrm{i}}^2[\mathbf{x}_{\mathrm{img}}] + S_{\mathrm{i}}[\mathbf{x}_{\mathrm{img}}]^2 \overline{s^2_{\mathrm{f,absirr},d}[\mathbf{x}_{\mathrm{det}}]} \; . \tag{39}$$

Note that we have used the mean variance $\overline{s^2_{\mathrm{f,absirr},d}[\mathbf{x}_{\mathrm{det}}]}$ to indicate that the variances of the unbinned signals can all be substituted with a single binned signal variance.

33 Radiance responsivity

The radiance responsivity correction implements the relation between the charge (measured in electrons) as generated in the detector and the absolute incoming photon radiance (measured in $\mathrm{mol\,s^{-1}m^{-2}nm^{-1}sr^{-1}}$). The total correction consists of two subsequent corrections. In this section, the so-called absolute radiance correction is performed. See Section 31 for details. Note that it is slightly artificial to define the absolute radiance for all pixels instead for the central row only (as dictated by the calibration measurements). However, the two-dimensional description enables us to cope with the spectral smile, if necessary.

33.1 Used parameters and symbols

Parameter	**Description**	**Units**
$S_{\mathrm{i}}[\mathbf{x}_{\mathrm{img}}]$	signal in image pixel $\mathbf{x}_{\mathrm{img}}$ before correction	$\mathrm{e^-\,s^{-1}}$
$\sigma_{\mathrm{i}}^2[\mathbf{x}_{\mathrm{img}}]$	signal variance in image pixel $\mathbf{x}_{\mathrm{img}}$ before correction	$\mathrm{e^{-2}\,s^{-2}}$
$S_{\mathrm{o}}[\mathbf{x}_{\mathrm{img}}]$	signal in image pixel $\mathbf{x}_{\mathrm{img}}$ after correction	$\mathrm{mol\,m^{-2}nm^{-1}sr^{-1}s^{-1}}$
$\sigma_{\mathrm{o}}^2[\mathbf{x}_{\mathrm{img}}]$	signal variance in image pixel $\mathbf{x}_{\mathrm{img}}$ after correction	$\mathrm{mol^2m^{-4}nm^{-2}sr^{-2}s^{-2}}$
$f_{\mathrm{absrad}}[\mathbf{x}_{\mathrm{det}}]$	conversion factor	$\mathrm{mol\,m^{-2}nm^{-1}sr^{-1}(e^-)^{-1}}$
$s^2_{\mathrm{f\_absrad}}[\mathbf{x}_{\mathrm{det}}]$	variance of conversion factor	$\mathrm{mol^2m^{-4}nm^{-2}sr^{-2}(e^-)^{-2}}$

33.2 Algorithm description

$$S_{\mathrm{o}}[\mathbf{x}_{\mathrm{img}}] = S_{\mathrm{i}}[\mathbf{x}_{\mathrm{img}}] \frac{\sum_{\mathbf{x}_{\mathrm{det}}\in\mathbf{x}_{\mathrm{img}}} f_{\mathrm{absrad}}[\mathbf{x}_{\mathrm{det}}]}{N_{\mathbf{x}_{\mathrm{det}}\in\mathbf{x}_{\mathrm{img}}}} \; . \tag{40}$$

The on-ground calibration provides the calibration key data $f_{\mathrm{absrad}}[\mathbf{x}_{\mathrm{det}}]$.

33.3 Error propagation

The radiometric responsivity calibration provides the calibration key data $s^2_{\mathrm{f\_absrad}}[\mathbf{x}_{\mathrm{det}}]$. Because of the binning operation, knowledge about the correlations between individual uncorrelated radiance responsivity values in row direction is needed. For now, we assume the correlations are perfect, hence

$$\sigma_{\mathrm{o}}^2[\mathbf{x}_{\mathrm{img}}] = \left(\frac{\sum_{\mathbf{x}_{\mathrm{det}}\in\mathbf{x}_{\mathrm{img}}} f_{\mathrm{absrad}}[\mathbf{x}_{\mathrm{det}}]}{N_{\mathbf{x}_{\mathrm{det}}\in\mathbf{x}_{\mathrm{img}}}}\right)^2 \sigma_{\mathrm{i}}^2[\mathbf{x}_{\mathrm{img}}] + S_{\mathrm{i}}[\mathbf{x}_{\mathrm{img}}]^2 \overline{s^2_{\mathrm{f\_absrad}}[\mathbf{x}_{\mathrm{det}}]} \; . \tag{41}$$

33.4 Earth-Sun distance normalization

The spectral photon radiance provided is normalized to the average SI Earth-Sun distance of 1 Astronomical Unit (AU). If the Earth spectral radiance is denoted by S_e and the Earth-Sun distance by r_es, then the Earth spectral radiance normalized at 1 AU is given by:

$$S_\mathrm{e}(r_\mathrm{au}) = \left(\frac{r_\mathrm{es}}{r_\mathrm{au}}\right)^2 S_\mathrm{e}(r_\mathrm{es}) \ , \tag{42}$$

where r_au is the Earth-Sun distance equal to 1 AU. Thus, the spectral photon radiance is normalized using the factor $\left(\frac{r_\mathrm{es}}{r_\mathrm{au}}\right)^2$. This algorithm is applied for both radiance *and* irradiance measurements.

33.4.1 Used parameters and symbols

Parameter	Description	Units
$S_\mathrm{i}[\mathbf{x}_\mathrm{img}]$	signal in image pixel $\mathbf{x}_\mathrm{img}$ before correction	$\mathrm{mol\,m^{-2}nm^{-1}(sr^{-1})s^{-1}}$
$\sigma_\mathrm{i}^2[\mathbf{x}_\mathrm{img}]$	signal variance in image pixel $\mathbf{x}_\mathrm{img}$ before correction	$\mathrm{mol^2m^{-4}nm^{-2}(sr^{-2})s^{-2}}$
$S_\mathrm{o}[\mathbf{x}_\mathrm{img}]$	signal in image pixel $\mathbf{x}_\mathrm{img}$ after correction	$\mathrm{mol\,m^{-2}nm^{-1}(sr^{-1})s^{-1}}$
$\sigma_\mathrm{o}^2[\mathbf{x}_\mathrm{img}]$	signal variance in image pixel $\mathbf{x}_\mathrm{img}$ after correction	$\mathrm{mol^2m^{-4}nm^{-2}(sr^{-2})s^{-2}}$
r_es	Earth-Sun distance at the time of the measurement	m
r_au	Average SI Earth-Sun distance; 1 AU = 149597870700	m

33.4.2 Algorithm description

$$S_\mathrm{o}[\mathbf{x}_\mathrm{img}] = \left(\frac{r_\mathrm{es}}{r_\mathrm{au}}\right)^2 S_\mathrm{i}[\mathbf{x}_\mathrm{img}] \tag{43}$$

33.4.3 Error propagation

$$\sigma_\mathrm{o}^2[\mathbf{x}_\mathrm{img}] = \left(\frac{r_\mathrm{es}}{r_\mathrm{au}}\right)^4 \sigma_\mathrm{i}^2[\mathbf{x}_\mathrm{img}] \tag{44}$$

34 Irradiance responsivity as a function of diffuser incident angle

The irradiances as computed using the irradiance responsivity correction (Section 32) pertain to the Sun azimuth and elevation angles at the time of the measurement. The relative irradiance algorithm translates these irradiances to irradiances at the nominal Sun azimuth and elevation angles. This algorithm step is only needed for the Solar_irradiance processing class.

34.1 Used parameters and symbols

Parameter	Description	Units
$S_\mathrm{i}[\mathbf{x}_\mathrm{img}]$	signal in image pixel $\mathbf{x}_\mathrm{img}$ before correction	$\mathrm{mol\,m^{-2}nm^{-1}s^{-1}}$
$S_\mathrm{o}[\mathbf{x}_\mathrm{img}]$	signal in image pixel $\mathbf{x}_\mathrm{img}$ after correction	$\mathrm{mol\,m^{-2}nm^{-1}s^{-1}}$
$f_{\mathrm{dIRRAD},d}[\mathbf{x}_\mathrm{img},\varphi,\varepsilon]$	correction factor, depending on diffuser d	1
φ	Sun azimuth angle	°
ε	Sun elevation angle	°

34.2 Algorithm description

A CKD parameter f_{dIRRAD} is provided as table-like data structure (hypercube)in four dimensions. It describes the dependence on Sun azimuth angle φ and elevation angle ε. This CKD parameter is obtained using binned in-flight irradiance data for years 2005–2016 regridded to a fine equidistant grid of 0.05° grid size resulting in n_{azimuth} by $n_{\text{elevation}}$ grid points. In order to avoid memory problems the pixels are reduced in wavelength region to wavelength bands. The resulting hypercube dimensions: n_{azimuth} by $n_{\text{elevation}}$ by n_{xtrack} by $n_{\text{lambda}_{\text{band}}}$.
Using interpolation, we can define the four-dimensional Sun angle dependence function as

$$f_{\text{dIRRAD},d}[\mathbf{x}_{\text{img}}, \varphi, \varepsilon] : \mathbb{N}^2 \times \mathbb{R}^2 \to \mathbb{R} \ , \tag{45}$$

where φ and ε are acquired from geometrical annotation. The irradiances are then converted as

$$S_{\text{o}}[\mathbf{x}_{\text{img}}] = S_{\text{i}}[\mathbf{x}_{\text{img}}] f_{\text{dIRRAD},d}[\mathbf{x}_{\text{img}}, \varphi, \varepsilon] \ . \tag{46}$$

35 Temporal CKDs and degradation

The properties of the OMI instrument change over time. This can be the result of degradation or some other effect that changes the output of the instrument. If the signal changes over time, the phenomenon that actually causes the change can be hard to determine. Sometimes some assumptions allow for a separation between the different optical pathways. The collection 4 processor differentiates between four types of degradation corrections: radiance, irradiance, diffuser degradation and spectrometer corrections. With the release of collection 4 calibration key data is provided for the quasi volume diffuser (used for the nominal daily irradiance measurements) and for the radiance degradation. The key data for the irradiance and spectrometer degradation is set to unity. Also, for the aluminum diffusers no degradation correction is applied. Other temporal effects, like for example gain drift, are combined with their respective main conversion or correction steps, see for example Section 21.

The degradation corrections are implemented by assuming for each of the stages of the optical pathway mentioned above, a map, or *degradation factor image* f. The map contains for each detector pixel the factor by which the signal needs to be multiplied to correct for the possible degradation. This map is given for a number of orbits, so that for any given orbit of L0 data that needs to be processed to L1b data, a value for each pixel can be determined by interpolating between the given values for the orbit numbers for which the map has been determined.

35.1 Diffuser degradation

To determine the diffuser degradation of the QVD reference irradiance data in the period 2005–2020 has been used. The diffuser degradation correction has been determined at the solar reference angle (azimuth angle = 23.75° and elevation angle = 0.0°) relative to the irradiance signal at the start of the mission assuming a constant solar irradiance over the mission. A 2D fit is performed to determine the dependence on orbit number and wavelength. For all three channels the degradation is different for different across track positions. For VIS a first order dependency is used. For UV2 and UV1 a second order dependency is used. The key data is extrapolated to orbits far beyond the expected remaining duration of the mission.

35.2 Radiance degradation

The radiance degradation is corrected by a row dependent factor that increases as a linear function of orbit number. The correction is based on analysis of Earth shine radiances of Antarctic ice at 340 nm. The correction is independent of the wavelength and the same for all three bands of OMI. For each (binned) detector row a compensation factor for the degradation is given as a function of the orbit number. It is implemented as a linear interpolation between the value 1 for orbit 0 and the provided value for orbit 100 000. For orbits beyond that, the values are extrapolated linearly.

35.3 Used parameters and symbols

Parameter	Description	Units radiance	Units irradiance
$S_\mathrm{i}[\mathbf{x}_\mathrm{img}]$	signal in image pixel $\mathbf{x}_\mathrm{img}$ before correction	mol s^{-1}nm^{-1}m^{-2}sr^{-1}	mol s^{-1}nm^{-1}m^{-2}
$\sigma_\mathrm{i}^2[\mathbf{x}_\mathrm{img}]$	signal variance in image pixel $\mathbf{x}_\mathrm{img}$ before correction	mol^{2}s^{-2}nm^{-2}m^{-4}sr^{-2}	mol^{2}s^{-2}nm^{-2}m^{-4}
$S_\mathrm{o}[\mathbf{x}_\mathrm{img}]$	signal in image pixel $\mathbf{x}_\mathrm{img}$ after correction	mol s^{-1}nm^{-1}m^{-2}sr^{-1}	mol s^{-1}nm^{-1}m^{-2}
$\sigma_\mathrm{o}^2[\mathbf{x}_\mathrm{img}]$	signal variance in image pixel $\mathbf{x}_\mathrm{img}$ after correction	mol^{2}s^{-2}nm^{-2}m^{-4}sr^{-2}	mol^{2}s^{-2}nm^{-2}m^{-4}
i_orb	current orbit number	1	1
$f_d(j_\mathrm{orb})$	degradation factor image, per band, for orbits j	1	1

35.4 Algorithm description

$$S_\mathrm{o}[\mathbf{x}_\mathrm{img}] = S_\mathrm{i}[\mathbf{x}_\mathrm{img}]\frac{\sum_{\mathbf{x}_\mathrm{det}\in\mathbf{x}_\mathrm{img}} f[\mathbf{x}_\mathrm{det}]}{N_{\mathbf{x}_\mathrm{det}\in\mathbf{x}_\mathrm{img}}} \,. \tag{47}$$

Here the degradation image f is acquired from linear interpolation of temporally neighboring CKD degradation images:

$$f[\mathbf{x}_\mathrm{det}] = (1-\alpha) f_d(j_\mathrm{orb,1}) + \alpha f_d(j_\mathrm{orb,2}), \tag{48}$$

$$\text{and where} \quad \alpha = \frac{i_\mathrm{orb} - j_\mathrm{orb,1}}{j_\mathrm{orb,2} - j_\mathrm{orb,1}} \,. \tag{49}$$

35.5 Error propagation

The current baseline is that the error in the correction term itself is set to zero.

$$\sigma_\mathrm{o}^2[\mathbf{x}_\mathrm{img}] = \left(\frac{\sum_{\mathbf{x}_\mathrm{det}\in\mathbf{x}_\mathrm{img}} f[\mathbf{x}_\mathrm{det}]}{N_{\mathbf{x}_\mathrm{det}\in\mathbf{x}_\mathrm{img}}}\right)^2 \sigma_\mathrm{i}^2[\mathbf{x}_\mathrm{img}] \,. \tag{50}$$

36 Irradiance averaging

The diffusers can introduce random-like features in the measured Sun spectrum. These features show up in the Sun-normalised radiance spectra because diffusers are not used for radiance measurements and therefore they form a serious source of errors in trace gas retrievals. To cope with this problem, an additional averaged signal is generated from irradiance signals: subsequent measurements from a single sunset are averaged. This is called elevation averaging. Note that, since the CKD f_relirr is available (and the irradiance has thus been corrected for Sun elevation angle dependencies), this averaging operation is allowed. This algorithm step is only needed for the Solar_irradiance processing class.

36.1 Used parameters and symbols

Parameter	Description	Units
$S_\mathrm{i}[\mathbf{x}_\mathrm{img}]$	signal in image pixel $\mathbf{x}_\mathrm{img}$ before correction	molm^{-2}nm^{-1}s^{-1}
$\sigma_\mathrm{i}^2[\mathbf{x}_\mathrm{img}]$	signal variance in image pixel $\mathbf{x}_\mathrm{img}$ before correction	mol^{2}m^{-4}nm^{-2}s^{-2}
$S_\mathrm{irr,avg}[\mathbf{x}_\mathrm{img}]$	averaged signal	molm^{-2}nm^{-1}s^{-1}
$\sigma_\mathrm{irr,avg}^2[\mathbf{x}_\mathrm{img}]$	variance of averaged signal	mol^{2}m^{-4}nm^{-2}s^{-2}
N	number of measurements involved	1

36.2 Algorithm description and error propagation

The averaged irradiance signal is

$$S_{\mathrm{irr,avg}}[\mathbf{x}_{\mathrm{img}}] = \frac{1}{N}\sum_{i=1}^{N} S_{\mathrm{i}}[\mathbf{x}_{\mathrm{img}}] \ , \tag{51}$$

where N is the size of the subset of available Sun measurements that meets a restriction based on a certain elevation range.

36.3 Error propagation

The variance of the resulting averaged signal is

$$\sigma^2_{\mathrm{irr,avg}}[\mathbf{x}_{\mathrm{img}}] = \frac{1}{N^2}\sum_{i=1}^{N} \sigma^2_{\mathrm{i}}[\mathbf{x}_{\mathrm{img}}] \ . \tag{52}$$

Part V
Annotation

The preceding sections dealt with correction and calibration functions applied to the raw instrument data to retrieve the radiance or irradiance entering the instrument.

In order to be able to use the data, it is necessary to know the context in which the measurements were performed and give an indication if the data is useful for scientific purposes. When did the measurement take place? What are the coordinates of the ground pixels? Under which angles was the radiation scattered by the atmosphere? Did any errors occur during the processing? Do parts of the data need to be excluded due to instrument or measurement quality issues? Answers to such questions are given by a number of dedicated algorithms and added to the Level 1b products as annotation and flagging data.

Annotation covers different subjects: assigning a wavelength to the pixels is described in Section 37, the annotation with measurement time and geolocation or angle information is described in Sections 38–40. Here also the movement of the spacecraft relative to Sun and Earth and the optical path length of the light are taken into account. Section 41 describes the assessment of the measurement and data quality and subsequent flagging.

37 Wavelength characterization

Each detector pixel is associated with a particular wavelength. Basically, this wavelength is a monotonously increasing function of the detector column number. However, the relationship between detector pixel and wavelength depends also on:

- detector row number, due to the ‘spectral smile’;
- spacecraft velocity, due to the Doppler effect;
- OBM temperature or temperature gradient (however note that the temperature within the OMI instrument is stabilized);
- inhomogeneous slit illumination, due to sub-pixel scenery variations.

The spectral smile cannot be neglected and has to be taken into account in the wavelength characterization, which means that each detector row is assigned a different wavelength scale. Doppler shift is only important for cases where the speed of the detector towards or away from the light source is non-negligible; that is, only for irradiance measurements. Inhomogeneous slit illumination only occurs when the observed scene changes, so only during radiance measurements.

Using in-flight measurements, an absolute or nominal wavelength map has been determined for all unbinned pixels of each band at an OPB temperature of approximately 264 K. Furthermore, a wavelength correction has been calibrated due to temperature changes of the instrument. Finally, calibration key data (CKD) has been derived which describes the relation of the wavelength changes with respect to inhomogeneous slit illumination. These calibration analyzes are treated briefly below.

Note that for the L01b radiance and irradiance output products no wavelength fit is performed in the processor. Wavelength fitting is performed in the L01b processor only for the calibration product and therefore not described here.

37.1 Nominal wavelength annotation

As a first approximation, the wavelength characterization can be considered to be independent of measurement. Therefore, the L1b products contains a single ‘image’ containing the nominal wavelength as a function of row and column number: this is sufficient for display purposes and can serve as a starting point for the wavelength calibration performed in the L1b to Level-2 processors.

The initial wavelength scale depends on the position and orientation of the optics, the slit, the gratings, and the detectors themselves. The wavelength annotation has been re-calibrated by fitting unbinned irradiance measurements with a high-resolution solar reference spectrum for a number of wavelength windows. The reference spectrum has been convoluted with the instrument slit function before-hand.

The nominal wavelength map has then been determined by fitting a 2D polynomial through the wavelength shift versus row (second degree) and wavelength fit window (third degree) dimensions. Using the central column of each fit window, a polynomials is then derived with respect to column number for each row. The choice for ordinary polynomials is also stemming from the need for backwards compatibility of the original wavelength annotation. The polynomials are the calibration key data input for the wavelength annotation in the L01b processor.

37.2 Wavelength correction due to the Doppler effect

When solar irradiance measurements are performed, the measured spectrum is affected by non-relativistic Doppler shift. In particular, the spacecraft moves away from the Sun over the North Pole with approximately 7 km/s, causing a wavelength shift towards the red. As a result, the irradiance signal that the detector measures is mapped on pixels associated with nominal wavelengths that are too high. To correct for this, the wavelength map for irradiance measurements has to be shifted. Note that for radiance measurements, no Doppler shift correction is needed since the velocity of the spacecraft is largely orthogonal to the Earth port field-of-view.

Starting from the general equation for the Doppler effect from classical physics, the observed frequency f_o is related to the source frequency f_s by

$$f_o = \frac{c+v}{c} f_s \,, \tag{53}$$

where c is the speed of light in vacuum, and v is the spacecraft velocity component towards the direction of the Sun. Using the relation between frequency and wavelength $f = c/\lambda$, the source wavelength is related to the observed wavelength as

$$\lambda_s = \frac{c+v}{c} \lambda_o \,. \tag{54}$$

It follows that the absolutely calibrated nominal wavelength map associated with the detector pixels needs to be be multiplied by a factor of $\frac{c+v}{c}$ for irradiance measurements, where v is negative as the spacecraft is moving away from the Sun. The Doppler shift is applied in the L01b processor for irradiance measurements. The inverse Doppler conversion factor $\frac{c}{c+v}$ can be used to convert the Doppler corrected irradiance wavelength map back to a nominal wavelength map, where needed.

37.3 Wavelength correction due to instrument temperature variations

The mapping of the light that goes through the optical system of the instrument is expected to depend on the temperature of the instrument, due to thermal deformations. During the first 15 years of the OMI mission the instrument temperature had been steadily increasing from about 264 K to 265 K, after which it was reduced again by almost one degree (see Section 8 for details). Furthermore, in the commissioning phase, the instrument temperature was increased to above 300 K.

For a large number of orbits over the entire OMI lifetime irradiance measurements have been analyzed to determine the way the wavelength distribution has shifted as a function of the temperature. By fitting the irradiance measurements with the solar reference spectrum, the wavelength shift has been determined, and related to the OPB temperature for all rows and fit windows. The shift is then expressed as a change of the polynomial coefficients that define the nominal wavelength annotation. For a set of temperatures the wavelength change is described by polynomials in CKD datasets, and through interpolation the change at a given instrument temperature is determined and applied to the wavelength assignment in the L01b processor.

37.4 Wavelength correction due to inhomogeneous slit illumination

When the entrance slit is not homogeneously illuminated, e.g. in the case of a partly cloudy scene when looking at the Earth, the way that the light is imaged onto the detector, expressed by the so-called slit function, can cause an effective shift of the wavelength on the detector. The small pixel column can give information on the distribution of the intensity of the signal as a function of the cross-track position or detector row for the various co-added images in a measurement, and with this information a inhomogeneity factor Q is calculated as

$$Q = 2 \cdot \frac{\mathbf{P}[x_{\text{spc}}](\text{last}, r_{\text{img}}) - \mathbf{P}[x_{\text{spc}}](\text{first}, r_{\text{img}})}{\mathbf{P}[x_{\text{spc}}](\text{last}, r_{\text{img}}) + \mathbf{P}[x_{\text{spc}}](\text{first}, r_{\text{img}})}, \tag{55}$$

resulting in a scalar between -2 and 2.

For a number of nominal orbits, this factor has been determined for all radiance measurements. By fitting the radiance signal with a Solar reference spectrum and an Ozone absorption spectrum, the shift in wavelength has been determined for a number of wavelength windows. By analyzing the relation between the Q factor and the wavelength shift for all rows and windows, a correction CKD has been determined. This CKD is then used by the L01b processor in combination with the Q factor to determine the correction applied to the polynomial coefficients that define the nominal wavelength annotation.

38 Time bases and conversions

Obviously, time constitutes one of the most important pieces of annotation data. Therefore, all measurements in the OMI Level 1b products will be augmented with a timestamp that indicates when the measurement was taken. The time of a measurement is also one of the main inputs to the geometrical algorithms. Depending on the algorithm, different time bases are needed and conversions between these time bases are required. The L01b processor has support for the time bases described in Table 10. The different time types that are used in Table 10 are described in Table 11. All the time definitions are relative to a specific epoch. This is necessary in order to be able to correlate the different time types and time bases and convert from one to another. The epochs that are used are described in Table 12.

Time base	Symbol	Unit	Epoch
CCSDS Unsegmented time Code (CUC)	t_{cuc}	s	1958-01-01 (UTC)
UTC since 2010	$t_{\mathrm{utc,2010}}$	s	2010-01-01 (UTC)
UTC since 1970	$t_{\mathrm{utc,1970}}$	s	1970-01-01 (UTC)
TAI since 1993	$t_{\mathrm{tai,1993}}$	s	1993-01-01 (UTC)
TAI since 2010	$t_{\mathrm{tai,2010}}$	s	2010-01-01 (UTC)
TAI since J2000.0	$t_{\mathrm{tai,J2000}}$	s	J.2000.0
UT1 since 2010	$t_{\mathrm{ut1,2010}}$	s	2010-01-01 (UTC)
UT1 since J2000.0	$t_{\mathrm{ut1,J2000}}$	s	J.2000.0
TT since J2000.0	$t_{\mathrm{tt,J2000}}$	s	J.2000.0
Julian Date (JD) J2000.0	J_{J2000}	JD	J.2000.0

Table 10: Time bases of the OMI L01b processor, their unit and epoch.

UT1 time follows the rotation of the Earth as closely as possible. As the duration of a solar day (i.e. the time for one full revolution of the Earth) is slightly larger than 86400 seconds, UT1 drifts in relation to TAI and UTC. The exact rotation of the Earth is monitored by the International Earth Rotation and Reference Systems Service (IERS). The difference between UTC and UT1 is published by the IERS in Bulletin B. A long-term overview of the difference between UT1 and UTC is given in Figure 22. The L01b processor will read the IERS Bulletin-B data products and use the data for conversion of time from UTC and TAI to UT1:

$$t_{\mathrm{ut1,2010}} = t_{\mathrm{utc,2010}} + T_{\mathrm{ut1-utc}}(t_{\mathrm{utc,2010}}) \;, \tag{56a}$$
$$t_{\mathrm{ut1,J2000}} = t_{\mathrm{utc,J2000}} + T_{\mathrm{ut1-utc}}(t_{\mathrm{utc,J2000}}) \;, \tag{56b}$$

where $T_{\mathrm{ut1-utc}}(t_{\mathrm{utc}})$ is the difference between UT1 and UTC for a UTC timestamp t_{utc}. As the difference between UT1 and UTC is always less than a second and the drift between UT1 and UTC is relatively slow, the same value is used for converting back to UTC, using the UT1 timestamp as a UTC timestamp. The corresponding error in the conversion is neglected:

$$t_{\mathrm{utc,2010}} = t_{\mathrm{ut1,2010}} - T_{\mathrm{ut1-utc}}(t_{\mathrm{ut1,2010}}) \;, \tag{57a}$$
$$t_{\mathrm{utc,J2000}} = t_{\mathrm{ut1,J2000}} - T_{\mathrm{ut1-utc}}(t_{\mathrm{ut1,J2000}}) \;. \tag{57b}$$

To keep the difference between UT1 and UTC within 1 seconds, leap seconds are introduced, which are published in IERS Bulletin C. These leap seconds need to be taken into account for conversions from the TAI time base to the UTC time base. Leap seconds are announced by the IERS and published in the IERS Bulletin C. The L01b processor will read these Bulletin-C data products to build a table containing all announced leap seconds. This table is used for the time conversions in the L01b processor. The leap seconds up to 2012 are shown in Table 13. To convert from TAI to UTC and vice-versa in the same epoch:

Time type	Description
CCSDS unsegmented time code (CUC)	Seconds since an epoch; identical to TAI. CUC times are used in the OMI telemetry and science data.
Coordinated universal time (UTC)	The primary time standard by which the world regulates clocks and time. UTC times in seconds do not include leap seconds. UTC time is generally used for presenting time in a human readable format.
International atomic time (TAI)	High-precision atomic coordinate time standard based on the notional passage of proper time on Earth's geoid. It is the basis for coordinated universal time (UTC), which is used for civil timekeeping all over the Earth's surface, and for terrestrial time, which is used for astronomical calculations. TAI timestamps are used in the L01b internally where possible, as they are the most convenient to work with.
Universal time (UT1)	Time scale based on the rotation of the Earth. UT1 is the same everywhere on Earth, and is proportional to the rotation angle of the Earth with respect to distant quasars, specifically, the international celestial reference frame (ICRF), neglecting some small adjustments. Time in UT1 is needed for carrying out certain reference frame transformations.
Terrestrial time (TT)	Astronomical time standard defined by the International Astronomical Union (IAU), primarily for time measurements of astronomical observations made from the surface of the Earth. Time in TT1 is needed for carrying out certain reference frame transformations.
Julian date (JD)	The Julian day number for the preceding noon plus the fraction of the day since that instant. Julian dates are expressed as a Julian day number with a decimal fraction added. The Julian day number (JDN) is the integer assigned to a whole solar day in the Julian day count starting from noon Greenwich mean time, with Julian day number 0 assigned to the day starting at noon on January 1, 4713 BC proleptic Julian calendar. (November 24, 4714 BC in the proleptic Gregorian calendar.) A Julian day is defined as 86400 s.

Table 11: Time types of the OMI L01b processor

Time epoch	Description
1958-01-01 (UTC)	This epoch is used for the time stamps in the OMI telemetry and science data.
1970-01-01 (UTC)	Epoch for the Unix clock and C times functions.
1993-01-01 (UTC)	This epoch was used in the collection 3 OMI L1b products and is maintained for backwards compatibility
2010-01-01 (UTC)	Internal epoch for the OMI L01b processor. Most time conversions in the L01b processor use this epoch as a common basis. This means that for time conversion a time is first converted to this epoch as an intermediate step.
J2000.0	The current standard epoch for astronomical calculations as designated by the International Astronomical Union (IAU). The J2000.0 epoch corresponds to: 1. The Julian date 2451545.0 TT (Terrestrial Time). 2. January 1, 2000, 11:59:27.816 TAI (International Atomic Time). 3. January 1, 2000, 11:58:55.816 UTC (Coordinated Universal Time).

Table 12: Time epochs of the OMI L01b processor

$$t_{\mathrm{tai},2010} = t_{\mathrm{utc},2010} + T_{\mathrm{leapsec,utc}}(t_{\mathrm{utc},2010}) \,, \tag{58a}$$

$$t_{\mathrm{utc},2010} = t_{\mathrm{tai},2010} - T_{\mathrm{leapsec,tai}}(t_{\mathrm{tai},2010}) \,, \tag{58b}$$

where $T_{\mathrm{leapsec,utc}}(t_{\mathrm{utc}})$ and $T_{\mathrm{leapsec,tai}}(t_{\mathrm{tai}})$ are the number of leap seconds for a UTC timestamp t_{utc} and that for a TAI timestamp t_{tai} respectively.

For conversion of a UTC timestamp to a different epoch, it is sufficient to add or subtract the difference in

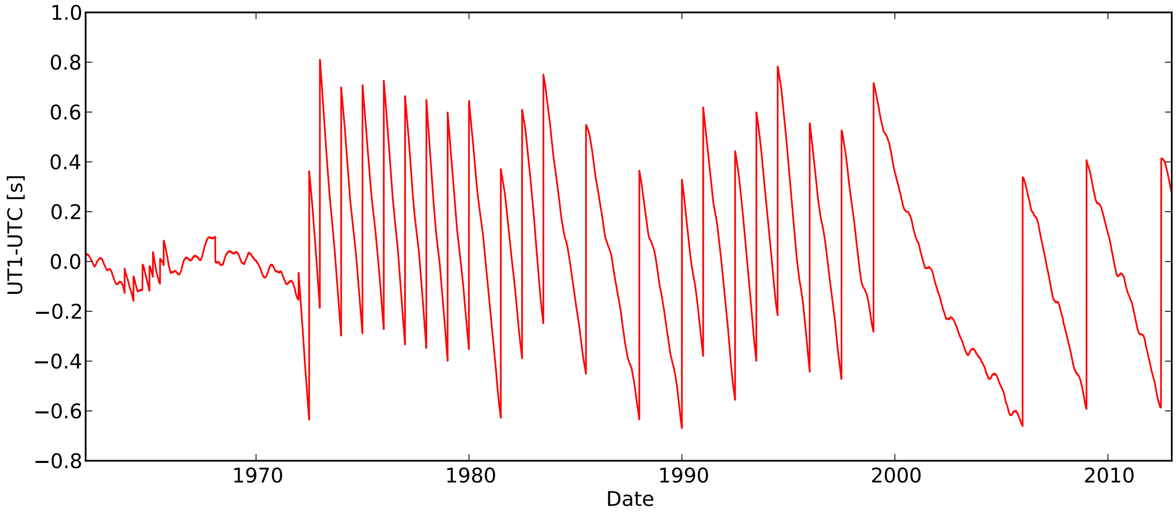

Figure 22: Long term difference between UT1 and UTC.

Starting from	Leap seconds	Starting from	Leap seconds
1972-01-01 00:00:00 UTC	10	1985-07-01 00:00:00 UTC	23
1972-07-01 00:00:00 UTC	11	1988-01-01 00:00:00 UTC	24
1973-01-01 00:00:00 UTC	12	1990-01-01 00:00:00 UTC	25
1974-01-01 00:00:00 UTC	13	1991-01-01 00:00:00 UTC	26
1975-01-01 00:00:00 UTC	14	1992-07-01 00:00:00 UTC	27
1976-01-01 00:00:00 UTC	15	1993-07-01 00:00:00 UTC	28
1977-01-01 00:00:00 UTC	16	1994-07-01 00:00:00 UTC	29
1978-01-01 00:00:00 UTC	17	1996-01-01 00:00:00 UTC	30
1979-01-01 00:00:00 UTC	18	1997-07-01 00:00:00 UTC	31
1980-01-01 00:00:00 UTC	19	1999-01-01 00:00:00 UTC	32
1981-07-01 00:00:00 UTC	20	2006-01-01 00:00:00 UTC	33
1982-07-01 00:00:00 UTC	21	2009-01-01 00:00:00 UTC	34
1983-07-01 00:00:00 UTC	22	2012-07-01 00:00:00 UTC	35

Table 13: Leap seconds up to 2012. The leap seconds specify the time difference in seconds between TAI and UTC. At the introduction of leap seconds in 1972, this difference already amounted to 10 seconds.

seconds between the epochs. So, to convert between epochs:

$$t_{\mathrm{utc},1970} = t_{\mathrm{utc},2010} + \Delta T_{\mathrm{epoch,utc}}[2010, 1970] \; , \tag{59a}$$

$$t_{\mathrm{utc},2010} = t_{\mathrm{utc},1970} + \Delta T_{\mathrm{epoch,utc}}[1970, 2010] \; , \tag{59b}$$

where $\Delta T_{\mathrm{epoch,utc}}[t_1, t_2]$ is the number of UTC seconds between two epochs t_1 and t_2. Here we use the convention that $\Delta T_{\mathrm{epoch,}}[t_1, t_2]$ is positive for $t_1 > t_2$. The various $\Delta T_{\mathrm{epoch}}$'s have the following values:

$$\Delta T_{\mathrm{epoch,utc}}[2010, 1970] = 14610 \cdot 86400\,\mathrm{s} \; , \tag{60a}$$

$$\Delta T_{\mathrm{epoch,utc}}[1970, 2010] = -14610 \cdot 86400\,\mathrm{s} \; . \tag{60b}$$

CUC time is essentially a TAI time, so for CUC time the same conversions as for TAI times apply.
The difference between TAI and TT is a fixed offset $\Delta T_{\mathrm{tai,tt}}$, which is independent of the epoch:

$$t_{\mathrm{tt,J2000}} = t_{\mathrm{tai,J2000}} + \Delta T_{\mathrm{tai,tt}} \; , \tag{61a}$$

$$t_{\mathrm{tai,J2000}} = t_{\mathrm{tt,J2000}} - \Delta T_{\mathrm{tai,tt}} \; , \tag{61b}$$

$$\Delta T_{\mathrm{tai,tt}} = 32.184\,\mathrm{s} \; . \tag{61c}$$

To retain the fixed offset between TAI and TT, this offset is not applied when converting a TAI time to or from the J2000.0 epoch. The fact that J2000.0 starts at noon rather than midnight will need to be accounted for. Conversion of TAI time to the J2000.0 epoch is as follows:

$$t_{\mathrm{tai,J2000}} = t_{\mathrm{tai,2010}} + \Delta T_{\mathrm{epoch,utc}}[2010,2000] - 0.5 \cdot 86400 + T_{\mathrm{leapsec}}[2010] \; , \tag{62a}$$

$$t_{\mathrm{tai,2010}} = t_{\mathrm{tai,J2000}} + \Delta T_{\mathrm{epoch,utc}}[2000,2010] + 0.5 \cdot 86400 - T_{\mathrm{leapsec}}[2010] \; , \tag{62b}$$

with

$$\Delta T_{\mathrm{epoch,utc}}[2010,2000] = 3653 \cdot 86400\,\mathrm{s} \; , \tag{63a}$$

$$\Delta T_{\mathrm{epoch,utc}}[2000,2010] = -3653 \cdot 86400\,\mathrm{s} \; . \tag{63b}$$

Julian Date (JD) J_{J2000} is based on Terrestrial Time (TT) and in the same epoch J2000.0, so deriving J_{J2000} from $t_{\mathrm{tt,J2000}}$ is straightforward:

$$J_{\mathrm{J2000}} = \frac{t_{\mathrm{tt,J2000}}}{86400} \; , \tag{64a}$$

$$t_{\mathrm{tt,J2000}} = J_{\mathrm{J2000}} \cdot 86400 \; . \tag{64b}$$

39 Geometrical definitions

For the geometrical algorithms that will be described in Section 40, a number of geometrical definitions need to be explained first. These consist of reference frames, reference frame transformations, and optical functions.

39.1 Reference frame definitions

The reference frames needed to define the positions, velocities and angles of the following geolocation calculations will be explained in this section. Most definitions have been adopted, modified and combined from [12], as well as other industry documents, unless stated otherwise.

39.1.1 WGS84 Earth reference ellipsoid

To simulate the geometry of the Earth, the WGS84 Earth reference ellipsoid is used. This ellipsoid is created by rotating the ellipse of Figure 23 about the axis of rotation (making it in effect an oblate spheroid or ellipsoid of revolution). The ellipse is defined as having a semi-major axis a (equatorial radius) of 6378137.0 m and the flattening $f = (a-b)/a$ of the ellipse is defined as 1/298.257223563 [13]. This results in a semi-minor axis b (polar radius) of 6356752.3142 m. Locations on the ellipsoid may be expressed as geocentric or geodetic coordinates. The axes cross at the center point (origin) of the ellipse, which is the center of mass of the Earth.

Geocentric coordinates are defined with respect to this center of mass of the Earth. This can be either in Cartesian coordinates (x,y,z) or spherical coordinates (δ', ϑ, r), defined as geocentric latitude, longitude and radius (see Figure 23). In the latter, the longitude ϑ is measured positive eastwards from the IERS reference meridian (Greenwich, see also Figure 25).

In contrast, the geodetic coordinates (δ, ϑ, h: geodetic latitude, longitude and altitude, respectively) that are used in the output Level 1b data for locations on Earth, are defined with respect to the WGS84 Earth reference ellipsoid. The longitude in the geodetic system is the same as for the geocentric system, and therefore has the same name and symbol in both systems. However, the geodetic latitude is defined by the angle of the normal from point P to the Earth reference ellipsoid and the equatorial plane. The altitude h is the distance from the point P measured perpendicular to the plane tangent to the Earth reference ellipsoid.

39.1.2 Inertial reference frame

The inertial reference frame is the geocentric mean-of-date reference frame at epoch J2000.0, with its:

- Origin at the center of mass of the Earth at epoch J2000.
- Z-axis in the direction of Earth's mean rotation axis at epoch J2000, pointing north.
- X-axis in the direction of the mean vernal equinox at epoch J2000.

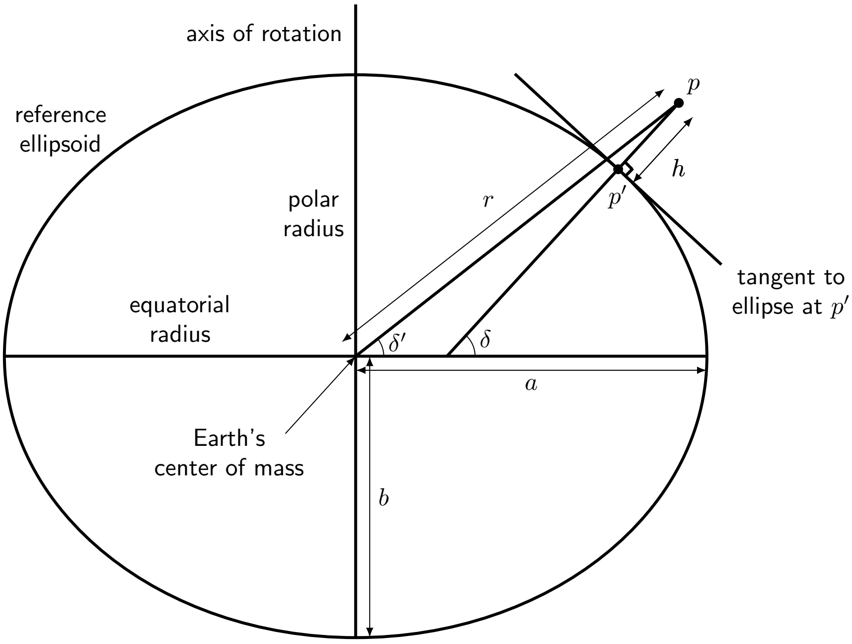

Figure 23: Geocentric versus geodetic coordinates with respect to the WGS84 Earth reference ellipsoid.

- Y-axis completing the right-handed orthogonal Cartesian coordinate system.

The vernal equinox is the intersection of the Earth's mean equator plane with the mean ecliptic, while the ecliptic is the orbital plane of the Earth around the Sun. The X-Y plane thus coincides with the predicted mean Earth equatorial plane, at the epoch J2000.0. Here, the word 'mean' indicates that the relatively short periodic nutation of the Earth, is smoothed out in the calculation of the mean equator and equinox. That is, only the mean precession of the Earth is taken into account.

This reference frame is based (in accordance with the recommendations of the International Astronomical Union (IAU)) on the Fifth Fundamental Star Catalog (FK5) for the epoch J2000.0, since the directions of its axes are defined relative to a given number of the FK5 catalog's positions and proper motions. The accuracy of this reference system, realized through FK5, is approximately 0.1 arcseconds. Figure 24 depicts a schematic of the inertial reference frame.

39.1.3 Mean-of-date reference frame

The mean-of-date reference frame has the same definition for its axes as the inertial reference frame. However, the coordinate axes of the system are now rotated with the Earth's precession from J2000.0, to the date used as epoch. The precession of the Earth is the secular effect of the gravitational attraction from the Sun and the Moon on the Earth's equatorial bulge (see also Section 39.2.3). Here, the expression 'mean' indicates that the relatively short periodic nutation of the Earth is smoothed out, in the calculation of parameters for that epoch.

39.1.4 True-of-date reference frame

The true-of-date reference frame also has the same definition for its axes as the inertial reference frame. In this case, however, the coordinate axes of this system are rotated with the Earth's precession *and* nutation from J2000.0, to the date used as epoch. Nutation is the short periodic effect of the gravitational attraction of the Moon and, to a lesser extent, other celestial bodies, on the Earth's equatorial bulge (see also Section 39.2.3). The expression 'true' indicates the usage of the true instantaneous Earth equatorial plane and vernal equinox, thus, no averaging of effects takes place.

39.1.5 Earth-fixed reference frame

The Earth-fixed reference frame in use is the IERS terrestrial reference frame (ITRF). The zero longitude ϑ_0 or IERS reference meridian, as well as the IERS reference pole (that define the ITRF), are maintained by the

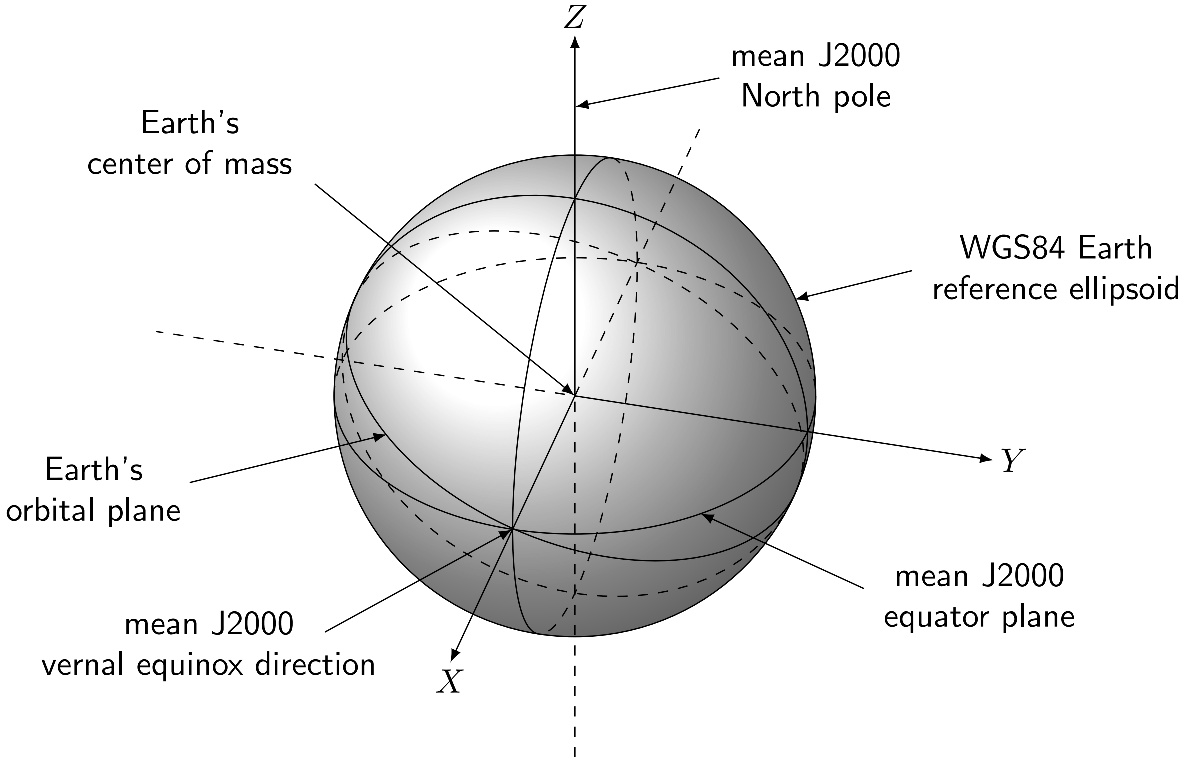

Figure 24: Definition of the inertial reference frame.

International Earth Rotation and Reference Systems Service (IERS), and are based on a large number of observing stations. This coordinate system is connected to, and rotates with the Earth, so velocities expressed in this coordinate system include the rotation of the Earth. Furthermore it is also connected to the WGS84 Earth reference ellipsoid. Precession, nutation, rotation about the pole, as well as the polar motion, are all taken into account (see also Section 39.2.3). The axes are defined as follows:

- The origin is the center of mass of the Earth (i.e., the center of the WGS84 Earth reference ellipsoid).
- The positive Z-axis goes out the north pole (i.e., the semi-minor axis of the WGS84 Earth reference ellipsoid).
- The X-Y plane is the equatorial plane (i.e., the plane spanned by the rotated semi-major axis in the WGS84 Earth reference ellipsoid).
- The X-axis is along the prime meridian (Greenwich; zero point of longitude ϑ_0).
- The Y-axis is then set to make the system right-handed. This results in the axis pointing through the Indian Ocean.

This definition is depicted in Figure 25, in which also the longitude ϑ and geocentric latitude δ' angles are indicated. Note that the WGS84 coordinate system as defined in [13] is *not* used, as it depends on the IERS reference meridian at epoch 1984, which is outdated.

39.1.6 Topocentric reference frame

The topocentric reference frame is attached to the Earth's surface. For the topocentric reference frame:

- The origin is defined by any longitude ϑ and latitude δ in the Earth-fixed reference frame, on the surface of the WGS84 Earth reference ellipsoid.
- The Z-axis coincides with the normal vector to the Earth reference ellipsoid, positive towards zenith (away from the Earth).

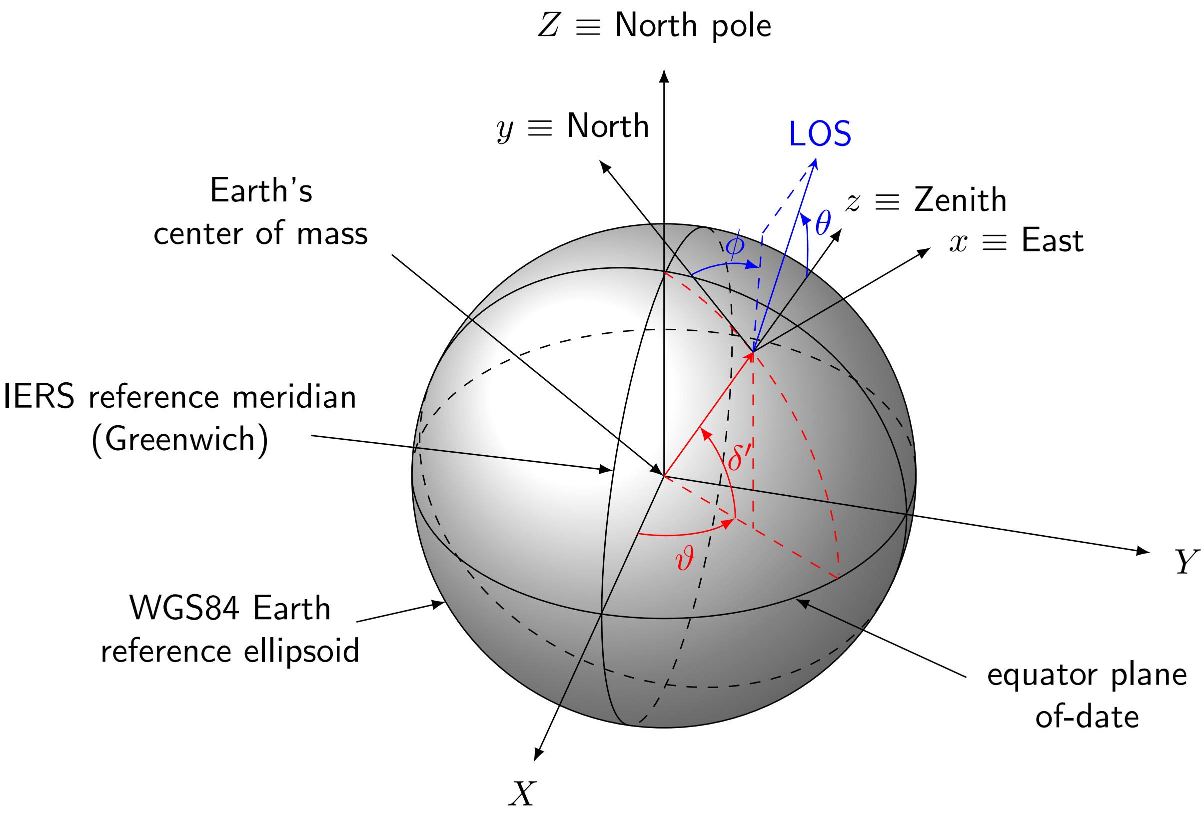

Figure 25: Definition of the Earth-fixed reference frame (ITRF) indicated by (X,Y,Z), including its longitude ϑ and geocentric latitude δ' angles, as well as the topocentric reference frame indicated by (x,y,z), with its topocentric azimuth ϕ and zenith θ angles.

- The X-Y plane is the plane orthogonal to the Z-axis, and thus tangent to the Earth reference ellipsoid.
- The X-axis points towards east.
- The Y-axis points towards north.

This is shown in Figure 25, in which also the topocentric azimuth ϕ and zenith θ angles, that define a direction vector in this frame, are indicated.

39.1.7 Local orbital reference frame

The position of the local orbital reference frame is defined by the position of the spacecraft, while the orientation is independent of the attitude of the spacecraft:

- The origin of the local orbital reference frame (T,R,L) is the satellite in-flight center of mass.
- The L-axis points in the direction opposite to the Earth's center.
- The R-axis is perpendicular to the L-axis and in the vertical plane containing V such that $\cos(\mathbf{V},\hat{\mathbf{r}}) > 0$, where $\mathbf{V}$ is the absolute velocity vector and $\hat{\mathbf{r}}$ is the unit vector in the direction of the R-axis.
- The T-axis completes the right-handed frame, $(\hat{\mathbf{t}} = \hat{\mathbf{r}} \times \hat{\mathbf{l}})$.

39.1.8 Local relative orbital reference frame

The local relative orbital reference frame (T_1,R_1,L_1) has a similar definition as the local orbital reference frame except for local normal pointing, i.e. the unit vector L_1 is parallel to the local normal of the WGS84 Earth reference ellipsoid, directed upward and crossing the spacecraft in-flight center of mass and the unit vector

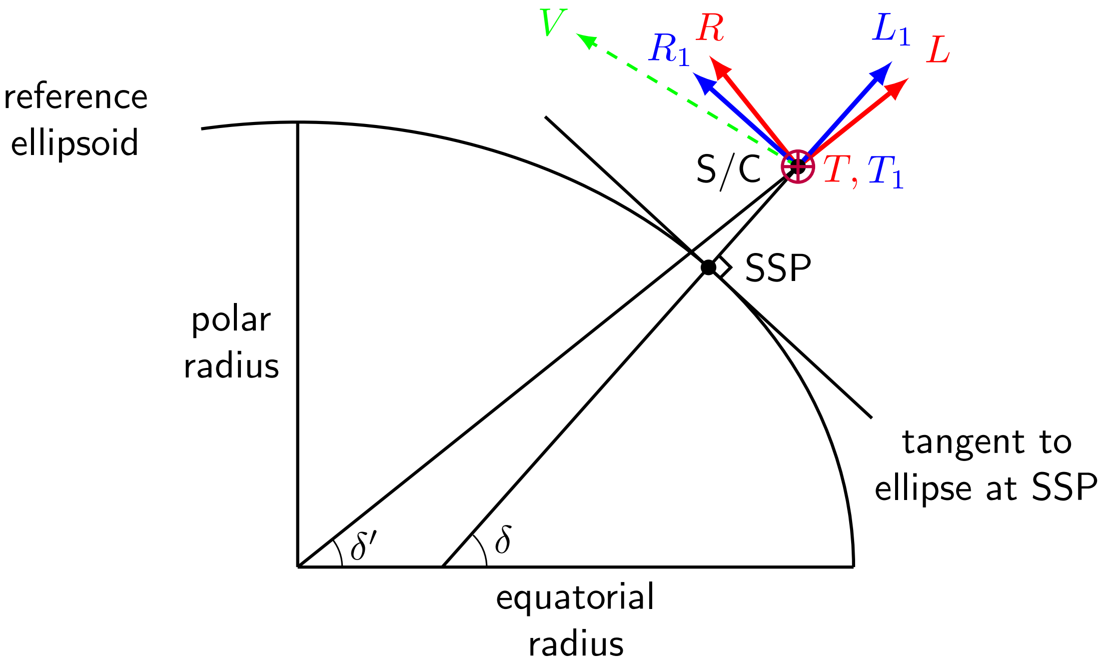

Figure 26: Local orbital reference frame (red) versus local relative orbital reference frame (blue) definition. The velocity vector V (green) is in the same plane as the R-L plane.

R_1 is in the plane containing the velocity vector in the Earth-fixed frame. This attitude is also known as local normal pointing (LNP).
The definitions of, and the relation between, the local orbital reference frame and local relative orbital reference frame are visualized in Figure 26.

39.1.9 Spacecraft reference frame and LOS angles

The spacecraft reference frame is defined with respect to the instrument hardware, i.e. it is “attached” to the spacecraft. The orientation (attitude) of this frame is measured with respect to the inertial reference frame. Furthermore, in this frame the LOS angles azimuth and elevation are defined, see Figure 27. These LOS angles were determined during calibration with respect to alignment cubes and were converted to the SRF.

The spacecraft reference frame holds a constant in-flight approximate orientation with respect to the inertial reference frame. It tries to control its attitude within certain boundary angles to align with the LNP attitude, which is exactly opposite to the local relative orbital reference frame, the coordinates of the latter being in a different order: (X_S, Y_S, Z_S) versus (R, T, L). This is defined as the Z_S axis pointing towards the center of the Earth, while the X_S axis is perpendicular to the Z_S, in the orbital plane and opposite to the velocity vector V. The Y_S then completes the orthogonal set pointing normal to the orbital plane.

This alignment only holds true when the spacecraft has the ideal LNP attitude, which never occurs exactly in practice, but is the goal of the attitude control subsystem; in practice the attitude of the spacecraft is misaligned with the local relative orbital reference frame within certain maximum allowed angles.

The in-flight attitude of the spacecraft reference frame with respect to the inertial reference frame is constantly measured at certain time instances by the on-board attitude control and determination subsystem, and defined in unit quaternions $\mathbf{q} = [q_0, q_1, q_2, q_3]$. The attitude determination system makes images in three orthogonal directions using a relatively small field-of-view and compares these to a nearly constant map of the star sky. This is used to determine the orientation of the spacecraft.

The definition of the LOS angles is as follows:

- The LOS elevation angle is defined as the counterclockwise rotation about the SRF Y-axis from the Z-axis in the direction of the X-axis of the projection onto the YZ-plane.
- The LOS azimuth angle is defined as the clockwise rotation about the SRF X-axis from the Z-axis in the direction of the Y-axis of the projection onto the XZ-plane.

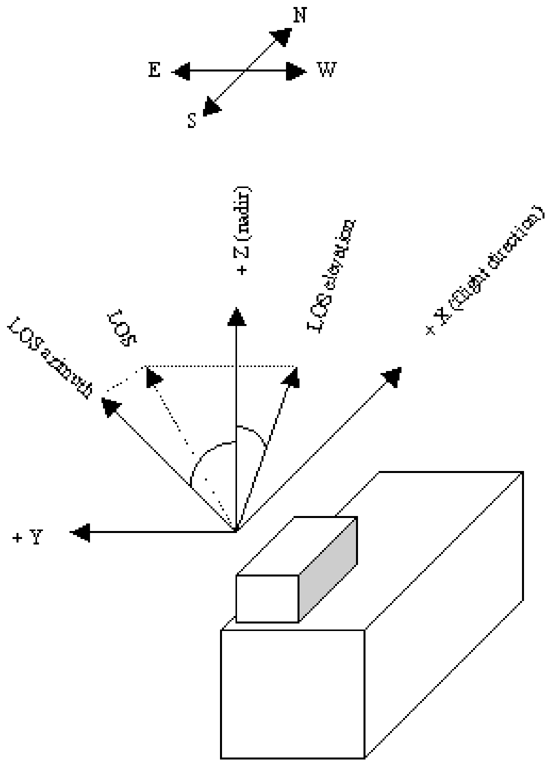

Figure 27: Definition of the LOS azimuth and elevation angles in the spacecraft reference frame. The spacecraft reference frame itself is defined with respect to the hardware.

In this way, when changing the angle approximately in swath direction, the azimuth angle varies from 0 towards the positive and negative numbers. When changing the angle approximately in velocity direction, the elevation varies from 0 towards the positive and negative numbers (up to about -8 or +8 degrees to span the field of view accounting for the spatial smile effect).

39.1.10 Optical alignment reference frame

For irradiance measurements, the Solar azimuth and elevation angles are defined in the Optical alignment reference frame. This reference frame is nearly identical to the SRF. The rotation matrix from the SRF to the OARF is determined during calibration measurements. The Solar direction angles are define as follows:

- The Solar azimuth angle is defined as the counterclockwise rotation about the OARF Z-axis from the X-axis in the direction of the Y-axis of the projection onto the XZ-plane.
- The Solar elevation angle is defined as the rotation of the projection onto the YZ-plane from the YZ-plane in the direction of the Z-axis.

39.1.11 Fundamental reference frame

For solar eclipse geometry purposes, the eclipse shadow axis is defined as the line between the center of the Sun and the center of the Moon. The fundamental reference frame relates to this axis, and is defined as follows:

- The origin is located at the center of the Earth.
- The Z-axis is parallel to the eclipse shadow axis, positive towards the Moon.
- The X-axis passes through the Earth's equator and is positive toward the East.
- The Y-axis complements the orthogonal right-handed reference frame and is positive towards the North.

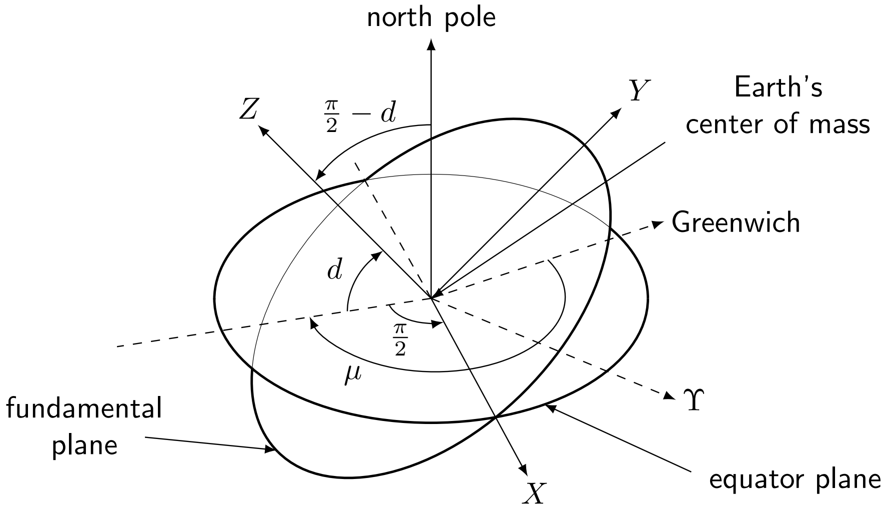

Figure 28: Solar eclipse fundamental reference frame definition. The geocentric equatorial declination angle d and the Greenwich Hour Angle μ of the Z-axis of the fundamental reference frame, describe the orientation of the frame with respect to the Earth-fixed reference frame. Greenwich here lies in the direction of the Greenwich reference meridian on the Equator plane.

- The XY-plane is called the fundamental plane.

The definition is illustrated in Figure 28. The reference frame is chosen in this way, such that the eclipse penumbral, umbral and/or antumbral shadows are always defined by two concentric circles in the fundamental frame, about the shadow's axis.

39.2 Reference frame transformations

To convert coordinates (that can for instance be based on positions or line-of-sight unit vectors) between the reference frames defined in Section 39.1, reference frame transformations are needed. These are based on a rotation matrix, where one definition of a reference frame is rotated with respect to another, and a translation vector, where the origin of one frame has a fixed offset to the other. Following up on this section, are the description of the geometrical algorithms, which refer back to parts of this section in their calculation steps.

39.2.1 Spacecraft reference frame to inertial reference frame

For the transformation of a point in the spacecraft reference frame to the inertial reference frame the attitude measurement of the on-board attitude control and determination subsystem is used, which is defined as a unit quaternion from the inertial reference frame to the spacecraft reference frame

$$\mathbf{q} = \begin{bmatrix} q_x \\ q_y \\ q_z \\ q_s \end{bmatrix} , \tag{65}$$

with which the passive right-handed rotation matrix from the inertial reference frame (IRF) to the spacecraft reference frame (SRF) is defined as

$$\mathbf{R}_{\mathrm{IRF}\to\mathrm{SRF}} = \begin{bmatrix} 1-2(q_y^2+q_z^2) & 2(q_xq_y+q_zq_s) & 2(q_xq_z-q_yq_s) \\ 2(q_xq_y-q_zq_s) & 1-2(q_x^2+q_z^2) & 2(q_yq_z+q_xq_s) \\ 2(q_xq_z+q_xq_s) & 2(q_yq_z-q_xq_s) & 1-2(q_x^2+q_y^2) \end{bmatrix} . \tag{66}$$

Using this matrix the transformation of a point $\mathbf{q}$ between the spacecraft reference frame and the inertial reference frame is obtained by evaluating

$$\mathbf{R}_{\mathrm{IRF}\to\mathrm{SRF}}(\mathbf{q}_{\mathrm{IRF}} - \mathbf{p}_{\mathrm{IRF}}) = \mathbf{q}_{\mathrm{SRF}} \;, \tag{67a}$$

$$\mathbf{q}_{\mathrm{IRF}} = (\mathbf{R}_{\mathrm{IRF}\to\mathrm{SRF}})^{-1}\mathbf{q}_{\mathrm{SRF}} + \mathbf{p}_{\mathrm{IRF}} = (\mathbf{R}_{\mathrm{IRF}\to\mathrm{SRF}})^{\mathrm{T}}\mathbf{q}_{\mathrm{SRF}} + \mathbf{p}_{\mathrm{IRF}} \;, \tag{67b}$$

as the rotation matrix is orthogonal and thus its inverse is equal to its transpose, and in which $\mathbf{p}_{\mathrm{IRF}}$ is the position of the spacecraft in the inertial reference frame to account for translation of the origin of the reference frame to the center of mass of the spacecraft.

To determine the intersection of a unit direction LOS vector extending from the known location of the spacecraft (reference frame) with the Earth reference ellipsoid in the Earth-fixed reference frame, only the rotation has to be applied. The equation for the LOS (and for direction vectors in general) therefore simplifies to

$$\hat{\mathbf{q}}_{\mathrm{IRF}} = (\mathbf{R}_{\mathrm{IRF}\to\mathrm{SRF}})^{\mathrm{T}}\hat{\mathbf{q}}_{\mathrm{SRF}} \;. \tag{68}$$

39.2.2 Aberration of Light

Due to the finite speed of light and the motion of the spacecraft (reference frame) with respect to the Earth(-fixed reference frame), an apparent motion of the point observed on Earth occurs. This astrophysical phenomenon is called the aberration of light, and the deviation in LOS angle depends only on the transverse velocity of the spacecraft, with respect to the LOS. As the spacecraft moves with a large velocity with respect to the Earth relative to the speed of light (approx. 7.44/300000 km/s), this effect can amount up to 50 meters at the edge of swath, where the distance to the ground pixel is largest, while the velocity of the spacecraft is approximately orthogonal to the LOS.

This effect is corrected for as follows, and can be configured to be set on or off. When the LOS vector in the spacecraft reference frame $\mathbf{q}_{\mathrm{SRF}}$ is rotated to the inertial reference frame $\mathbf{q}_{\mathrm{IRF}}$ (hereafter denoted simply as $\mathbf{q} = (x,y,z)$), the vector is first normalized as

$$\hat{\mathbf{q}} = \frac{\mathbf{q}}{||\mathbf{q}||} = \frac{x}{||\mathbf{q}||}\hat{\mathbf{x}} + \frac{y}{||\mathbf{q}||}\hat{\mathbf{y}} + \frac{z}{||\mathbf{q}||}\hat{\mathbf{z}} \;, \tag{69}$$

in which $||\mathbf{q}||$ denotes the length of the vector $\mathbf{q}$ defined as

$$||\mathbf{q}|| = \sqrt{x^2 + y^2 + z^2} \;. \tag{70}$$

The velocity of the spacecraft in the inertial reference frame $\mathbf{v}$ relative to the speed of light c is subtracted from this normalized vector as

$$[\hat{\mathbf{q}}]_{\mathrm{abb}} = \hat{\mathbf{q}} - \frac{\mathbf{v}}{c} \;, \tag{71}$$

which is normalized again as

$$\hat{\mathbf{q}}_{\mathrm{abb}} = \frac{[\hat{\mathbf{q}}]_{\mathrm{abb}}}{||[\hat{\mathbf{q}}]_{\mathrm{abb}}||} \;, \tag{72}$$

and then scaled back to the original length as

$$\mathbf{q}_{\mathrm{abb}} = ||\mathbf{q}||\,\hat{\mathbf{q}}_{\mathrm{abb}} \;. \tag{73}$$

This resulting vector that is corrected for aberration of light can now be translated in the inertial reference frame, if needed. When the input vector in the spacecraft reference frame is already a unit vector, Equations (69) and (73) can be skipped.

A similar effect, called light-time, which occurs due to the rotation of the Earth during the time the light has travelled from the Earth to the spacecraft, amounts to a maximum of about 3 meters at the edge of swath, and is ignored here.

39.2.3 Inertial reference frame to Earth-fixed reference frame

The transformation of either a position or velocity vector from the inertial to the Earth-fixed reference frame, are described separately.

39.2.3.1 Position transformation The transformation between the inertial reference frame and the Earth-fixed reference frame, is rigorously documented in [14] (Chapter 5). However, in this reference document, the reference frames are called geocentric celestial reference system (GCRS) and international terrestrial reference system (ITRS), respectively.

The transformation is performed by multiplying the Cartesian coordinates in the inertial reference frame (IRF) with three rotation matrices, to obtain the coordinates in the Earth-fixed reference frame:

$$\begin{bmatrix} x \\ y \\ z \end{bmatrix}_{\mathrm{EFRF}} = \mathbf{W}(t)\mathbf{R}(t)\mathbf{Q}(t) \begin{bmatrix} x \\ y \\ z \end{bmatrix}_{\mathrm{IRF}} . \tag{74}$$

Here, $\mathbf{Q}(t)$, $\mathbf{R}(t)$ and $\mathbf{W}(t)$ are three transformation matrices, which are functions of TT and UT1 in JD, and are described below.

$\mathbf{Q}(t)$ arises from the motion of the celestial pole in the inertial reference frame. This motion consists of two superimposed motions, called precession and nutation. These are both shown schematically in Figure 29. Precession is a circular motion of the polar axis with an angular radius of about 23.4°, centered on the ecliptic North pole and directed West. Nutation is a relatively small sinusoidal motion superposed on precession. Both are mainly caused by the gravitational attraction of the Sun and the Moon, the gravitational effect of their changing relative positions, the excess of mass at the Earth's equator and, to a lesser extent, by other celestial bodies.

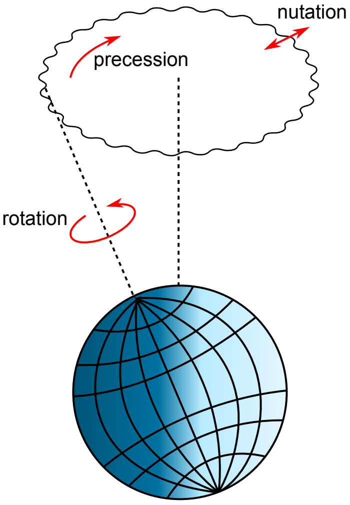

Figure 29: Schematic of two motions of the Earth's polar axis, precession and nutation, and the rotation about this axis.

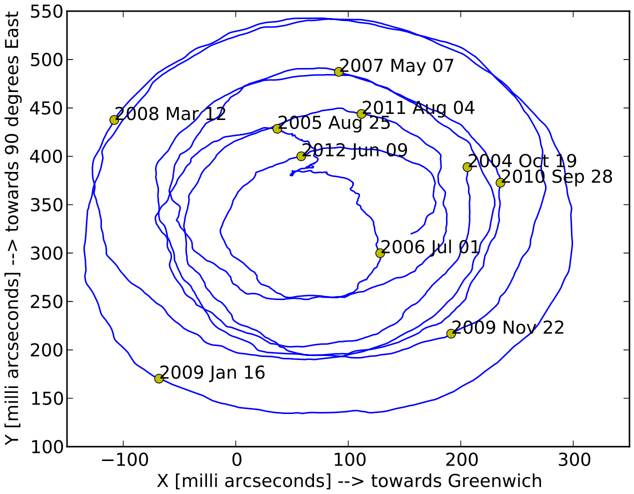

Figure 30: Plot of the polar coordinate x_p versus y_p.

$\mathbf{R}(t)$ arises from the rotation of the Earth around the axis associated with the pole. The Earth rotates about its polar axis to the East, with a nominal angular velocity in inertial space of about $7.292 \cdot 10^{-5}$ rad/s, as indicated in Figure 29. The Earth rotates once in about 24 hours from the point of view of the Sun and once every 23 hours, 56 minutes and 4 seconds from the point of view of the stars. The Earth's rotation is slowing slightly with time. This is due to the tidal effects of the Moon on the Earth's rotation. Atomic clocks show that a modern day is longer by about 17 milliseconds than a century ago, slowly increasing the rate at which UTC is adjusted by leap seconds.

Finally, $\mathbf{W}(t)$ arises from polar motion. The polar motion of the Earth is the movement of the Earth's rotational axis across its surface, and is measured with respect to the Earth-fixed Reference Frame. The variation here is only a few meters. It consists of two quasi-periodic components and a gradual drift. This gradual drift is defined as the movement of the Earth's instantaneous rotational axis or North pole, from the CIO (Conventional International Origin), mostly in the direction of the 80th meridian west. The CIO is a conventionally agreed reference axis, defined as the pole's average location over the year 1900. The two periodic parts describe an almost circular motion called Chandler wobble, with a period of about 435 days, and a yearly circular motion, including a small drift. These motions are illustrated in Figure 30.

The transformation expressed by Equation (74) can be performed in two ways, as described in [14]. The classical procedure realizes a “true equinox and equator of date system” at date t, that uses the Celestial Intermediate Pole (CIP) as its Z-axis and the equinox as its X-axis. It uses apparent Greenwich Sidereal Time (GST) in the transformation matrix $\mathbf{R}(t)$ and the classical precession and nutation parameters in the transformation matrix $\mathbf{Q}(t)$. The newer method realizes a “Celestial Intermediate Reference System” (CIRS) at date t. The CIRS uses the CIP as its Z-axis and the CIO as its X-axis. The “Earth Rotation Angle” is used in the transformation matrix $\mathbf{R}(t)$, and the two coordinates of the Celestial Intermediate Pole (CIP) in the GCRS in the transformation matrix $\mathbf{Q}(t)$. However, the last step, multiplying with the rotation matrix $\mathbf{W}(t)$ for polar motion, which transforms from the terrestrial intermediate reference system (TIRS) to the ITRS, is the same for both methods. The exact details of these implementations can be found in [14].

The required input is: the time instance for which the transformation matrix is needed, as Terrestrial Time (TT) and Universal Time (UT1), expressed in Julian Days, and the polar coordinates x_p and y_p. Monthly bulletin B, which is published by the IERS, contains daily values for these polar coordinates, along with the difference between UTC (which can be converted to TT using Equations (58) and (61)) and UT1. These values can then be interpolated to yield an approximation that holds for the time instance at hand.

The celestial motion of the CIP (precession-nutation), includes all the terms with periods greater than two days in the GCRS, i.e. frequencies between -0.5 cycles per sidereal day (cpsd) and +0.5 cpsd. The terrestrial motion of the CIP (polar motion), includes all the terms outside the retrograde diurnal band in the ITRS i.e. frequencies lower than -1.5 cpsd or greater than -0.5 cpsd.

39.2.3.2 Velocity transformation Differentiating the equation for the transformation of a position vector from the inertial to the Earth-fixed reference frame, yields

$$\frac{d\mathbf{p}_\mathrm{EFRF}}{dt} = \frac{d[\mathbf{W}(t)\mathbf{R}(t)\mathbf{Q}(t)]}{dt}\mathbf{p}_\mathrm{IRF} + [\mathbf{W}(t)\mathbf{R}(t)\mathbf{Q}(t)]\frac{d\mathbf{p}_\mathrm{IRF}}{dt} \; . \tag{75}$$

However, employing the conversion method involving the CIRS and TIRS using the CIO, this can be approximated stepwise as

$$\frac{d\mathbf{p}_\mathrm{CIRS}}{dt} = \mathbf{Q}(t)\frac{d\mathbf{p}_\mathrm{IRF}}{dt} \tag{76}$$

$$\frac{d\mathbf{p}_\mathrm{TIRS}}{dt} = \mathbf{R}(t)\frac{d\mathbf{p}_\mathrm{CIRS}}{dt} + \frac{d\mathbf{R}(t)}{dt}\mathbf{p}_\mathrm{CIRS} \tag{77}$$

$$\frac{d\mathbf{p}_\mathrm{EFRF}}{dt} = \mathbf{W}(t)\frac{d\mathbf{p}_\mathrm{TIRS}}{dt} \; , \tag{78}$$

in which the time rate of change of $\mathbf{W}(t)$ and $\mathbf{Q}(t)$ are assumed to be negligably small. For an analogous derivation using the classical method involving precession/nutation and GST, see the Appendix of [15].
This results in

$$\frac{d\mathbf{p}_\mathrm{EFRF}}{dt} = \mathbf{W}(t)\left[\mathbf{R}(t)\mathbf{Q}(t)\frac{d\mathbf{p}_\mathrm{IRF}}{dt} + \frac{d\mathbf{R}(t)}{dt}\mathbf{Q}(t)\mathbf{p}_\mathrm{IRF}\right] \; , \tag{79}$$

in which the rotation about the CIP is defined as

$$\mathbf{R}(t) = \begin{bmatrix} +\sin\theta & +\cos\theta & 0 \\ -\cos\theta & +\sin\theta & 0 \\ 0 & 0 & 1 \end{bmatrix} \; , \tag{80}$$

in which θ is the Earth Rotation Angle (ERA).
The time rate of change of this rotation matrix is evaluated as

$$\frac{d\mathbf{R}(t)}{dt} = \begin{bmatrix} -\dot{\theta}\sin\theta & +\dot{\theta}\cos\theta & 0 \\ -\dot{\theta}\cos\theta & -\dot{\theta}\sin\theta & 0 \\ 0 & 0 & 0 \end{bmatrix} \; , \tag{81}$$

in which the rate of advance of ERA is given in [14] as

$$\dot{\theta} = 1.00273781191135448 \quad \mathrm{rev/day_{UT1}} \; , \tag{82}$$

which can be converted as

$$\dot{\theta} = \frac{1.00273781191135448 * 2 * \pi}{86400 + \mathrm{LOD}} \quad \mathrm{rad/s} \ , \tag{83}$$

in which The Length of Day (LOD) is the difference between a day as measured by UT1 and a 86400 seconds SI day, which is supplied in the IERS Bulletin B file.

39.2.4 Geocentric to geodetic coordinates

As follows from Figures 23 and 25, the conversion from geocentric (c) spherical to geocentric (c) Cartesian coordinates is given by

$$\begin{bmatrix} x \\ y \\ z \end{bmatrix}_{\mathrm{c}} = r \begin{bmatrix} \cos\delta' \cos\vartheta \\ \cos\delta' \sin\vartheta \\ \sin\delta' \end{bmatrix}_{\mathrm{c}} , \tag{84}$$

while conversion from geodetic (d) to geocentric (c) Cartesian coordinates is given by

$$\begin{bmatrix} x \\ y \\ z \end{bmatrix}_{\mathrm{c}} = \begin{bmatrix} (N_\delta + h)\cos\delta\cos\vartheta \\ (N_\delta + h)\cos\delta\sin\vartheta \\ ((1-e^2)N_\delta + h)\sin\delta \end{bmatrix}_{\mathrm{d}} , \tag{85}$$

where e is the eccentricity of the ellipsoid

$$e \equiv \frac{\sqrt{a^2 - b^2}}{a} = \sqrt{2f - f^2} \tag{86}$$

and N_δ is the ellipsoidal radius of curvature in the meridian, given by

$$N_\delta \equiv \frac{a}{\sqrt{1 - e^2 \sin^2\delta}} \ . \tag{87}$$

Conversion from geocentric Cartesian to geocentric spherical coordinates is given by

$$\begin{bmatrix} \delta' \\ \vartheta \\ r \end{bmatrix}_{\mathrm{c}} = \begin{bmatrix} \arctan\left(\frac{z}{\sqrt{x^2+y^2}}\right) \\ \arctan 2(y,x) \\ \sqrt{x^2 + y^2 + z^2} \end{bmatrix}_{\mathrm{c}} , \tag{88}$$

where $\delta' = \arcsin(z/r)$ can also be used, and $\arctan 2$ ensures ϑ is evaluated as $-\pi < \vartheta \leq \pi$.

However, a solution for the conversion from geocentric Cartesian to geodetic coordinates is not that simple, as has been documented in many references. The conversion is performed here with the fastest available method up to date, as described in [16]. With this method the WGS84 Earth reference ellipsoid is set as the reference ellipsoid for which the conversion is performed.

39.2.5 Earth-fixed reference frame to topocentric reference frame

The rotation matrix from the geocentric Cartesian coordinates in the Earth-fixed reference frame to the topocentric reference frame depends only on the longitude ϑ and geodetic latitude δ, and is derived as

$$\mathbf{R}_{\mathrm{EFRF}\rightarrow\mathrm{TRF}} = \begin{bmatrix} -\sin\vartheta & \cos\vartheta & 0 \\ -\sin\delta\cos\vartheta & -\sin\delta\sin\vartheta & \cos\delta \\ \cos\delta\cos\vartheta & \cos\delta\sin\vartheta & \sin\delta \end{bmatrix} . \tag{89}$$

And so a transformation of a point $\mathbf{q}$ is performed as

$$\mathbf{q}_{\mathrm{TRF}} = \mathbf{R}_{\mathrm{EFRF}\rightarrow\mathrm{TRF}}(\mathbf{q}_{\mathrm{EFRF}} - \mathbf{r}_{\mathrm{EFRF}}) \ , \tag{90}$$

in which $\mathbf{r}_{\mathrm{EFRF}}$ is the radius vector of the origin of the topocentric reference frame, which is obtained by using $h = 0$ in Equation (85), to account for the translation of the origin of this frame.

39.2.6 Inertial reference frame to local orbital reference frame

Since the local orbital reference frame is defined by the position $\mathbf{p} = [x, y, z]$ and velocity $\mathbf{v} = [\dot{x}, \dot{y}, \dot{z}]$ of the spacecraft in the inertial reference frame, the rotation matrix from the inertial reference frame (X,Y,Z), with unit vectors $(\hat{\mathbf{x}}, \hat{\mathbf{y}}, \hat{\mathbf{z}})$, to the local orbital reference frame (T,R,L), with unit vectors $(\hat{\mathbf{t}}, \hat{\mathbf{r}}, \hat{\mathbf{l}})$, can be based upon this state-vector only. To this end the provided state-vector by flight operations in the inertial reference frame is used. Following the definition of the local orbital reference frame from Section 39.1.7, the position vector $\mathbf{p}$ points in the direction of the L-axis, and thus the unit vector $\hat{\mathbf{l}}$ of that axis is obtained by normalizing $\mathbf{p}$

$$\hat{\mathbf{l}} = \hat{\mathbf{p}} = \frac{\mathbf{p}}{||\mathbf{p}||} = \frac{x}{||\mathbf{p}||}\hat{\mathbf{x}} + \frac{y}{||\mathbf{p}||}\hat{\mathbf{y}} + \frac{z}{||\mathbf{p}||}\hat{\mathbf{z}} \,, \tag{91}$$

in which $||\mathbf{p}||$ denotes the length of the vector $\mathbf{p}$ defined as

$$||\mathbf{p}|| = \sqrt{x^2 + y^2 + z^2} \,. \tag{92}$$

Then, since the velocity vector $\mathbf{v}$ does lie in the orbital plane but is not necessarily directed along the R-axis, the component of $\mathbf{v}$ in the direction of $\hat{\mathbf{l}}$ is first determined by using the geometrical inner product rule, and using $||\hat{\mathbf{l}}|| = 1$, as

$$v_{\hat{\mathbf{l}}} = \frac{(\mathbf{v}, \hat{\mathbf{l}})}{||\hat{\mathbf{l}}||} = \mathbf{v}^{\mathrm{T}}\hat{\mathbf{l}} = \frac{x\dot{x}}{||\mathbf{p}||} + \frac{y\dot{y}}{||\mathbf{p}||} + \frac{z\dot{z}}{||\mathbf{p}||} \,, \tag{93}$$

which is subtracted from $\mathbf{v}$ to yield the component of $\mathbf{v}$ in the direction of $\hat{\mathbf{r}}$ as

$$\mathbf{v}_{\hat{\mathbf{r}}} = \mathbf{v} - \mathbf{v}_{\hat{\mathbf{l}}} = \mathbf{v} - v_{\hat{\mathbf{l}}}\hat{\mathbf{l}} \,, \tag{94}$$

which is normalized to yield the unit vector $\hat{\mathbf{r}}$ of the R-axis as

$$\hat{\mathbf{r}} = \frac{\mathbf{v}_{\hat{\mathbf{r}}}}{||\mathbf{v}_{\hat{\mathbf{r}}}||} \,. \tag{95}$$

Then, the unit vector $\hat{\mathbf{t}}$ of the T-axis is derived by taking the cross product of $\hat{\mathbf{r}}$ and $\hat{\mathbf{l}}$

$$\hat{\mathbf{t}} = \hat{\mathbf{r}} \times \hat{\mathbf{l}} \,. \tag{96}$$

Equation (91) is used for $\hat{\mathbf{l}}$. Equation (93) is substituted in Equation (94), and the result in Equation (95) to get an expression for $\hat{\mathbf{r}}$. Then, the resulting expressions for $\hat{\mathbf{l}}$ and $\hat{\mathbf{r}}$ are substituted in Equation (96) to yield equations for the unit vectors which we denote now in the form

$$\hat{\mathbf{t}} = \hat{t}_{\hat{\mathbf{x}}}\hat{\mathbf{x}} + \hat{t}_{\hat{\mathbf{y}}}\hat{\mathbf{y}} + \hat{t}_{\hat{\mathbf{z}}}\hat{\mathbf{z}} \,, \tag{97a}$$

$$\hat{\mathbf{r}} = \hat{r}_{\hat{\mathbf{x}}}\hat{\mathbf{x}} + \hat{r}_{\hat{\mathbf{y}}}\hat{\mathbf{y}} + \hat{r}_{\hat{\mathbf{z}}}\hat{\mathbf{z}} \,, \tag{97b}$$

$$\hat{\mathbf{l}} = \hat{l}_{\hat{\mathbf{x}}}\hat{\mathbf{x}} + \hat{l}_{\hat{\mathbf{y}}}\hat{\mathbf{y}} + \hat{l}_{\hat{\mathbf{z}}}\hat{\mathbf{z}} \,, \tag{97c}$$

in which the components are all evaluated as functions of (x, y, z) and $(\dot{x}, \dot{y}, \dot{z})$. These components are then inserted in the rotation matrix $\mathbf{R}_{\mathrm{IRF}\rightarrow\mathrm{LORF}}$ as

$$\mathbf{R}_{\mathrm{IRF}\rightarrow\mathrm{LORF}} = \begin{bmatrix} \hat{\mathbf{t}}^{\mathrm{T}} \\ \hat{\mathbf{r}}^{\mathrm{T}} \\ \hat{\mathbf{l}}^{\mathrm{T}} \end{bmatrix} = \begin{bmatrix} \hat{t}_{\hat{\mathbf{x}}} & \hat{t}_{\hat{\mathbf{y}}} & \hat{t}_{\hat{\mathbf{z}}} \\ \hat{r}_{\hat{\mathbf{x}}} & \hat{r}_{\hat{\mathbf{y}}} & \hat{r}_{\hat{\mathbf{z}}} \\ \hat{l}_{\hat{\mathbf{x}}} & \hat{l}_{\hat{\mathbf{y}}} & \hat{l}_{\hat{\mathbf{z}}} \end{bmatrix} \,, \tag{98}$$

which is used to transform any point $\mathbf{q}$ in the inertial reference frame to a point in the local orbital reference frame as

$$\mathbf{q}_{\mathrm{LORF}} = \mathbf{R}_{\mathrm{IRF}\rightarrow\mathrm{LORF}}(\mathbf{q}_{\mathrm{IRF}} - \mathbf{p}_{\mathrm{IRF}}) \,, \tag{99}$$

in which also the translation of the origin of the reference frame to the center of mass of the spacecraft is included.

39.2.7 Spacecraft reference frame to Optical Alignment reference frame

The transformation from the spacecraft reference frame (Section 39.1.9) to the Optical Alignment reference frame (Section 39.1.10) is needed to determine the LOS from the spacecraft towards the Sun with respect to the Sun port. As the dimensions of the spacecraft are negligible with respect to the distance towards the Sun, translations are neglected here, and so only a rotation is needed for the transformation. The rotation matrix from the spacecraft reference frame to the Optical Alignment reference frame is determined during calibration to be

$$\mathbf{R}_{\mathrm{SRF}\rightarrow\mathrm{OARF}} = \begin{bmatrix} +0.999999821000 & -0.000279920991 & +0.000479443988 \\ +0.000279520988 & +0.999999642000 & +0.000834749022 \\ -0.000479676994 & -0.000834615028 & +0.999999523000 \end{bmatrix} , \tag{100}$$

The transformation of a point $\mathbf{q} = [x, y, z]$ from the spacecraft reference frame to the Optical Alignment reference frame can then be evaluated as

$$\begin{bmatrix} x \\ y \\ z \end{bmatrix}_{\mathbf{q}_{\mathrm{OARF}}} = \mathbf{R}_{\mathrm{SRF}\rightarrow\mathrm{OARF}} \begin{bmatrix} x \\ y \\ z \end{bmatrix}_{\mathbf{q}_{\mathrm{SRF}}} . \tag{101}$$

39.2.8 Earth-fixed reference frame to Fundamental reference frame

The rotation from the geocentric Cartesian coordinates in the Earth-fixed reference frame to the (solar eclipse) fundamental reference frame (see Section 39.1.11) depends only on the Greenwich Hour Angle μ and the geocentric equatorial declination angle d of the Z-axis of the Fundamental reference frame, and is given in [17] as

$$\rho_{\mathrm{F}} = \mathbf{R}_1\left(\frac{\pi}{2} - d\right)\mathbf{R}_3\left(-\left(\mu - \frac{\pi}{2}\right)\right)\rho_{\mathrm{G}} \tag{102}$$

from which the following rotation matrix is derived

$$\mathbf{R}_{\mathrm{EFRF}\rightarrow\mathrm{FRF}} = \begin{bmatrix} \sin\mu & \cos\mu & 0 \\ -\sin d\cos\mu & \sin d\sin\mu & \cos d \\ \cos d\cos\mu & -\cos d\sin\mu & \sin d \end{bmatrix} . \tag{103}$$

And so a transformation of a point $\mathbf{q}$ is performed as

$$\mathbf{q}_{\mathrm{FRF}} = \mathbf{R}_{\mathrm{EFRF}\rightarrow\mathrm{FRF}}\mathbf{q}_{\mathrm{EFRF}} , \tag{104}$$

as the origins of both frames coincide.

39.3 Intersection between a line and an ellipsoid

Now follows an analysis on the intersection points of any line in 3-dimensional space and an ellipsoid that is attached to a reference frame. The equation of an ellipsoid centered at the origin of an Cartesian orthogonal coordinate system (X,Y,Z), and with axis extents (e_x, e_y, e_z) in the direction of the (X,Y,Z) axes, respectively, is

$$\frac{x^2}{e_x^2} + \frac{y^2}{e_y^2} + \frac{z^2}{e_z^2} = 1 . \tag{105}$$

The equation for a point $\mathbf{p}$ on a line in this coordinate system is

$$\mathbf{p} = \mathbf{p}_0 + t\mathbf{v} , \tag{106}$$

or, expanded:

$$\begin{bmatrix} x \\ y \\ z \end{bmatrix} = \begin{bmatrix} x_0 \\ y_0 \\ z_0 \end{bmatrix} + t \begin{bmatrix} \dot{x} \\ \dot{y} \\ \dot{z} \end{bmatrix} , \tag{107}$$

in which $\mathbf{p}_0 = [x_0, y_0, z_0]$ is an initial point and $\mathbf{v} = [\dot{x}, \dot{y}, \dot{z}]$ is a constant (direction) vector. Set up a convenient matrix $\mathbf{M}$ as

$$\mathbf{M} = \begin{bmatrix} e_x^{-2} & 0 & 0 \\ 0 & e_y^{-2} & 0 \\ 0 & 0 & e_z^{-2} \end{bmatrix} , \tag{108}$$

so we can write for the ellipsoid equation

$$\mathbf{p}^{\mathrm{T}}\mathbf{M}\mathbf{p} = 1 . \tag{109}$$

Substituting the equation for the line yields a quadratic equation

$$(\mathbf{p}_0 + t\mathbf{v})^{\mathrm{T}}\mathbf{M}(\mathbf{p}_0 + t\mathbf{v}) = 1 , \tag{110a}$$

$$(\mathbf{v}^{\mathrm{T}}\mathbf{M}\mathbf{v})t^2 + (2\mathbf{p}_0^{\mathrm{T}}\mathbf{M}\mathbf{v})t + (\mathbf{p}_0^{\mathrm{T}}\mathbf{M}\mathbf{p}_0 - 1) = 0 , \tag{110b}$$

that can be solved for two constants t_1 and t_2 with the quadratic formula as

$$t_1, t_2 = \frac{-b \pm \sqrt{b^2 - 4ac}}{2a} , \tag{111}$$

with the coefficients (a, b, c) as

$$a = \mathbf{v}^{\mathrm{T}}\mathbf{M}\mathbf{v} = \frac{\dot{x}^2}{e_x^2} + \frac{\dot{y}^2}{e_y^2} + \frac{\dot{z}^2}{e_z^2} , \tag{112a}$$

$$b = 2\mathbf{p}_0^{\mathrm{T}}\mathbf{M}\mathbf{v} = 2\left(\frac{x_0\dot{x}}{e_x^2} + \frac{y_0\dot{y}}{e_y^2} + \frac{z_0\dot{z}}{e_z^2}\right) , \tag{112b}$$

$$c = \mathbf{p}_0^{\mathrm{T}}\mathbf{M}\mathbf{p}_0 - 1 = \frac{x_0^2}{e_x^2} + \frac{y_0^2}{e_y^2} + \frac{z_0^2}{e_z^2} - 1 . \tag{112c}$$

Now there are three possibilities:

1. When the quadratic equation yields two distinct real roots for t_1, t_2, the line intersects the ellipsoid, and these solutions yield two intersection points.
2. When there is only one real solution, the line is tangent to the ellipsoid, and this solution yields the only 'intersection' point.
3. When there are only complex solutions, the line does not intersect the ellipsoid, and there are no intersection points.

Filling in the value(s) for t in Equation (106) and (107) yields the intersection point(s). For the OMI situation, the LOS extending from the spacecraft will hit the Earth on the front side first. So, the smallest absolute value for t is the intersection we are looking for, as the second intersection, with the largest absolute value for t, occurs at the backside of the Earth, as seen from the spacecraft. Furthermore, using the theory above, intersections also occur for lines extending from the spacecraft in a direction opposite to that of the Earth. The intersection will then happen at negative values for t, as the 3D line will have a direction away from the Earth, but the mathematical description of this line will extent backwards too. One solution for t being positive while the other is negative is not possible here, as the spacecraft would have to reside within the Earth! So, the way to go about this intersection determining for OMI is as follows:

- When possibility #3 occurs (i.e. the determinant $D = b^2 - 4ac < 0$), the LOS misses the Earth.
- When possibility #1 occurs (i.e. the determinant $D = b^2 - 4ac > 0$), and both solutions for t are negative, the LOS misses the Earth.
- When possibility #1 occurs (i.e. the determinant $D = b^2 - 4ac > 0$), and both solutions for t are positive, only the smallest solutions for t is used as the intersection of the LOS with the Earth.
- When possibility #2 occurs (i.e. the determinant $D = b^2 - 4ac = 0$), and the only solutions for t is negative, the LOS misses the Earth.
- When possibility #2 occurs (i.e. the determinant $D = b^2 - 4ac = 0$), and the only solutions for t is positive, this solution is used as the 'intersection' of the LOS with the Earth.

40 Geometrical algorithms

The main goal of the geometrical algorithms is to correlate each detector or image row r to the latitude δ and longitude ϑ of the corresponding ground pixel. Or in other words, to determine from which location of the Earth's surface (or more precisely: column of atmosphere) each detector is receiving radiation during a measurement. In order to perform this calculation, the following parameters are required:

1. Position of the spacecraft in the Earth-fixed reference frame, transformed from the inertial reference frame, which is provided by flight operations.

2. Attitude of the spacecraft reference frame with respect to the inertial reference frame, which is continuously measured in-flight by the attitude control and determination subsystem.

3. Line-of-sight angles, i.e., the azimuth angle ϕ and elevation angle ε of each detector pixel, which are defined with respect to the Spacecraft reference frame during the calibration campaign.

The applicable reference frames are explained in Section 39.1. The location of the center point is determined as well as four cornerpoints of the ground pixel. Subsequently, from the location of a ground pixel, the azimuth angle ϕ and zenith angle θ of the spacecraft are determined, as well as the azimuth and zenith angles ϕ_0 and θ_0, respectively, of the Sun. Also the ground pixel elevation and water fraction are determined by making use of an external Digital Elevation Model (DEM). Furthermore, the Sun angles with respect to the Spacecraft, and the velocity of the spacecraft in the direction of the Sun are calculated as well. Other geometrical algorithms are used to calculate the orbit phase and the location of the sub-satellite point (SSP) as well as the distance to the Sun.

Finally, a list of quality algorithms determine if the measurement or ground pixel should be flagged for shadow, Sun glint, a spacecraft maneuver, the South Atlantic Anomaly, descending, boundaries..

40.1 Ground pixel position

The position of a measurement on Earth i.e., the center of a ground pixel, in terms of longitude ϑ and latitude δ, is given by the intersection of the line of sight vector with the reference ellipsoid. This line of sight vector is determined by the direction of the barycenter of the measurement polychromatic spatial response function. The line of sight vector will need to be sequentially transformed between the following reference frames:

spacecraft reference frame
↓
inertial reference frame
↓
Earth-fixed reference frame

For the transformation steps within the vicinity of the spacecraft, only rotations are taken in to account while translations are ignored. This can be safely applied as the translations within the spacecraft only amount to meters while the resolution on-ground is in the order of kilometers. To be able to transform the line of sight from the spacecraft reference frame to the inertial reference frame, this LOS direction vector $\mathbf{l}_{\mathrm{SRF}}$ first needs to be converted to a unit direction vector $\hat{\mathbf{l}}_{\mathrm{SRF}}$. Using the definition of the detector pixel LOS azimuth ϕ and elevation ε from Section 39.1.9 the LOS unit vector ($r = \sqrt{x^2+y^2+z^2} = 1$) is determined as

$$z = \sqrt{\frac{1.0}{1.0+\tan^2\varepsilon+\tan^2\phi}}\ , \tag{113}$$

$$\hat{\mathbf{l}}_{\mathrm{SRF}} = \begin{bmatrix} \hat{l}_{\mathrm{SRF,x}} \\ \hat{l}_{\mathrm{SRF,y}} \\ \hat{l}_{\mathrm{SRF,z}} \end{bmatrix} = \begin{bmatrix} z\cdot\tan\varepsilon \\ -z\cdot\tan\phi \\ z \end{bmatrix}\ . \tag{114}$$

To determine the intersection of a LOS in the spacecraft reference frame with the WGS84 Earth reference ellipsoid, the LOS first has to be transformed to the inertial reference frame with the rotation matrix from Section 39.2.1 to yield the direction of this unit LOS vector in the inertial reference frame. Subsequently it has to be transformed to the Earth-fixed reference frame as described in Section 39.2.3. The position vector of the spacecraft in the Inertial reference frame as provided by flight operations, is also transformed to the Earth-fixed reference frame. The satellite position and LOS direction in the EFRF together now define the Line-of Sight.

The intersection of this resulting line of sight is then taken with the WGS84 Earth reference ellipsoid, as described in Section 39.3. Since this yields two intersection points, care has to be taken to determine which of the two intersection points is the one which is needed. This intersection point is then converted from geocentric Cartesian to geodetic coordinates as described in Section 39.2.4, to yield the final ground pixel location in latitude δ and longitude ϑ.

40.1.1 Ground pixel corner points

The extent of a ground pixel is ill-determined due to the fact that an arbitrary choice has to be made about which extent of the measurement polychromatic spatial response function is representative for the OMI instrument. During on-ground calibration the instantaneous line of sight (ILOS) is determined for each detector pixel under static conditions. The instantaneous line of sight is the barycenter of the pixel polychromatic spatial response function. In flight, the line of sight of one detector pixel sweeps over a range of ground positions during one exposure (blue peaks in the middle of Figure 31). The exposures of one co-addition period are added up to one *measurement*, depicted as a dark blue envelope in the figure. The center time T_{center} of the measurement in combination with the ILOS of the detector pixel, is used to determine the center point of a ground pixel with the geolocation algorithms.

For the center points, the lines of sight are averaged in the spectral direction per detector band. This transforms the wavelength dependence of the geolocation into a detector band dependence. Polarization effects are not measured and thus not accounted for. In the following step, the lines of sight are binned in the spatial direction, according to the binning scheme. That is, the lines of sight of a group of binned pixels are averaged. The resulting averaged LOS parameters (azimuth, elevation) are then used to determine the ground pixel center point. This ground pixel is now correlated to an image pixel, consisting of a number of binned detector pixels.

To determine the area that a ground pixel extends, its corner points have to be determined. This is done by taking the groups of binned LOS values in the spatial direction on the detector, and interpolating neighboring detector (i.e. unbinned) pixel LOS values to obtain the LOS edges of these groups. The azimuth and elevation curves versus detector pixel are expected to be sufficiently smooth to be able to safely apply this method. The interpolated values for azimuth and elevation are then used to determine the corner point lines in along-track direction (dotted horizontal lines in the right panel of Figure 31). These lines fix the corner points distribution in across-track direction.

To determine the distribution of the corner points in along-track direction, the corner point lines in across-track direction (dashed-dotted vertical line in the illustration) are obtained by interpolation between the previously determined center points. The interpolation in along-track direction is achieved by taking the average of the timestamps of two following measurements in a sequence, and then interpolating the position and attitude coordinates of the spacecraft. By using these interpolated input parameters along with the interpolation over the lines of sight of the binned image pixels, one can determine the corner points of each ground pixel as visualized in the right schematic of Figure 31.

To determine the most East and West corner points of the scanline, the LOS of the last detector pixel is extrapolated in across track direction to yield the bounding lines of sight. To determine the start corner points of the first scanline, and the end corner points of the last scanline in a measurements sequence, the measurement time is extrapolated. The same procedure is used when a measurement in the series is missing, faulty or corrupted, which effectively divides a measurement sequence in multiple sequences. If there is only a single measurement, the start and end time of the measurement are used to determine the timestamps of the bounding corner points.

These extrapolated timestamps are then used in combination with the inter-/extrapolated lines of sight in across-track direction to obtain the start and end corner point boundaries.

Concluding, the method to compute ground pixel corner points has the following properties:

- Since these corner points are determined directly from interpolated values for the lines of sight, time, position and attitude parameters, only one grid of corner points has to be determined, once. As a result, the ground pixel tiles in this grid will neither have overlap, nor gaps between them.
- The keystone effect is accounted for by using this method, since the corner points of the ground pixels are defined by direct intersection of the interpolated lines of sight with the Earth reference ellipsoid.
- Due to the divided approach for the center- and corner points determination, the center points do not exactly lie at the spatial interpolation points of the corner points, nor are the corner points located at the spatial inter-/extrapolation of the center points.

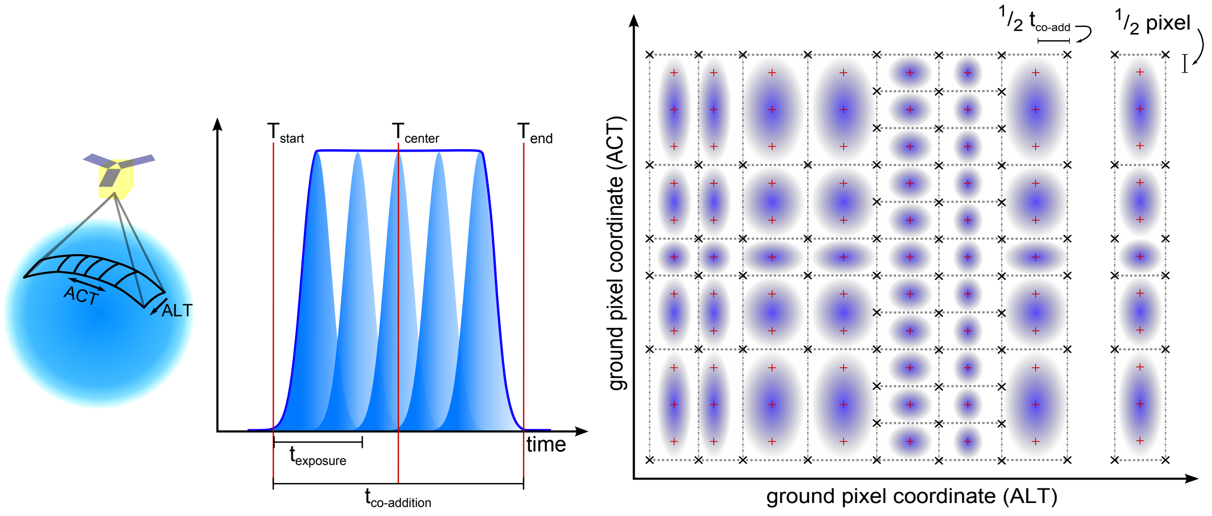

Figure 31: The along-track (ALT) and across-track (ACT) directions along one scanline (left). The movement of the instantaneous line of sight of one detector pixel during one exposure (blue peaks) added to one measurement during the co-addition period (dark blue envelope). The center point for the measurement is determined from T_{center}(middle). The inter- and extrapolation of the center times and the lines of sight resulting in the corner points definition (right), for a single measurement and for a sequence.

- The spatial response functions of the pixels are not needed for the calculation of the ground pixel corner point positions: only the LOS angles of the rows are.

40.2 Satellite position

Using the position of the satellite, the sub-satellite point (SSP) and the relative position of the spacecraft in the orbit, quantified by the orbit phase, are determined as described below.

40.2.1 Satellite position and velocity interpolation

The position and velocity of the satellite at any moment in time is determined by interpolating ephemeris data, which include the position and velocity Cartesian components (x,y,z) at on-board time (OBT) instances as provided by flight operations. Since the orbit can be approximated by an ellipse, one could fit an ellipse through some of these ephemeris position points around the requested time, and so interpolate the position for the requested time geometrically. However, in reality the orbit is not an ellipse but on top of this approximation there are secular, long-period and short-period perturbations. By using just a fitted ellipse for the interpolation the velocity would always point outward of the ellipse while the interpolation position would always lay outward of the used ephemerides.

However, in reality the velocity could also act inwards of the ellipse and the resulting position could lay inward of the ellipse. Therefore, a cubic Hermite spline interpolation method is used that fits a third-degree polynomial through the ephemeris points before (subscript 0) and after (subscript 1) the requested time, and uses the velocity and position of these points. The interpolation is done separately for each position p and velocity v Cartesian component. First, four polynomial coefficients (subscripts 0-3) are determined as

$$c_0 = p_0 \ , \tag{115}$$

$$c_1 = \Delta t v_0 \ , \tag{116}$$

$$c_2 = 3(p_1 - p_0) - \Delta t(2v_0 + v_1) \ , \tag{117}$$

$$c_3 = 2(p_0 - p_1) + \Delta t(v_0 + v_1) \ , \tag{118}$$

where $\Delta t = t_1 - t_0$ is the difference in time between the two ephemeris points. To interpolate to the requested time t, this time in converted to a relative fraction of the interval as

$$t_{\mathrm{rel}} = \frac{t - t_0}{\Delta t} \ , \tag{119}$$

and the position and velocity component can then be obtained by using

$$p = c_0 + c_1 t_{\text{rel}} + c_2 t_{\text{rel}}^2 + c_3 t_{\text{rel}}^3 \ , \tag{120}$$

$$v = \frac{c_1 + 2c_2 t_{\text{rel}} + 3c_3 t_{\text{rel}}^2}{\Delta t} \ . \tag{121}$$

40.2.2 Satellite attitude interpolation

To determine the attitude of the spacecraft at any given time, the attitude measurements as unit quaternion rotation from the inertial to the spacecraft reference frame are interpolated linearly, for all four components separately, as

$$q = \frac{(t_1 - t)q_0 + (t - t_0)q_1}{t_1 - t_0} \ , \tag{122}$$

after which it is normalised, for a valid reversible rotation.

40.2.3 Sub-satellite point and altitude

The SSP is defined as the intersection of the line from the position of the spacecraft normal to the surface of the WGS84 Earth reference ellipsoid, see Figure 26. It is described by the longitude and geodetic latitude of the spacecraft in the Earth-fixed reference frame. The altitude of the spacecraft is defined as the distance between the spacecraft and the sub-satellite point.

To obtain the above SSP parameters, one first has to know the position of the spacecraft in the Earth-fixed reference frame (transformed from the inertial reference frame as provided by flight operations), after which the intersection point with the WGS84 Earth reference ellipsoid can be determined. The conversion from the Earth-fixed reference frame geocentric Cartesian coordinates to geodetic coordinates is then performed as described in Section 39.2.4.

40.2.4 Orbit phase

The orbit phase is defined as $1/(2\pi)$ times the angle in radians traversed by the spacecraft since spacecraft midnight as seen from the center of the Earth. Spacecraft midnight is the point on the night side of the Earth where the spacecraft crosses the orbital plane of the Earth about the Sun. This makes the orbit phase a quantity that runs from 0 to 1, while the spacecraft moves between each spacecraft midnight. Note that the orbit phase depends almost linearly on elapsed time, but not exactly, since the Sentinel-5p orbit is not a perfect circle. See Figure 32 for a graphical illustration of the orbit phase definition.

To determine the orbit phase Φ at a measurement time instance, first the position of the Sun is determined in the true-of-date reference frame as described in Section 40.3.1, which is converted to the inertial reference frame by multiplying with rotation matrix $[\mathbf{Q}(t)]^{\mathrm{T}}$ to subtract the precession and nutation since the epoch J2000.0, see section 39.2.3. The positions of the Earth (i.e., the origin) and the Sun are then transformed to the orbital reference frame as derived in Section 39.2.6. These position vectors are then both projected onto the orbital plane by setting the first coordinate (T) in the local orbital reference frame, which is the coordinate perpendicular to the orbital plane, to 0. The resulting vectors are then translated such that the center of the Earth is at the origin instead of the center of the spacecraft. The orbit phase Φ is now determined as

$$\Phi = \frac{\arctan 2(y_{\text{S/C,Orb}}, z_{\text{S/C,Orb}}) - \arctan 2(-y_{\text{Sun,Orb}}, -z_{\text{Sun,Orb}})}{2\pi} \ , \tag{123}$$

in which the $\arctan 2$ function determines an angle in the range $(-\pi, \pi]$ instead of the normal $\arctan$ function which has results within $(-\pi/2, \pi/2]$. Finally, the integer 1 needs to be subtracted or added until Φ lies in the range $[0, 1)$.

40.3 Solar angles

For the solar angles algorithms, first the location of the Sun is determined. Following, the Sun's LOS angles in the payload reference frame, the velocity scalar of the spacecraft towards the Sun, and the LOS from the ground pixel towards the Sun and the spacecraft can be determined, which are described below.

40.3.1 Position of the Sun in the true-of-date reference frame

The Sun's position (x,y,z) can be determined in the true-of-date reference frame using [18]. The reference describes low-precision (1 arcminute) formulae for planetary positions, including the Sun, and includes a large number of coefficients to be used with these formulae. The algorithms described use as input only the Julian date (in UT or Greenwich Mean Time (GMT)) since J2000, assigned t, from which the time T in Julian centuries since the epoch 1900 is determined as

$$T = \frac{t}{36525} + 1 \ . \tag{124}$$

To determine the position of the Sun, the following fundamental arguments of the Moon (Mo), the Sun (S), Venus (V), Mars (Ma) and Jupiter (J) are needed:

$$\begin{aligned}
L_{\mathrm{Mo}} &= 0.606434 + 0.03660110129t \ , && \text{(125a)}\\
\Omega_{\mathrm{Mo}} &= 0.347343 - 0.00014709391t \ , && \text{(125b)}\\
L_{\mathrm{S}} &= 0.779072 + 0.00273790931t \ , && \text{(125c)}\\
G_{\mathrm{S}} &= 0.993126 + 0.00273777850t \ , && \text{(125d)}\\
G_{\mathrm{V}} &= 0.140023 + 0.00445036173t \ , && \text{(125e)}\\
G_{\mathrm{Ma}} &= 0.053856 + 0.00145561327t \ , && \text{(125f)}\\
G_{\mathrm{J}} &= 0.056531 + 0.00023080893t \ , && \text{(125g)}
\end{aligned}$$

where L is the mean longitude and G is the mean anomaly of a certain planet, while Ω is the longitude of the lunar ascending node. Then, the geocentric equatorial coordinates right ascension (α), declination (δ) and geocentric distance (ρ) are determined as

$$\begin{aligned}
\alpha &= L + \arcsin\left[\frac{W}{\sqrt{U - V^2}}\right] \ , && \text{(126a)}\\
\delta &= \arcsin\left(\frac{V}{\sqrt{U}}\right) \ , && \text{(126b)}\\
\rho &= \bar{\Delta}\sqrt{U} \ , && \text{(126c)}
\end{aligned}$$

where $\bar{\Delta}$ is a scaling factor which is 1.00021 for the Sun, and U,V,W are intermediaries which can be determined using (co)sine series with coefficients listed in the Appendix of [18] in combination with T and the fundamental arguments L, G, and Ω of above. The coordinates (α,δ,ρ) are simply the longitude, geocentric latitude

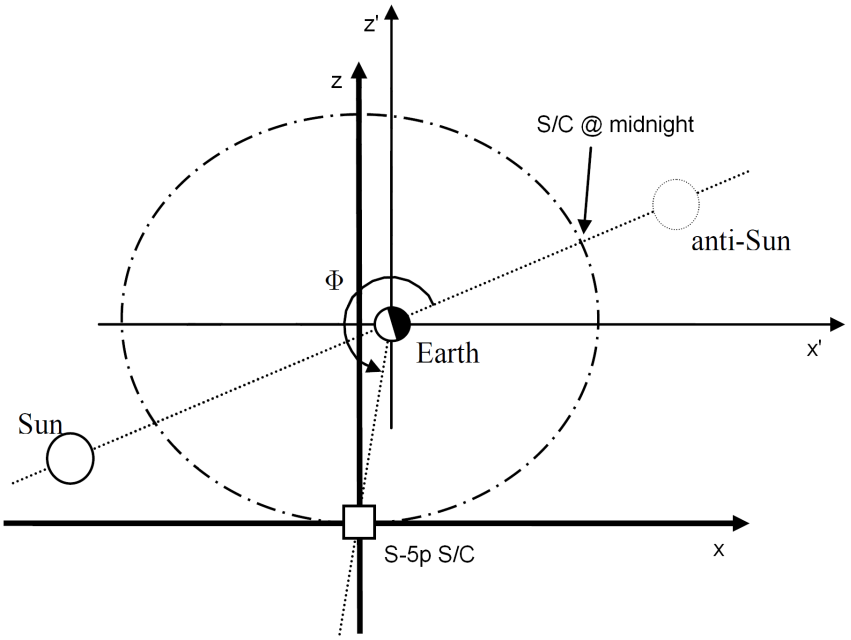

Figure 32: Definition of the orbit phase Φ.

and radius (ϑ, δ', r) in the true-of-date reference frame which can be converted to Cartesian components $(x_{\mathrm{Sun,TODRF}}, y_{\mathrm{Sun,TODRF}}, z_{\mathrm{Sun,TODRF}})$ as explained in Section 39.2.4. The Earth-Sun distance $D_{\mathrm{Earth-Sun}}$ is then evaluated as

$$D_{\mathrm{Earth-Sun}} = \sqrt{x^2_{\mathrm{Sun,TODRF}} + y^2_{\mathrm{Sun,TODRF}} + z^2_{\mathrm{Sun,TODRF}}} \,, \tag{127}$$

which can then be divided by $AU = 149,597,870,700$ m to convert from meters to Astronomical Units. One AU is the mean orbital distance from the Earth to the Sun.

40.3.2 Solar line of sight in the optical alignment reference frame

Using the ephemeris of the Sun, the position of the spacecraft in the inertial reference frame, and the attitude of the spacecraft reference frame with respect to the inertial reference frame, one can determine the azimuth ϕ and elevation ε of the line of sight from the spacecraft to the Sun in the Sun port reference frame. The angles ϕ and ε are defined here as described in Section 39.1.10.

The Sun's position can be determined in the true-of-date reference frame as described in Section 40.3.1. This position vector can then be transformed to the inertial reference frame by deducting the precession and nutation since J2000.0 as described in Section 39.2.3, which means multiplying by the transpose of the rotation matrix $\mathbf{Q}(t)$. Then, the position vector is transformed to the spacecraft reference frame as described in Section 39.2.1. Finally, it is transformed to the Optical alignment reference frame, as described in Section 39.2.7. The solar elevation ε and azimuth ϕ in the Sun port reference frame can then be determined as

$$\phi_{\mathrm{Sun,OARF}} = \arctan\left(\frac{y_{\mathrm{Sun,OARF}}}{x_{\mathrm{Sun,OARF}}}\right) \,, \tag{128a}$$

$$\varepsilon_{\mathrm{Sun,OARF}} = \arctan\left(\frac{y_{\mathrm{Sun,OARF}}}{\sqrt{x^2_{\mathrm{Sun,OARF}} + y^2_{\mathrm{Sun,OARF}}}}\right) \,. \tag{128b}$$

40.3.3 Velocity of spacecraft towards Sun

The position and velocity components of the spacecraft follow from the ancillary data as determined by flight operations, and are provided in the inertial reference frame. Using the Sun's position in the inertial reference frame as determined in the previous section, the position vector $\mathbf{p}_{\mathrm{S/C-Sun,IRF}}$ of the Sun relative to the spacecraft in the inertial reference frame is now determined as

$$\mathbf{p}_{\mathrm{S/C\rightarrow Sun,IRF}} = \mathbf{p}_{\mathrm{Sun,IRF}} - \mathbf{p}_{\mathrm{S/C,IRF}} \,, \tag{129}$$

with which the amplitude of the velocity $\mathbf{v}_{\mathrm{S/C\rightarrow Sun,IRF}}$ of the spacecraft in the direction of the Sun is computed as

$$\left\|\mathbf{v}_{\mathrm{S/C\rightarrow Sun,IRF}}\right\| = \frac{(\mathbf{p}_{\mathrm{S/C\rightarrow Sun,IRF}}, \mathbf{v}_{\mathrm{S/C,IRF}})}{\left\|\mathbf{p}_{\mathrm{S/C\rightarrow Sun,IRF}}\right\|} \,, \tag{130}$$

in which the length of the position vector of the Sun relative to the spacecraft in the inertial reference frame is defined as

$$\left\|\mathbf{p}_{\mathrm{S/C\rightarrow Sun,IRF}}\right\| = \sqrt{x^2_{\mathrm{S/C\rightarrow Sun,IRF}} + y^2_{\mathrm{S/C\rightarrow Sun,IRF}} + z^2_{\mathrm{S/C\rightarrow Sun,IRF}}} \,. \tag{131}$$

40.3.4 Spacecraft and Sun lines of sight from ground pixel

Level-2 data processors need information on the lines of sight from the ground pixel position to the spacecraft and to the Sun, in the topocentric reference frame. These are defined by the solar azimuth ϕ_0 and zenith θ_0 angles for the incident sunlight, and spacecraft azimuth ϕ and zenith θ angles for the scattered sunlight, and are indicated in Figure 33. With these angles the level-2 data processors can for instance determine the scattering angle Θ.

In order to determine these LOS angles for the spacecraft, the position of the spacecraft in the Earth-fixed reference frame is transformed to the topocentric reference frame, as described in Section 39.2.5.

To determine the LOS angles for the Sun, the position of the Sun in true-of-date reference frame is computed as indicated in Section 40.3.1. Then, this position is transformed to the Earth-fixed reference frame by first multiplying with $[\mathbf{Q}(t)]^{\mathrm{T}}$ to get to the inertial reference frame and then with $\mathbf{W}(t)\mathbf{R}(t)\mathbf{Q}(t)$ (since this total matrix was already calculated) as described in Section 39.2.3. Then the position is further transformed to the topocentric reference frame as explained in Section 39.2.5.

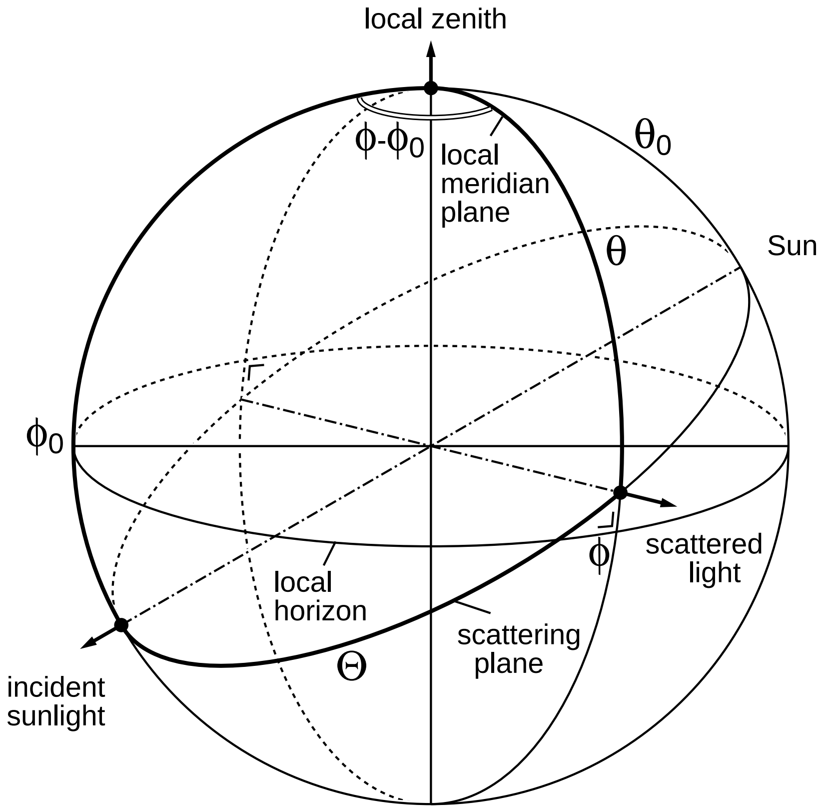

Figure 33: Definition of the LOS zenith θ and azimuth ϕ angles from the ground pixel location to the spacecraft and Sun (θ_0, ϕ_0), and scattering angle Θ.

The LOS angles are then determined as

$$\theta_0 = \arctan \frac{\sqrt{x^2+y^2}}{z} \,, \tag{132a}$$

$$\phi_0 = \arctan 2(x,y) \,, \tag{132b}$$

$$\theta = \arctan \frac{\sqrt{x^2+y^2}}{z} \,, \tag{132c}$$

$$\phi = \arctan 2(x,y) \,, \tag{132d}$$

in which the $\arctan 2$ determines an angle in the range $-\pi - \pi$ instead of the normal $\arctan$ function which results in an angle from $-\pi/2 - \pi/2$. There are no minus signs in front of x and y for the solar azimuth and thus the azimuth angle of the Sun direction itself is determined, and not the incident ray of the Sun, like indicated in Figure 33.

40.3.5 Atmospheric Refraction of Light

All geolocation analysis so far has been done assuming there is no refraction of the light beam due to the Earth's atmosphere. However, in reality, this does occur, which changes the solar and viewing angles as well as the position of the ground pixels. Since each point in the variable atmosphere has its own density, pressure, temperature and humidity (which are influenced by current local weather conditions) it also has its own refraction coefficient. Thus, to precisely account for all atmospheric refraction effects, an atmospheric model would have to be set up, through which the 3D light beam path, with a certain wavelength, would have to be integrated. Unfortunately, this would be too computationally intensive to implement in detail, as it would cost far too much CPU-time.

However, the effect of atmospheric refraction at zenith angles of 90 degrees can reach approximately half a degree, and should thus be corrected for. To include this effect, some assumptions have to be made. Using a simple model for the atmosphere that is concentrically homogeneous, the same conditions apply at the same altitude anywhere on Earth. Furthermore, assuming an observation point at sea-level with an atmospheric pressure of 1010 millibars and a temperature of 10° Celsius, where the refraction is calculated for a yellow light beam in the visible part of the electromagnetic spectrum. Then, an empirical equation that approximates the refraction R in arcminutes can be set up [19] based on the true altitude h in degrees:

$$R = \frac{1.02}{\tan\left(h + \frac{10.3}{h+5.11}\right)} , \tag{133}$$

in which the true altitude h is connected to the true zenith angle θ as

$$h = \pi - \theta \; . \tag{134}$$

The apparent zenith angle at which the light beam reaches the ground pixel location is now determined from

$$\theta_a = \theta - R \; . \tag{135}$$

as the light beam is always refracted towards the zenith. That is, the zenith angle decreases during its path through the atmosphere from top to bottom.

This empirical formula is accurate to about 0.15 arcminutes for true altitude angles h smaller than 3 degrees, while for angles more than 5 degrees it is accurate to the arcsecond level. Resulting from the assumptions, the azimuth angle has no refraction. Plenty of these approximating equations exist (Bennet, Meeus, Explanatory Supplement to the Astronomical Almanac), but were all verified to give similar results.
The atmospheric refraction correction can be turned on or of in the configuration.

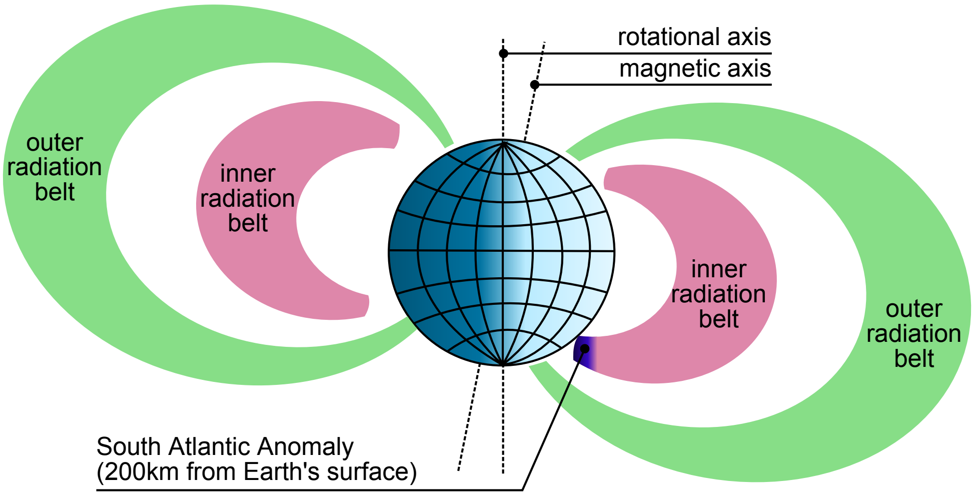

Figure 34: Indication of the location and size of the Van Allen radiation belts, the location of the South Atlantic Anomaly (SAA), and the difference in magnetic and rotational axes of the Earth.

41 Quality assessment

In case of errors in one of the algorithms, the pertinent image pixels are marked ("flagged") as such, invalidating them for use in L01b processor algorithms. In addition, a number of dedicated algorithms are designed to detect other issues that relate to the quality of the measurements. These algorithms do not affect the measured signal or its error, but augment these with the results of these quality assessments, often in the form of additional flags.

Flagging denotes the annotation of individual Level-1b data values with detailed processing information. Generally, these are answers to simple yes/no questions such as "has a processing error occurred for this particular spectral sample?" or "was this measurement performed while the spacecraft was in the path of a solar eclipse?"

Users of the Level-1b data are advised to use these data fields to assess the quality of the Level-1b data and filter it before use. In flag fields, the individual bits of the elements matter. For instance, a particular bit of a flag field may indicate "missing data", so that a value of 1 (when the flag is said to be "raised" or "set") signifies "yes", and a value of 0 ("lowered" or "unset") signifies "no". This is in contrast to other data fields, where all the bits combined form a real or countable value. Using bitwise operators and a well-chosen bit mask, a user can tailor the selection criteria for his or her purpose.

In the following flags are described which are the most relevant for the L2 radiance and irradiance output products. The flags can be found in the fields `spectral_channel_quality`, `measurement_quality`, `ground_pixel_quality` and `xtrack_quality` of the L01b radiance and irradiance data. A detailed description of all flags can be found in the IODS [6].

41.1 Spacecraft in South Atlantic Anomaly

One source of high amounts of radiation near Earth are trapped particles (protons, electrons) in the Earth's magnetic field. These particles are concentrated in two large belts around the Earth, called the Van Allen radiation belts, see Figure 34. Due to the offset and tilt of the magnetic axis with respect to rotational axis of the Earth, one region of the inner belt causes high levels of radiation very close to the Earth. This region is called the South Atlantic Anomaly (SAA), and is illustrated in Figure 35. The SAA is also visualized in Figure 36, around AURA/OMI's altitude.

41.1.1 Point-in-polygon problem

As the SAA is defined by a series of latitude and longitude coordinates at a certain altitude, and thus a polygon, one needs to determine whether the spacecraft resides within this polygon or not. Therefore, the latitude and longitude of the spacecraft's position are tested against this polygon.

Let us call the spacecraft's coordinates $(\vartheta_\mathrm{s}, \delta_\mathrm{s})$ and that of a polygon point (ϑ_i, δ_i) with i ranging from 0 to n, the number of polygon points. The polygon is drawn by connecting each following point in order of n. The

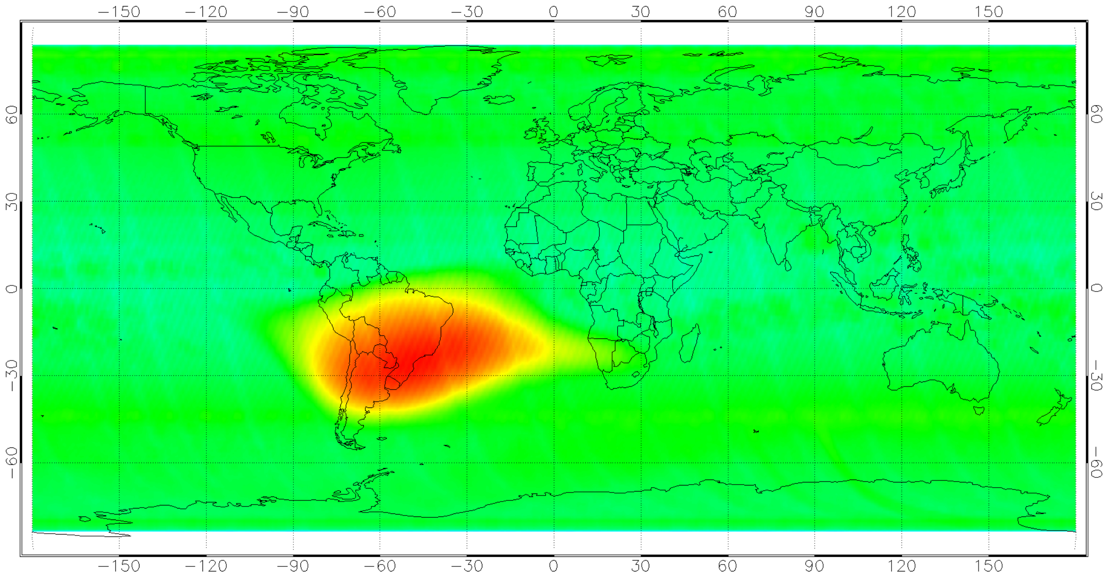

Figure 35: Transient signals density as measured by the OMI instrument onboard NASA's AURA satellite. The plot is the aggregate of one year of data measured at an altitude of 700 km.

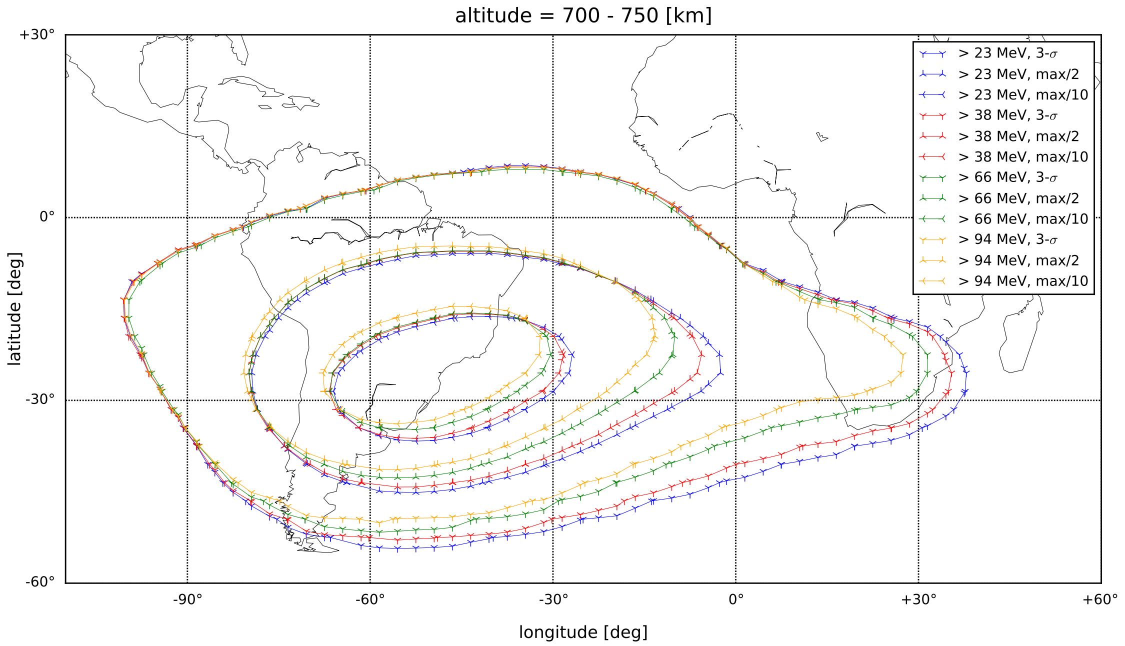

Figure 36: Contour plots of the South Atlantic Anomaly (SAA) for 700-750 km altitude, which is around the AURA/OMI mean altitude of approximately 715 km. The numbers indicate the limiting proton energies in MeV, while p stands for peak value. '>23, p/10' thus means a contour for proton energy levels higher than 23 MeV, while the area is defined by energy values higher than the peak value divided by ten.

angle α_i that a polygon point i makes with the standard angle reference (eastwards vector) as seen from the spacecraft can be determined by

$$\alpha_i = \arctan 2((\delta_i - \delta_\text{s}), (\vartheta_i - \vartheta_\text{s})) \; , \tag{136}$$

which results in a range of $-\pi < \alpha_i < \pi$, which is converted to the range $0 < \alpha_i < 2\pi$. The angle $\Delta\alpha_i$ between two polygon points, α_i and α_{i+1} can then be calculated as

$$\Delta\alpha_i = \alpha_{i+1} - \alpha_i \; , \tag{137}$$

which is converted to the range $-\pi < \Delta\alpha_i < \pi$. Then adding all polygon angles together results in

$$\alpha = \sum_{i=0}^{n} \Delta\alpha_i = \sum_{i=0}^{n} \left[\arctan 2((\delta_{i+1} - \delta_\text{s}), (\vartheta_{i+1} - \vartheta_\text{s})) - \arctan 2((\delta_i - \delta_\text{s}), (\vartheta_i - \vartheta_\text{s}))\right] . \tag{138}$$

Dividing this angle by 2π results in the *winding number* of the position of the spacecraft with respect to the SAA polygon. If the winding number equals 0, the spacecraft is outside of the SAA polygon, if it equals 1, the spacecraft is inside of the SAA polygon. This theory can be safely applied as the SAA does not cross any dateline or pole boundary.

41.2 Spacecraft manoeuvring

When the spacecraft is manoeuvring, the measurements will be disturbed due to the swath deviating from its usual course. Therefore, the instrument will be put into idle mode when this is the case. However, in the event that measurements are still performed while manoeuvring, the manoeuvre flag is raised for these measurements.

This manoeuvre flag is based on the local normal pointing (LNP) operation mode of the spacecraft, which means that the on-board attitude control system will constantly try to point the spacecraft with the boresight towards the SSP. The nadir point of the spacecraft (the intersection of the boresight with the Earth's surface) will be kept within certain limits of proximity to the SSP. When the spacecraft is manoeuvring, the attitude will no longer be in LNP mode, so this can be tested by checking the distance between the nadir point of the spacecraft and the SSP ($d_{\text{ssp}\leftrightarrow\text{nadir}}$). If this distance is larger than the attitude offset threshold manoeuvre distance $d_{\text{man,thr}}$, the spacecraft is said to be manoeuvring and the manoeuvre flag is raised.

First, the nadir point is determined at the measurement time instance. That is, the intersection of the Z-axis (boresight) of the payload reference frame with the surface of the Earth is calculated, resulting in a nadir longitude ϑ_nadir and latitude δ_nadir. This is done analogous to the ground pixel determination of Section 40.1, using the line of sight that travels along the boresight which has an elevation and azimuth angle of 0 degrees.

The distance $d_{\text{ssp}\leftrightarrow\text{nadir}}$ between the nadir point of the spacecraft and the SSP is calculated with the haversine formula as

$$a = \sin^2\left(\frac{\delta_\text{nadir} - \delta_\text{SSP}}{2}\right) + \sin^2\left(\frac{\vartheta_\text{nadir} - \vartheta_\text{SSP}}{2}\right)\cos(\delta_\text{ssp})\cos(\delta_\text{nadir}) \; , \tag{139a}$$

$$c = 2\arctan 2(\sqrt{a}, \sqrt{1-a}) \; , \tag{139b}$$

$$d_{\text{ssp}\leftrightarrow\text{nadir}} = R_\text{e} c \; , \tag{139c}$$

where R_e is the equatorial radius of the Earth. This is an approximation of the distance, by simplifying the problem using a sphere instead of the ellipsoid. A maximum error of 0.3% is now made around the poles, but this is considered small enough compared to the chosen threshold distance.

41.3 Irradiance solar elevation out-of-range

During irradiance measurements, the Sun port with its limited field-of-view is directed towards the Sun. The angles with respect to this port are calculated. When the solar elevation angle ε_sun as seen from the Sun port is above or below certain range angles, no valid measurements can be obtained anymore. When this happens, a measurement flag for "irradiance out-of-range" is set. This happens when either of the following equations holds true

$$\varepsilon_\text{sun} < -3.0 \; , \tag{140}$$

$$\varepsilon_\text{sun} > +3.0 \; . \tag{141}$$

41.4 Spacecraft in Earth's shadow

During its lifetime, the orbit of AURA might change. In particular when the longitude of the ascending node is changed, the spacecraft will spent shorter or longer parts of its orbit in the shadow of the Earth with respect to the Sun. This shadow can be penumbral: the spacecraft still receives direct sunlight but not from the whole Solar disk, or umbral: the spacecraft is in complete shadow. This is illustrated for a Solar eclipse in Figure 38, but the same principle applies here.

To determine if the S/C is in any shadow of the Earth, and to what degree, the angle between the center of the Earth and the center of the Sun must be calculated. First the Position of the Sun in the True-of-Data reference frame is determined, like in Section 40.3.1, and converted to the Inertial reference by multiplying with rotation matrix $[\mathbf{Q}(t)]^{\mathrm{T}}$ as in Section 39.2.3 and then to the Spacecraft reference frame as in 39.2.1. Then, the Vector [0,0,0] in the Inertial reference frame, indicating the center of the Earth, is transformed to the Spacecraft reference frame. Both the Sun's position $p_{\mathrm{sun,srf}}$ and the Earth's position $p_{\mathrm{earth,srf}}$ are now known as a 3D Cartesian vector in the Spacecraft reference frame. The angle between these two vectors as seen from the spacecraft is determined as

$$\delta_{earth\angle sun} = \arctan 2(|\vec{p}_{earth} \times \vec{p}_{sun}|, \vec{p}_{earth} \cdot \vec{p}_{sun}) \ , \tag{142}$$

in which the × symbol indicates the vector (outer) cross product and the $\cdot$ symbol indicates the vector (inner) dot product, while the $||$ symbols denote a vector's length and the $\arctan 2$ function generates a result in the full range $[-\pi, +\pi]$.

Furthermore, the Earth's and Sun's horizon angles need to be known, which are defined by the *apparent* disk of these bodies as seen by the spacecraft. The horizon angle is the angle extended from the center of the body to the point where the Line-of-sight just touches the outside of this body: the true outer horizon. This angle ρ is calculated by making use of the distance to the center of the body r and the radius of that body R as follows:

$$\rho_{\mathrm{earth}} = \arcsin\left(\frac{R_{\mathrm{earth}}}{r_{\mathrm{earth,srf}}}\right) , \tag{143}$$

$$\rho_{\mathrm{sun}} = \arcsin\left(\frac{R_{\mathrm{sun}}}{r_{\mathrm{sun,srf}}}\right) . \tag{144}$$

N.B. this angle is *larger* then just calculating the angular extension of the body's disk (for which the $\arctan$ function would be used).

To determine the type of shadow, an umbral angle α_{umbral} and penumbral angle $\alpha_{\mathrm{penumbral}}$ are further defined as

$$\alpha_{\mathrm{umbral}} = \rho_{\mathrm{earth}} - \rho_{\mathrm{sun}} \ , \tag{145}$$

$$\alpha_{\mathrm{penumbral}} = \rho_{\mathrm{earth}} + \rho_{\mathrm{sun}} \ . \tag{146}$$

A floating point value f_{shadow} is now constructed which defines the type and degree of shadow. There are four shadow cases defined as a decimal number between 0 and 4:

0-1 Umbral shadow Sun is not visible from S/C

$$0 \leq \delta_{earth\angle sun} \leq \alpha_{\mathrm{umbral}} \tag{147}$$

$$f_{\mathrm{shadow}} = \frac{\delta_{earth\angle sun}}{\alpha_{\mathrm{umbral}}} \tag{148}$$

1-2 Penumbral shadow Sun is partly visible from S/C

$$\alpha_{\mathrm{umbral}} < \delta_{earth\angle sun} \leq \alpha_{\mathrm{penumbral}} \tag{149}$$

$$f_{\mathrm{shadow}} = 1 + \frac{\delta_{earth\angle sun} - \alpha_{\mathrm{umbral}}}{2\rho_{\mathrm{sun}}} \tag{150}$$

2-3 No shadow (shadow side) Sun is fully visible from S/C, on shadow hemisphere of Earth

$$\alpha_{\mathrm{penumbral}} < \delta_{earth\angle sun} \leq \frac{\pi}{2} \tag{151}$$

$$f_{\mathrm{shadow}} = 2 + \frac{\delta_{earth\angle sun} - \alpha_{\mathrm{penumbral}}}{\frac{\pi}{2} - \alpha_{\mathrm{penumbral}}} \tag{152}$$

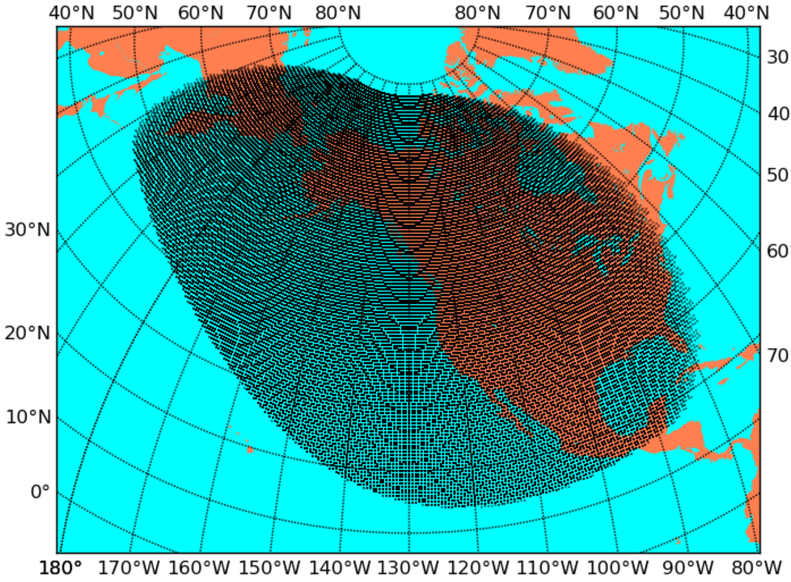

Figure 37: Penumbral shadow cast on the Earth's surface due to the solar eclipse by the Moon on the 23rd of October 2014 during the total eclipse period, as calculated with algorithms implemented in the L01b Processor.

3-4 No shadow (Sun side) Sun is fully visible from S/C, on Sun hemisphere of Earth

$$\frac{\pi}{2} < \delta_{earth\angle sun} \leq \pi \tag{153}$$

$$f_{\text{shadow}} = 2 + \frac{2\delta_{earth\angle sun}}{\pi} \tag{154}$$

This method was checked by two other ways of determining this shadow: one as taken from [20], in which the Earth is approximated as a sphere, and one by making use of the intersection of the LOS with the Earth reference ellipsoid, as determined in Section 39.3. A measurement flag is set for "penumbral shadow" or "umbral shadow" accordingly.

41.5 Ground pixel in Solar eclipse

During a solar eclipse, the OMI instrument might receive less reflected sunlight from certain areas on the surface of the Earth than when there would be no eclipse. As an example, Figure 37 shows the area on the Earth that was in the shadow of the Moon during the total solar eclipse of 21 August 2017.

Since solar eclipses may affect Level-2 retrievals, the L01b processor flags ground pixels that reside within the umbra (total eclipse) *or* antumbra (annular eclipse) *or* penumbra (partial eclipse) of an eclipse. See Figure 38 for an illustration of the difference between these three types of shadow. The eclipse begins and ends when the penumbral shadow makes first, and last contact with the Earth's shadow, respectively. The eclipse period is defined as the time between these two points.

41.5.1 Eclipse geometry

The full geometry of a solar eclipse at a certain time instance can be described by a set of just 8 parameters: the Besselian elements, as explained in [17]. Six of these elements change rather smoothly with time, and can be described accurately with a low-order polynomial expression for the duration of the eclipse. The other two stay practically constant during one eclipse. Table 14 lists the Besselian elements with their symbol, description and unit. Some of the Besselian elements, which were not yet defined in Section 39.2.8, are illustrated in Figure 39.

The Besselian elements can be retrieved from NASA's solar eclipse website (currently [21], click on the gamma value of a certain eclipse) as third-order polynomials (with four coefficients c_n), and are evaluated at

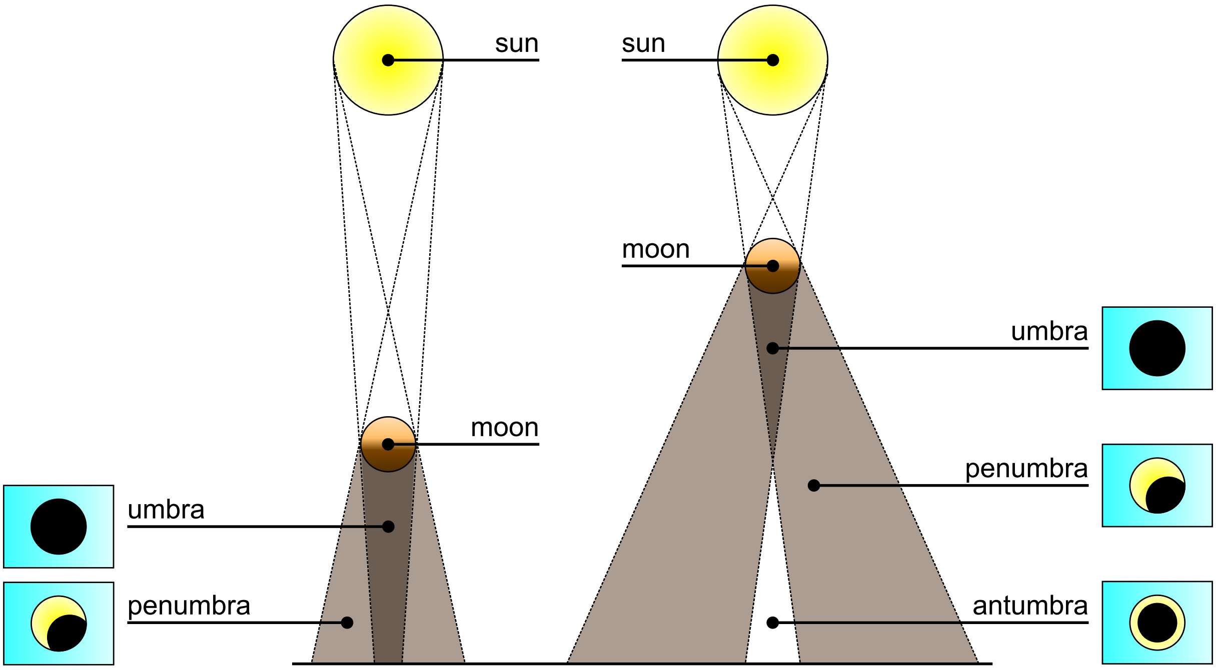

Figure 38: Definition of solar eclipse umbra (total eclipse), antumbra (annular eclipse) and penumbra (partial eclipse).

time t_1 as

$$b = \sum_{n=0}^{3} c_n t^n \ , \tag{155}$$

in which b is any Besselian element and t is obtained from

$$t = t_1 - t_0 \ , \tag{156}$$

by using the Besselian reference time t_0. All times here are in decimal hours (like a day consists of 24.0 hours).

symbol	**description**	**unit**
x	x-position of the shadow's axis in the fundamental plane	a
y	y-position of the shadow's axis in the fundamental plane	a
d	Declination of the shadow's axis from the equator plane	deg
l_1	Radius of the penumbral shadow circle on the fundamental plane	a
l_2	Radius of the (ant)umbral shadow circle on the fundamental plane	a
μ	Greenwich Hour Angle of the shadow's axis in the equator plane	deg
f_1	Penumbral vertex angle of the shadow's axis	deg
f_2	(Ant)umbral vertex angle of the shadow's axis	deg

Table 14: The symbol, description and unit of the Besselian elements, which describe the geometry of a solar eclipse at a certain time instance. The unit for distance is the Earth's equatorial radius a.

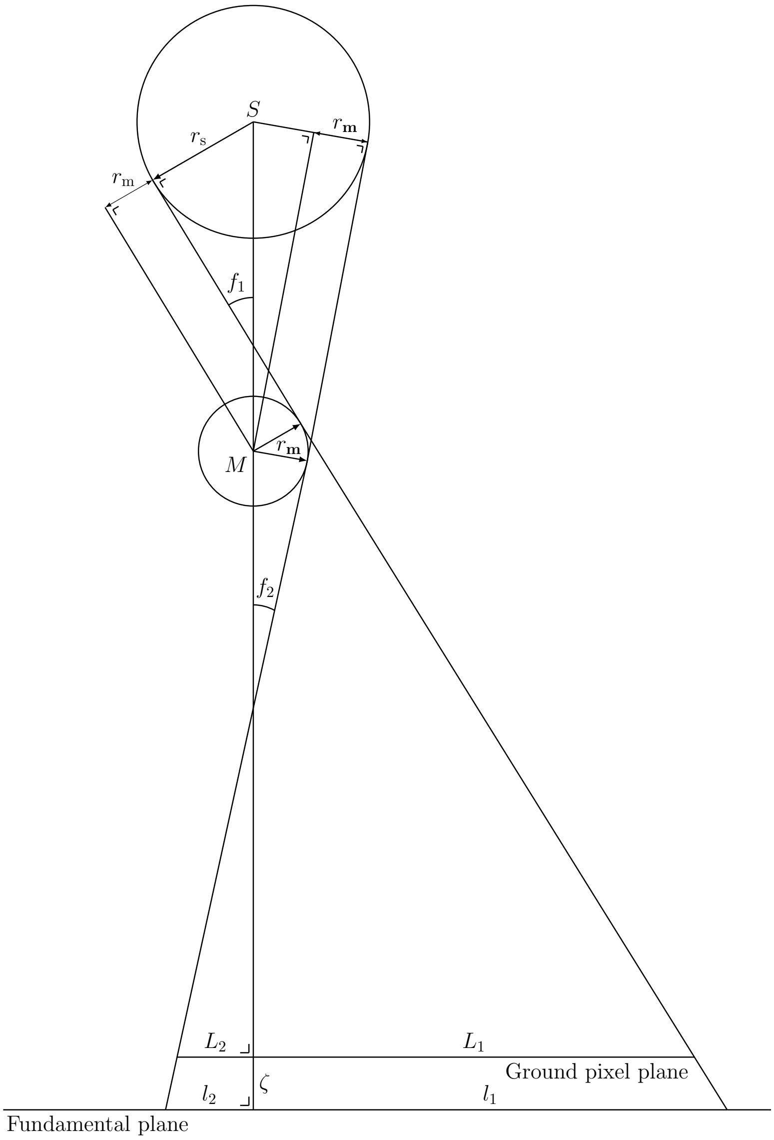

Figure 39: Definition of solar eclipse geometry parameters. Only l, L, f and ζ are used in the equations. When l_2 is negative, it defines an umbra, when it is positive, an antumbra. The latter is shown here. l_1 is always positive.

41.5.2 Eclipse period

From the Besselian elements, the eclipse period can be derived. For an eclipse shadow to fall on the surface of the Earth, the following condition must be fulfilled

$$\sqrt{x^2+y^2}-l_1<1\ , \tag{157}$$

that is, the distance of the shadow axis to the center of the Earth minus the penumbral shadow radius on the fundamental plane must be larger than 1 equatorial radius of the Earth. Thus, when

$$\sqrt{x^2+y^2}>l_1+1\ , \tag{158}$$

there is no eclipse shadow on the surface of the Earth, and when

$$\sqrt{x^2+y^2}=l_1+1\ , \tag{159}$$

the penumbral shadow of the eclipse is just starting or stopping to touch the Earth.

t_0 is always given as a whole decimal hour close to the point of greatest eclipse, and no eclipse lasts longer than six hours. The second equation can be tested numerically for a range of t, say [-4.0,+4.0], with a small stepsize Δt, and for each time t the polynomial expression is evaluated for the Besselian elements x, y and l_1. Starting at 0 and then both increasing and decreasing t, when the second equation is fulfilled, the time t respectively describes the beginning or the end of the eclipse. The accuracy depends on the size of the stepsize Δt.

41.5.3 Solar eclipse flagging

First, a check will be performed to determine if the measurement time lies within any of the eclipse periods from 2000 until 2100. This is done by adding the start and stop decimals hour of the day t of the eclipse period to the beginning of the Julian Day (TT) of the point of greatest eclipse, which is given with the Besselian elements, and converting to Julian Days since J2000 (TT). Furthermore, the measurement time is also converted to JD since J2000 (TT), after which they can be quantitatively compared. If the measurement time does not lie within any of the eclipse periods, the algorithm is exited and none of the ground pixels are flagged for this measurement.

If the measurement time does lie within an eclipse period, then for all ground pixels of this measurement it is checked whether or not any of its corner points lie in a penumbral, antumbral or umbral eclipse shadow at the measurement time. To this end the measurement time is converted to t_1 and then to t by making use of the Besselian reference time t_0.

For the eclipse at hand, all Besselian elements are evaluated with the polynomial expression. All geodetic corner points belonging to a ground pixel position, which was determined in Section 40.1.1, are converted to geocentric Cartesian coordinates as described in Section 39.2.4, after which they are transformed to the Fundamental reference frame by making use of Section 39.2.8 and the evaluated Besselian elements.

Then, as can be seen in Figure 39, the correct radius of the eclipse penumbral and L_1 ant(umbral) L_2 shadow are determined at the height of the ground pixel corner point above the fundamental plane as

$$L_1=l_1-\zeta\tan f_1\ , \tag{160}$$

$$L_2=l_2-\zeta\tan f_2\ , \tag{161}$$

in which ζ is the z-coordinate of the ground pixel corner point in the Fundamental reference frame. L_2 is negative for an umbral shadow, and positive for an antumbral shadow.

The distance D of the ground pixel corner point to the shadow axis is determined as

$$D=\sqrt{x^2+y^2}\ . \tag{162}$$

Then, a series of tests is performed for the corner points:

- If ζ is smaller than 0, the corner point lies on the far (night) side of the Earth with respect to the Sun, and can thus not be in an eclipse shadow.
- If l_2 is negative, and $0\leq D\leq|L_2|$, the corner point is in the umbral shadow of the eclipse.
- If l_2 is positive, and $0\leq D\leq L_2$, the corner point is in the antumbral shadow of the eclipse.
- If $|L_2|<D\leq L_1$, the corner point is in the penumbral shadow of the eclipse.
- If any of the ground pixel corner points are in any of the three shadow's of the solar eclipse, flag the ground pixel.

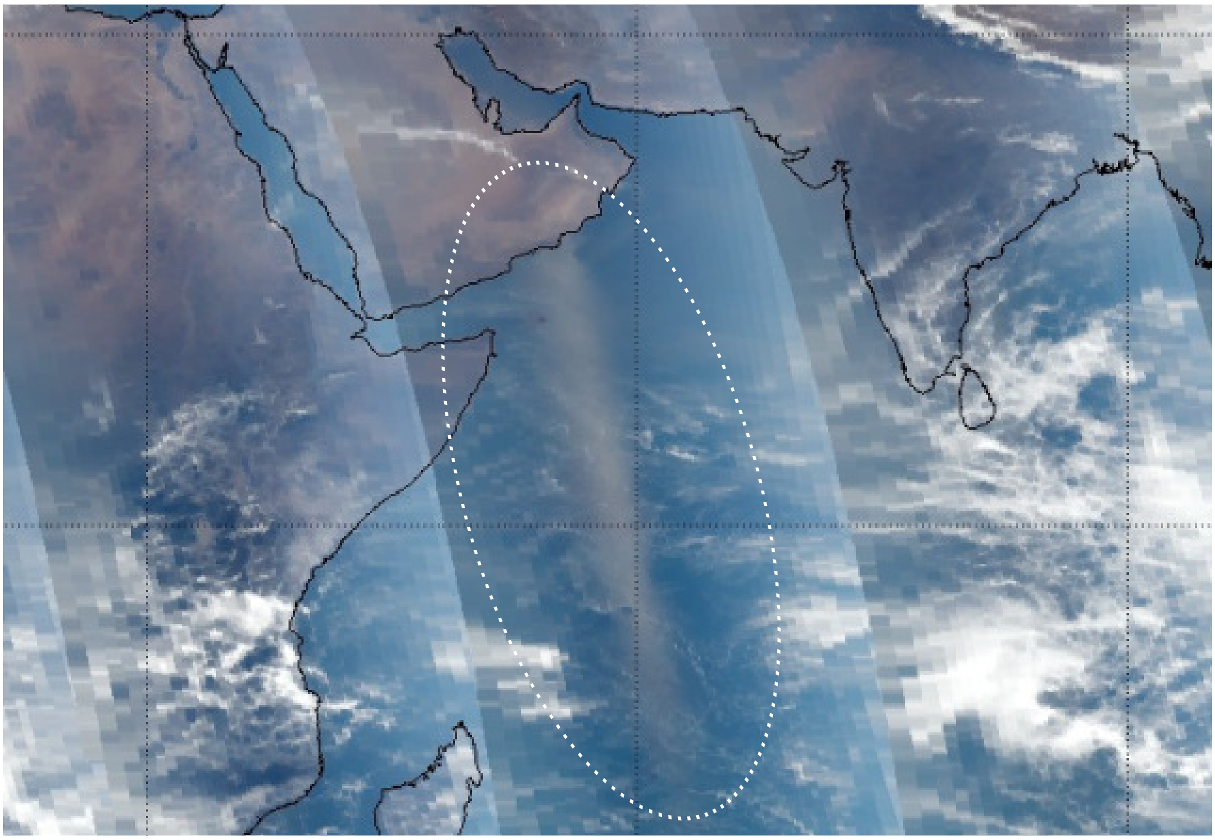

Figure 40: False-color image of OMI data collected on 29 March 2005, showing the sun glint off the coast of the Arabian peninsula. The area where sun glint occurs is indicated by a dotted line.

41.6 Ground pixel in Sun glint

When the spacecraft is crossing the equator and the local time is near noon, sun glint can occur above water when the sky is clear and the Sun is near ground pixel zenith. When these conditions occur, the surface reflectivity is increased, due to increasing specular reflection of sunlight by the sea surface. This effect is depicted in Figure 40, which shows the sun glint's effect on OMI data as a grey stripe in the middle of the swath.

Since sun glint may adversely affect Level-2 retrievals, the OMI L01b processor flags the ground pixels that are potentially affected by sun glint. Now, the extent of the area that is affected by sun glint and the magnitude of the effect depend on the smoothness of the (sea) surface. As this smoothness is unknown to the L01b processor, the sun glint flagging algorithm uses a static criterion, namely that the sun glint flag is raised if the scattering angle Θ is less than a threshold angle $\Theta_{\max}$:

$$\Theta = \arccos[\cos\theta\cos\theta_0 - \sin\theta\sin\theta_0\cos(\phi_0 - \phi)] \leq \Theta_{\max} , \tag{163}$$

in which θ_0 and θ are the zenith angles ($= \pi/2 - \varepsilon$) of the Sun and spacecraft, as seen from the ground pixel, respectively, while ϕ_0 and ϕ stand for the azimuth angle of the Sun and spacecraft, as seen from the ground pixel, respectively. Note that this criterion does not discriminate between ground pixels over land and those over water.

The value of $\Theta_{\max}$, based on TOMS, is 30 degrees. Although lower values have been used, e.g. in Sciamachy and GOME-2, the former choice will be the baseline until new information forces us to reassess this decision.

41.7 Ground pixel night

When a ground pixel is on the night side of the Earth, that is, there is no direct sunlight shining on it, the pixel is flagged as "night". When this happens, is determine by setting a limit on the Solar zenith angle θ_0. When this variable is larger than 90 degrees, the center of the Sun is geometrically belowe the horizon with respect to the center of the ground pixel. As the atmosphere refracts the lights downwards and the ground pixel has a certain extent until the corner points, the threshold Solar zenith angle technically needs to be set somewhat higher than 90 degrees. A ground pixel is currently flagged as “night”, when

$$\theta_0 > 90\ . \tag{164}$$

41.8 Ground pixel descending

When the spacecraft is in orbit from the South to the North pole, it is said to be ‘ascending’ (in latitude). The part of the orbit from the North towards the South pole, it is said to be ‘descending’. Similarly, for a ground pixel, it can be determined if it is ascending or descending. A ground pixel is flagged ‘descending’ when the latitude of one of the leading two ground pixel cornerpoints is smaller than the trailing one. This happens when either of the following equations holds true for the latitude values of the four corner points:

$$\delta_{\mathrm{corn},3} < \delta_{\mathrm{corn},0}\ , \tag{165}$$

$$\delta_{\mathrm{corn},2} < \delta_{\mathrm{corn},1}\ . \tag{166}$$

(167)

41.9 Ground pixel on boundary

When a ground pixel area within the cornerpoints overlaps with the dateline or pole (by definition a pole overlap is also a dateline overlap), a situation occurs whereby the longitude of the cornerpoints crosses the $+180 \rightarrow -180$ degrees boundary. In certain applications, it can be a challenge using these ground pixels for purposes like plotting or calculations. Therefore, these ground pixel are flagged as “boundary”. To determine when a ground pixel is crossing the dateline, the Geodetic coordinates are first converted to Cartesian coordinates in the Earth-fixed reference frame, like explained in Section 39.2.4. By definition, the dateline is defined by the XZ-plane on the negative side of the Y-axis of the Earth-fixed reference frame. Thus, when at least one of the Y-coordinates of all cornerpoints of a ground pixel is negative, while at least one other is positive *and* at least one of the X-coordinates is negative, the ground pixel must be crossing the dateline. This happens when *all* of the following equations hold true for at least one of the four cornerpoints *i*:

$$x_{\mathrm{geoc,corn,i}} < 0\ , \tag{168}$$

$$y_{\mathrm{geoc,corn,i}} < 0\ , \tag{169}$$

$$y_{\mathrm{geoc,corn,i}} > 0\ . \tag{170}$$

41.10 Row anomaly flagging

As discussed in Section 5.3.2 the instrument suffers from an anomaly which affects the quality of the OMI radiance data for all wavelengths at certain viewing angles, or rows, hence the name ’row anomaly’. From offline analysis the affected rows have been identified and are provided as calibration key data. The description of this flagging includes the orbit number that the anomaly starts (and ends), the affected detector rows, the severity of the impact and the nature of the anomaly, divided into a combination of Earth straylight, solar straylight, blocking of the incoming light and a wavelength shift of the light.

41.11 Transient pixel flagging

The purpose of the transient pixel flagging algorithm is to identify pixels that have anomalously high signal for a single measurement. These observed signal spikes are caused by the excess charge being dumped on a detector pixel by cosmic particles, mainly protons and electrons, impinging on the detector surface. Transient signals occur mostly in the South Atlantic Anomaly (SAA), but also outside it. We define transient signals as having the following three properties:

1. Since a transient signal dumps charge on a pixel, a transient signal only increases and never decreases the amount of signal. The increase is additive, not multiplicative.
2. The duration of a transient signal is so short that it covers only one single measurement. More specific, it is not expected that the duration is longer than the smallest exposure time.
3. The spatial extent of a transient signal is small but can cover multiple detector pixels. Even large regions are observed in the form of stripes, due to particles hitting the detector at low inclination angles.

To detect and flag the pixels affected by transient events that have these properties, two algorithms have been developed: one for calibration measurements like background, WLS, LED and Electronics measurements, and another for Radiance and Irradiance measurements. These algorithms take place in the processing flow after the binning correction, but before dark current correction.

41.11.1 Detection algorithm

The calibration measurements are relatively constant in time. For the same ICID/version group of measurements, the instrument settings are constant, and so is the light source. Thus, jumps in signal versus time can be identified by subtracting the signal of a pixel by its value in a subsequent or previous measurement, if they exist. To make the determination of this jump J more safe, the maximum of these two adjacent pixel signal values is taken before subtracting it.

$$J[\mathbf{x}_{\mathrm{img}},f] = S_{\mathrm{i}}[\mathbf{x}_{\mathrm{img}},f] - \max\left\{S_{\mathrm{i}}[\mathbf{x}_{\mathrm{img}},f-1], S_{\mathrm{i}}[\mathbf{x}_{\mathrm{img}},f+1]\right\} \tag{171}$$

For measurements at the beginning or end of a sequence, only one adjacent value is present, which is subtracted without taking any maximum. Furthermore, pixels with negative signal values are not taken into account.

To remove any natural signal jumps in time, the median of neighboring jump values is also determined.

$$\begin{aligned} J_{\mathrm{median}}[\mathbf{x}_{\mathrm{img}},f] = \mathrm{median}\{&J[r_{\mathrm{img}}+r, c_{\mathrm{img}}, f]\ \forall\, r \in \{-n_{\mathrm{row}}, -n_{\mathrm{row}}+1, \ldots, n_{\mathrm{row}}-1, n_{\mathrm{row}}\} \notin 0, \\ &J[r_{\mathrm{img}}, c_{\mathrm{img}}+c, f]\ \forall\, c \in \{-n_{\mathrm{col}}, -n_{\mathrm{col}}+1, \ldots, n_{\mathrm{col}}-1, n_{\mathrm{col}}\} \notin 0\} \end{aligned} \tag{172}$$

When a pixel is located at the edge of the detector region (band), only pixels that are inside this region are taken into account for the median set. Because transient events can span regions of pixels, care should be taken to make the area over which the median is taken large enough. In practice this means at least 5-10 unbinned rows or columns on either side should be taken into account.

The median jump of the neighbors is then subtracted from the pixel jump, after which the result is compared to a threshold value. When the following equation holds true, the pixel is flagged as transient.

$$J[\mathbf{x}_{\mathrm{img}},f] - J_{\mathrm{median}}[\mathbf{x}_{\mathrm{img}},f] > \frac{k}{\sqrt{n_{\mathrm{coadd}}[f] \cdot n_{\mathrm{bin}}[r_{\mathrm{img}},f]}} \tag{173}$$

The threshold value here is dependent on the number of co-additions n_{coadd} of the measurement, and on binning factor $n_{\mathrm{bin}}[r_{\mathrm{img}},f]$ of the image row. When flagged, the quality parameter Q of a pixel is decreased by multiplying it by $J_{\mathrm{median}}[\mathbf{x}_{\mathrm{img}},f]/J[\mathbf{x}_{\mathrm{img}},f]$.

In the above equations, the parameters defined as calibration key data (CKD) are the threshold value k and the number of rows n_{row} and columns n_{col} on either side of the pixel to include in the jump median region.

41.11.2 Transient signals in radiance and irradiance measurements

The radiance and irradiance measurements are not constant in time. The pixel signal value can have large natural jumps in measurement, row and column direction. To determine the jump of a pixel signal, the signal is estimated ($S_{\mathrm{est}}[\mathbf{x}_{\mathrm{img}},f]$) by scaling the spectrum of the adjacent measurements in the vicinity of the pixel. The median is then taken over a set of these estimated values to filter out outliers caused by neighboring transient signals or transient events affecting regions of more than one pixel.

$$S_{\mathrm{est}}[\mathbf{x}_{\mathrm{img}},f] = \mathrm{median}\left\{S_{\mathrm{i}}[\mathbf{x}_{\mathrm{img}},f+m] \cdot \frac{S_{\mathrm{i}}[r_{\mathrm{img}}, c_{\mathrm{img}}+c, f]}{S_{\mathrm{i}}[r_{\mathrm{img}}, c_{\mathrm{img}}+c, f+m]}\ \forall\, c \in \{-n_{\mathrm{col}} < c \leq n_{\mathrm{col}}, c \neq 0\}\ \forall\, m \in \{-1,1\}\right\} \tag{174}$$

When a pixel is located at the edge of the detector region (band), only pixels that are inside this region are taken into account for the median set. Signals smaller than zero are not taken into account.

Subtracting the estimated signal from the pixel signal value then yields the signal jump $J[\mathbf{x}_{\mathrm{img}},f]$, while dividing yields the jump factor $J_{\mathrm{factor}}[\mathbf{x}_{\mathrm{img}},f]$.

$$J[\mathbf{x}_{\mathrm{img}},f] = S_{\mathrm{i}}[\mathbf{x}_{\mathrm{img}},f] - S_{\mathrm{est}}[\mathbf{x}_{\mathrm{img}},f] \tag{175}$$

$$J_{\mathrm{factor}}[\mathbf{x}_{\mathrm{img}},f] = \frac{S_{\mathrm{i}}[\mathbf{x}_{\mathrm{img}},f]}{S_{\mathrm{est}}[\mathbf{x}_{\mathrm{img}},f]} \tag{176}$$

A pixel is now flagged as transient when either the jump or the jump factor exceed a threshold value.

$$J[\mathbf{x}_{\text{img}}, f] > k \tag{177}$$

$$J_{\text{factor}}[\mathbf{x}_{\text{img}}, f] > k_{\text{factor}} \tag{178}$$

Due to errors made in the estimation, these thresholds are only applied to estimated signal values larger than this threshold $S_{\text{est}}[\mathbf{x}_{\text{img}}, f] > k$, while for signals smaller then the threshold value a lower jump threshold applies, but no jump factor threshold.

$$J[\mathbf{x}_{\text{img}}, f] > k_{\text{low}} \tag{179}$$

In the above equations, the parameters defined as CKD are the threshold values k, k_{factor} and k_{low} and the number of columns n_{col} on either side of the pixel to include in signal estimation scaling. When flagged, the quality parameter Q of a pixel is decreased by dividing it by the jump factor $J_{\text{factor}}[\mathbf{x}_{\text{img}}, f]$.

41.12 Detector pixel quality flagging

Based on in-flight calibration, maps of the detector pixel quality are produced. These DPQF maps consist of real values between 0 (lowest quality) and 1 (highest quality) for each detector pixel. These values only make sense for image section pixels. Therefore, pre-, post-, or overscan pixels are not represented in the maps. Binning in the context of this algorithm means taking the minimum of the quality flag of the individual unbinned pixels.

A defective pixel is not used for the calculation of correction parameters. For example for the straylight correction the defective pixels are excluded while ensuring that a sufficient number of pixels remain for the straylight algorithm to function properly. However, all subsequent L01b Processor algorithms are applied to all image pixels, including the defective ones. The resulting data is not useful for scientific purposes but may still be useful for calibration and monitoring products.

41.13 Random telegraph signal pixels

Random telegraph signal (RTS) refers to the phenomenon where the dark current of pixels is jumping between distinct levels with time. The frequency of these jumps is higher for higher temperature. RTS is mainly caused by cosmic radiation.

In case an image pixel displays RTS behavior, it is not used for the calculation of correction parameters. However, as with defective pixels, all subsequent L01b Processor algorithms are applied to all image pixels, including the ones showing random telegraph signal. The resulting data is not useful for scientific purposes but may still be useful for calibration and monitoring products.

The background radiance signal, being constituted mainly of dark current, is constructed on a daily basis during the OMI mission. As this involves multiple orbits, sufficient statistics is available to monitor the noise per pixel, see also Section 25. The frequency and size of dark current jumps results in a higher than expected noise; this is translated into an RTS level factor per pixel. An unbinned pixel map of RTS level factors is the calibration key data input for the L01b Processor. From unbinned (detector) pixel maps, binned (image) pixel maps are constructed. The conversion rule is that the RTS level factor of a binned pixel is the average of the RTS factors of the unbinned pixels. If, after binning, the RTS level factor is above a certain threshold, the L01b Processor will set an RTS flag in the corresponding L01b product map.

41.14 Saturation flagging

In case of high signals or improper instrument configuration, saturation of the signal or an overflow may occur. This can happen in several places:

- pixel full well saturation
- register full well saturation
- DEM saturation
- ADC overflow
- co-addition overflow

If a pixel is flagged for any of these reasons, it will not be used in calculations. However, it will be used in subsequent correction algorithms in the L01b processor, even though the eventual computed radiance or irradiance is not useful for scientific purposes.

Pixel full well saturation occurs if an individual detector pixel holds too many electrons. Since the excess signal may spill over into adjacent pixels ('blooming' or 'crosstalk'), this not only makes the signal data of the saturated pixel unreliable, but potentially also the surrounding pixels. For images without binning and and co-addition, pixel full well saturation can be detected by comparing the observed signal with the known pixel full well value. For binned and/or co-added images, the signals for individual detector pixels are lost, so that in this case, pixel full well saturation of a single detector pixel may go unnoticed if the detector pixels with which it is binned or co-added together are not saturated. Therefore, pixel full well saturation of the combined image pixel can only be detected if most of the constituent detector pixels are saturated, although data from the small pixel column may provide some more information on saturation of individual binned detector pixels. For radiance and irradiance measurements the instrument settings are such, that in general pixel full well does not occur.

Register full well saturation occurs if a CCD read-out register pixel holds too many electrons. This may occur without pixel full well saturation if the binning factor is high enough. Conversely, in the case with pixel full well saturation and low binning factor, the register will not be saturated. Register full well saturation is detected by comparing the observed signal with the known register full well value.

For high signals an amplifier in the the analogue chain in the DEM can saturate. This results in an underflow of the signal and is therefore flagged as such (and not as "'saturated"') in the spectral_channel_quality flag.

ADC saturation occurs if the signal is such that it overflows the ADC. This is checked on-board for each co-addition separately. If ADC saturation is detected for a single co-addition, the combined co-added signal is set to a special value in the Level-0 data. If the L01b processor finds such a special value, it flags the pertinent pixel as saturated. Also, when multiple measurements are co-added, they might overflow their particular storage, even when the individual measurements do not overflow the ADC.

Co-addition overflow occurs if an improper instrument configuration is chosen where the co-addition is larger than 16. With the instrument using the nominal baseline settings, this is not expected to occur.

41.15 Other notable flags

41.15.1 Offset flagging

In case the dynamic offset as described in Section 19 deviates strongly from the static offset provided in the calibration key data, a flag is raised.

41.15.2 Thermal instability

Non-nominal temperatures can have an impact on the calibration status of the data, notably the spectral calibration. Measurements are flagged if the temperatures of the detectors or the optical bench are outside their nominal range.

Part VI

Appendix

A Philosophy on noise and errors

The leitmotiv of this document is the tension between what we know about the instrument and the physics, and our understanding and apprehension of the observations that the instrument generates. The three large parts in this document, the instrument description, the forward model and the reverse model, reflect this tension. The instrument transforms the signals we want to know, i.e. irradiance and radiance, into mere digital numbers. This process is described in the forward model, which in turn makes use of the combined understanding of the instrument (described in the instrument model) on the one hand and physics on the other hand. The reverse model describes our attempt to invert, as completely as possible, the forward path of the signals. The resulting *reconstructed* radiance and irradiance signals should be viewed with this thought in mind. In order to obtain a better grasp of the caveats involved, we formally divide the level 1b product into three parts. This will be explained below.

A.1 Signal, noise and error

It is important to make a strict distinction between noise and error.

A.1.1 Error

The reverse model is implemented in the L01b Processor: a set of consecutive algorithms that transforms a specific measured signal leaving the instrument back towards (ir)radiance entering the instrument.

During this process, *errors* can be introduced at every step. A specific pixel on the ground is observed only once, under specific illumination conditions. The radiance at the entrance of the instrument is transformed in one digital number, that has no associated error. The processor will apply the required corrections to that digital number to arrive at the best estimate of the photon count at the entrance of the instrument. In this process, two kinds of errors are made.

Algorithm errors Each algorithm in the processor is associated with some step in the forward model. In an ideal situation, the algorithm applies exactly the inverse operation as the associated forward step. For example, an offset that is added to the signal in the forward model is corrected in the reverse model by subtracting the same offset. In this example, the inverse operation can be described exactly and no information is lost. However, some steps in the forward model involve information loss by reducing data (binning, co-addition). Other steps are in theory deterministic and therefore invertible while in practice some approximations and discretizations have to be made (e.g., in the case of straylight). Further, numerical errors can occur. Examples are long computations that cause loss of significance (like algorithms for computing standard deviations) and matrix inversion by iterative methods.

Calibration errors Most (but not all) correction steps consist of applying additive or multiplicative operations to the signal. The terms and factors have been acquired from on-ground and in-flight calibration. These so-called calibration key data parameters (CKDs) contain errors. These errors can originate from measurement noise (more on this below) or from the calibration algorithms that extract the CKD from raw measurement data. Calibration errors can operate on different scopes. The error on gain ratio affects the entire measurement while an error in pixel-response non-uniformity (PRNU) is pixel-dependent.

Whatever their origin, the calibration and algorithm errors are systematic in the sense that they operate on each input signal and they will change a signal. If a particular signal is fed twice to the processor, the calibration errors will change the signal in exactly the same way. In the reverse model, we can calculate the associated variance due to the various calibration and algorithm errors in each step. These systematic errors are propagated together with the signal. Note that at the start, before any algorithm has been applied, the signal has no variance.

A.1.2 Noise

Now consider the situation that a ground pixel has been measured several times. Each of the digital numbers is propagated through the reverse model, acquiring propagated variances stemming from the same systematic algorithm and calibration errors. However, these digital numbers at the start are not the same. This is due to *measurement noise*, or noise in shorthand. The idea is that an estimate of the noise is provided together with a single signal measurement. This is not quite a contradiction: we repeat that an individual measurement contains no noise. However, theory and/or associated measurements give information of the noisiness of the signal. Measurement noise is, stemming from two physical sources, split into two terms: read-out noise and shot noise.

Read-out noise Read-out noise is a consequence of the imperfect operation of the physical electronic detector chain. This involves the whole process from the incidence of photons on the detector pixel, the amplifiers, the conversion from electrons to volts to digital numbers. The read-out noise does not depend on the magnitude of the signal. Read-out noise can be injected in the reverse model in two ways:

- It is actually a CKD in itself; it is a by-product of the offset determination calibration algorithm. The variations of the offset in the same picture during several measurements provide the estimate of the read-out noise.
- The current measurement, containing thousands of pixels, can provide information about the read-out noise from a subset of these pixels with known behavior.

Once the estimate has been made, somewhere in the processing chain, it has to be transferred through the conversion steps in order to compare it with the resulting (ir)radiance signal.

Shot noise Shot noise exists because light and electric current consist of the movement of discrete ‘packets’. These packets are photons in the case of light and electrons in the case of electric current. Light coming from the Sun hits a detector pixel, which creates an electric charge. The fundamental physical processes that govern light emission are such that these photons are emitted from the Sun at random times; but the many billions of photons are so many that the brightness of the Sun, expressed as the number of photons per unit time, varies only infinitesimally with time.

However, if the amount of light and the size of the receiving pixel is small, only a moderate amount of photons hit the specific pixel every second. Thus the relative fluctuations in number of photons, i.e. the signal received by the detector pixel will be significant, just as when tossing a coin a few times. These fluctuations are shot noise. The process is adequately described by a Poisson distribution. The standard deviation of the shot noise is equal to the square root of the number of electrons generated. This shot noise transfers through the correction steps in the reverse model. Details follow in Section A.3.

A.1.3 Summary

To summarize, the processor provides for each measurement the following three quantities:

- The signal, as reconstructed by the algorithm chain, in radiance/irradiance units.
- The error, stemming from calibration and algorithm errors, propagated through the same chain using formal error propagation rules and expressed in the associated radiance/irradiance units.
- The noise, consisting of shot noise and read-out noise, converted to the radiance/irradiance units. In Section A.3, the propagation of the two measurement noise terms is further explained.

A.2 Signal propagation and flagging

The signal S is propagated in the L01b processor from one algorithm to the next: the output signal S_o of one algorithm is the input signal S_i for the next. However, signal values are used in an algorithm depending on an assessment of their quality. This quality assessment is performed in a number of so-called flagging algorithms that assign quality flags and quality numbers to image pixels, ground pixels, or measurements. See Section 41.12 for more information on quality assessment.

The philosophy in the algorithms of the L01b is that it calculates correction parameters using only image pixels that may be considered reliable. That is, image pixels that are flagged ‘defective’ or ‘missing’, or for which a processing error has occurred in a previous correction algorithm, may not occur on the right-hand side of an equation describing the correction of another pixel.

On the other hand, the calculated correction parameters are applied to *all* image pixels, even those with errors. Even though the signal values for such image pixels are not useful for scientific purposes, they may still be of use for calibration purposes. Thus, flagged pixels may occur on the left-hand side of an equation describing the current correction algorithm. The exception is that image pixels for which data is missing, are not corrected.

Like the signal and the noise, the quality flags are also propagated through the L01b processor; i.e., they are updated if in a particular algorithm certain conditions are met. At the end of processing, quality assessment information is added as annotation data to the Level-1b data products so that users may use it to assess the quality of the Level-1B data and filter them before use.

A.3 Measurement noise propagation

We described in the introduction (and Section A.1.2) the two types of measurement noise. We now elaborate on their role in the reverse model.

Read-out noise Read-out noise can be administrated in the reverse model once the signal has passed, in the reverse sense, the electronic circuit. The read-out noise annotation is defined in electrons. It is applied after the non-linearity correction. The read-out noise $\varepsilon^2_{\text{readout}}$ can be acquired from a CKD or by using data from the current measurement. In both cases, we have to take the number of co-additions of the current measurement into account, see below. The noise depends on the band and the gain setting. However, it does not depend on the magnitude of the signal. Introducing the read-out noise halfway in the processing flow requires the unit conversion algorithms later in the processing flow to also convert this noise. The binning division algorithm does not play a role here since this noise occurs at the read-out node. Other elementary correction algorithms do not influence the read-out noise: only the signal changes, while the read-out noise has already been defined.

Shot noise The shot noise can be computed once, in the forward model sense, the number of photons from the Sun have been converted to electrons and the signal has been corrected for effects that are independent of the generated amount of electrons. We can therefore choose to establish the shot noise somewhere between the end of the voltage-to-charge algorithm and the start of the exposure time division. It can be argued that we want to start with the signal that has undergone the smallest number of corrections, since that signal has actually been measured. Hence the choice to inject the noise directly after the read-out noise annotation. In this way, we count the number of electrons in a large, binned pixel.

Note that another location choice (e.g. after the smear correction algorithm) would alter the signal-to-noise ratio slightly, but has otherwise no large impact since binning effects cancel.

A.4 Noise propagation in forward and reverse directions; rules and characteristics

Our goal is to define the noise at each stage in the reverse model. In particular, we need values for the shot noise and read-out noise near the start of the reverse model. In order to do that, we must follow the path, in the forward model, from the ‘creation’ of the noise towards the end (when the signal is actually read). In these forward steps, we consider the physical changes that occur, such as conversions and the co-addition of several signals into one combined signal. The measurement noise in these steps is expressed algebraically (as a function of signal, instrument settings and CKDs), since we do not know the actual signal and CKD yet. At the end of the forward model, we can read the signal in digital numbers; only then can we define the start value for the measurement noise. Then, following the reverse model, we can propagate the measurement noise, along with the signal in a purely mathematical way, both algebraically and explicitly.
We use the following assumptions:

Shot noise is defined as the noise of a measurement, measured in electrons, registered by a binned pixel $\mathbf{x}_{\text{img}}$. The value of the shot noise (expressed as variance, with unit electrons squared) is equal to the number of electrons of the signal (in electrons) itself. It does not matter if we consider the shot noise of a large binned pixel or the n_{bin} shot noise values of the original detector pixels (each with its own signal S_i). In the first case, the shot noise equals $s^2_{\text{shot}}\{\sum_{\text{bins}} S_i\} = \sum_{\text{bins}} S_i$. In the second case, the total shot noise is $\sum_{\text{bins}} s^2_{\text{shot}}\{S_i\} = \sum_{\text{bins}} S_i$.

Note that we use the bracket notation $\{\cdots\}$ to link the noise to the signal at a certain stage (see also the symbol table below).

Read-out noise is the noise, measured in volts, at the read-out node. It depends on the electronic settings: gain and offsets. It is always measured for a binned pixel (signals are per definition binned before they are read out). Alternatively, the read-out noise can also be expressed in electrons (this is just a standard conversion) to align it with the shot noise.

Propagation of noise is purely mathematical for multiplicative algorithms in the reverse model, in particular the algorithms where the unit of the signal changes. There are no rules to cope with additive algorithm steps. In this way, the signal-to-noise ratio along the entire algorithm chain will approximately be the same, except for signals where offset contributions are relatively large.

Parameter	Description	Units
$S_{i,\mathrm{source}}$	Signal generated at binned pixel, un-coadded measurement	e$^-$
$S_{i,\mathrm{DN}}$	Signal propagated towards read-out node, un-coadded measurement	DN
$S_{\mathrm{meas,DN}}$	Co-added signal, at start of reverse model, as measured	DN
S'_{DN}	Signal after co-addition correction	DN
S'_{source}	Signal after voltage-to-charge correction	e$^-$
$S'_{\mathrm{corr-bin}}$	Signal after binning correction	e$^-$
$S'_{\mathrm{corr-dc}}$	Signal after dark current correction, before residual correction	e$^-$
$S'_{\mathrm{res,corr-dc}}$	Residual signal before residual correction	e$^-$
$S'_{\mathrm{corr-res}}$	Signal after residual correction	e$^-$
$s^2_{\mathrm{meas}}\{S_{i,\mathrm{source}}\}$	Measurement noise, when created, of a single measurement	e^{-2}
$\varepsilon^2_{\mathrm{ckd}}$	read-out noise as CKD parameter	e^{-2}
$s^2_{\mathrm{meas}}\{S_{i,\mathrm{DN}}\}$	Measurement noise, propagated towards read-out node, of a single measurement	DN^2
$s^2_{\mathrm{meas}}\{S_{\mathrm{meas,DN}}\}$	Measurement noise of co-added signal, start of reverse model	DN^2
$s^2_{\mathrm{meas}}\{S'_{\mathrm{DN}}\}$	Measurement noise of after co-addition correction	DN^2
$s^2_{\mathrm{meas}}\{S'_{\mathrm{source}}\}$	Measurement noise after voltage-to-charge correction	e^{-2}
$s^2_{\mathrm{meas}}\{S'_{\mathrm{corr-bin}}\}$	Measurement noise after binning correction	e^{-2}
$s^2_{\mathrm{meas}}\{S'_{\mathrm{res,corr-dc}}\}$	Measurement noise of an aggregated residual signal	e^{-2}
$s^2_{\mathrm{meas}}\{S'_{\mathrm{corr-res}}\}$	Measurement noise after residual correction	e^{-2}

We consider a binned pixel of a measurement S_i, $1 \leq i \leq N_{\mathrm{coadd}}$ that is part of a co-addition. We start, in forward sense, at the read-out register with the signals $S_{i,\mathrm{source}}[\mathbf{x}_{\mathrm{img}}]$. These signals are measured in electrons (e$^-$). The measurement noise, defined as the sum of read-out noise and shot noise, is:

$$s^2_{\mathrm{meas}}\{S_i,\mathrm{source}\}[\mathbf{x}_{\mathrm{img}}] = S_{i,\mathrm{source}}[\mathbf{x}_{\mathrm{img}}] + \varepsilon^2_{\mathrm{ckd}}[\mathbf{x}_{\mathrm{img}}] \quad \text{in e}^{-2}\ . \tag{180}$$

Here we use the fact that the shot noise variance is equal to the signal itself. The pixel index for the read-out noise is skipped for simplicity. Further, it has no frame index i attached since its estimation stems from previous data: it is a CKD parameter.

Proceeding in forward direction, the signal undergoes some conversions to arrive in digital units at the start of the co-addition register. These conversions are, in this order: conversion from charge to voltage; the multiplication by relative and absolute gain; and the conversion from voltage to digital numbers. The conversions are lumped together in a factor k; the measurement noise, therefore, is multiplied by a factor k^2. More specifically:

$$S_{i,\mathrm{DN}} = kS_{i,\mathrm{source}}\ , \tag{181}$$

$$s^2_{\mathrm{meas}}\{S_{i,\mathrm{DN}}\} = k^2(S_{i,\mathrm{source}} + \varepsilon^2_{\mathrm{ckd}})\ . \tag{182}$$

Then, all N_{coadd} signals are added together to one signal that is actually measured: $S_{\text{meas,DN}}$. For the measurement noise, we use the summation rule for uncorrelated variables.

$$S_{\text{meas,DN}} = \sum_{i=1}^{N_{\text{coadd}}} S_{i,\text{DN}} = k \sum_{i=1}^{N_{\text{coadd}}} S_{i,\text{source}} \ , \tag{183}$$

$$\begin{aligned} s^2_{\text{meas}}\{S_{\text{meas,DN}}\} &= \sum_{i=1}^{N_{\text{coadd}}} s^2_{\text{meas}}\{S_{i,\text{DN}}\} = k^2 \sum_{i=1}^{N_{\text{coadd}}} (S_{i,\text{source}} + \varepsilon^2_{\text{ckd}}) \\ &= kS_{\text{meas,DN}} + k^2 N_{\text{coadd}} \varepsilon^2_{\text{ckd}} \ . \end{aligned} \tag{184}$$

Note that $\varepsilon^2_{\text{ckd}}$ is still defined in e^{-2}. Equation (184) immediately provides the starting values for the shot noise and the read-out noise; we only need the measured signal in DN, the read-out noise CKD in electrons, the total conversion factor from electrons to digital numbers and the co-addition number. Note that the total conversion factor will depend on the electronics settings, more specific the combination of gain settings (denoted by the gain code $\mathbf{g}$): $k = k(\mathbf{g})$.

From now on, we follow the reverse model back to where we started. We have a single signal and its propagation is purely mathematical. Likewise, the related noise is propagated in the multiplicative algorithms. First, the co-addition division gives a factor $1/N^2_{\text{coadd}}$ in the measurement noise.

$$S'_{\text{DN}} = \frac{1}{N_{\text{coadd}}} S_{\text{meas,DN}} \ , \tag{185}$$

$$\begin{aligned} s^2_{\text{meas}}\{S'_{\text{DN}}\} &= \frac{1}{N^2_{\text{coadd}}} \left(kS_{\text{meas,DN}} + k^2 N_{\text{coadd}} \varepsilon^2_{\text{ckd}}\right) \\ &= \frac{1}{N_{\text{coadd}}} \left(kS'_{\text{DN}} + k^2 \varepsilon^2_{\text{ckd}}\right) \ . \end{aligned} \tag{186}$$

Then, the inverse conversion to electrons cancels the factor k^2. Therefore, the signal and the measurement noise at the injection point after the voltage-to-charge conversion algorithm are defined as

$$S'_{\text{source}} = \frac{1}{k} S'_{\text{DN}} \ , \tag{187}$$

$$s^2_{\text{meas}}\{S'_{\text{source}}\} = \frac{1}{N_{\text{coadd}}} \left(S'_{\text{source}} + \varepsilon^2_{\text{ckd}}\right) \ . \tag{188}$$

Here we have another good point to establish the measurement noise. Given the read-out noise CKD and the signal value at this stage, we have to divide both components by the number of co-additions. If it is not deemed necessary to have the measurement noise available at the first steps in the reverse model, this is the preferred alternative starting point.

We continue to follow the signal in the reverse model. Note that from now on, the measurement noise is virtual but we want to provide it to the L01b product. Binning gives an extra factor n^2_{bin} to the noise. Note that one power of n_{bin} vanishes in the shot noise part:

$$S'_{\text{corr}-\text{bin}} = \frac{1}{n_{\text{bin}}} S'_{\text{source}} \ , \tag{189}$$

$$s^2_{\text{meas}}\{S'_{\text{corr}-\text{bin}}\} = \frac{1}{N_{\text{coadd}}} \left(\frac{1}{n_{\text{bin}}} S'_{\text{corr}-\text{bin}} + \frac{1}{n^2_{\text{bin}}} \varepsilon^2_{\text{ckd}}\right) \ . \tag{190}$$

After the binning correction, conversions for exposure time division and to (ir)radiance units follow, giving the virtual measurement noise for the L01b product.

B Binning

Some of the following information is reproduced from the TROPOMI ATBD [8].

B.1 Binning tables

Many CKD parameters are derived on detector resolution. To use these CKD parameters in an algorithm, they will first have to be binned in the same way as the measurement has. For this, the concept of the 'row binning table' is introduced.

A binning table consists of a number of entries. Each entry consists of a) the binning factor, and b) the number of *image* rows or *image* columns for which that binning factor applies. In case rows or columns are skipped, this is indicated in a binning table entry with a binning factor of 0 and the number of *detector* rows or *detector* columns that are skipped. In a binning table, the entries are listed in increasing row or column number.

For OMI, there are restrictions to the way in which row binning can occur. The binning occurs through a fixed scheme of rows that are binned and skipped. This scheme is described in Table 15. The detector is always read-out in the order of this scheme. Within the L01b Processor, this instrument binning scheme is translated to a more generic data structure.

ID	minimum binning factor	maximum binning factor	binning factor resolution	binned rows range	remark
ROR	1	1	1	1	read-out register; may be used for e.g. offset determination. The ROR will always be read out.
LDA	0	20	20	1*	Lower dark area, intended for reading out the shielded rows close to the ROR.
SkipRows1	0	14	2	0	Skip rows, intended for skipping / discarding the transition rows from the shielded to the non-shielded area.
LSA	0	28	4	1*	Lower straylight area, intended for reading out unshielded rows that are not illuminated by the spectrometer output. These can be used for e.g. straylight estimation.
SkipRows2	0	511	1	0	Skip rows, intended for skipping / discarding the transition rows between the straylight area and the spectrometer output area.
Image	0	15	1	0..255	Image area, intended for reading the area that is illuminated by the spectrometer output. Variation of the binning factor can be used to change the cross-track spatial resolution of the instrument.
SkipRows3	0	252	4	0	Skip rows, intended for skipping / discarding the transition rows between the spectrometer output area and the second straylight area.
USA	0	28	4	1*	Upper straylight area, intended for reading out unshielded rows that are not illuminated by the spectrometer output. These can be used for e.g. straylight estimation.
SkipRows4	0	14	2	0	Skip rows, intended for skipping / discarding the transition rows from the non-shielded to the shielded area.
UDA	0	14	2	1*	Upper dark area, intended for reading out the shielded rows furthest away from the ROR.

Table 15: OMI binning scheme. The binning resolution specifies the step size with which the binning factor can be configured. For example, LDA can be set to 0 or 20, LSA can be set to 0, 4, 8, ... 28. For areas with the binned rows marked with *, setting a binning factor of 0 will caused these areas to be skipped, i.e. there will be no binning and no read-out.

In addition, there are limitations within the instrument that restrict the total number of pixels that can be read-out. The maximum read-out time of 400 ms allows to read approximately 52000 pixels. In addition, the total number of pixels that can be downlinked is restricted to 57316, including the small pixels. For the most commonly used measurements, the Earth radiance measurements, the binning scheme as described in table 16 is used. The instrument is also operated regularly in a spatial zoom-in mode for radiance measurements, using the binning scheme in Table 17.

ID	**binning factor**	**binned rows**	**unbinned rows**	**detector start row**	**detector end row**
ROR	1	1	1	0	1
LDA	20	1	20	1	21
SkipRows1	12	0	12	21	33
LSA	12	1	12	33	45
SkipRows2	4	0	4	45	49
Image	8	60	480	49	529
SkipRows3	4	0	4	529	533
USA	20	1	20	533	553
SkipRows4	4	0	4	553	557
UDA	14	1	14	557	571

Table 16: OMI binning scheme for global Earth radiance measurements.

ID	**binning factor**	**binned rows**	**unbinned rows**	**detector start row**	**detector end row**
ROR	1	1	1	0	1
LDA	20	1	20	1	21
SkipRows1	12	0	12	21	33
LSA	12	1	12	33	45
SkipRows2	124	0	124	45	169
Image	4	60	240	169	409
SkipRows3	124	0	124	409	533
USA	20	1	20	533	553
SkipRows4	4	0	4	553	557
UDA	14	1	14	557	571

Table 17: OMI binning scheme for spatial zoom-in Earth radiance measurements.

The restrictions on the number of pixels that can be read out also mean that it will be impossible to read out the detector at its full resolution. There are two solutions to overcome this. For long exposure measurements, which are typically used for dark current characterization, the instrument provides a separate long exposure mode. For this long exposure mode, the exposure time is set to a multiple of the master clock period (MCP) and the detector can also be read out in a multiple of master clock periods. During this read-out across MCPs, the detector is not cleared using a frame transfer. Thus, each MCP a next part of the detector is read out, allowing to read out the full detector in 10 MCPs.

The second option is read out the detector in a multiple of measurements. For this, the LDA, LSA, USA and UDA are set to binning factor 0. The Image binning factor is set to 1, the number of binned image rows to 58. The SkipRows settings are varied, so that for the first measurement, the first 58 rows of the detector are read. In the next measurement, the next 58 rows are read, and so on, until after 10 separate measurements, the full detector has been read. This method is of course only suitable if the measured signal is not changing from measurement to measurement. It is therefore only suitable for specific calibration measurements. The L01b Processor will recognize this sequence of measurements and combine the individual measurements into a single measurement for processing.

B.2 Effects of binning on signal and variance

All algorithm steps in the reverse model are applied to image pixels. However, pixel-dependent CKD parameters are provided unbinned, while the signal that is to be corrected is binned. The concerned algorithms are PRNU, straylight, slit irregularity and (ir-)radiance responsivity. (Note that the binning correction algorithm step, which is in itself a simple multiplication, is not related to this issue.) The binning process in the ROR has two negative effects on the correctness of the model: both the signal itself and its error propagation are affected. These effects are discussed below.

B.2.1 Effect of binning on the signal

Consider a group of N consecutive detector pixels $\mathbf{x}_{\mathrm{det},r}$ on the same column c but different rows r. Then consider that these are binned together into an image pixel $\mathbf{x}_{\mathrm{img}}$. Thus N is the binning factor. Forgetting about the column number c, and writing $r = r_{\mathrm{det}}$ and $R = r_{\mathrm{img}}$, the average binned input signal for the image pixel is expressed in terms of the original input signals of the binned detector pixels as

$$S_{\mathrm{i}}[R] = \frac{1}{N}\sum_r S_{\mathrm{i}}[r] \; . \tag{191}$$

Note that the individual $S_{\mathrm{i}}[r]$ are not known to the L01b Processor, but for this section, it is assumed that they are. Consider now two hypothetical corrections, one additive and one multiplicative, on this input signal. The additive terms and multiplicative factors for these corrections are available as unbinned calibration key data parameters $c[r]$ and $d[r]$, respectively. To apply these corrections on the binned input signal $S_{\mathrm{i}}[R]$, these CKD parameters have to be binned likewise:

$$c[R] = \frac{1}{N}\sum_r c[r] \; ; \tag{192a}$$

$$d[R] = \frac{1}{N}\sum_r d[r] \; . \tag{192b}$$

Now, in the L01b Processor, the additive correction would be implemented as:

$$S_{\mathrm{o,computed}}[R] = S_{\mathrm{i}}[R] + c[R] = \frac{1}{N}\sum_r S_{\mathrm{i}}[r] + \frac{1}{N}\sum_r c[r] \; . \tag{193}$$

If, however, the correction could be applied before binning,

$$S_{\mathrm{o,true}}[R] = \frac{1}{N}\sum_r \left(S_{\mathrm{i}}[r] + c[r]\right) \; , \tag{194}$$

it is clear that the exact same result is obtained. For the multiplicative correction, however, the computed and true results are not equal. The computed result is:

$$S_{\mathrm{o,computed}}[R] = d[R] S_{\mathrm{i}}[R] = \frac{1}{N^2}\sum_r d[r] \sum_r S_{\mathrm{i}}[r] \; , \tag{195}$$

while the true result is:

$$S_{\mathrm{o,true}}[R] = \frac{1}{N}\sum_r d[r] S_{\mathrm{i}}[r] \; . \tag{196}$$

These expressions are equal only if either the $S_{\mathrm{i}}[r]$, the $d[r]$, or both, are constant as a function of row number r. When both the detector signal and CKD parameter have a non-zero gradient as a function of r, this can lead to errors. This can be elaborated on. Note that each of the $d[r]$ are known, but the $S_{\mathrm{i}}[r]$ are not. Write

$$\begin{aligned} S_{\mathrm{o,true}}[R] &= \frac{1}{N}\sum_r d[r]\left\{S_{\mathrm{i}}[R] + \left(S_{\mathrm{i}}[r] - S_{\mathrm{i}}[R]\right)\right\} \\ &= \frac{1}{N} S_{\mathrm{i}}[R] \sum_r d[r] + \frac{1}{N}\sum_r d[r]\left\{S_{\mathrm{i}}[r] - S_{\mathrm{i}}[R]\right\} \\ &= S_{\mathrm{o,computed}}[R] + \frac{1}{N}\sum_r d[r] \Delta S_{\mathrm{i}}[r] \; . \end{aligned} \tag{197}$$

So the error can be described in terms of the deviations $\Delta S_\mathrm{i}[r]$. Of course, $\sum_r \Delta S_\mathrm{i}[r] = 0$. Although the individual $S_\mathrm{i}[r]$ cannot be known, the following can be considered: If the binned signals $S_\mathrm{i}[R]$ form a smooth function in the image row direction, it can be expected that this smoothness is propagated on the smaller scale of the detector rows, not taking noise into account, the suppression of which was one of the argued advantages of binning to begin with. This reasoning allows to proclaim the estimates $\widetilde{\Delta S_\mathrm{i}[r]}$ for the individual $\Delta S_\mathrm{i}[r]$, using interpolating from neighboring binned $S_\mathrm{i}[R]$ and the zero summation property. This allows for correcting the computed binned signal as follows:

$$S_\mathrm{o,corrected}[R] = S_\mathrm{o,computed}[R] + \frac{1}{N}\sum_r d[r]\widetilde{\Delta S_\mathrm{i}[r]} \; . \tag{198}$$

A major issue is the smoothness of the signal. Apart from the fact that spikes in the row direction could cause problems, the radiance signals will in general not be smooth in row direction. This leaves the irradiance and internal sources. Applicable pixel-dependent CKS are for example the PRNU and absolute irradiance. Numerical tests show that the differences in true and computed signal are typically less than 0.1 %, and that is for perfect estimates of the $\widetilde{\Delta S_\mathrm{i}[r]}$. Therefore this approach will not be used.

B.2.2 Effects of binning on error propagation

For the hypothetical additive correction of the previous section, the formal error propagation is

$$\sigma_\mathrm{o}^2[R] = \sigma_\mathrm{i}^2[R] + s_c^2[R] \; . \tag{199}$$

A similar equation holds for the multiplicative case. In either case, the not yet defined binned variance $s_c^2[R]$ must be expressed in something meaningful. Assuming that the CKD parameter for two neighboring pixels in the row direction is completely uncorrelated, Bienaymé's formula $\mathrm{Var}(\sum_i X_i) = \sum_i \mathrm{Var}(X_i)$ applies. This gives

$$\sigma_\mathrm{o}^2[R] = \sigma_\mathrm{i}^2[R] + \frac{1}{N^2}\sum_r s_c^2[r] = \sigma_\mathrm{i}^2[R] + \frac{1}{N}\overline{s_c^2[r]} \; , \tag{200}$$

where the mean variance over the binned rows is defined as

$$\overline{s_c^2[r]} = \frac{1}{N}\sum_r s_c^2[r] \; . \tag{201}$$

The notation implies that the average is taken over the unbinned detector pixels related to the image pixel under consideration. On the other hand, if the CKD parameter for two neighboring pixels in row direction is completely correlated (for example if the parameter pixels are locally constant), then the general rule applies that the variance of the sum is the sum of their N^2 covariances (including the covariances of pixels with themselves, which are of course the variances).

A special case arises when the unbinned CKD pixels are all equal. Then $s_c^2[R] = \overline{s_c^2[r]}$ to indicate that the variances of the equal unbinned signals can all be substituted with a single binned signal variance. More formally: $\mathrm{Var}(\sum_i X) = \mathrm{Var}(NX) = N^2\mathrm{Var}X$. (Note that the provided CKD pixels variances can still be different even when the CKD pixels are not!) Now the N^2 in numerator and denominator cancel:

$$\sigma_\mathrm{o}^2[R] = \sigma_\mathrm{i}^2[R] + s_c^2[R] = \sigma_\mathrm{i}^2[R] + \overline{s_c^2[r]} \; . \tag{202}$$

Note that the mean variance in the second equality is always well-defined. Between these two extremes the propagation formula needs an explicit covariance matrix. If it can be assumed that correlations between different pixels are not negative, the mean binned variance $\overline{s_c^2[r]}$ can be computed, and the differential propagation error is constrained as follows:

$$\frac{1}{N}\overline{s_c^2[r]} \le \sigma_\mathrm{o}^2[R] - \sigma_\mathrm{i}^2[R] \le \overline{s_c^2[r]} \; . \tag{203}$$

Note, however, that in the case of negative correlations the first inequality does not hold (assume, for example, a bin of size 2 where the second pixel signal correlates exactly opposity to the first; both variances cancel and the combined variance is then zero.

We now claim that the second inequality always holds, whatever the covariances are, and that we can choose this (i.e. $\sigma_\mathrm{o}^2[R] - \sigma_\mathrm{i}^2[R] \le \overline{s_c^2[r]}$) to be the standard strategy in the algorithms concerned. Suppose we have N signals in a bin; we assume first that each signal is completely correlated in some way to the first signal.

$$S[i] = \alpha_i S[1] + \beta_i, \quad 1 \le i \le N \; . \tag{204}$$

Signal $S[i]$ has variance $\sigma^2[i]$. We can relate the variances of the other signals to $\sigma[1]^2$: $\sigma^2[i] = \alpha_i^2\sigma[1]^2$. Further, the covariance between $S[i]$ and $S[j]$ equals $\sigma[i]\sigma[j] = \sigma[1]^2\alpha_i\alpha_j$. We can now write the covariance matrix for the completely correlated case as

$$\mathrm{Cov}[S[i], S[j]] = \sigma[1]^2 \left(\alpha_i\alpha_j\right). \tag{205}$$

The binned signal is $S[R] = (1/N)\sum_{i=1}^{N} S[i]$. Define $A_n = (1/N)\sum_i \sigma^2[i]$ (this is the mean variance $\overline{s_c^2[r]}$) and $B_n = \mathrm{Var}\, S[R] = (1/N^2)\mathrm{Var}\sum_i S[i] = (1/N^2)\sum_i\sum_j \mathrm{Cov}[S[i], S[j]]$. We want to prove that $A_n \geq B_n$ for all bin sizes N. In the remainder, we omit the scaling factor $\sigma[1]^2$.

We use a proof by induction. Trivially, $A_1 = B_1$. Also, $A_2 - B_2 = \frac{1}{4}(\alpha_1 - \alpha_2)^2 \geq 0$. Assume $A_n - B_n \geq 0$ for some $n > 1$. Then

$$A_{n+1} = \frac{1}{n+1}\sum_{i=1}^{n+1}\alpha_i^2 = \frac{1}{n+1}\left[nA_n + \alpha_{n+1}^2\right] \tag{206}$$

and

$$\begin{aligned} B_{n+1} &= \frac{1}{(n+1)^2}\sum_{i}^{n+1}\sum_{j}^{n+1}\alpha_i\alpha_j = \frac{1}{(n+1)^2}\left[\sum_{i=1}^{n}\sum_{j=1}^{n}\alpha_i\alpha_j + 2\sum_{i=1}^{n}\alpha_i\alpha_{n+1} + \alpha_{n+1}^2\right] \\ &= \frac{1}{(n+1)^2}\left[n^2B_n + 2\sum_{i=1}^{n}\alpha_i\alpha_{n+1} + \alpha_{n+1}^2\right]. \end{aligned} \tag{207}$$

Then

$$\begin{aligned} A_{n+1} - B_{n+1} &= \frac{1}{(n+1)^2}\left[n(n+1)A_n + (n+1)\alpha_{n+1}^2 - n^2B_n - 2\sum_{i=1}^{n}\alpha_i\alpha_{n+1} - \alpha_{n+1}^2\right] \\ &= \frac{1}{(n+1)^2}\left[n^2(A_n - B_n) + nA_n + n\alpha_{n+1}^2 - 2\sum_{i=1}^{n}\alpha_i\alpha_{n+1}\right] \\ &= \frac{1}{(n+1)^2}\left[n^2(A_n - B_n) + \sum_{i=1}^{n}\left(\alpha_i^2 + \alpha_{n+1}^2 - 2\alpha_i\alpha_{n+1}\right)\right] \\ &= \frac{1}{(n+1)^2}\left[n^2(A_n - B_n) + \sum_{i=1}^{n}(\alpha_i - \alpha_{n+1})^2\right]. \end{aligned} \tag{208}$$

The first expression between the square brackets is non-negative because of the induction hypothesis, while the second expression is a sum of squares.

If the sequence of individual signals is less than fully correlated, then the off-diagonal entries in the covariance matrix become smaller; this follows easily from $\mathrm{Cov}[S[i], S[j] = \mathrm{Corr}[S[i], S[j]] \cdot \sigma[i] \cdot \sigma[j]$. In that case, A_n stays the same while B_n decreases.

This ends the proof of the claim that we are allowed to use the mean binned variance $\overline{s_c^2[r]}$ as an upper limit to the error increase. The current descriptions of binned CKDs are consistent with this policy.

C Smear

The purpose of the smear correction algorithm is to negate the effect of frame transfer smear, or smear for short in this context. Per definition, smear is the added contribution of the signal due to continued exposure during read-out. More specifically, each row continues to receive photons during its transfer through the CCD image section. The smear is therefore always positive and the correction should consist of a subtraction.

Since we have detailed knowledge of the row transfer process it is in principle possible to compute the exact amount of smear generated. However, in the reverse model we only have the measured (uncorrected) signal to start with. This signal contains less information than the original signal due to non-invertible operations like row binning and co-addition. The goal of the algorithm is to provide an inverted smear addition model that is as good as possible.

C.1 Used parameters and symbols

Parameter	Description	Units
$S_\mathrm{i}[\mathbf{x}_\mathrm{img}]$	signal in image pixel $\mathbf{x}_\mathrm{img}$ before correction	e^-
$\sigma_\mathrm{i}^2[\mathbf{x}_\mathrm{img}]$	signal variance in image pixel $\mathbf{x}_\mathrm{img}$ before correction	e^{-2}
$S_\mathrm{o}[\mathbf{x}_\mathrm{img}]$	signal in image pixel $\mathbf{x}_\mathrm{img}$ after correction	e^-
$\sigma_\mathrm{o}^2[\mathbf{x}_\mathrm{img}]$	signal variance in image pixel $\mathbf{x}_\mathrm{img}$ after correction	e^{-2}
t_exp	exposure time (excluding frame transfer time)	s
τ	row transfer time	s
n	number of detector rows: 581	1
$n_\mathrm{unshielded}$	number of unshielded detector rows	1
n_shielded	number of shielded detector rows (including two storage rows)	1
n_usable	number of unflagged (trusted), unskipped (readable), unshielded (illuminated) detector rows	1
m	number of binned (image) rows	1
f_r	signal rate in detector row r	$\mathrm{e}^-\mathrm{s}^{-1}$
g_r	signal rate in image row r	$\mathrm{e}^-\mathrm{s}^{-1}$
v_r	ROR signal in unbinned row r	e^-
w_r	ROR signal in binned row r	e^-
w'_r	ROR signal in binned row r after binning correction	e^-
a_r	factor between mean and start signal	1
b_r	factor between mean and end signal	1
$a_{r,i}$	factor between mean signal and end signal at co-add instance i	1
N_coadd	number of co-additions	1
M	smear	e^-
s^2_smear	total increase of variance due to smear	e^-

C.1.1 Algorithm description: general

First we describe the creation of smear in the forward sense in more detail than in the forward model section. We start with the most general situation, in which all information is available. We then move to more realistic situations in which some assumptions have to be made. Since the smear is independent of columns, we only consider a single column on the CCD. The CCD has n unbinned rows; the first row is situated closest to the read-out register. *Note that we count here the amount of rows in the storage section: this is the number of rows that is actually transferred during a frame transfer and the frame transfer time is, per definition, $n\tau$. Although the amount of image section rows is 581, we must not forget the extra two rows, and that they are in principle available for reading. Fortunately they can be considered shielded rows so we know their behavior.* The development of the algorithm demands that we start with unbinned rows. Later on, we devote a section to the binned situation.

Let f_r denote the signal rate on a pixel on row r due to illumination. This signal rate is, in general, not constant. We can define the signal rate more correctly by

$$f_r = \frac{1}{t_{\text{exp}}} \int_{t_{\text{start}}}^{t_{\text{end}}} f(u)du \; , \tag{209}$$

where $t_{\text{end}} = t_{\text{start}} + t_{\text{exp}}$. The variation of the scene, and hence of f_r, is important since the smear depends only on the signal rate $f_{r,t_{\text{start}}}$ and $f_{r,t_{\text{end}}}$. Consider a certain pixel on row r. Its cousin pixel 1 will enter the visual region from above at $t_{\text{start}} - n\tau$. The pixel r itself enters the CCD at $t_{\text{start}} - (n-r+1)\tau$. During the first τ seconds, it briefly receives some electrons destined for the upper row; this amount of electrons is $\tau \cdot f_{n,t_{\text{start}}-(n-r+1)\tau}$. In the following τ seconds, some more (exactly: $\tau \cdot f_{n-1,t_{\text{start}}-(n-r+2)\tau}$) electrons are added. At this point we are, for practical reasons, forced to introduce our first assumption:

Assumption 1. The signal rate at pixel r between $t = t_{\text{start}} - n\tau$ and $t = t_{\text{start}}$ is assumed constant and denoted $f_{r,\text{start}}$.

We can justify this assumption by the fact that it is nearly impossible to observe changes in the scene on a shorter timescale than $n\tau$ seconds. More important, the assumption is entirely harmless since in our forward smear model we will establish a relation between f_r and $f_{r,\text{start}}$. Any information we might obtain about the signal rate evolution between $t_{\text{start}} - n\tau$ and t_{start} can be incorporated in this relation.

This movement through the rows continues until the pixel reaches its designated position r, where it receives an additional $\tau \cdot f_{r,\text{start}}/2$ amount of electrons (the factor $1/2$ is evident when one considers that the center point of the pixel does not enter the pixel 'box' until the last $\tau/2$ seconds). Then, during the true exposure time, between t_{start} and t_{end}, the pixel receives its designated $t_{\text{exp}} f_r$ electrons. After that, there are again $r-1$ small time steps during which the pixel resides in the lower $r-1$ positions, receiving, at each position k $(0 < k < r)$, $\tau \cdot f_{k,\text{end}}$ electrons. Therefore we can express the relation between the illumination rate f and the ROR signal $\mathbf{v}$ by the matrix equation

$$\begin{pmatrix} v_1 \\ v_2 \\ \vdots \\ \vdots \\ v_n \end{pmatrix} = t_{\text{exp}} \begin{pmatrix} f_1 \\ f_2 \\ \vdots \\ \vdots \\ f_n \end{pmatrix} + \tau \begin{pmatrix} \frac{1}{2} & 1 & 1 & \dots & 1 \\ 0 & \frac{1}{2} & 1 & \dots & 1 \\ \vdots & \ddots & \ddots & \ddots & \vdots \\ 0 & & \ddots & \frac{1}{2} & 1 \\ 0 & \dots & \dots & 0 & \frac{1}{2} \end{pmatrix} \begin{pmatrix} f_{1,\text{start}} \\ f_{2,\text{start}} \\ \vdots \\ \vdots \\ f_{n,\text{start}} \end{pmatrix} + \tau \begin{pmatrix} \frac{1}{2} & 0 & 0 & \dots & 0 \\ 1 & \frac{1}{2} & 0 & \dots & 0 \\ \vdots & \ddots & \ddots & \ddots & \vdots \\ 1 & & \ddots & \frac{1}{2} & 0 \\ 1 & \dots & \dots & 1 & \frac{1}{2} \end{pmatrix} \begin{pmatrix} f_{1,\text{end}} \\ f_{2,\text{end}} \\ \vdots \\ \vdots \\ f_{n,\text{end}} \end{pmatrix} . \tag{210}$$

Our goal is to write the expression above as a single matrix-vector equation: $\mathbf{v} = \mathbf{A}\mathbf{f}$. The inverse of matrix $\mathbf{A}$ can then be used in the reverse processor to acquire $\mathbf{f}$ from $\mathbf{v}$. One way to achieve this goal is by expressing $f_{r,\text{start}}$ and $f_{r,\text{end}}$ into f_r. An easy solution is simply setting $f_{r,\text{start}} = f_{r,\text{end}} = f_r$. This choice, which we will call the pseudo-static variant from now on, will eventually be implemented in the L01b Processor. However, it is good to acquire insight in the drawbacks and alternatives.

For scenes that vary strongly in the temporal dimension, this assumption can result in considerable errors in some pixels.

Although we do not have time-dependent information of the image itself, we can use the previous and following images. We can use the average signal rates of these frames, f_r^{prev} and f_r^{next} to obtain good guesses for $f_{r,\text{start}}$ and $f_{r,\text{end}}$; a simple linear interpolation (taking into account different exposure times) will do. Of course, at this stage we only have the read-out signal $\mathbf{v}$, not $\mathbf{f}$. Clearly, the problem is circular: the signal rate $\mathbf{f}$ is not available before we solved the smear problem. But, at least, the read-outs $\mathbf{v}$ for the frame considered and the previous and following images give a good approximation. For co-added scenes, the small pixel columns typically provide temporal information. Later, we will elaborate on this aspect (see Section C.3).

Regardless of the method we choose, we can write

$$f_{r,\text{start}} = \alpha_r f_r , \tag{211a}$$

and

$$f_{r,\text{end}} = \beta_r f_r \; . \tag{211b}$$

The α_r and β_r will always be non-negative. Equation (210) can now be reduced. We first introduce $\varepsilon = \tau / t_{\text{exp}}$

and then $a_i = \varepsilon\alpha_i$ and $b_i = \varepsilon\beta_i$. We get

$$\begin{pmatrix} v_1 \\ v_2 \\ \vdots \\ \vdots \\ \vdots \\ v_n \end{pmatrix} = t_{\exp} \begin{pmatrix} 1+\frac{1}{2}(a_1+b_1) & a_2 & a_3 & \dots & \dots & a_n \\ b_1 & 1+\frac{1}{2}(a_2+b_2) & a_3 & \dots & \dots & a_n \\ \vdots & \ddots & \ddots & \ddots & & \vdots \\ \vdots & & \ddots & \ddots & \ddots & \vdots \\ b_1 & & & \ddots & 1+\frac{1}{2}(a_{n-1}+b_{n-1}) & a_n \\ b_1 & \dots & \dots & \dots & b_{n-1} & 1+\frac{1}{2}(a_n+b_n) \end{pmatrix} \begin{pmatrix} f_1 \\ f_2 \\ \vdots \\ \vdots \\ \vdots \\ f_n \end{pmatrix} . \tag{212}$$

The smear M is defined as the contribution outside the true exposure time interval, therefore:

$$\begin{aligned} M(\mathbf{v}) &= \mathbf{Af} - t_{\exp}\mathbf{f} = (\mathbf{A} - t_{\exp}\mathbf{I})\mathbf{f} = \\ & (\mathbf{A} - t_{\exp}\mathbf{I})\mathbf{A}^{-1}\mathbf{v} = (\mathbf{I} - \mathbf{A}^{-1}t_{\exp})\mathbf{v} . \end{aligned} \tag{213}$$

Now we have expressed the smear in terms of the read-outs v_j. The f_j, which are not available before the smear correction, are no longer needed. Note further that, although M is a function of $\mathbf{v}$, it is the same for a pixels in the column: $M(v_i) = M(v_j)\forall i,j$; therefore we may also write M(c_{img}).
As an intermezzo, we note that in the pseudo-static variant (where the choice for α and β was simply $\alpha = \beta = 1$) $\mathbf{A}$ reduces to

$$t_{\exp} \begin{pmatrix} 1+\varepsilon & \varepsilon & \dots & \dots & \varepsilon \\ \varepsilon & \ddots & \ddots & & \vdots \\ \vdots & \ddots & \ddots & \ddots & \vdots \\ \vdots & & \ddots & \ddots & \varepsilon \\ \varepsilon & \dots & \dots & \varepsilon & 1+\varepsilon \end{pmatrix} . \tag{214}$$

As remarked above, this choice can produce considerable errors. An advantage is that the matrix is easy to invert. Having established this exact result, the smear correction problem boils down to the following questions:

1. How accurately can the coefficients a_i and b_i be chosen?
2. In what way will row binning influence the result?
3. In what way will row skipping influence the result?
4. How can we incorporate co-adding using this result?
5. Is the inverse of the matrix A easily computed?

These questions are interrelated. For example, more binning and skipping decreases the accuracy of the coefficients a_i and b_i. Some choices of the coefficients permit a simpler matrix structure regarding inversion.

C.2 Algorithm description: binning, skipping and flagging

We consider the effect of binning, skipping, and flagging, without taking the binning factor division into account. Suppose there are m binned rows. w_j is the binned signal in the read-out register, and g_j the illumination rate. The w_j and g_j have the same binning factor n_j. We need some more administration in the form of a binning table. Define q_j^{start} and q_j^{end} as a mapping from image row j, towards the corresponding rows on the CCD. It always holds that $q_j^{\text{start}} + n_j - 1 = q_j^{\text{end}}$. Further, $q_j^{\text{start}} = q_{j-1}^{\text{end}} + 1$. Clearly

$$g_j = \sum_{i=0}^{n_j} f_{i+q_j^{\text{start}}}, \quad w_j = \sum_{i=0}^{n_j} v_{i+q_j^{\text{start}}} . \tag{215}$$

Our strategy regarding skipped rows is to assume, for as long as possible, as if no rows are skipped at all. This makes sense since the rows considered are binned with their own binning factors like normal rows. The only difference is that, in the end, the information is discarded. Flagged pixels can be treated the same as skipped pixels: during read-out the information of the signal value is unreliable.

The binning matrix $\mathbf{B}$ has dimensions $m \times n$ and has a simple shape: row j contains zeroes except for the entries between column q_j^{start} and column q_j^{end}, which are filled with n_j ones. The matrix $\mathbf{B}$ is not invertible, so the construction $\mathbf{w} = \mathbf{B}\mathbf{v} = \mathbf{B}\mathbf{A}\mathbf{f} = \mathbf{B}\mathbf{A}\mathbf{B}^{-1}\mathbf{g}$ will not work. Instead, we explicitly try to write down $\mathbf{w} = \mathbf{B}\mathbf{A}\mathbf{f}$. Since we only have binned information available, we cannot determine the exact values of a_i and b_i. We are therefore forced to invoke the following assumption:

Assumption 2. The a_i and b_i in rows belonging to the same bin j are all equal.

Define $a_j^b = a_{q_j^{\text{start}}} = a_{q_j^{\text{start}}+1} = \ldots = a_{q_j^{\text{end}}}$ and a similar definition for b_j^b. Now $\mathbf{w} = \mathbf{B}\mathbf{A}\mathbf{f}$ where $\mathbf{w} = (w_1 \ldots w_m)^{\mathrm{T}}$ and $\mathbf{B}\mathbf{A}$ is the $m \times n$ matrix

$$t_{\text{exp}} \begin{pmatrix} 1+\frac{1}{2}a_1^b+(n_1-\frac{1}{2})b_1^b & \ldots & 1+(n_1-\frac{1}{2})a_1^b+\frac{1}{2}b_1^b & n_1 a_2^b & \ldots & n_1 a_m^b \\ n_2 b_1^b & \ldots & n_2 b_1^b & 1+\frac{1}{2}a_2^b+(n_2-\frac{1}{2})b_2^b & \ldots & n_2 a_m^b \\ \vdots & \ddots & \ddots & \ddots & & \vdots \\ n_{m-1} b_1^b & & \ddots & \ddots & \ddots & n_{m-1} a_m^b \\ n_m b_1^b & \ldots & \ldots & \ldots & \ldots & 1+(n_m-\frac{1}{2})a_m^b+\frac{1}{2}b_m^b \end{pmatrix} . \tag{216}$$

For a certain entry w_j we get

$$w_j = \sum_{i=1}^{j-1} \sum_{k=q_i^{\text{start}}}^{q_i^{\text{end}}} n_j b_i^b f_k + \sum_{i=j+1}^{m} \sum_{k=q_i^{\text{start}}}^{q_i^{\text{end}}} n_j b_i^b f_k + \sum_{k=q_j^{\text{start}}}^{q_j^{\text{end}}} [1+(\tilde{k}-\frac{1}{2})a_j^b+(n_j-\tilde{k}-\frac{1}{2})b_j^b] f_k \; , \tag{217}$$

with, in the last term, $\tilde{k} = k - q_j^{\text{start}} + 1$. The first term of this expression reduces to

$$n_j \sum_{i=1}^{j-1} b_i^b \sum_{k=q_i^{\text{start}}}^{q_i^{\text{end}}} f_k = n_j \sum_{i=1}^{j-1} b_i^b g_i \tag{218}$$

and a similar expression holds for the second term. To reduce the third term, we need another assumption:

Assumption 3. The convolution $\sum_{k=q_j^{\text{start}}}^{q_j^{\text{end}}} [1+(\tilde{k}-\frac{1}{2})a_j^b+(n_j-\tilde{k}-\frac{1}{2})b_j^b] f_k$ may be simplified to

$$[1+\frac{1}{2}n_j(a_j^b+b_j^b)] \sum_{k=q_j^{\text{start}}}^{q_j^{\text{end}}} f_k \; . \tag{219}$$

In effect, the mean of the term between square brackets is taken. This assumption introduces an error if the f_k are not all equal. We now have reached the matrix equation

$$\mathbf{w} = \mathbf{C}\mathbf{g} \; , \tag{220}$$

where $\mathbf{C}$ is an $m \times m$ matrix:

$$t_{\text{exp}} \begin{pmatrix} 1+\frac{1}{2}n_1(a_1^b+b_1^b) & n_1 a_2^b & n_1 a_3^b & \ldots & \ldots & n_1 a_m^b \\ n_2 b_1^b & 1+\frac{1}{2}n_2(a_2^b+b_2^b) & n_2 a_3^b & \ldots & \ldots & n_2 a_m^b \\ \vdots & \ddots & \ddots & \ddots & & \vdots \\ \vdots & & \ddots & \ddots & \ddots & \vdots \\ n_{m-1} b_1^b & & & \ddots & 1+\frac{1}{2}n_{m-1}(a_{m-1}^b+b_{m-1}^b) & n_{m-1} a_m^b \\ n_m b_1^b & \ldots & \ldots & \ldots & n_m b_{m-1}^b & 1+\frac{1}{2}n_m(a_m^b+b_m^b) \end{pmatrix} . \tag{221}$$

Note the similarities between the unbinned equation (212) and this binned equation (220). In particular, the two equations become the same if all n_j are equal to 1. The smear is, as before, defined as the contribution outside the true exposure time interval, therefore:

$$\begin{aligned} M(\mathbf{w}) &= \mathbf{Cg} - t_{\mathrm{exp}}\mathbf{g} = (\mathbf{C} - t_{\mathrm{exp}}\mathbf{I})\mathbf{g} = \\ &\quad (\mathbf{C} - t_{\mathrm{exp}}\mathbf{I})\mathbf{C}^{-1}\mathbf{w} = (\mathbf{I} - \mathbf{C}^{-1}t_{\mathrm{exp}})\mathbf{w} \ . \end{aligned} \tag{222}$$

At this point we finally have to take the possibility of skipped or flagged pixels into account. Suppose the binned row r is skipped. In Equation (220), this means the following:

- The read-out value w_r is actually not read out, by definition. However, it is needed in the right-hand side of Equation (222). Therefore we need to interpolate the w_r from the neigboring binned $w_{r-k}, \cdots w_{r+k}$ pixels in the same column.

- The binned illumination g_r is not needed since it will not be used in Equation (222).

- In matrix $\mathbf{C}$, the cross consisting of row r and column r can be highlighted. The matrix row will not be used, but the matrix column, including the coefficients a_r and b_r is needed to compute the unskipped entries of $\mathbf{w}$. Eventually, however, we need $\mathbf{C}^{-1}$. That means we have guess the coefficients a_r and b_r (in the pseudo-static approach, they are of course equal to 1). The coefficients can be interpolated from neighboring columns. If the skipped row has special characteristics (if the row is in a straylight area or is not illuminated) care must be taken; a fallback strategy is to choose $a_r = b_r = 1$.

Concluding, the equations stay the same, and the unknowns a_r, b_r and w_r are estimated by interpolation. For flagged pixels, there are two possibilities, dependent on the reliability of the signal value of the pixel.

- For most flagging types, the signal value of the pixel is either nonsense or unrealiable. Then it is best to treat such a pixel as skipped, i.e. act if the pixel does not contain information at all and interpolation is the best option.

- Some flagged pixels nevertheless contain signal values that may not be very wrong. An example is a saturated pixel: its value will be very high, but this value will be a rather good estimate since the actual charge cannot be much higher than measured. In the extreme case of blooming, the excess charge will be transferred to neighboring pixels: conservation of charge. In this case, it is better to proclaim the pixel value as reliable and treat the pixel as a normal pixel.

The interpolation of the skipped pixel w_r can be done in several ways:

- Direct linear interpolation from the previous and next binned row. At top and bottom, extrapolation has to be used. Further, if the skipped row is different in terms of illumination/shielding from neighboring rows, the interpolation will not yield good results.

- Extrapolation from the total unskipped column sum. That means that the column sum of all the available binned pixels is multiplied with a factor $n_{\mathrm{unshielded}}/n_{\mathrm{usable}}$ where the denominator contains the number of unskipped pixels expressed in the amount of the associated detector pixels. A disadvantage is that it is less accurate since the extrapolation is global, not local. This can be ameliorated by extrapolating per region, where the rows in each region have similar characteristics (e.g., the fully illuminated science region). Note that in both the numerator and the denominator we only count the pixels that are expected to have a properly illuminated signal; hence the exclusion of shielded pixels.

- Extrapolation from a total unskipped partial column sum. A partial column is for example the union of all 'illuminated pixels'. Here each skipped pixel can belong to a group with the same characteristics (shielded, non-illuminated, illuminated). The same disadvantage as the second method holds.

Since we expect that skipped or flagged rows will be rare, the baseline is the second (easiest) method. As mentioned before, saturated pixels (which are *not* rare) should be treated as normal pixels.

C.3 Algorithm description: co-addition

When we take co-addition into account, some things change, some things stay the same. Note that Equation (210) refers to a single frame in a co-added series. We introduce some notation. Forgetting binning for the moment, we still assume we have n detector rows. Suppose the image is a sum of N_{coadd} frames. The total amount of time that the image will be illuminated is $T_{\text{illum,tot}} = N_{\text{coadd}}(t_{\text{exp}} + n\tau)$ s. Using Assumption 1, we define the times where smear is added as t_0 (this is the t_{start} described above), $t_1, t_2, \ldots t_{N_{\text{coadd}}}$. As explained before, these times are in reality time intervals of length $n\tau$. Further, we define the mean signal rate for frame i as

$$f_r^i = \frac{1}{t_{\text{exp}}} \int_{t_{\text{start};i}}^{t_{\text{end};i}} f(u)du \ , \tag{223}$$

where $t_{\text{end};i} = t_{\text{start};i} + t_{\text{exp}}$. For a pixel in row r we get:

$$\begin{aligned} v_r &= \tau \sum_{j=r+1}^{n} f_{j,t_0} + t_{\text{exp}} f_r^1 + \tau \sum_{j=1}^{r-1} f_{j,t_1} + \frac{1}{2}\tau(f_{r,t_0} + f_{r,t_1}) \\ &+ \tau \sum_{j=r+1}^{n} f_{j,t_1} + t_{\text{exp}} f_r^2 + \tau \sum_{j=1}^{r-1} f_{j,t_2} + \frac{1}{2}\tau(f_{r,t_1} + f_{r,t_2}) \\ &+ \ldots \\ &+ \tau \sum_{j=r+1}^{n} f_{j,t_{N_{\text{coadd}}-1}} + t_{\text{exp}} f_p^{N_{\text{coadd}}} + \tau \sum_{j=1}^{r-1} f_{j,t_{N_{\text{coadd}}}} + \frac{1}{2}\tau(f_{r,t_{N_{\text{coadd}}-1}} + f_{r,t_{N_{\text{coadd}}}}) \ . \end{aligned} \tag{224}$$

This can be simplified to:

$$\begin{aligned} v_r &= \tau \sum_{i=r+1}^{n} f_{i,t_0} + t_{\text{exp}} \sum_{i=1}^{N_{\text{coadd}}} f_r^i + \tau \sum_{i=1}^{N_{\text{coadd}}-1} \left(\sum_{j=1}^{n} f_{j,t_i}\right) \\ &+ \tau \sum_{j=1}^{r-1} f_{j,t_{N_{\text{coadd}}}} + \frac{1}{2}\tau(f_{r,t_0} + f_{r,t_{N_{\text{coadd}}}}) \ . \end{aligned} \tag{225}$$

This expression should be incorporated into a matrix equation similar to Equation 212. That means we define the average signal rate f_r as

$$f_r = \frac{1}{N_{\text{coadd}}} \sum_{i=1}^{N_{\text{coadd}}} f_r^i \approx \frac{1}{T_{\text{illum,tot}}} \int_{t_0}^{t_{N_{\text{coadd}}}} f(u)\,du \ . \tag{226}$$

Further, we have to establish relations between f_r and *all* $N_{\text{coadd}} + 1$ signal rates during the frame transfers. So, instead of just choosing a_i and b_i following Equations (211a) and (211b) in the case without co-additions, we define

$$f_{r,t_i} = \alpha_{r,i} f_r, \quad 1 \le r \le n; \quad 0 \le i \le N_{\text{coadd}} \ . \tag{227}$$

The resulting matrix has a similar structure as in Equation (212), using again $a_{r,i} = (\tau/t_{\text{exp}})\alpha_{r,i}$, with on the diagonal:

$$A_{r,r} = t_{\text{exp}}(N_{\text{coadd}} + \frac{1}{2}a_{r,0} + a_{r,1} + \ldots + a_{r,N_{\text{coadd}}-1} + \frac{1}{2}a_{r,N_{\text{coadd}}}) \ , \tag{228}$$

below the diagonal:

$$A_{r,q} = t_{\text{exp}} \sum_{i=1}^{N_{\text{coadd}}} a_{q,i} \quad 1 \le q < r \le n \ , \tag{229}$$

and above the diagonal:

$$A_{r,q} = t_{\text{exp}} \sum_{i=0}^{N_{\text{coadd}}-1} a_{q,i} \quad 1 \le r < q \le n \ . \tag{230}$$

Here we see again that the entries in a column q are independent of the row number r. When we finally move to the binned situation, invoking Assumptions 2 and 3 for each individual frame transfer, we obtain again the row dependency in terms of the binning factor similar as in Equation (220). We return to the discussion on how to obtain the factors $\alpha_{j,i}$. The small pixel column provides a possibility to obtain some temporal information.

Fortunately, the correlation between the small pixel column and the other columns in the same image is rather high.

Therefore, $\alpha_{r,i}$, $0 \leq i \leq N_{\text{coadd}}$, $1 \leq r \leq n$ can be chosen as the average of the values in the small pixel columns for co-additions i and $i-1$. For $\alpha_{r,0}$, the last small pixel column of the previous image together with the small pixel column of frame 0 should be used. For $\alpha_{r,N_{\text{coadd}}}$, the first small pixel column of the next image together with the small pixel column of frame N_{coadd} should be used. Moreover, we have the *complete* previous and next images. These help in making good estimates of time gradients and prevent us to be completely dependent on the small pixel column estimates.

In the pseudo-static approach the matrix $\mathbf{A}$ can be simplified: It reduces, after dividing by N_{coadd}, to the matrix in Equation (214) in the unbinned case and to a similarly simplified version of $\mathbf{C}$ in Equation (220) in the binned case. This is helpful for the L01b Processor, since the pseudo-static approach is the baseline.

C.4 Algorithm description: computing the inverse of the matrix

We can explicitly compute the inverse with the Gauss algorithm. This does not involve many computations: after swapping the bottom and top rows, one sweep will create an upper triangular matrix except for the bottom row. After elimination of that bottom row, inverse substitution immediately gives the inverse. This inverse can be computed for each image column (if we choose different factors $\alpha_{j,i}$ for each image column) or for all image columns simultaneously (if we only make use of the small pixel columns in our choices of $\alpha_{j,i}$).

An alternative is to use Gauss-Seidel iterations. There are two approaches. Either we try to find a solution for each (of the more than 1000) column vector $\mathbf{v}$ or we construct all m columns of the matrix using the columns of the identity matrix of size m. Our first iteration guess in the latter case would be the inverse matrix in the pseudo-static approach (see immediately below). Whatever choice will be made, restrictions for the computational time have to be taken into account.

In the baseline pseudo-static approach the matrix inverse can be written down directly (and, therefore, fast):

$$\mathbf{C}^{-1} = \frac{1}{t_{\text{exp}}(1+n\varepsilon)} \begin{pmatrix} 1+\varepsilon(n-n_1) & -n_1\varepsilon & -n_1\varepsilon & \dots & \dots & -n_1\varepsilon \\ -n_2\varepsilon & 1+\varepsilon(n-n_2) & -n_2\varepsilon & \dots & \dots & -n_2\varepsilon \\ \vdots & \ddots & \ddots & \ddots & & \vdots \\ \vdots & & \ddots & \ddots & \ddots & \vdots \\ -n_{m-1}\varepsilon & & & \ddots & 1+\varepsilon(n-n_{m-1} & -n_{m-1}\varepsilon \\ -n_m\varepsilon & \dots & \dots & \dots & -n_m\varepsilon & 1+\varepsilon(n-n_m) \end{pmatrix} . \tag{231}$$

Applying the formula for smear (Equation (222)) for a signal in binned row r immediately gives

$$M(w_r) = (\mathbf{I} - \mathbf{C}^{-1} t_{\text{exp}})\, \mathbf{w}_r = \frac{1}{1+n\varepsilon} \sum_{j=1}^{m} n_r \varepsilon w_j = n_r \frac{\tau}{t_{\text{exp}}+n\tau} \sum_{j=1}^{m} w_j \; . \tag{232}$$

However, the smear correction takes place after the binning correction step. Define the measured signal after binning correction $w'_r = w_r/n_r$. In vector form, $\mathbf{w}' = \mathbf{N}^{-1}\mathbf{w}$, where $\mathbf{N} = \operatorname{diag}(n_1, n_2, \cdots n_m)$. Then

$$M(\mathbf{w}') = M(\mathbf{N}^{-1}\mathbf{w}) = (\mathbf{I} - \mathbf{C}^{-1} t_{\text{exp}})\, \mathbf{N}^{-1}\mathbf{w} = \mathbf{N}^{-1} M(\mathbf{w}) \tag{233}$$

and for a signal after binning division in binned row r this gives

$$M(w'_r) = \frac{1}{n_r} M(w_r) = \frac{\tau}{t_{\text{exp}}+n\tau} \sum_{j=1}^{m} n_j w'_j, \tag{234}$$

where w'_r is of course the measured signal $S_{\text{i}}[\mathbf{x}_{\text{img}}]$.

We claim that the smear correction works as a simple multiplicative operation on the column average and (by extension) image average: We have

$$S_{\text{o}}[r_{\text{det}}] = S_{\text{i}}[r_{\text{det}}] - \frac{\tau}{t_{\text{exp}}+n\tau} n \cdot \overline{S_{\text{i}}} \tag{235}$$

where the $\overline{S_\mathrm{i}}$ *denotes the signal average over all rows in a column. Then for the column average we have*

$$\begin{aligned}\overline{S_\mathrm{o}} =& \frac{1}{n}\sum_{r_\mathrm{det}=1}^{n} S_\mathrm{o}[r_\mathrm{det}] && (236)\\ =& \frac{1}{n}\sum_{r_\mathrm{det}=1}^{n}\left(S_\mathrm{i}[r_\mathrm{det}] - \frac{\tau}{t_\mathrm{exp}+n\tau}n\cdot\overline{S_\mathrm{i}}\right) && (237)\\ =& \overline{S_\mathrm{i}} - \frac{\tau}{t_\mathrm{exp}+n\tau}n\overline{S_\mathrm{i}} = (1-\frac{n\tau}{t_\mathrm{exp}+n\tau})\overline{S_\mathrm{i}}. && (238)\end{aligned}$$

As a rule of thumb, this implies that for tropical radiance measurements, the smear fraction with respect to the average signal amounts to ca. $n\tau/t_\mathrm{exp} = 576\times 7.5\times 10^{-5}/0.4 \approx 1\%$.

C.5 Practical aspects

When computing the column sum, we encounter the practical problem that the we assumed that each pixel signal can be measured. Because the image section is two rows smaller than the storage section, this is not the case. Also, pixels may be unavailable (skipped) /untrustworthy (flagged). We cope with this problem in two steps. First, we know beforehand the number and location of shielded pixels. These pixels receive no light flux and they will therefore only contain the smear signal. The two storage section pixels can also be considered as shielded. These pixels can be split from the summation and moved to the left-hand side of the equation:

$$\begin{aligned}M(w'_r) =& M(c_\mathrm{img}) = \frac{\tau}{t_\mathrm{exp}+n\tau}\sum_{j=1}^{m} n_j S_\mathrm{i}[j] = \frac{\tau}{t_\mathrm{exp}+n\tau}\left(\sum_{\mathrm{unshielded,binned}} n_j S_\mathrm{i}[j] + \sum_{\mathrm{shielded,binned}} n_j S_\mathrm{i}[j]\right) && (239)\\ =& \frac{\tau}{t_\mathrm{exp}+n\tau}\sum_{\mathrm{unshielded,binned}} n_j S_\mathrm{i}[j] + \frac{\tau}{t_\mathrm{exp}+n\tau} n_\mathrm{shielded} M(c_\mathrm{img}) && (240)\\ \Longrightarrow& \frac{t_\mathrm{exp}+n\tau-n_\mathrm{shielded}\tau}{t_\mathrm{exp}+n\tau} M(c_\mathrm{img}) = \frac{\tau}{t_\mathrm{exp}+n\tau}\sum_{\mathrm{unshielded,binned}} n_j S_\mathrm{i}[j] && (241)\\ \Longrightarrow& M(c_\mathrm{img}) = \frac{\tau}{t_\mathrm{exp}+\tau(n-n_\mathrm{shielded})}\sum_{\mathrm{unshielded,binned}} n_j S_\mathrm{i}[j]. && (242)\end{aligned}$$

Now we have to decide how to handle flagged pixels. As mentioned before, the basic philosophy is that flagged pixels are unreliable and should not be used on right-hand side of an equation. Therefore we treat a flagged pixel as 'skipped': we extend the unreliability to the policy that we do not possess any information. The exception is saturated pixels: they should be promoted to unflagged/usable pixels for this purpose.

Baseline is again that we extrapolate from the total unskipped column sum. That means that the column sum of all the available non-flagged binned pixels is multiplied with a factor $f_\mathrm{column-scaling} = n_\mathrm{unshielded}/n_\mathrm{usable}$ where the denominator contains the number of unflagged/unskipped pixels expressed in the amount of the associated detector pixels. Note that in both the numerator and the denominator we have already excluded the shielded pixels. Therefore, we write

$$M(c_\mathrm{img}) \approx \frac{\tau}{t_\mathrm{exp}+(n-n_\mathrm{shielded})\tau} f_\mathrm{column-scaling} \sum_{\text{usable binned pixels}} n_j S_\mathrm{i}[q,c]. \tag{243}$$

We stress that the summation index q involves only the image rows in the unshielded region that are available to read and do not contain any flags.

C.6 On two approaches

We will first assess the following trade-off: We can use the pseudo-static approach (which does not need any information beside the image itself, and provides an easy inverse matrix) but introduces an error due to the time dependency. On the other hand, we can use the potentially exact approach involving the three assumptions and the estimates that have to be made, while the matrix inversion is less simple.

We start with some estimates for the co-added, unbinned case. The smear computed according to the pseudo-static approach in a row r , as a function of the signal rate, is

$$M_\mathrm{psa}(r) = \tau\sum_{j=1}^{n} f_j = \tau n\bar{\mathbf{f}} \tag{244}$$

where $\bar{\mathbf{f}}$ is the flow rate averaged over all rows of the averaged (over the entire illumination period) signal rate $\mathbf{f}$ (Equation (226)). We again define the average signal rate in terms of the flow rates of individual frames (see Equation (223)) as

$$f_r = \frac{1}{N_{\text{coadd}}} \sum_{i=1}^{N_{\text{coadd}}} f_r^i \approx \frac{1}{2N_{\text{coadd}}} \sum_{i=1}^{N_{\text{coadd}}-1} (f_{r,t_i} + f_{r,t_{i+1}}) = \ldots , \tag{245}$$

while we note that the equality holds for piecewise linear behavior of the individual flow rates. The approximation becomes worse for lower numbers of co-additions. We continue:

$$\ldots = \frac{1}{N_{\text{coadd}}} \left[\frac{1}{2}(f_{r,t_0} + f_{r,t_{N_{\text{coadd}}}}) + \sum_{i=1}^{N_{\text{coadd}}-1} f_{r,t_i} \right] = f_r \frac{1}{N_{\text{coadd}}} \left[\frac{1}{2}(\alpha_{r,0} + \alpha_{r,N_{\text{coadd}}}) + \sum_{i=1}^{N_{\text{coadd}}-1} \alpha_{r,i} \right] . \tag{246}$$

This gives a useful property of the $\alpha_{r,i}$. We use this to expand Equations (228) through (230):

$$\begin{aligned}
A_{r,r} &= t_{\text{exp}} (N_{\text{coadd}} + \frac{\tau}{t_{\text{exp}}} N_{\text{coadd}}) = (t_{\text{exp}} + \tau) N_{\text{coadd}} , && (247)\\
A_{r,q,LD} &= t_{\text{exp}}((\sum_{i=1}^{N_{\text{coadd}}-1} a_{q,i}) + a_{q,N_{\text{coadd}}}) = t_{\text{exp}} \left(\left[\sum_{i=1}^{N_{\text{coadd}}-1} a_{q,i} + \frac{1}{2}(a_{q,0} + a_{q,N_{\text{coadd}}}) \right] + \frac{1}{2}(a_{q,N_{\text{coadd}}} - a_{q,0}) \right) \\
&= \tau([N_{\text{coadd}}] + \frac{1}{2}(\alpha_{q,N_{\text{coadd}}} - \alpha_{q,0})) , && (248)\\
A_{r,q,UD} &= \tau([N_{\text{coadd}}] + \frac{1}{2}(\alpha_{q,0} - \alpha_{q,N_{\text{coadd}}})) , && (249)
\end{aligned}$$

The smear expressed in flow rates is therefore

$$\begin{aligned}
N_{\text{coadd}} M(r) &= \sum_{q=1}^{n} A_{r,q} f_q = \tau N_{\text{coadd}} \sum_{q=1}^{n} f_q + \frac{1}{2}\tau \left[\sum_{q=1}^{r-1} (\alpha_{q,N_{\text{coadd}}} - \alpha_{q,0}) f_q + \sum_{q=r+1}^{n} (\alpha_{q,0} - \alpha_{q,N_{\text{coadd}}}) f_q \right] = \\
&= \tau N_{\text{coadd}}\, n \bar{\mathbf{f}} + \frac{1}{2}\tau \left[\sum_{q=1}^{r-1} (f_{q,t_{N_{\text{coadd}}}} - f_{q,t_0}) + \sum_{q=r+1}^{n} (f_{q,t_0} - f_{q,t_{N_{\text{coadd}}}}) \right] . && (250)
\end{aligned}$$

After division by the co-addition factor, we recognize in the first term the smear $M_{\text{psa}}(r)$.

We pause here for a moment: in this derivation we see that we are able to upgrade the pseudo-static approach to the nonstatic approach once we have the scaling factors for (only) the first and last co-addition. In this way we do not need the difficult matrix inversion described above. Keeping this in mind, we continue:

We want to quantify the maximum error that will be made in the pseudo-static approach (Equation (244)). For row r, we can achieve a maximum error by maximizing $f_{q,t_0} - f_{q,t_{N_{\text{coadd}}}}$ for $q > r$ and, simultaneously, maximizing $f_{q,t_{N_{\text{coadd}}}} - f_{q,t_0}$ for $q < r$. Consider the maximum intensity factor of a changing scene to be K, i.e.

$$\frac{1}{K} \leq \frac{f_{p,t_i}}{f_{p,t_j}} \leq K, \quad \text{for all rows} \quad p \quad \text{and all times} \quad t_i, t_j. \tag{251}$$

In words, the maximum contrast in a column is the maximum of all temporal pixel contrasts in a column.

We now define a low flow rate f_L and a high flow rate $f_H = K f_L$. Further, an error in the smear is most critical if it adds to a low-signal pixel. We therefore find for the maximum relative error in the smear

$$\frac{M_{\text{max}} - M_{\text{psa}}}{f_L (t_{\text{exp}} + n\tau)} = \frac{1}{2}\tau(K-1) n \frac{1}{(t_{\text{exp}} + n\tau) N_{\text{coadd}}} . \tag{252}$$

An example of such a scene is a high signal for negative cross-track angles in the first half of a co-addition period combined with a high signal for positive cross-track angles in the second half of the co-addition period: a 2 x 2 checkerboard pattern.

We see that the maximum error is independent of the number of co-additions given the integration time $N_{\text{coadd}} (t_{\text{exp}} + n\tau)$.

C.7 Error propagation

The error increase of this algorithm step will stem purely from the reconstruction process, since there are no CKD parameters involved. We will address the possible sources of error, without going into much detail yet:

- Determination of coefficients a_r, b_r (or $a_{j,i}$ in the co-added case). Computed factors far from one are suspicious and can introduce large errors. Small pixel columns contain more noise than the signal and applying them to other columns introduces new errors. The fall-back approach is to choose $a_r = b_r = 1$ for all r.

- Concerning Assumption 1. This effect is expected to be incorporated in the choice of the coefficients.

- Concerning Assumptions 2 and 3. The error will be a function of the gradients of the detector pixels belonging to the same bin. These assumptions were necessary to derive the matrix $\mathbf{C}$. Errors are expected to be smaller than those of the derivation of the factors themselves.

- Concerning skipped/flagged rows. Many neighboring skipped rows covering an unexpected image gradient (for example, rows in a straylight area) can be the source of a significant error. The baseline of linear interpolation from neighboring visible rows will limit this error considerably.

- The computation of the matrix inverse. The inverse is either exact or will be acquired by some iteration algorithm, while the stop criterion can be set as strictly as needed. The variances will not change in a significant way.

- Concerning number of co-additions and exposure times. The amount of smear is roughly related to the ratio of row transfer time and exposure time. If we keep the integration time constant, the effects of lower exposure times are exactly balanced by the higher number of co-additions.

- The measurement itself is used for the correction. In particular, the transfer from v to f is influenced by shot noise and read-out noise. This has to be taken into account.

An assessment of some scenarios, including the ‘hole in the clouds’ scenario, can help providing estimates for the remaining error after using the smear correction algorithm. The error term is expected to be small for stationary images without skipped/flagged rows, while the pseudo-static approach will perform worse for scenarios that vary during the integration time.

Because the pseudo-static approach will be the baseline, we formulate the error in more detail. From the list above, the coefficients and the matrix inverse are known and give no error. The three assumptions are no longer needed. That leaves, besides the formal error propagation (directly following from our model equation) , three error sources: noise, time-varying scenes and (possibly) flagged/skipped rows. Note that, even if row skipping has not been planned in a configuration, an unsaturated flagged pixel has to be treated as a skipped pixel since the value of its signal is unknown.

Formal error propagation from the smear correction According to equation Equation (234), the signal in a row r changes due to a multiplication and an additive term based on all other signals in the column c :

$$S_\mathrm{o}[\mathbf{x}_\mathrm{img}] = S_\mathrm{i}[\mathbf{x}_\mathrm{img}] - M(S_\mathrm{i}[\mathbf{x}_\mathrm{img}]) = S_\mathrm{i}[\mathbf{x}_\mathrm{img}] - \frac{\tau}{t_\mathrm{exp} + n\tau} \sum_{q=1}^{m} n_q S_\mathrm{i}[q,c] \tag{253}$$

$$= \left(1 - \frac{\tau n_r}{t_\mathrm{exp} + n\tau}\right) S_\mathrm{i}[\mathbf{x}_\mathrm{img}] - \frac{\tau}{t_\mathrm{exp} + n\tau} \sum_{q \neq r} n_q S_\mathrm{i}[q,c] \tag{254}$$

For the error propagation, the best-case scenario is a full correlation of all signals in the entire column: it results in an error multiplier smaller than one. We assume here, however, that the signals in the column are uncorrelated. This assumption is still rather conservative: a negative correlation between signal $S_\mathrm{i}[\mathbf{x}_\mathrm{img}]$ and the other signals in the column is unlikely, given our knowledge of the instrument. We therefore get for the *modeled* error propagation

$$s^2_\mathrm{model}[\mathbf{x}_\mathrm{img}] = \left(1 - \frac{\tau n_r}{t_\mathrm{exp} + n\tau}\right)^2 \sigma_\mathrm{i}^2[\mathbf{x}_\mathrm{img}] + \left(\frac{\tau}{t_\mathrm{exp} + n\tau}\right)^2 \sum_{q \neq r} n_q^2 \sigma_\mathrm{i}^2[q,c]. \tag{255}$$

As above, we might approximate the summation as

$$\sum_{q \neq r} n_q^2 \sigma_\mathrm{i}^2[q,c] \approx f_\mathrm{column-scaling} \sum_{q \neq r;\ \ \mathrm{usable}} n_q^2 \sigma_\mathrm{i}^2[q,c]. \tag{256}$$

Noise We start with Equation (234). The propagated measurement noise for each binned pixel $s^2_{\text{meas}}[\mathbf{x}_{\text{img}}]$ is available; it has been corrected for the binning factor. This gives, similar as for the error:

$$s^2_{\text{noise}}[\mathbf{x}_{\text{img}}] = (\frac{\tau}{t_{\text{exp}} + n\tau})^2 \sum_{q \neq r} n_q^2 s^2_{\text{meas}}[q, c] \ . \tag{257}$$

where again

$$\sum_{q \neq r} n_q^2 s^2_{\text{meas}}[q, c] \approx f_{\text{column-scaling}} \sum_{q \neq r; \quad \text{usable}} n_q^2 s^2_{\text{meas}}[q, c]. \tag{258}$$

This component of the error will be optional as its magnitude seems negligible. Note that the noise of the pixel signal itself does not change since this is an additive algorithm.

Time-varying scenes We use Equation (250). This is a better approximation than the worst-case scenario described in Equation (252).

The small pixel column can be used to estimate the scaling factors $\alpha_{q,0}$ and $\alpha_{q,N_{\text{coadd}}}$. The flux f_q can be approximated with $S[q, c_{\text{img}}]/(t_{\text{exp}} + n\tau)$.

So we set, using the notation c_{spc} for the image column that is associated with the small pixel column: $\alpha_{q,t_0} = w'_{\text{spc}}[q][1]/w'[q, c_{\text{spc}}]$ and $\alpha_{q,t_{N_{\text{coadd}}}} = w'_{\text{spc}}[q][N_{\text{coadd}}]/w'[q, c_{\text{spc}}]$ for a binned pixel q. The two summations in Equation (250) must be performed in the binned sense, therefore

$$s^2_{\text{nonstatic}}[\mathbf{x}_{\text{img}}] = \left[\frac{1}{2}\tau \frac{1}{(t_{\text{exp}} + n\tau) N_{\text{coadd}}} \left(\sum_{q=1}^{r_{\text{img}}-1} n_q S[q, c_{\text{img}}](\alpha_{q,t_{N_{\text{coadd}}}} - \alpha_{q,t_0}) + \sum_{q=r_{\text{img}}+1}^{m} n_q S[q, c_{\text{img}}](\alpha_{q,t_0} - \alpha_{q,t_{N_{\text{coadd}}}}) \right)\right]^2 \tag{259}$$

Note that the summation should ignore flagged pixels; potential effects can be expected to cancel.

From these formula we see that the error for one co-addition is estimated to be zero, which of course need not to be the case. Because of the assumption of piecewise linear approximation, only the small pixel data for the first and last co-addition have to be used. A better approximation would be achieved if we also use the small pixel columns from the previous and next image. Further, if the scene is monotonous in the across-track direction, then the largest errors will occur at both low and high row numbers. Finally, the sum between brackets is again largest for a 2x2 checkerboard pattern (temporally increasing signals in low-numbered rows combined with temporally decreasing signals in high-numbered rows or vice versa).

Skipping/flagging In a skipped/flagged pixel r , we use an estimate for the unknown w_r: The signal is interpolated from neighboring signals. The worst case scenario is that the skipped row does not receive any light, such that the order or magnitude of the error is the same as the neighboring signals. Equation (234) can be split in two:

$$M(w'_r) = \frac{\tau}{t_{\text{exp}} + n\tau} \left[\sum_{j \text{ not skipped}} n_j w'_j + \sum_{j \text{ skipped}} n_j w'_j \right] \ . \tag{260}$$

Therefore, we can estimate the skip/flag error as

$$\sigma^2_{\text{skip,flag}}[c_{\text{img}}] = \left[\frac{1}{2} \frac{\tau}{t_{\text{exp}} + n\tau} \sum_{j \text{ skipped}} n_j (S[j-1] + S[j+1]) \right]^2 \tag{261}$$

Because this estimate is very conservative, the influence of this error component may be too large in practice. We therefore decide to ignore this term and instead decrease the quality number of the pixels in the column. We set

$$Q[\mathbf{x}_{\text{img}}] = max\left(0, Q[\mathbf{x}_{\text{img}}] - \alpha(1 - \frac{1}{f_{\text{column-scaling}}})\right) \tag{262}$$

The factor α is an algorithm parameter between 0 and 1 that can ameliorate the negative effect on the quality number.
For completeness, we give the formal propagation:

$$\sigma^2_{\text{o}}[\mathbf{x}_{\text{img}}] = s^2_{\text{model}}[\mathbf{x}_{\text{img}}] + s^2_{\text{nonstatic}}[\mathbf{x}_{\text{img}}] + \mathbf{I}_{\text{include-noise-term}} \, s^2_{\text{noise}}[\mathbf{x}_{\text{img}}] \tag{263}$$

C.8 Concluding remarks

The pseudo-static approach gives a fast smear correction that is almost exact. An implementation that handles binning, skipping and flagging has been described in the previous sections (Equations 234 and 243).

Using dark areas (smear areas) in-flight makes it possible to compare measurement with theory.

D Nonlinearity

For each detector the non-linearity is determined in the following way: LED measurements for a range of exposure times are performed such that the highest exposure times result in up to 100% register full well, while the lower exposure times show a linear behavior of the register charge as function of the exposure time. Ideally, the latter measurements coincide with the gain ratio calibration measurements. The non-linearity is now defined as the difference between the expected linear behavior and the actually measured register charges. This difference is then converted to a function of the measured signal, instead of the exposure time.

The derived non-linearity curves and their uncertainties are CKD parameters. Per construction and per definition, the non-linearity is zero for zero signal. If not, an extra offset would be introduced in the correction.

D.1 Used parameters and symbols

Parameter	Description	Units
$S_\mathrm{i}[\mathbf{x}_\mathrm{img}]$	signal in image pixel $\mathbf{x}_\mathrm{img}$ before correction	e$^-$
$\sigma_\mathrm{i}^2[\mathbf{x}_\mathrm{img}]$	signal variance in image pixel $\mathbf{x}_\mathrm{img}$ before correction	e^{-2}
$S_\mathrm{o}[\mathbf{x}_\mathrm{img}]$	signal in image pixel $\mathbf{x}_\mathrm{img}$ after correction	e$^-$
$\sigma_\mathrm{o}^2[\mathbf{x}_\mathrm{img}]$	signal variance in image pixel $\mathbf{x}_\mathrm{img}$ after correction	e^{-2}
$f_\mathrm{ccd}(S_\mathrm{i}[\mathbf{x}_\mathrm{img}])$	non-linearity correction function, per detector	e$^-$ / e$^-$
$s_\mathrm{ckd}^2(S_\mathrm{i}[\mathbf{x}_\mathrm{img}])$	variance of the non-linearity correction function	e^{-2}
$s_\mathrm{noise}^2(S_\mathrm{i}[\mathbf{x}_\mathrm{img}])$	noise part of the non-linearity error	e^{-2}
$s_\mathrm{ccd}(S_\mathrm{i}[\mathbf{x}_\mathrm{img}])$	envelope of the calibration measurements for the non-linearity function	e$^-$
L_max	upper limit of linear range for read-out values	e$^-$
L_sat	saturation threshold, related to register full well	e$^-$
N	order of the polynomials describing non-linearity and its error	1
$s_\mathrm{coadd}^2[\mathbf{x}_\mathrm{img}]$	variance due to co-additions	e^{-2}

D.2 Algorithm description

A polynomial function f_ccd is evaluated for the measured pixel signal; the outcome is subtracted from the signal.

$$S_\mathrm{o}[\mathbf{x}_\mathrm{img}] = S_\mathrm{i}[\mathbf{x}_\mathrm{img}] - f_\mathrm{ccd}(S_\mathrm{i}[\mathbf{x}_\mathrm{img}]) \ . \tag{264}$$

We expect all signals with low charges to behave as a linear function of the corrected exposure time. More specific, we define the line describing this behavior by two points, associated with zero charge and a predefined charge L_max. The choice for L_max depends on the expected behavior of the CCD and must be the same for all pixels.

The non-linearity function f_ccd can be rather complicated. Its definition depends on the input value S_i. We have $f_\mathrm{ccd}(0) = 0$ and $f_\mathrm{ccd}(L_\mathrm{max}) = 0$. Further, it is expected that f_ccd is small, in absolute sense, for charges in the interval $(0, L_\mathrm{max})$. Above the saturation threshold L_sat, which is related to the register full well, the polynomial regression fit no longer holds and the function is undefined. Below the L_sat threshold, the non-linearity is described using a Chebyshev polynomial of a certain order N. The corresponding $N+1$ Chebyshev coefficients, together with the two threshold values, are sufficient to evaluate the function.

D.3 Error propagation

The non-linearity function $f_\mathrm{ccd}(Q)$ can be regarded as the mean correction term for a certain charge Q. Likewise, an accompanying function $s_\mathrm{ckd}(Q)$ denotes the standard deviation of the correction term for the same Q. That is, both the non-linearity correction and its standard deviation/variance depend on the value of the signal S_i.

We addressed some difficulties in establishing the variance of the calibration key data already in the aforementioned document [8]. The total CKD error is constituted of three terms: The inherited L01b Processor error s_l01b^2, the error stemming from the noise s_noise^2 and the error in the polynomial approximation s_curve^2 of the actual, albeit unknown, function. These three terms are defined as a function of signal S_i instead of pixel $\mathbf{x}_\mathrm{img}$.

After adding these three terms, this total error is again described with a Chebyshev polynomial, on the same interval as the non-linearity function itself. Note that we could, in principle, recursively define a curve error of the polynomial expansion of the error, but then we would try to model second-order effects. We discuss three aspects of the error: The noise part of the CKD error, the implementation of the propagation, and the role of co-additions.

First, the **noise part of the CKD error**. In order to model the error stemming from the noise, we first consider the simplified case of linear regression. Note that, in the case of linear regression instead of Chebyshev polynomial regression with order N, the variance would be:

$$s^2_{\text{lin}}(S_{\text{i}}[\mathbf{x}_{\text{img}}]) = s^2_{\text{ccd}}(S_{\text{i}}[\mathbf{x}_{\text{img}}])(1 + \frac{1}{n_{\text{ref}}} + \frac{(S_{\text{i}}[\mathbf{x}_{\text{img}}] - \overline{X}_{\text{ref}})^2}{S_{\text{XX,ref}}}) \ . \tag{265}$$

We argue that the first term 1 is to be dropped since we are not performing individual observations with measurement noise here and therefore only consider the mean value of the non-linearity function. Here a few ancillary symbols are introduced: n_{ref} denotes the number of observations involved in the linear part of the calibration, $\overline{X}_{\text{ref}}$ denotes the mean of the signal observations in the linear part of the calibration, and $S_{\text{XX,ref}}$ denotes the sum of squared deviations from the mean $\sum_i (X_i - \overline{X}_{\text{ref}})^2$. The subscript ‘ref’ is a reminder that the non-linearity calibration measurements have been performed with the reference gain, in order for them to be compared with the gain ratio calibration measurements.

Now, we move on to the actual case of higher order regression. Clearly, the standard deviation of an individual measurement is $s_{\text{ccd}}(Q)$ as obtained during the computation of the CKD. Graphically, it is the width of the envelope around the cloudy function to be parametrized by the Chebyshev polynomial f_{ccd}.

We would like to use a variant of Equation (265) that works for higher orders. The third term of the equation, invoking the pivoting of the slope around $\overline{X}$ is now meaningless since there is no longer a slope coefficient with global influence. Instead, we should recognize the localized character of the regression curve and change the variable n_{ref} into a localized definition: $n_{\text{ref}} = n_{\text{obs}}/N$ where N is the order of the polynomial describing the curve. To state the matter loosely, we expect that per Chebyshev node only the nearby surrounding observations are important. Therefore:

$$s^2_{\text{noise}}(S_{\text{i}}[\mathbf{x}_{\text{img}}]) = s^2_{\text{ccd}}(S_{\text{i}}[\mathbf{x}_{\text{img}}])(0 + \frac{N}{n_{\text{obs}}}) \ , \tag{266}$$

where we again discard the first term 1 as being the instrumental error.

Another possibility is that the said envelope is persistent, i.e. does not become thinner when the noise is decreased. This can be the case if instrument behavior remains outside a model, for example an unknown additional non-linearity. In that case s^2_{noise} must be replaced by s^2_{ccd}. This gives the CKD error as obtained from on-ground calibration:

$$s^2_{\text{ckd}}[S_{\text{i}}] = s^2_{\text{l01b}}[S_{\text{i}}] + s^2_{\text{noise}}[S_{\text{i}}] + s^2_{\text{curve}}[S_{\text{i}}]. \tag{267}$$

Then, the **implementation of the error propagation.** The signal is propagated as $S_{\text{o}} = S_{\text{i}} - f_{\text{ccd}}(S_{\text{i}})$. Formally, we can write the error propagation of a function $g(S_{\text{i}}) = S_{\text{i}} - f(S_{\text{i}})$ as

$$s^2_g = (1 - \frac{df_{\text{ccd}}}{dS_{\text{i}}})^2 s^2_{S_{\text{i}}} = (1 - \frac{df_{\text{ccd}}}{dS_{\text{i}}})^2 \sigma^2_{\text{i}}. \tag{268}$$

However, we have to take into account that f_{ccd} is not known exactly: it has its own error $s^2_{f,\text{ccd}}$, in this case given by the available CKD function s^2_{ckd}. We cannot formalize this but instead choose a pragmatic solution: this error serves as an extra additive term. (Alternatively, we can write $g = g(S_{\text{i}}, f)$ and error propagation gives an extra term $(dg/df)^2 s^2_f = (-1)^2 s^2_{\text{ckd}}$. This seems to work well, although the correlation between S_{i} and f is hard to define.) Note further that, although we can write $f_{\text{ccd}} = \sum c_j T_j$, we are not allowed to perform formal error propagation using $g = g(S_{\text{i}}, c_0, \cdots c_N)$ since the c_j are correlated. Therefore we state that the error propagation formula is

$$\sigma^2_{\text{o}} = (1 - \frac{df_{\text{ccd}}}{dS_{\text{i}}})^2 \sigma^2_{\text{i}} + s^2_{\text{ckd}}. \tag{269}$$

Equation (269) makes it necessary to evaluate not only the non-linearity function itself, but also its derivative, expressed in Chebyshev polynomials. Fortunately, the derivative of a Chebyshev polynomial expression is easily computed.

Finally, we discuss the **role of co-additions**. We make an error because we are correcting the co-added signal instead of the individual original signals. This is a second-order effect. It is difficult to get an indication of the size of the error since we do not have the original signals of each frame. However, we can make use of the small pixel columns to get a rough estimation. In case of co-addition, any signal S is the mean of N_{coadd} frame signals $S_{\mathrm{coadd},j}$. So we make the following error, where we use the shorthand notation S as argument for the non-linearity function:

$$\sigma^2_{\mathrm{coadd}} = \left[f_{\mathrm{ccd}}(S) - \frac{1}{N_{\mathrm{coadd}}} \sum_{j=1}^{N_{\mathrm{coadd}}} f_{\mathrm{ccd}}(S_{\mathrm{coadd},j}) \right]^2 . \tag{270}$$

We repeat that we do not know the original $S_{\mathrm{coadd},j}$. Instead we make an estimate by using scaling factors based on the small pixel data:

$$s^2_{\mathrm{coadd}} = \left[f_{\mathrm{ccd}}(S) - \frac{1}{N_{\mathrm{coadd}}} \sum_{j=1}^{N_{\mathrm{coadd}}} f_{\mathrm{ccd}}(\alpha_j S) \right]^2 . \tag{271}$$

Here the α_j give an estimate of the temporal change of the entire image, based on the two small pixel columns, such that $\sum_{j=1}^{N_{\mathrm{coadd}}} \alpha_j = N_{\mathrm{coadd}}$. If this estimate cannot be made, we can as a worst-case scenario choose the set of α_j and therefore the non-linearities $f_{\mathrm{ccd}}(\alpha_j S)$ such that the deviations are largest.

The total error propagation is now

$$\sigma^2_{\mathrm{o}}[\mathbf{x}_{\mathrm{img}}] = \left(1 - \frac{d f_{\mathrm{ccd}}}{dS_{\mathrm{i}}} (S_{\mathrm{i}}[\mathbf{x}_{\mathrm{img}}]) \right)^2 \sigma^2_{\mathrm{i}}[\mathbf{x}_{\mathrm{img}}] + s^2_{\mathrm{ckd}}(S_{\mathrm{i}}[\mathbf{x}_{\mathrm{img}}]) + s^2_{\mathrm{coadd}}[\mathbf{x}_{\mathrm{img}}] . \tag{272}$$

Allowed values	Measurement types executed	IC value	Measurement class	Orbit
8	solar cal, volume diffuser, BF8	8, 9	1 "Sun", 4 "Dark"	Daily
14	solar cal, volume diffuser, BF1	14, 15	1 "Sun", 4 "Dark"	Weekly 1
18	solar cal, regular diffuser, BF8	18, 19	1 "Sun", 4 "Dark"	Weekly 2
30	solar cal, backup diffuser, BF8	30, 31	1 "Sun", 4 "Dark"	Monthly 2
50	solar cal, volume diffuser, BF4 (spatial)	50, 51	1 "Sun", 4 "Dark"	Nominal 2
62	solar cal, volume diffuser, BF4 (spectral)	62, 63	1 "Sun", 4 "Dark"	Nominal 4

Table 18: Measurement types in the solar calibration SIS. The allowed values in the first column are the allowed instrument configuration values at the start of a SIS.

Exit code	Description
4	Normal end of solar calibration SIS
40	FMM error when moving FMM to nominal position at end of SIS
41	DifM error when moving DifM to nominal position at end of SIS
42	FMM and DifM error when moving FMM and DifM to nominal position at end of SIS
43	SAM error when moving SAM to nominal (closed) position after solar light measurement
44	DifM error when moving DifM to required calibration position
45	Prohibited instrument configuration value defined at start of SIS
46	DifM error when moving DifM to reference end position
47	SAM error when moving SAM to calibration (open) position
48	FMM error when moving FMM to calibration position

Table 19: User defined exit codes generated by the solar calibration SIS.

E Stored instruction sequences for calibration measurements

This appendix gives details on a selection of stored instruction sequences (SISs). The different SIS types can each perform a number of calibration measurements. Which type of measurement is performed depends on the instrument configuration value as defined in the ELU register. The instrument configuration value must therefore be defined in the master command load (MCL) before the SIS is executed. Within the SIS, the instrument configuration value as well as the measurement class value are updated before a new measurement type starts. When a SIS finishes a user defined exit code is generated. In the following the instrument configuration values (IC values) and exit codes are given for a selection of calibration SISs.

E.1 Solar calibration SIS

The solar calibration SIS covers twelve different types of solar calibration measurements. Table 18 shows which solar calibrations are performed by the solar calibration SIS depending on the instrument configuration value. Table 19 shows the exit codes that can be generated by the solar calibration SIS.

E.2 LED calibration SIS

The LED calibration SIS can perform eight different types of LED calibration measurements. Table 20 shows which LED calibrations are performed by the LED calibration SIS depending on the instrument configuration value. Table 21 shows the exit codes that can be generated by the LED calibration SIS.

Allowed values	Measurement types executed	IC value	Measurement class	Orbit
10	LED source (dark & light)	10, 11	4 "Dark", 3 "LED"	Daily
26	LED stability (dark & light)	26, 27	4 "Dark", 3 "LED"	Weekly 3
32	LED 4 gains, LED 1 gain (dark), LED 4 gains, LED 1 gain (light)	32, 33, 34, 35	4 "Dark", 3 "LED"	Monthly 2

Table 20: Measurement types in the LED calibration SIS.The allowed values in the first column are the allowed instrument configuration values at the start of a SIS.

Exit code	Description
5	Normal end of LED calibration SIS
50	LED not switched off at end of SIS
51	FMM error when moving FMM from calibration position to nominal position
52	FMM error after applying HT in calibration position
53	Prohibited instrument configuration value defined at start of SIS
54	FMM error when moving FMM to calibration position

Table 21: User defined exit codes generated by the LED calibration SIS.

Allowed values	Measurement types executed	IC value	Measurement class	Orbit
20	WLS PRNU (dark & light)	20, 21	4 "Dark", 2 "WLS"	Weekly 2
28	WLS radiometric stability (dark & light)	28, 29	4 "Dark", 2 "WLS"	Weekly 3
36	WLS 4 gains, WLS 1 gain (dark), WLS 4 gains, WLS 1 gain (light), WLS linearity[†] (dark & light)	36, 37, 38, 39, 40, 41	4 "Dark", 3 "WLS"	Monthly 2

Table 22: Measurement types in the WLS calibration SIS.The allowed values in the first column are the allowed instrument configuration values at the start of a SIS.
[†] The linearity measurement was removed in August 2005

Exit code	Description
6	Normal end of WLS calibration SIS
60	WLS not switched off at end of SIS
61	FMM error when moving FMM to nominal position
62	Prohibited instrument configuration value defined at start of SIS
63	DifM error when moving DifM from ref. end position to transmission position
64	DifM error when moving DifM from initial position to reference end position
65	FMM error when moving FMM from nominal position to calibration position

Table 23: User defined exit codes generated by the WLS calibration SIS.

E.3 WLS calibration SIS

The WLS calibration SIS can perform ten different types of WLS calibration measurements. Table 22 shows which WLS calibrations are performed by the WLS calibration SIS depending on the instrument configuration value. Table 23 shows the exit codes that can be generated by the WLS calibration SIS.

Allowed values	Measurement types executed	IC value	Measurement class	Orbit
3	short global dark tropical, midlatitude, arctic, ozone hole	3, 4, 5, 6	4 "Dark"	Nominal 1
4	long global dark tropical, midlatitude, arctic, ozone hole	3, 4, 5, 6	4 "Dark"	Nominal 1
16	Long exposure dark, 4 gains used, 1 gain used	16, 17	4 "Dark"	Weekly 1
22	Global dark with FMM tropical, midlatitude, arctic, ozone hole	22, 23, 24, 25	4 “Dark”	Weekly 2
45	Spatial dark tropical, midlatitude, arctic, ozone hole	45, 46, 47, 48	4 "Dark"	Nominal 2
52	Spatial dark with FMM tropical, midlatitude, arctic, ozone hole	52, 53, 54, 55	4 "Dark"	Monthly 1
59	Spectral dark tropical, midlatitude, arctic	59, 60, 61	4 "Dark"	Nominal 3
64	Spectral dark with FMM tropical, midlatitude, arctic	64, 65, 66	4 "Dark"	Nominal 4

Table 24: Measurement types in dark calibration SIS. The allowed values in the first column are the allowed instrument configuration values at the start of a SIS.

Exit code	Description
7	Normal end of Dark Calibration SIS
70	FMM error when moving FMM to nominal position at end of SIS
71	Prohibited Instrument Configuration value defined at start of SIS
72	FMM error when moving FMM from nominal position to calibration position at beginning of SIS

Table 25: User defined exit codes generated by the dark calibration SIS.

Allowed values	Measurement types executed	IC value	Measurement class	Orbit
12	Long exposure dark, exp. time 42s, exp. time 158s	12, 13	4 "Dark"	Monthly 3 orbit
141	Long exposure dark, exp. time 42s, exp. time 158s, short bad pixels 42s, short bad pixels 158s	12, 13, 141, 142	4 "Dark"	Daily
103	LEO dark; long exposure middle	103	4 "Dark"	Daily

Table 26: Measurement types in dark orbit SIS. The allowed values in the first column are the allowed instrument configuration values at the start of a SIS.

E.4 Dark calibration SIS

The dark calibration SIS can perform 24 different types of dark calibration measurements. Table 24 shows which dark calibrations are performed by the dark calibration SIS depending on the instrument configuration value. Table 25 shows the exit codes that can be generated by the dark calibration SIS.

E.5 Dark orbit SIS

The dark orbit calibration SIS can perform five different types of dark calibration measurements. Table 26 shows which dark orbit calibrations are performed by the dark orbit calibration SIS depending on the instrument configuration value. Table 27 shows the exit codes that can be generated by the dark orbit SIS.

Exit code	Description
9	Normal end of dark orbit SIS
90	FMM not in nominal position at end of SIS
91	FMM not in calibration position after applying holding torque before moving from calibration to nominal position
92	Prohibited instrument configuration value defined at start of SIS
93	FMM not in calibration position after moving from nominal to calibration position
94	SIS control has invalid value

Table 27: User defined exit codes generated by the dark orbit SIS.